

# Mass transport and structural properties of liquid iron alloys at high pressure

---

eingereicht an der **Bayreuther Graduiertenschule für  
Mathematik und Naturwissenschaften (BayNAT)**

submitted to the **Bayreuth Graduate School of  
Mathematics and Natural Sciences (BayNAT)**

zur Erlangung der Würde eines Doktors der Naturwissenschaften  
– Dr. rer. nat. –

**Dissertation**

vorgelegt durch

**Esther Posner**  
aus Detroit (U.S.A.)

Bayreuth, 2017



Die vorliegende Arbeit wurde in der Zeit von Januar 2013 bis April 2017 in Bayreuth am Lehrstuhl Bayerischen Geoinstitut unter Betreuung von Herrn Professor Dr. David Rubie angefertigt.

Vollständiger Abdruck der von der Bayreuther Graduiertenschule für Mathematik und Naturwissenschaften (BayNAT) der Universität Bayreuth genehmigten Dissertation zur Erlangung des akademischen Grades eines Doktors der Naturwissenschaften (Dr. rer. nat.).

Dissertation eingereicht am: 02.02.2017

Zulassung durch das Leitungsgremium: 06.02.2017

Wissenschaftliches Kolloquium: 26.04.2017

Amtierender Direktor: Prof. Dr. Stephan Kümmel

Prüfungsausschuss:

Prof. Dr. David Rubie	(Erstgutachter)
Dr. Katharina Marquadt	(Zweitgutachterin)
Prof. Dr. Daniel Frost	(Vorsitz)
Prof. Dr. Hans Keppeler	



Dedicated with loving gratitude to Andreas



# Summary

Mass transport properties of molten iron and iron alloys at high pressures ( $P$ ) and temperatures ( $T$ ) are important for understanding large-scale geochemical processes related to the thermochemical evolution of planetary cores. In particular, the diffusivities of light and siderophile elements in liquid iron under the extreme  $P$ - $T$  conditions of the Earth's core and its formation place important kinetic constraints on the time and length scales of (1) chemical equilibration between metal and silicate during core formation, (2) compositional convection in the Earth's liquid outer core, and (3) potential chemical stratification and exchange between mantle and core during cooling. In order to better understand the effects of  $P$  and  $T$  on Si, O, and Cr diffusion in liquid iron, as well as Fe self-diffusion, we have conducted both chemical diffusion-couple experiments using a multi-anvil press and theoretical calculations using first principles molecular dynamics (FP-MD). This is the first study to jointly use and compare experimental and computational results, conducted under similar conditions, to determine the effect of pressure on diffusion in liquid iron and iron alloys.

Diffusion coefficients calculated from FP-MD simulations are in excellent agreement with experimental results. Arrhenian activation terms obtained by both methods are in good agreement with previous empirical estimates and computational results and substantially smaller than previously reported experimental values derived from much smaller data sets. Our findings corroborate theoretical estimates that diffusion coefficients are scalable to homologous temperature ( $T_m/T$ , where  $T_m$  is the absolute melting temperature), yielding constant diffusivities of approximately  $5 \times 10^{-9} \text{ m}^2 \text{ s}^{-1}$  for Si, Cr, and Fe and  $\sim 1 \times 10^{-8} \text{ m}^2 \text{ s}^{-1}$  for O along the entire melting curve

from ambient to core pressures. Verification of a homologous temperature relation for diffusion in liquid iron implies that low-pressure diffusion data can be used with confidence to predict rates of mass transport in the Earth's liquid outer core.

Mass transport properties are sensitive to structural properties of liquid metals and can therefore be used as 'indicators' of the liquid structure and mechanisms of alloying element incorporation, which are challenging to measure directly. The wide range of  $P$ - $T$  conditions accessible by FP-MD simulations provides new insights into compression mechanisms operating in liquid iron alloys, as well as the relationship between transport and structural properties that may be used as a proxy to estimate the solubility and/or solid-liquid partition coefficients of relevant solute species. Accordingly, a second aspect of the dissertation is the investigation of structural properties of liquid iron alloys, i.e., average interatomic distances and local coordination environments, using partial radial distribution functions obtained from the FP-MD simulations.

We report a change in compression mechanism in liquid  $\text{Fe}_{0.96}\text{O}_{0.04}$  at a simulation density of approximately  $8 \text{ g cm}^{-3}$ . Below this density, compression is accommodated by a closer packing of both iron and oxygen atoms with an increase in coordination numbers from  $\sim 10$  to  $\sim 13$  and  $\sim 3$  to  $\sim 6$ , respectively. This structural transformation coincides with an increase in the average Fe-O distances while average Fe-Fe distances remain essentially constant. Additionally, oxygen self-diffusion coefficients calculated from the atomic trajectories over this density range show a negligible pressure dependence, consistent with our experimental results up to 18 GPa. Above  $\sim 8 \text{ g cm}^{-3}$ , the liquid is essentially close-packed and compression is accommodated by a reduction of the atomic volume of both iron and oxygen. Above  $\sim 8 \text{ g cm}^{-3}$ , interatomic distances and diffusion rates for both species decrease

monotonically with increasing density. The coordination of oxygen reaches a maximum of  $\sim 8.5$  at  $\sim 9.4 \text{ g cm}^{-3}$  and does not further increase upon further compression to  $11.6 \text{ g cm}^{-3}$ , indicating a local B2 packing structure for Fe around O under conditions of the Earth's core. The stable crystal structure of iron at inner core pressures is widely regarded to be hexagonal close-packed, which implies that the large strain energies associated with oxygen incorporation may result in its strong fractionation into the liquid outer core during inner core crystallization, as suggested by previous theoretical studies. Additionally, the liquid-liquid structural transformation reported here may be a viable explanation to the previously reported change from a negative to a positive pressure dependence of the solubility of oxygen in liquid iron.



# Zusammenfassung

Transporteigenschaften von flüssigem Eisen und flüssigen Eisenlegierungen bei hohem Druck ( $P$ ) und hoher Temperatur ( $T$ ) spielen eine wichtige Rolle für das Verständnis von großräumigen geochemischen Prozessen im Innern von Planeten sowie bei deren thermischer und chemischer Entwicklung. Zu solchen Prozessen gehören die Zeit- und Längenskalen, die zum Erreichen eines chemischen Gleichgewichts zwischen Silikaten und Metallen notwendig sind, was zum Beispiel für den Stoffaustausch an der Kern-Mantel-Grenze eines Planeten bei dessen Abkühlen als auch bei der Kernbildung in jungen Planeten eine zentrale Rolle spielt. Die Bestimmung von chemischen Diffusionskonstanten leichter und siderophiler Elemente in flüssigem Eisen bei  $P$ - $T$  Bedingungen des Erdkerns sowie bei der Kernbildung ist notwendig, um dessen Zusammensetzung und seine mögliche Stratifizierung zu verstehen. Darüber hinaus helfen sie dabei, den chemischen Auftrieb im äußeren Kern zu bestimmen, der einen wichtigen Beitrag zur dynamischen Erzeugung des Magnetfelds der Erde leistet. Um den Einfluss von Druck und Temperatur auf die Diffusion von Si, O und Cr in flüssigem Eisen – sowie auf Fe-Selbstdiffusion – zu charakterisieren, haben wir eine Reihe von Untersuchungen durchgeführt. Dies sind zum einen Laborexperimente mit Diffusionspaaren in der Vielstempelpresse in einem Druckbereich von 1 bis 18 GPa sowie Temperaturen von 1873 bis 2643 K, zum anderen *ab-initio* Molekulardynamik-Simulationen zwischen 0 und 330 GPa sowie 2200 und 5500 K. Die vorliegende Dissertation ist die erste Arbeit über Diffusion in flüssigem Eisen bei hohem Druck und hoher Temperatur, in der sowohl Experimente als auch Simulationen bei ähnlichen Bedingungen durchgeführt und die Ergebnisse direkt miteinander verglichen werden.

Diffusionskonstanten, die in den Molekulardynamik-Simulationen bestimmt wurden, stimmen hervorragend mit den experimentell gemessenen Werten überein. Eine Anpassung beider Datenreihen mit Hilfe einer Arrhenius-Gleichung ergibt Werte für die Aktivierungskoeffizienten, die mit empirischen und bereits veröffentlichten Ergebnissen aus Molekulardynamik besser übereinstimmen als mit vorhergehenden experimentellen Messungen, die allerdings auch auf deutlich kleineren Datenreihen beruhen. Unsere Ergebnisse bestätigen auch theoretische Überlegungen, dass Diffusionskonstanten mit der homologen Temperatur ( $T_m/T$ , wobei  $T_m$  die Schmelztemperatur ist) skalieren. Diese Skalierung ergibt konstante Diffusionskonstanten entlang der gesamten Schmelzkurve von Eisen für Drücke von der Oberfläche bis zum Kern, mit Werten von ungefähr  $5 \cdot 10^{-9} \text{ m}^2 \cdot \text{s}^{-1}$  für Si, Cr und Fe sowie  $1 \cdot 10^{-8} \text{ m}^2 \cdot \text{s}^{-1}$  für O. Die Bestätigung dieser Skalierung bedeutet, dass Messungen, die bei niedrigem Druck im Labor durchgeführt werden, auch für hohen Druck im Erdkern verwendet werden können.

Transporteigenschaften hängen stark von Struktureigenschaften des flüssigen Metalls ab und geben damit indirekt Hinweise auf die Schmelzstruktur und die Mechanismen der Einbindung von Legierungselementen. Während es schwierig ist, Struktureigenschaften von flüssigen Metallen in Experimenten zu messen, können Molekulardynamik-Simulationen neue Einblicke in Kompressionsmechanismen geben, die in flüssigen Metallen auftreten. Diese können dabei auch mit Transporteigenschaften der verschiedenen Elemente in der Metall-Schmelze in Verbindung gebracht werden und zum Verständnis der Löslichkeit bestimmter Elemente sowie deren Fraktionierung zwischen Flüssigkeit und Festkörper verwendet werden. Deshalb bilden Untersuchungen von Struktureigenschaften von flüssigem Eisen sowie seiner Legierungen unter hohem Druck und hoher

Temperatur den zweiten Schwerpunkt der vorgelegten Dissertation. Wir bestimmen dabei mit Hilfe der radialen Verteilungsfunktion, die aus den *ab-initio* Molekulardynamik-Simulationen errechnet wird, mittlere Abstände zwischen Atomen in der Flüssigkeit sowie deren Koordination unter hohem Druck.

In den Simulationen für geschmolzenes  $\text{Fe}_{0.96}\text{O}_{0.04}$  beobachten wir bei einer Dichte von ca.  $8 \text{ g}\cdot\text{cm}^{-3}$  einen Strukturübergang von einer kubisch-innenzentrierten zu einer dichtest-gepackten Flüssigkeit. In einem Dichtebereich von  $5,4 \text{ g}\cdot\text{cm}^{-3}$  und  $8 \text{ g}\cdot\text{cm}^{-3}$  zeigen berechnete Diffusionskonstanten für Sauerstoff eine ungewöhnlich niedrige Druckabhängigkeit, was mit den von uns durchgeführten Experimenten bis 18 GPa übereinstimmt. Innerhalb dieses Kompressionsbereichs steigt der mittlere Fe-O Abstand mit der Dichte an, während der Fe-Fe Abstand ungefähr gleich bleibt. Dies deutet darauf hin, dass die Kompression der Flüssigkeit durch eine dichtere Packung von Atomen erzielt wird, was auch durch die berechnete Koordinationszahlen von O und Fe bestätigt wird: Die Koordination von Eisen steigt von ca. 10 auf ca. 13, die von O von ca. 3 auf ca. 6. Für Dichten größer als  $\sim 8 \text{ g}\cdot\text{cm}^{-3}$  verkleinern sich die Abstände zwischen den Atomen ebenso wie die Diffusionskonstanten. Die Koordination von O erreicht einen Maximalwert von ca. 8.5 bei einer Dichte von ca.  $9,4 \text{ g}\cdot\text{cm}^{-3}$  und steigt bis zu Dichten von  $11,6 \text{ g}\cdot\text{cm}^{-3}$  nicht weiter an. Die Koordinationszahl weist auf eine Art lokal kubisch-raumzentrierte Struktur von Fe um O bei Bedingungen des Erdkerns hin. Üblicherweise wird die Kristallstruktur von festem Eisen unter Bedingungen des inneren Erdkerns als hexagonal dichteste Kugelpackung betrachtet und in diesem Zusammenhang weist die Koordination von O darauf hin, dass die große Verformungsenergie, die mit dem Einbinden eines Sauerstoffatoms in die Struktur einhergeht, bei der Kristallisation des inneren Erdkerns zu einer bevorzugten Fraktionierung von

O in die flüssige Phase führt. Die Information, die wir hier über die Struktureigenschaften von in Fe gelöstem Sauerstoff gewonnen haben, kann auch eine Änderung in der Löslichkeit von O in flüssigem Eisen – von einer negativen zu einer positiven Druckabhängigkeit – erklären, die in Experimenten bei hohem Druck beobachtet wurde.

Summary

Zusammenfassung

1. Introduction .....	1
1.1 Accretion and core formation.....	1
1.2 Structure of the Earth's core .....	4
1.3 Composition of the core .....	7
1.4 Review of previous studies .....	11
1.5 Aims of this study.....	15
1.6 References .....	16
2. Methods.....	25
2.1 Fundamentals of diffusion theory .....	25
2.2 Diffusion couple experiments .....	28
2.2.1 Multi-anvil sample assembly and procedure .....	28
2.2.2 Analytical procedure.....	29
2.2.3 Experimental data fitting.....	31
2.3 Computational methods.....	32
2.3.1 First-principles molecular dynamic simulations .....	32
2.3.2 Calculation of diffusion coefficients.....	34
2.3.3 Radial pair distribution function .....	36
2.4 References .....	38
3. Synopsis of Results.....	41
3.1 Mass transport and structural properties of Si and Cr in liquid iron at high pressure.....	41
3.2 Mass transport properties of oxygen in liquid iron at high pressure.....	45
3.3 Mass transport and structural properties of $\text{Fe}_{0.96}\text{O}_{0.04}$ at high pressure.....	48
3.4 References .....	53
4. Individual contribution to publications .....	55
5. High $P$ - $T$ experiments and first principles calculations of the diffusion of Si and Cr in liquid iron .....	57
5.1 Abstract .....	57
5.2 Introduction .....	59
5.3 Experimental procedure and analysis.....	62
5.3.1 Multi-anvil sample assembly and procedure .....	62
5.3.2 Analytical procedure.....	65
5.3.3 Melting criteria for diffusion modeling.....	65
5.3.4 Experimental data fitting and calculation of diffusion parameters .....	67
5.4 Computational methods.....	71
5.4.1 FP-MD.....	71
5.4.2 Calculation of self-diffusion coefficients and viscosities.....	72
5.5 Results .....	73

5.5.1	Experimental results of Si and Cr chemical diffusion .....	73
5.5.2	Computational results of Si, Cr, and Fe self-diffusion .....	80
5.5.3	Structural properties .....	83
5.5.4	Effect of pressure on activation enthalpy .....	85
5.5.5	Pressure dependence at constant temperature .....	88
5.5.6	Arrhenius model .....	89
5.6	Discussion .....	92
5.6.1	Diffusion at homologous temperature .....	92
5.6.2	Mass transport contrast and element partitioning across ICB.....	96
5.6.3	Viscosity profile of the outer core .....	97
5.6.4	Chemical equilibration during core formation.....	101
5.7	Conclusions .....	104
5.8	Acknowledgements.....	105
5.9	References .....	106
5.10	Supplemental Material .....	113
5.10.1	Introduction .....	113
5.10.2	Gravitational stability in diffusion experiments.....	113
5.10.3	Concentration dependence of diffusion.....	116
6.	Experimental determination of oxygen diffusion at high pressure.....	125
6.1	Abstract .....	125
6.2	Introduction .....	125
6.3	Experimental procedure and analysis.....	128
6.3.1	Multi-anvil sample assembly and procedure .....	128
6.3.2	Analytical procedure .....	131
6.3.3	Experimental data fitting and calculation of diffusion parameters .....	132
6.4	Results .....	135
6.4.1	Quench products and image analysis .....	135
6.4.2	Oxygen diffusion at high $P$ - $T$ .....	137
6.4.3	Temperature dependence of oxygen diffusion at constant pressure .....	139
6.4.4	Effect of pressure .....	141
6.5	Discussion .....	142
6.5.1	Extrapolation to Earth's outer core .....	142
6.5.2	Length and timescales of chemical equilibration.....	143
6.5.3	Metal-silicate equilibration of oxygen in a magma ocean.....	146
6.6	Conclusions .....	149
6.7	Acknowledgements.....	149
6.8	References .....	150
6.9	Supplemental Material.....	154
6.9.1	Introduction .....	154

7. Structural changes and anomalous self-diffusion of oxygen in liquid iron at high pressure .....	157
7.1 Abstract .....	157
7.2 Introduction .....	158
7.3 Computational methods.....	161
7.4 Results and discussion .....	163
7.4.1 Structural properties.....	163
7.4.2 Self-diffusion of oxygen and iron.....	169
7.4.3 Implications for planetary cores.....	175
7.5 Conclusions .....	177
7.6 Acknowledgements.....	178
7.7 References .....	178
7.8 Supplemental Material.....	182
8. Conclusions and Outlook.....	185



# Chapter 1

## Introduction

The core is Earth's most inaccessible region yet it plays a fundamental role in the evolution and habitability of our planet. Heat transfer out of the planet's core generates powerful convection currents in the liquid outer core that powers the geodynamo and drives our planet's magnetic field (Merrill et al., 1998) – as well as large-scale convection in the Earth's mantle that drives plate tectonics (Turcotte and Schubert, 2007). Despite its tremendous importance, however, many fundamental aspects of the Earth's core, including its origin and evolution, composition, thermal structure, processes and properties remain enigmatic. In this chapter, I review the state of knowledge of the formation and structure of Earth's core, constraints on core composition, as well as a summary of previous studies.

### 1.1 Accretion and core formation

The physical and chemical segregation of the Earth into a dense metallic core and silicate mantle represents the largest differentiation event in our planet's history and is closely related to the manner in which the planet accreted. According to current astrophysical models of solar system formation, the accretion process began shortly ( $< 10^3$  years) after the condensation of dust in a rotating and contracting molecular cloud, which collapsed under its own gravity and flattened into a disc-shaped solar nebula. Through direct

contact, dust grains coalesced and grew to form planetesimals ranging between 10-100 km in size. Internal heating due to the decay of short-lived radioactive nuclides (e.g.  $^{26}\text{Al}$  and  $^{60}\text{Fe}$ ) was sufficient to induce widespread melting of the earliest-formed planetesimals, including the parent bodies of magmatic iron meteorites (Schersten et al., 2006; Qin et al., 2008; Lichtenberg et al., 2016). During such melting events, dense metallic liquids separated from more buoyant oxygen-rich molten silicate and descended towards the center of the planet, releasing more heat through the reduction of gravitational potential energy. Precise  $^{182}\text{Hf}$ - $^{182}\text{W}$  measurements show that planetesimals and asteroids that accreted later, including parent bodies of the chondritic meteorites, did not have sufficient  $^{26}\text{Al}$  and  $^{60}\text{Fe}$  to melt and did not undergo core formation (Schersten et al., 2006; Qin et al., 2008).

As the planetesimals grew, they began to gravitationally interact with one another and their orbits crossed, resulting in collisions and rapid growth into larger (Moon- to Mars-sized) planetary embryos. Numerical simulations suggest that over a timescale of approximately  $10^5$ – $10^6$  years, tens to hundreds of embryos could form at a distance of approximately 1 astronomical unit (AU) from the Sun (Wetherill and Stewart, 1993; Weidenschilling et al., 1997). The final stage of accretion was dominated by mutual gravitational interactions between embryos that resulted in large and violent collisions and the formation of Mars- to Earth-sized bodies over a timescale of  $10^7$ – $10^8$  years (e.g. Chambers and Wetherill, 1998; Morbidelli et al., 2000; Raymond et al., 2014). The amount of heat produced in such giant impact events was sufficient to cause widespread and even planetary-scale melting (Tonks and Melosh, 1993; Rubie et al., 2007; 2015), which facilitated the metal-silicate differentiation process, as described below. The formation of the Moon and

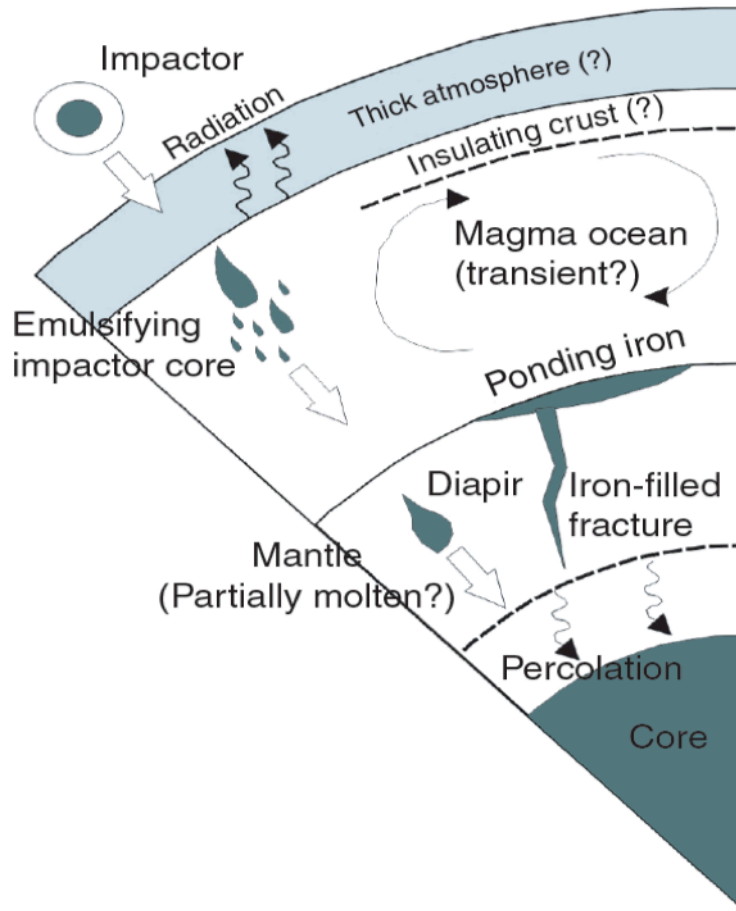


*Figure 1.1: Mechanisms of metal-silicate differentiation during accretion and core formation. Core formation is most efficient in a magma ocean scenario in which differentiated impactor cores may completely emulsify, partially breakup, or remain largely intact. Core formation may also occur via diapirism in a partially crystalline silicate mantle or via percolation in a fully crystalline mantle if the dihedral angle is smaller than  $60^\circ$ . (Rubie et al., 2007)*

Earth's final 'magma ocean' episode, for example, are thought to have resulted from the last giant impact on the Earth involving a Mars-sized impactor (Hartmann and Davis, 1975; Cameron and Ward, 1976; Canup and Asphaug, 2001; Ćuk and Stewart, 2012).

The mechanics, efficiency, and extent of chemical equilibration during metal-silicate differentiation depend largely on the degree of partial melt within the silicate (e.g. Rubie, 2007), as well as the extent of break-up of impacting bodies (i.e. complete or partial emulsification versus remaining largely intact, etc.). A sketch of these processes is shown in Figure 1.1. Core formation in a fully molten magma ocean provides a rapid and efficient differentiation mechanism due to the large density difference between liquid iron and liquid silicate and the low viscosity of ultramafic silicate melts under pressure (Liebske et al., 2005). On the other extreme, percolation of liquid metal through a crystalline silicate aggregate depends on melt connectivity (von Bagen and Waff, 1986; Stevenson, 1990). Other studies have suggested that core formation may occur via diapirism and dyking that result due to gravitational instability developed by liquid iron ponded at the base of a magma ocean (Karato and Murthy, 1997). In the latter two scenarios, chemical exchange between metal and silicate would be limited due to exceedingly slow rates of atomic diffusion in solids ( $\sim 10^{-14} - 10^{-16} \text{ m}^2 \text{ s}^{-1}$ ; Van Orman and Crispin, 2010) compared to those in liquids ( $10^{-8} - 10^{-9} \text{ m}^2 \text{ s}^{-1}$ ; Vočadlo et al., 2003). Metal-silicate chemical equilibration in a magma ocean, on the other hand, is largely controlled by the radius of and diffusion rates in liquid metal droplets, as discussed further in Chapter 6.

## 1.2 Structure of the Earth's core

Knowledge of the Earth's internal layered structure comes largely from discontinuities in the velocity of seismic waves, which are attributed to phase

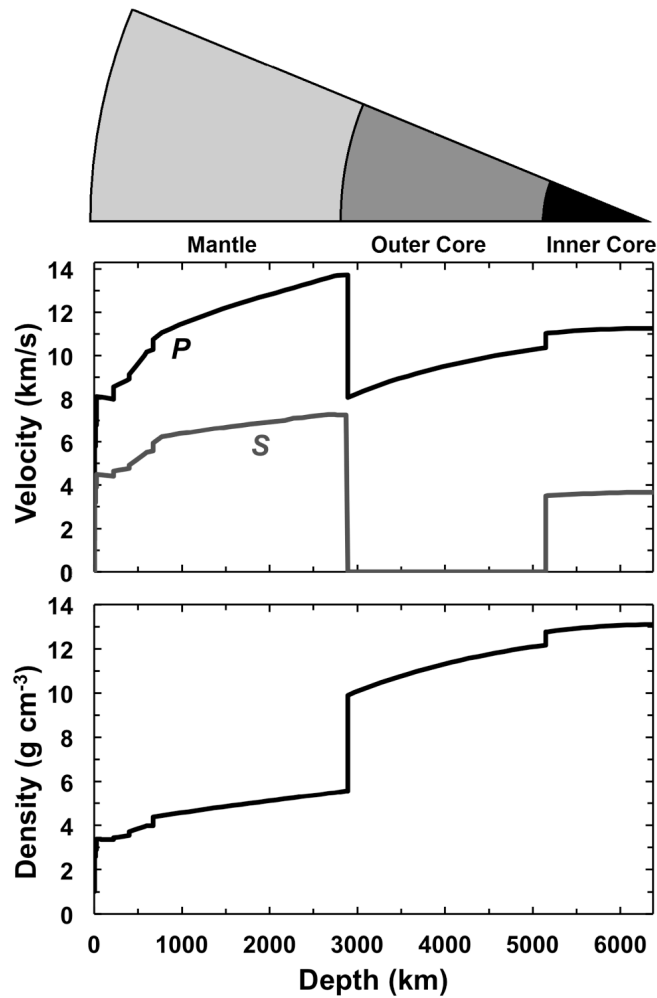
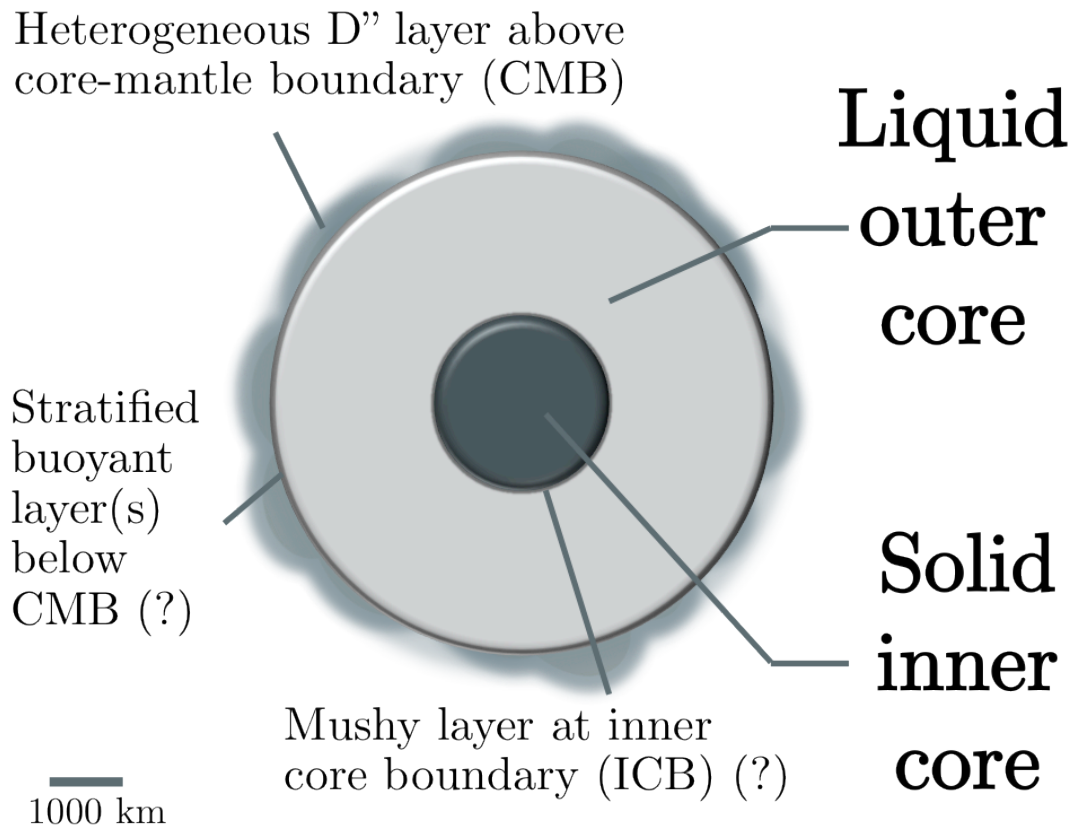


Figure 1.2: The Earth's compressional wave velocity ( $P$ ), shear wave velocity ( $S$ ), and density are shown as a function of depth. Plotted values are from the Preliminary Reference Earth Model (PREM) of Dziewonski and Anderson (1981). The structure of the Earth's interior layering is designated according to large discontinuities of the seismic wave velocities.

transformations of the material at depth (e.g. Mohorovičić, 1910; Birch, 1952) (Figure 1.2). The Earth's largest seismic discontinuity occurs at a depth of 2891 km where the compressional wave velocity ( $V_p$ ) drops from  $\sim 14$  km/s to  $\sim 8$  km/s and the shear wave velocity ( $V_s$ ) drops from  $\sim 7$  km/s to zero (Figure 1.2). This dramatic interface represents the boundary between the mantle and



*Figure 1.3: Schematic representation of the Earth's core and its potential thermochemical boundary layers denoted by deviations from PREM at the uppermost and lowermost outer core, as well as at the base of the lower mantle in the D'' region.*

core. The disappearance of shear waves between depths of 2891—5150 km indicates that this vast outer core region, which accounts for nearly 10% of the Earth's volume and 30% of its mass, is in the liquid state. The presence of a solid inner core is demarcated at a depth of 5150 km by an abrupt increase in  $V_p$  and non-zero  $V_s$  which gradually increase to the Earth's centermost point at a depth of 6370 km (Dziewonski and Anderson, 1981).

The majority (95 volume %) of the core is liquid (Figure 1.3). Densities of the liquid outer core range between  $9.9 \text{ g cm}^{-3}$  below to core mantle boundary to  $12.2 \text{ g cm}^{-3}$  above the inner core-boundary (Dziewonski and

Anderson, 1981; Kennett et al., 1995; Montagner and Kennett, 1996). Gradually increasing  $V_P$  within the outer core is consistent with that expected for a well-mixed liquid, although deviations from reference model wave velocities within the upper most  $\sim 300$  km (e.g. Helffrich and Kaneshima, 2000) and lowermost  $\sim 150$  km (e.g. Gubbins et al., 2008) have been proposed to represent thermochemical boundary layers, which may influence thermal and chemical interactions between the mantle and core and inner and outer core, respectively. The density of the inner core is larger ( $12.8 \text{ g cm}^{-3} - 13.1 \text{ g cm}^{-3}$ ) (Figure 1.2) due tighter packing of atoms in the solid state as well as a likely compositional difference to that of the liquid, as discussed below.

### 1.3 Composition of the core

In the past several decades, a primary research goal of high-pressure mineral physics has been to precisely measure phase relations and elastic properties of relevant compositions in order to understand the nature and behavior of materials in the planet's interior in accord with seismic observations. Recent developments in diamond-anvil cells, laser heating and high intensity synchrotron radiation allow for *in situ* measurement of a growing number of structural properties, i.e. density, elasticity, phase relations, etc., which have greatly contributed to our understanding of the structure and composition of the Earth's interior and its core. Experimental investigations of core materials under such extreme pressure ( $P$ ) and temperature ( $T$ ) conditions are technically challenging with large analytical uncertainties (e.g. Fischer, 2016). As a consequence, physical properties of the core are currently more thoroughly explored using first principles molecular dynamic (FP-MD) calculations (e.g. Vočadlo et al., 1997; Alfè et al. 1999; 2000; Pozzo et al.,

2013), however, simulations are typically conducted at pressures  $> 100$  GPa, which does not allow for sufficient overlap for comparison with lower pressure experiments.

Although the core has never been sampled, its composition is estimated based on a combination of different criteria. First, its density and elasticity at the  $P$ - $T$  conditions of the core must match with the observed seismic data. Second, the major element(s) of the core must be cosmochemically abundant and sufficiently refractory to have been retained during accretion. Additionally, the planet's magnetic field, as sustained by magnetohydrodynamic convection, constrains the outer core to be a metallic liquid.

According to these lines of evidence, iron is considered the dominant – although not sole – element of the Earth's core. Iron is the sixth most abundant element in the universe due its maximal stability in the stellar nucleosynthesis of elements (i.e. energy is required to synthesize elements heavier than  $^{56}\text{Fe}$ , while energy is released during synthesis of elements lighter than  $^{56}\text{Fe}$ ) and the second most abundant element in the bulk Earth ( $\sim 19$  mol %), following oxygen ( $\sim 49$  mol %). Results from shock experiments show that the density range of pure iron under  $P$  of the Earth's core is similar to that calculated from the Preliminary Reference Earth Model (PREM) (Dziewonski and Anderson, 1981) (Figure 1.2), albeit  $\sim 5$ - $10\%$  too dense (e.g. Brown and McQueen, 1986; Anderson and Ahrens, 1994).

The density deficit of the Earth's core – compared to Fe – is attributed to the presence of substantial portions of elements lighter than Fe (Birch, 1952). Additionally, the density discontinuity across the Earth's inner core boundary ( $\sim 0.6$  g cm $^{-3}$ ) (e.g. Masters and Gubbins, 2003) is a few times larger than that reconciled by only the density difference between liquid and solid

( $\sim 0.2 \text{ g cm}^{-3}$ ) (e.g. Hirose et al., 2013), which implies that the liquid outer core is enriched in light element(s) relative to the solid inner core. Fractionation of incompatible light elements during inner core crystallization is considered to drive compositional convection in the liquid outer core due to buoyancy differences (Braginsky, 1963; Gubbins et al., 2003; 2004).

In recent decades, the leading candidates for the core's light element budget have been identified to include silicon, oxygen, sulfur, carbon, and hydrogen, however, the nature and concentration remains largely debated. Several studies have predicted different light element contents of the core using a variety of criteria, e.g., abundance, solubility in liquid iron, depletion in the Earth's mantle relative to undifferentiated chondrites, density, elasticity, etc., as listed in Table 1.1. Many recent studies (e.g. Allegrè et al., 2001; Alfè et al., 2002; McDonough, 2003; Wood et al., 2006; Rubie et al., 2011; Fischer et al., 2015) tend to favor Si as the most abundant light element in the Earth's core with some exceptions (e.g. Badro et al., 2007; Siebert et al., 2013). The most commonly cited evidence for Si in the core is its (1) cosmochemical abundance, (2) increasing solubility in liquid Fe metal at elevated temperatures (Gessman et al. 2001), and (3) high Mg/Si ratios in the bulk silicate Earth (BSE) relative to chondrites. Oxygen is also a strong candidate although experiments on the simultaneous partitioning of Si and O between liquid Fe alloy and peridotite melt reveal these two elements are mutually exclusive in liquid Fe at temperatures below 3000 K (Tsuno et al. 2013). Above 3000 K, however, the concentrations of both Si and O can become significant. The solubility of both Si and O in liquid iron is strongly dependent on  $f_{\text{O}_2}$ , with Si favoring reducing conditions and O favoring oxidizing conditions (O'Neill et al., 1998; Gessman et al., 1999).

Table 1.1. Proposed light elements (wt. %) in the Earth’s core

Grounds for estimate	Si	O	S	C	H	Study
Mantle geochemistry	7	5	1.21	-	-	Allegre et al. (2001)
Density contrast across ICB	5.6 <sup>b</sup>	2.5-2.6	6.4 <sup>b</sup>			Alfè et al. (2002)
Mantle geochemistry	6(0) <sup>c</sup>	0(3) <sup>c</sup>	1.9	0.2	0.06	McDonough (2003)
Density and sound velocity	-	1.5	10.5	-	-	Helffrich & Kaneshima (2004)
Mantle geochemistry	4-5	<1	1.9	0.2	0.1	Wood et al. (2006)
Sound velocity	2.8	5.3	0	-	-	Badro et al. (2007)
Density contrast across ICB	4.6 <sup>b</sup>	4.3	5.3 <sup>b</sup>	-	-	Alfè et al. (2007)
Density and sound velocity	-	0.1	5.7	-	-	Huang et al. (2011)
Metal-silicate equilibrium	8	0.5	-	-	-	Rubie et al. (2011)
Metal-silicate equilibrium	1.5-2.2	4.5-5.5	-	-	-	Siebert et al. (2013)
Metal-silicate equilibrium	7.1-9.9	1.3-1.9				Fischer et al. (2015)
<i>Maximum abundance of each element (assuming a single light element)</i>						
Density deficit	18	11	9	-	-	Poirier (1994)
Density deficit	12	8	13	12	1	Li & Fei (2007)
Density deficit	12.5	7.7	12.1	7.7	-	Sata et al. (2010)

<sup>a</sup>Element estimate of the outer core

<sup>b</sup>Proposed either S or Si in addition to O

<sup>c</sup>Estimated either a Si- or O-bearing core

While the bulk composition of the core was primarily established during its early formation during accretion, it is possible – if not likely – that the core evolves chemically over its entire history. Chemical stratification has been suggested to occur at both the base of the outer core due to inner core crystallization (Loper and Roberts, 1981; Fearn et al., 1981; Deguen et al., 2007), as well as at the top of the outer core where light element-enriched liquids rise due to their buoyancy (Buffett, 2000; Buffett and Seagle, 2010; Gubbins and Davies, 2013). Helffrich (2014) suggested that a buoyant enriched layer might have been present since the core’s formation. In either case, the metal-silicate partition coefficient of several light elements – including Si (Mann et al., 2009), O (Fischer et al., 2015), and potentially Mg (Badro et al., 2016) – has been found to be strongly temperature dependent, which implies that their solubilities in the core should decrease during cooling. Chemical exchange at the Earth’s core-mantle boundary has been proposed to

be a potential driving force for compositional convection (e.g. O'Rourke et al., 2016).

Although the timescale of geologic activity on planetesimals was much shorter, there is evidence to suggest that their cores may have also evolved chemically during cooling. According to current models of the Earth's core-mantle differentiation, substantial amounts of Si and Cr should have partitioned into the metallic Fe-Ni cores of early accretionary bodies (Rubie et al., 2011). In contrast to these predictions, however, the Si and Cr contents of iron meteorites, which are derived from the metallic cores of early-formed planetesimals, are surprisingly low (e.g.  $< 1$  ppm) (Pack et al., 2011; Palme, unpubl. data). Recent studies of magnetized achondrites reveal that planetesimal parent bodies likely possessed liquid metallic cores that underwent convection during their formation (Weiss et al., 2008, 2010; Sterenborg and Crowley, 2013). Such convection would result in the chemical mixing and transport of chemical components in liquid iron, such as Si and Cr, to the body's core-mantle boundary (CMB), which could result in a loss of these elements to the mantle due to their decreased solubility in liquid iron during cooling at a rate controlled by their diffusivities across boundary layers.

## 1.4 Review of previous studies

Solid and liquid metals have been extensively studied at ambient pressure owing to their important industrial applications in steel-making (e.g. Campbell, 2008), however, the effects of  $P$  and  $T$  on their physical properties, which are required for understanding the Earth's core, remain largely unconstrained. As discussed above, mass transport properties, namely diffusivity and viscosity, of molten iron and its alloys are required for understanding large-scale planetary processes related to the Earth's core,

including the length- and timescale of chemical equilibration during core formation and the origin and evolution of geomagnetism that is generally considered to result from thermochemical convection in the liquid outer core (e.g. Merrill et al., 1988).

Diffusion in liquid metals is described well by the traditional Arrhenian model,

$$D(P,T) = D_0 \exp\left(-\frac{Q}{RT}\right) , \quad (1.1)$$

where  $D_0$  is the pre-exponential diffusion coefficient,  $R$  is the universal gas constant, and  $Q$  is the activation energy:

$$Q = \Delta H(P) + P\Delta V(T) , \quad (1.2)$$

where  $\Delta H$  and  $\Delta V$  are the activation enthalpy and activation volume defined as:

$$\frac{\partial \ln D}{\partial (1/T)} = -\frac{\Delta H}{R} \quad (1.3)$$

and

$$\frac{\partial \ln D}{\partial P} = -\frac{\Delta V}{RT} , \quad (1.4)$$

respectively. The magnitudes of activation parameters are therefore particularly important for extrapolating transport coefficients beyond the  $P$  and  $T$  conditions achieved in the laboratory.

Experimental studies of self-diffusion in liquid Fe (Dobson, 2002), liquid FeS (Dobson, 2000; Dobson et al., 2001), and liquid Fe<sub>3</sub>C (Dobson and Wiedenbeck, 2002) report a mixture of either very large or very small  $\Delta H$  ( $\sim 40$ – $250$  kJ mol<sup>-1</sup>) and  $\Delta V$  ( $\sim 1$ – $9$  cm<sup>3</sup> mol<sup>-1</sup>). Disagreement between the extrapolated experimental data and high  $P$ - $T$  computational results yield large uncertainties in the diffusion coefficients of the outer core with values ranging over ten orders of magnitude (e.g. Poirier, 1988; Secco, 1995; Dobson, 2002). FP-MD calculations (de Wijs et al., 1998; Alfè et al., 2000; Pozzo et al., 2013;

Ichikawa and Tsuchiya, 2015; Umemoto and Hirose, 2015) have been conducted mostly under extreme  $P$ - $T$  conditions of the Earth's core, far removed from those currently accessible in laboratory experiments ( $\leq 25$  GPa). Additionally, high-pressure experimental data for chemical diffusion in liquid iron alloys, which are required for understanding length and timescales of chemical equilibration of light (Si, O, S, C, H, etc.) and siderophile ('iron-loving', Cr, V, Mn, W, etc.) elements during core formation and compositional convection processes in the Earth's outer core, have not been reported in the literature.

Several properties of pure liquid metals at ambient  $P$ , including the activation enthalpy ( $\Delta H$ ) of diffusivity and viscosity, have been found to be scalable to homologous temperature ( $T_m/T$ ) where  $T_m$  is the absolute melting temperature (e.g. Poirier, 1988; Iida and Gutherie, 2015). Based on experiments on liquid Hg over a very limited pressure range (1 to  $\sim 11$  bar; Bridgman, 1958), Poirier (1988) proposed a homologous temperature relation for diffusion in liquid metals, defined as

$$D = D_h \exp(-gT_h) \quad , \quad (1.5)$$

where  $D_h$  and  $g$  are constants. A homologous temperature relation for diffusion is particularly convenient for modeling the kinetics of mass transport over a wide range of  $P$  and  $T$ , such as those associated with metal-silicate differentiation in a magma ocean, but has not been verified for liquid metals at higher  $P$ .

Metallurgical studies have shown that liquid metals generally possess a short-range order reminiscent of the structure of the solid state coexisting with the liquid (e.g. Campbell, 2008) and that some solid phase transformations are mimicked in the liquid (e.g. Sidorov et al., 1997). The phase diagram of iron (Figure 1.5) provides an important framework for

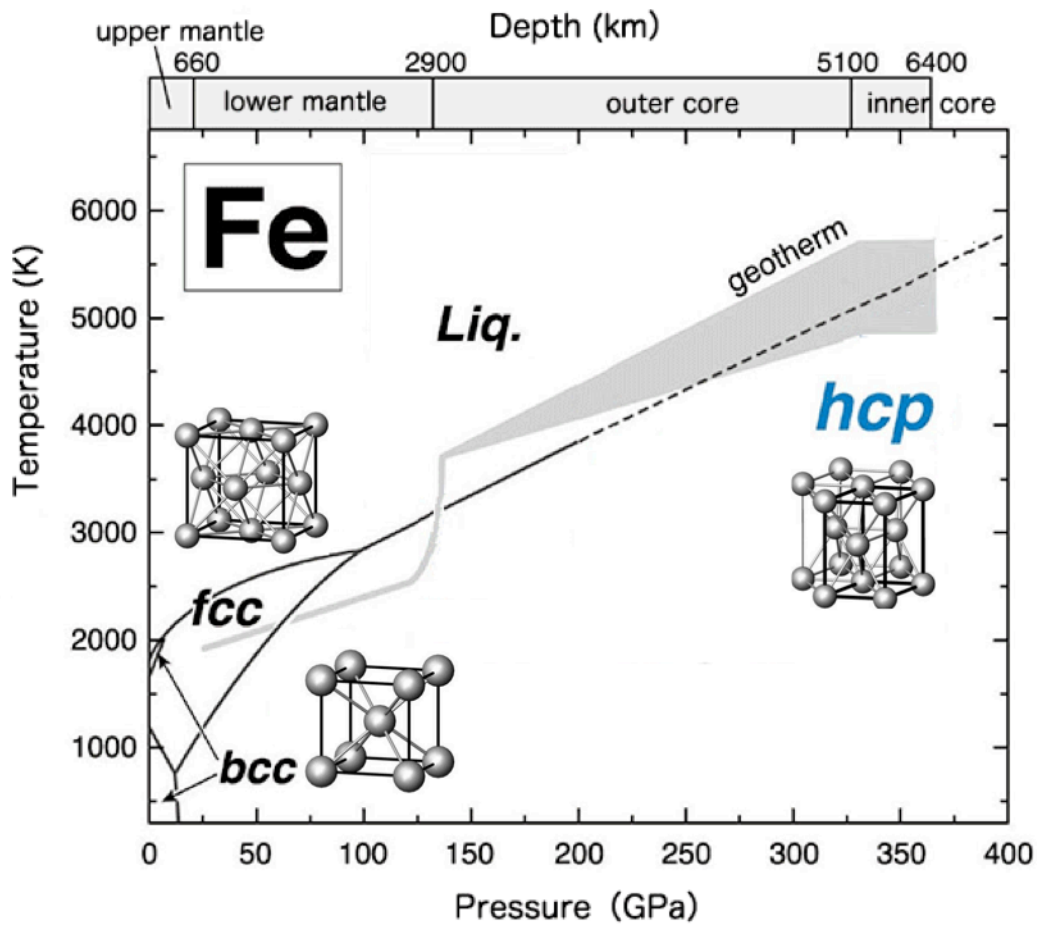


Figure 1.4: Phase diagram of iron. Body centered cubic (bcc) structures are stable at low pressure while close-packed structures, face-centered cubic (fcc) and hexagonal close-packed (hcp), are stable at higher pressures and temperatures. The uncertainty of the Earth's core thermal structure is illustrated by the thickness of the geotherm. Dashed lines in the melting curve represent several hundreds of degrees of uncertainty in the melting curve above  $\sim 135$  GPa. (Modified from Tateno et al., 2010).

core. Structural changes have been reported in both liquid iron (Sanloup et al., 2000) and liquid Fe-C (Shibazaki et al., 2015) near the  $\gamma$ - $\delta$ -liquid triple point ( $\sim 5$  GPa) from a bcc-like to an fcc-like liquid. Similarly, structural properties of liquid alloys near inner core boundary conditions have been used to

understanding the structural properties and phase relations of its alloys in the estimate the degree of solid-liquid partitioning of dissolved alloys (e.g. Alfè et al., 1999).

Pressure-induced structural changes have been shown to have important consequences for the solubility of alloying elements in solid iron. For example, it is well known from metallurgy and material science that the solubility of interstitial carbon in iron, which is fundamental to the manufacturing of steel, is nearly 100 times higher in  $\gamma(\text{fcc})\text{-Fe}$  than  $\alpha(\text{bcc})\text{-Fe}$  (Goldschmidt, 1967). This is attributed to differences in the size and distortion of voids (interstices) within the different packing arrangements of iron atoms. However, the effect of pressure-induced structural changes in liquid iron on elemental solubilities – which has important implications for the metal-silicate equilibrium coefficient in a magma ocean – has not yet been explored.

## 1.5 Aims of the study

- In order to measure the effects of pressure and temperature on Si, O, and Cr diffusion in liquid iron, which are required to estimate the length- and timescales of chemical equilibration between metal and silicate during core formation, I have performed chemical diffusion experiments using a multi-anvil press from 1 to 18 GPa and 1873 to 2643 K. This is the first study to measure chemical diffusion in liquid iron at high pressure.
- In order to compare the experimental data with diffusion rates calculated by first-principles molecular dynamics (FP-MD) and to extend our dataset to the Earth's core, I have performed FP-MD simulations and calculated diffusion coefficients in liquid Fe,  $\text{Fe}_{0.92}\text{Si}_{0.08}$ ,  $\text{Fe}_{0.96}\text{O}_{0.04}$ , and  $\text{Fe}_{0.92}\text{Cr}_{0.08}$

compositions from 0 GPa to 330 GPa and 2200 to 5500 K, which overlaps with the  $P$ - $T$  conditions of the experiments.

- The wide  $P$ - $T$  range accessible with the computations allows for (1) determination of the pressure derivative on the Arrhenian activation terms, (2) evaluation of the homologous temperature model for diffusion in liquid metals proposed by Poirier (1988), (3) investigation of structural properties (i.e. short-range order) of liquid iron alloys, and (4) evaluation of diffusion mechanisms of alloying elements and structural changes in liquid iron alloys, and (5) calculation of the viscosity profile of planetary cores.

## 1.6 References

- Alfè D., Price G.D. and Gillan M. (1999) Oxygen in the Earth's core: a first-principles study. *Phys. Earth. Planet. Inter.* **110**, 191-210.
- Alfè, D., Kresse, G. and Gillan M.J. (2000) Structure and dynamics of liquid iron under Earth's core conditions. *Phys. Rev. B* **61**, 132-142.
- Alfè, D., Gillan, M.J. and Price G.D. (2002) Composition and temperature of the Earth's core constrained by combined ab initio calculations and seismic data. *Earth Planet. Sci. Lett.* **195**, 91-98.
- Allègre C.J., Poirier J.P., Humler E. and Hofmann A.W. (1995) The chemical composition of the Earth, *Earth Planet. Sci. Lett.*, **134**, 515–526.
- Anderson W.W. and Ahrens T.J. (1994) An equation of state for liquid iron and implications for the Earth's core. *J. Geophys. Res.* **99**, 4273-4284.
- Badro J., Fiquet G., Guyot F., Gregoryanz E., Occelli F., Antonangeli D. and d'Astuto M. (2007) Effect of light elements on the sound velocities in solid

iron: implications for the compositions of the Earth's core. *Earth Planet. Sci. Lett.* **254**, 233-238.

Badro J., Siebert J. and Nimmo F. (2016) An early geodynamo driven by exsolution of mantle components from Earth's core. *Nature*. **536**, 326-328.

Birch F. (1952) Elasticity and constitution of the Earth's interior. *J. Geophys. Res.* **57**, 227-286.

Braginsky S. (1963) Structure of the F layer and reasons for convection in the Earth's core. *Dokl. Akad. Nauk. SSR Engl. Trans.* **149**, 1311-1314.

Bridgman P.W. (1958) *The Physics of High-Pressure*, G. Bell & Sons Ltd, London, pp. 398.

Brown J.M. and McQueen R.G. (1986) Phase transitions, Grüneisen parameter and elasticity of shocked iron between 77 GPa and 400 GPa. *J. Geophys. Res.* **91**, 7485-7494.

Buffett B.A., Garnero E.J., Jeanloz R. (2000) Sediments at the top of the Earth's core. *Science*. **290**, 1338-1342.

Buffett B.A. and Seagle C.T. (2010) Stratification of the top of the core due to chemical interactions with the mantle. *J. Geophys. Res.* **115**, doi:10.1029/2009JB006751.

Cameron A.G.W. and Ward W.R. (1976) The origin of the moon. *Lunar Sci.* VII:120-122 (abstract).

Campbell F.C. (2008) *Elements of Metallurgy and Engineering Alloys*, ASM International, Materials Park, Ohio, pp. 672.

Canup R.M. and Asphaug E. (2001) Origin of the Moon in a giant impact near the end of the Earth's formation. *Nature*. **412**, 708-712.

Chambers J.E. and Wetherill G.W. (1998) Making the terrestrial planets: N-body integrations of planetary embryos in three dimensions. *Icarus*. **136**, 304-327.

Ćuk M. and Stewart S.T. (2012) Making the Moon from a fast-spinning Earth: a giant impact followed by resonant despinning. *Science*. **23**, 1047-1052.

Deguen, R., Albuoussière, T. and Brito D. (2007) On the existence and structure of a mush at the inner core boundary of the Earth. *Phys. Earth Planet. Int.* **164**, 36-49.

de Wijs, G.A., Kresse, G., Vočadlo, L., Dobson, D., Alfè, D., Gillan, M.J. and Price G.D. (1998) The viscosity of liquid iron at the physical conditions of the Earth's core. *Lett. Nature* **392**, 805-807.

Dobson D.P. (2000)  $^{57}\text{Fe}$  and Co tracer diffusion in liquid Fe-FeS at 2 and 5 GPa. *Phys. Earth. Planet. Int.* **120**, 137-144.

Dobson, D.P. (2002) Self-diffusion in liquid Fe at high pressure. *Phys. Earth Planet. Int.* **130**, 271-284.

Dobson, D. P., Brodholt, J.P., Vočadlo, L., and Crichton W.A. (2001) Experimental verification of the Stokes-Einstein relation in liquid Fe-FeS at 5 GPa. *Mol. Phys.* **99**, 773-777.

Dobson, D.P. and Wiedenbeck M. (2002) Fe- and C-self-diffusion in liquid Fe<sub>3</sub>C to 15 GPa. *Geophys. Res. Lett.* **29**, doi:10.1029/2002GL015536.

Dziewonski A.M. and Anderson D.L. (1981) Preliminary reference Earth model. *Phys. Earth Planet. Int.* **25**, 297-356.

Fearn, D.R., Loper, D.E. and Roberts P.H. (1981) Structure of the Earth's inner core. *Nature* **292**, 232-233.

Fischer, R.A., Nakajima, Y., Campbell, A.J., Frost, D.J., Harries, D., Langenhorst, F., Miyajima, N., Pollok, K. and Rubie D.C. (2015) High pressure metal-silicate partitioning of Ni, Co, V, Cr, Si and O. *Geochim. Cosmochim. Acta* **167**, 177-194.

Gessmann C.K., Rubie D.C., McCammon C. (1999) Oxygen fugacity dependence of Ni Co, Mn, Cr, V and Si partitioning between liquid metal and magnesiowüstite at 9–18 GPa and 2200 °C. *Geochim. Cosmochim. Acta* **63**, 1853–1863.

Gessman C.K., Wood B.J., Rubie D.C. and Kilburn M.R. (2001) Solubility of silicon in liquid metal at high pressure: implications for the composition of the Earth's core. *Earth Planet. Sci. Lett.* **84**, 367-376.

Goldschmidt H.J. (1967) *Interstitial Alloys*. Plenum, New York.

Gubbins, D., Alfè, D., Masters, T.G., Price, D. and Gillan M.J. (2003) Can the Earth's dynamo run on heat alone? *Geophys. J. Int.*, **155**, 609-622.

Gubbins, D., Alfè, D., Masters, G., Price, G.D. and Gillan M. (2004) Gross thermodynamics of two-component core convection. *Geophys. J. Int.* **157**, 1407-1414.

Gubbins D. and Davies C.J. (2013) The stratified layer at the core-mantle boundary caused by barodiffusion of oxygen, sulphur and silicon. *Phys. Earth Planet. Int.* **215**, 21-28.

Gubbins D., Masters G. and Nimmo F. (2008) A thermochemical boundary layer at the base of the Earth's outer core and independent estimate of core heat flux. *Geophys. J. Int.* **174**, 1007-1018.

Hartmann W.K. and Davis D.R. (1975) Satellite-sized planetesimals and lunar origin. *Icarus*. **24**, 504-514.

Helfrich G. and Kaneshima S. (2010) Outer-core compositional stratification from observed core wave speed profiles *Nature*. **468**, 807-810.

Helfrich G. (2014) Outer core compositional layering and constraints on core liquid transport properties. *Earth Planet. Sci. Lett.* **391**, 256-262.

Hirose K., Labrosse S. and Hernlund J. Composition and state of the core. *Annu. Rev. Earth Planet. Sci.* **41**, 657-691.

Huang H., Fei Y., Cai L., Jing F., Hu X., Xie H., Zhang L. and Gong Z. (2011) Evidence for an oxygen-depleted liquid outer core of the Earth. *Nature*. **479**, 513-516.

Ichikawa, H. and Tsuchiya T. (2015) Atomic transport property of Fe-O liquid alloys in the Earth's outer core  $P,T$  condition. *Phys. Earth Planet. Int.* **247**, 27-35.

Iida T. and Guthrie R.I.L (2015) The thermophysical properties of metallic liquids. Volume 1: Fundamentals. Oxford University Press: Oxford, pp. 418.

Karato, S. and Murthy V.R. (1997) Core formation and chemical equilibration in the Earth-I. Physical conditions. *Phys. Earth. Planet. Int.* **100**, 61-79.

Kennett B. L. N., Engdahl E. R. and Buland R. P. (1995) Constraints on seismic velocities in the Earth from travel times. *Geophys. J. Int.* **122**, 108-124.

Li J. and Fei Y. (2007) Experimental constraints on core composition. In *Treatise on Geochemistry Update*. Holland H.D. and Turekian K.K. (eds) Elsevier: New York, 521-546.

Lichtenberg T., Golabek G.J., Gerya T.V. and Meyer M.R. (2016) The effects of short-lived radionuclides and porosity on the early thermo-mechanical evolution of planetesimals. *Icarus*. **274**, 350-365.

Liebske, C., Schmickler, B., Terasaki, H., Poe, B.T., Suzuki, A., Funakoshi, K., Ando, R. and Rubie D.C. (2005) Viscosity of peridotite liquid up to 13 GPa: implications for magma ocean viscosities. *Earth Planet. Sci. Lett.* **240**, 589-604.

Loper, D.E. and Roberts P.H. (1981) A study of conditions at the inner core boundary of the Earth. *Phys. Earth Planet. Int.* **24**, 302-307.

Mann U., Frost D.J. and Rubie D.C. (2009) Evidence for high pressure core-mantle differentiation from the metal-silicate partitioning of lithophile and weakly-siderophile elements. *Geochim. Cosmochim. Acta.* **73**, 7360-7386.

Masters G. and Gubbins D. (2003) On the resolution of density within the Earth. *Phys. Earth Planet. Int.* **140**, 159-167.

McDonough W.F. (2003) Compositional model for the Earth's core. In: Carlson, R.W. (Ed.), *Treatise on Geochemistry, Vol. 2: The Mantle and Core*, ed. RW Carlson, pp. 547-68. Oxford: Elsevier-Pergamon.

Merrill R.T., McElhinny M.W. and McFadden P.I. (1998) *The magnetic field of the Earth, paleomagnetism, the core, and the deep mantle*. Academic Press: London.

Mohorovičić A. (1910) Godišnje izvješće zagrebačkog meteorološkog opservatorija za godinu 1909. Godina IX, dio IV. - polovina 1. Potres od 8. X. 1909.

Montagner J.P. and Kennett B.L.N. (1996) How to reconcile body-wave and normal-mode reference Earth models? *Geophys. J. Int.* **125**, 229-248.

Morbidelli A., Chambers J., Lunine J., Petite J.M., Robert F., Valsecchi G. and Cyr K. (2000) Source regions and timescales for the delivery of water to the Earth. *Meteor. Planet. Sci.* **35**, 1309-1320.

O'Neill H. S. C., Canil D. and Rubie D.C. (1998) Oxide-metal equilibria to 2500°C and 25 GPa: Implications for core formation and the light component in the Earth's core, *J. Geophys. Res.*, **103**, 239–260.

O'Rourke J.G. and Stevenson D.J. (2016) Powering Earth's dynamo with magnesium precipitation from the core. *Nature.* **529**, 387-391.

Pack, A., Vogel, I., Rollion-Bard, C., Lurias, B. and Palme H. (2011) Silicon in iron meteorite metal. *Meteor. Planet. Sci.* **46**, 1470-1483.

Poirier J.P. (1988) Transport properties of liquid metals and viscosity of the Earth's core. *Geophys. J.* **92**, 99-105.

Poirier J.-P. (1994) Light elements in the Earth's outer core: A critical review. *Phys. Earth Planet. Int.* **85**, 319–337.

Pozzo, M., Davies, C., Gubbins, D. and Alfè D. (2013) Transport properties for liquid silicon-oxygen-iron mixtures at Earth's core conditions. *Phys. Rev. B.* **87**, doi: 10.1103/PhysRevB.87.014110.

Qin L., Dauphas N., Wadhwa M., Masarik J. and Janney P.E. (2008) Rapid accretion and differentiation of iron meteorite parent bodies inferred from  $^{182}\text{Hf}$ - $^{182}\text{W}$  chronometry and thermal modeling. *Earth Planet. Sci. Lett.* **273**, 94-104.

Raymond S.N., Kokubo E., Morbidelli A., Morishima R. and Walsh K.J. (2014) Terrestrial planet formation at home and abroad. In: Beuther H., Klessen R., Dullemond C. and Henning T. (eds) *Protostars and planets VI*. University of Arizona Press, Tucson, 595-618.

Rubie, D. C., F. Nimmo, and H. J. Melosh (2007), Formation of the Earth's core. *Treatise on Geophysics. In: Stevenson, D. (Ed.), Evolution of the Earth*, 9. Elsevier, Amsterdam, pp. 51–90.

Rubie D.C., Frost D.J., Mann U., Asahara Y., Nimmo F., Tsuno K., Kegler P., Holzheid A. and Palme H. (2011) Heterogeneous accretion, composition and core-mantle differentiation of the Earth. *Earth Planet. Sci. Lett.* **301**, 31-42.

Rubie, D.C., Jacobson, S.A., Morbidelli, A., O'Brien, D.P., Young, E.D., de Vries, J., Nimmo, F., Palme, H. and Frost D.J. (2015) Accretion and differentiation of the terrestrial planets with implications for the compositions of early-formed Solar System bodies and accretion of water. *Icarus* **248**, 89-108.

Sanloup C., Guyot F., Gillet P., Fiquet G., Hemley R.J., Mezouar M. and Martinez I. (2000) Structural changes in liquid Fe at high pressures and temperatures from synchrotron X-ray diffraction. *Europhys. Lett.* **52**, 151-157.

Secco R.A. (1995) Viscosity of the outer core. In *Handbook of physical constants* (ed. T.J. Ahrens), American Geophysical Union reference shelf 2, Washington, D.C., p. 218–227.

Scherstén A., Elliot T., Hawkesworth C., Russell S. and Masarik J. (2006) Hf-W evidence for rapid differentiation of iron meteorite parents bodies. *Earth Planet. Sci. Lett.* **241**, 530-542.

Shibazaki Y., Kono Y. and Fei Y. (2015) Microscopic structural change in a liquid Fe-C alloy of ~5 GPa. *Geophys. Res. Lett.* **42**. 5236-5242.

Sidorov V., Popel P., Son L., Malyshev L. (1997) Phase transitions and phase diagrams for liquid iron-based melts. *Materials Sci. Engineer. A*: 226-228; 317-320.

Siebert, J., Badro, J., Antonangeli, D. and Ryerson F.J. (2013) Terrestrial accretion under oxidizing conditions. *Science*. **339**(6124), 1194-1197.

Sata N., Hirose K., Shen G., Nakajima Y., Ohishi Y., Hirao N. (2010) Compression of FeSi, Fe<sub>3</sub>C, Fe<sub>0.95</sub>O, and FeS under core pressures and

implication for light element in the Earth's core. *J. Geophys. Res.* **115**, B09204.

Sterenberg M.G. and Crowley J.W. (2013) Thermal evolution of early solar system planetesimals and the possibility of sustained dynamos. *Phys. Earth Planet. Int.* **214**, 53-73.

Stevenson D.J. (1990) Fluid dynamics of core formation, In *The Origin of the Earth* (eds. H. Newsom and J.H. Jones), Oxford Press, London, 1990, pp. 231-249.

Tateno S., Hirose K., Ohishi Y. and Tatsumi Y. (2010) The structure of iron in Earth's inner core. *Science*. **330**, 359-361

Tonks W.B. and Melosh H.J. (1993) Magma ocean formation due to giant impacts. *J. Geophys. Res.* **98**, 5319-5333.

Tsuno K., Frost D.J., Rubie D.C. (2013) Simultaneous partitioning of silicon and oxygen into the Earth's core during early Earth differentiation. *Geophys. Res. Lett.* **40**, 66-71.

Turcotte D.L. and Schubert G. (2007) *Geodynamics*. Cambridge University Press: Cambridge.

Umemoto, K. and Hirose K. (2015) Liquid iron-hydrogen alloys at outer core conditions by first-principles calculations. *Geophys. Res. Lett.* **42**, 7513-7520.

Van Orman J.A. and Crispin K.L. (2010) Diffusion in Oxides. *Rev. Min. Geochem.* **72**, 757-825.

Vočadlo L., de Wijs G.A., Kresse G., Gillan M. and Price G.D. (1997) First principles calculations on crystalline and liquid iron at Earth's core conditions. *Faraday Discuss.* **106**, 205-217.

Vočadlo L., Alfè D., Gillan M.J., Price G.D. (2003) The properties of iron under core conditions from first principles calculations. *Phys. Earth Planet. Int.* **140**, 101-125.

Von Bergen N. and Waff H.S. (1986) Permeabilities, interfacial areas and curvatures of partially molten systems: results of numerical computations of equilibrium microstructures. *J. Geophys. Res.* **91**, 9261-9276.

Weidenschilling S.J., Spaute D., Davis D.R., Marzari F. and Ohtsuki K. (1997) Accretional evolution of a planetesimal swarm. *Icarus*. **128**, 429-455.

Weiss B.P., Berdahl J.S., Elkins-Tanton L., Stanley S., Lima E.A. and Carporzen L. (2008) Magnetism on the angrite parent body and the early differentiation of planetesimals. *Science*. **322**, 713-716.

Weiss B.P., Gattacceca J., Stanley S., Rochette P. and Christensen U.R. (2010) Paleomagnetic records of meteorites and early planetesimal differentiation. *Space Sci. Rev.* **152**, 341-390.

Wetherill G.W. and Stewart G.R. (1993) Formation of planetary embryos: effects of fragmentation, low relative velocity, and independent variation of eccentricity and inclination. *Icarus*. **106**, 190-209.

Wood B.J., Walter M.J. and Wade J. (2006) Accretion of the Earth and segregation of its core. *Nature*. **441**, 825-833.

# Methods

In this chapter, I summarize the theory and methods employed in this study to measure mass transport and structural properties of liquid metals using both experimental and computational approaches.

## 2.1 Fundamentals of diffusion theory

Diffusion is generally defined as the movement of a species (atoms, ions, molecules) through a medium (gas, liquid, mineral, glass) in the absence of bulk flow. Diffusive transport occurs as a result of atomic motions that, in the presence of a chemical or isotopic potential gradient, can lead to a net flux of particles, most commonly from regions of high concentration to regions of low concentration (Figure 2.1).

The mathematics of diffusion is well understood (Crank, 1980; Carslaw and Jaeger, 1986) and is usually treated in terms of Fick's Laws. When considering one-dimensional diffusion in an isotropic medium, Fick's 1<sup>st</sup> Law for a single component is given as:

$$J_i^j = -D_i^j \frac{\partial C_i}{\partial x} \quad (2.1)$$

which relates the flux,  $J$ , of a species  $i$  through a medium  $j$  with the concentration gradient,  $\frac{\partial C_i}{\partial x}$ , with  $C_i$  decreasing in the direction of decreasing  $x$ , and diffusivity,  $D$ , of  $i$  through  $j$ .  $D$  has dimensions of  $L^2t^{-1}$ . Fick's 2<sup>nd</sup> Law is

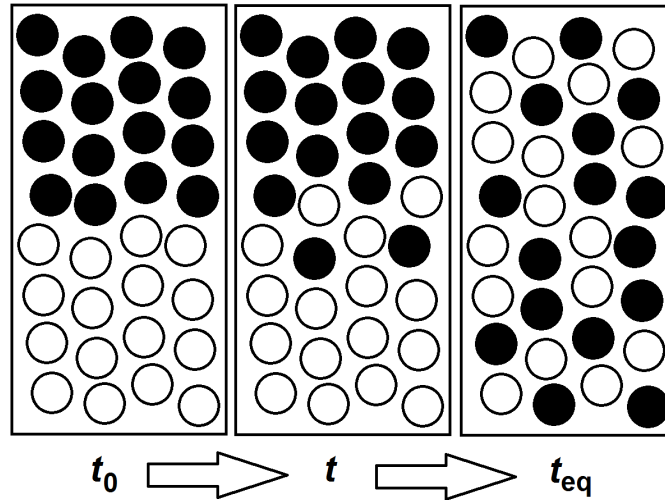


Figure 2.1: Schematic diagram of random motion of particles. Initially (left panel), all particles represented by unfilled circles (A) are in the lower side, and all particles represented by filled circles (B) are in the upper side. Over time (middle panel), there is a net flux of B from the upper side to the lower side and A from the lower side to the upper side due to random motion. As time increases (right panel), the distribution of A and B will eventually become random and uniform.

often called simply ‘the diffusion equation’ and can be used to evaluate the time-dependence of diffusion. For one-dimensional diffusion of a single component in an isotropic medium, it is given as:

$$\frac{\partial C_i}{\partial t} = D_i^j \frac{\partial^2 C}{\partial x^2} \quad (2.2)$$

This equation is simply a continuity relation utilizing the expression of flux given by Eq. 2.1. Solutions to the diffusion equation with appropriate initial and boundary conditions are used as a model to retrieve diffusion coefficients from experimental data.

It is useful to note that self-diffusion involves the Brownian motion of particles, while chemical interdiffusion characterizes the motion of particles in the presence of a chemical potential gradient. If two or more components

diffuse simultaneously in a given medium, their fluxes become coupled. For the intermixing of components  $A$  and  $B$ , the chemical interdiffusion coefficient,  $D_{A-B}$ , is given as:

$$D_{A-B} = x_A D_B + x_B D_A \quad (2.3)$$

where  $X$  are the molar fractions and  $D_A$  and  $D_B$  are the self-diffusivities of  $A$  and  $B$ , respectively (Darken, 1948). It can be seen that in a dilute solution, as employed in this study, the chemical interdiffusion coefficient approaches that of the self-diffusion coefficient of the dilute species (i.e.  $D_{A-B} \rightarrow D_B$  as  $x_B \rightarrow 0$ ).

Diffusion has been shown to be sensitive to changes in  $T$  and, to a lesser extent,  $P$ ,  $f_{O_2}$ , and composition. Diffusion in most systems is described well by the traditional Arrhenian model (Eq. 1.1). The magnitudes of activation parameters, (Eqs. 1.3, 1.4) are particularly important for extrapolating transport coefficients beyond the  $P$  and  $T$  conditions accessible in the laboratory, as discussed further in Chapter 5.

Additionally, self-diffusion coefficients in dissociated liquids, such as metallic melts, have been shown to be related to viscosity,  $\eta$ , via the Stokes-Einstein relation,

$$D\eta = \frac{k_B T}{2\pi a} \quad , \quad (2.4)$$

where  $a$  is an atomic diameter and  $k_B$  is the Boltzmann constant. The Stokes-Einstein relation has been verified experimentally for liquid metals (e.g. Saxton and Sherby, 1962; Dobson et al., 2001), and can be justified theoretically (e.g. Zwanzig, 1983). The Stokes-Einstein relation exemplifies the close relationship between mass transport and structural properties, the latter of which can be difficult to measure in experiments at high  $P$ . Mass transport properties can therefore be used as an indicator of the liquid structure, as discussed in the following section.

## 2.2 Diffusion couple experiments

### 2.2.1. Multi-anvil sample assembly and procedure

Diffusion couple starting materials consisted of 0.9 or 1.2 mm diameter cylinders of iron and an iron alloy of one of the following compositions: Fe-8wt%Si, Fe-4wt%Si, Fe-1wt%Cr, Fe-5wt%O, Fe-8wt%Si-1wt%Cr, or Fe-4wt%Si-1wt%Cr. Iron cylinders of 99.98% purity were machined and one end was polished to a 0.25-micron finish. Alloys were sintered into a solid rod from powder mixtures of the desired composition in a piston-cylinder apparatus, as discussed in Section 5.3.1. Chemical diffusion experiments were performed over the  $P$ - $T$  range of 1-18 GPa and 1873-2643 K using 1200 and 5000 tonne multi-anvil presses. Diffusion couples were contained vertically within an MgO capsule with the lighter alloy on top to maintain gravitational stability, as discussed in Section 5.10.2. We employed Cr<sub>2</sub>O<sub>3</sub>-doped MgO octahedra with 18 mm edge lengths as the pressure medium, tungsten carbide cubes with 11 mm corner truncations, stepped LaCrO<sub>3</sub> heaters and a W<sub>97</sub>Re<sub>3</sub>—W<sub>75</sub>Re<sub>25</sub> thermocouple, as discussed further in Sections 5.3.1 and 5.3.1. A cross-section of the typical experimental set-up is shown in Figure 2.2.

Experiments were performed at 1, 3, 7, and 18 GPa by compressing slowly to the desired press load and then heated to high temperature with output values (e.g. thermocouple temperature, power) recorded every 100 ms. Due to rapid diffusion in the small liquid samples, experiments were very short ( $> 180$  s). In most experiments, a combination of automatic and manual heating was used in order to minimize a decrease in heating rate upon approaching the target temperature. A fictive target temperature was set using a PID controller several hundred degrees above the peak temperature ( $T_f$ ) and then switched to manual control about 50 K below the true target

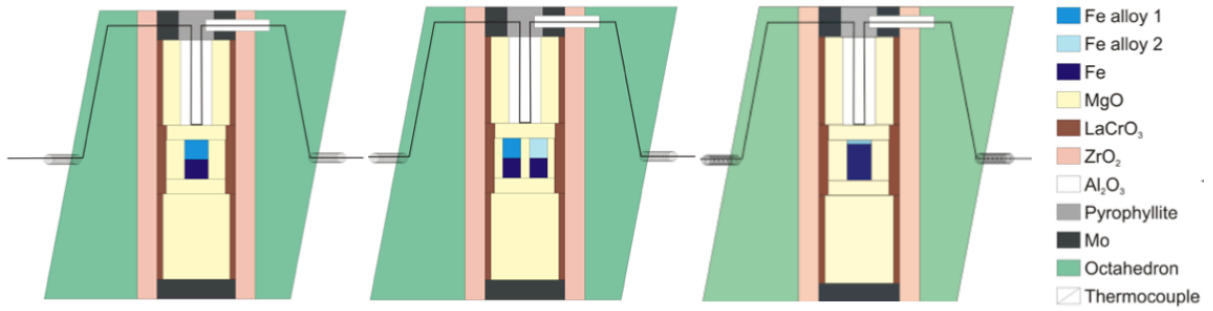


Figure 2.2: Schematic representation of 18/11 multi-anvil assembly used in the diffusion experiments. Diffusion couples were contained vertically within an MgO capsule with the alloy (light blue) on top of the pure iron (dark blue) to maintain gravitational stability. The initial height of alloy cylinders in the Fe-Si and Fe-Cr diffusion couple experiments were identical (1 mm) to those of pure Fe (left two panels), while FeO discs and pure iron in the Fe-O diffusion couple experiments were initially 0.2 mm and 1.8 mm, respectively (right panel). A limited number of experiments were conducted using a double chamber capsule (center panel) by annealing two diffusion couples of different solute concentration or composition simultaneously.

temperature. The upper and lower power limits were then fixed to a very small interval ( $\sim 0.1$  W) so that the temperature would not fluctuate and the temperature profile would flatten very quickly to  $T_f$ . The sample was quenched by shutting off the electrical power at an initial rate in excess of  $\sim 500$  K  $s^{-1}$ . A typical heating profile is shown in Figure 2.3 A fully automated heating protocol was also employed in some experiments but due to the gradual decrease of the heating rate as  $T_f$  was approached, errors associated with  $T_f$  were then slightly larger. More details on the annealing procedure and melting criteria are given in Sections 5.3.1 and 5.3.3, respectively.

### 2.2.2. Analytical procedure

Recovered capsules were cut and polished parallel to the axis of the

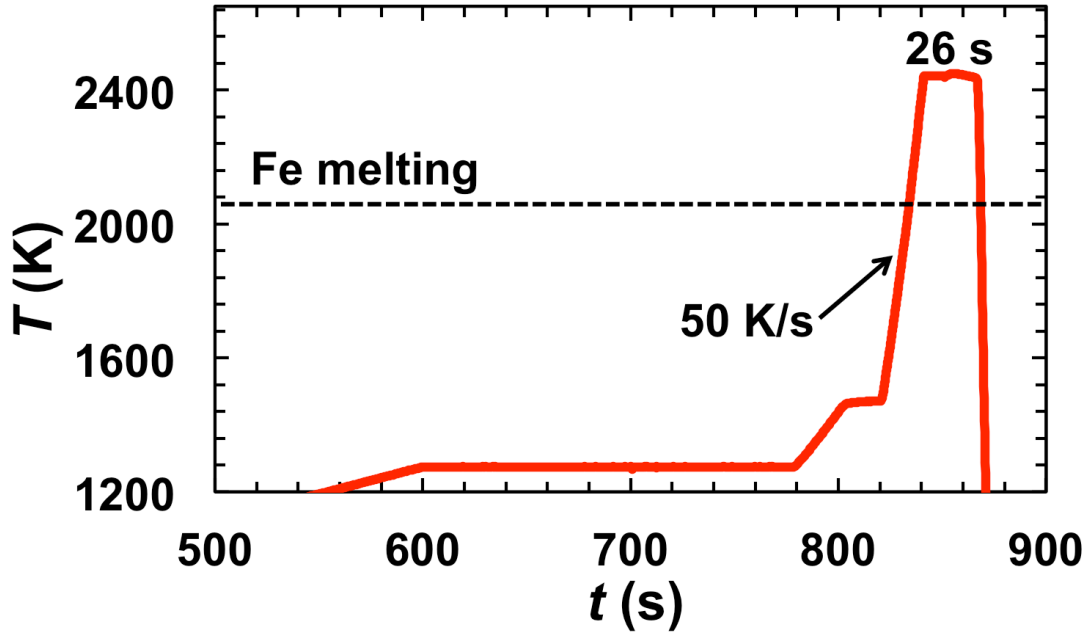


Figure 2.3: Thermocouple signal during a diffusion experiment as recorded by the  $T$ - $t$  logger at intervals of 100 ms. The sample was compressed to 7 GPa at room temperature, heated to 1273 K over 10 minutes and then allowed to stay at 1273 K for 180 s and 1473 K for 18 s. Solid-state diffusion during these periods at low  $T$  ( $\ll T_m$ ) was negligible. The sample was then heated at a rate of  $50 \text{ K s}^{-1}$  to above the melting temperature  $T_m$  of pure iron ( $2059 \pm 25 \text{ K}$ ; shown as a dashed line) to a peak temperature of  $T_f = 2428 \pm 4 \text{ K}$ , maintained at  $T_f$  for 26 seconds, and then quenched by shutting off the electrical power.

cylindrical sample. Spot analyses were acquired along the full length of the diffusion couple on a line perpendicular to the original diffusion couple interface using a JEOL-JXA-8200 electron probe micro-analyzer. For Si and Cr diffusion experiments, the probe current and accelerating voltage were 15 nA and 15 kV, respectively, with a beam diameter of 20  $\mu\text{m}$ . Standards used were Fe metal, Cr metal and natural andradite. Counting times were 20 s on peak and 10 s on background. For O diffusion experiments, the probe current and accelerating voltage were 15 kV and 50 nA, respectively, with an effective

beam diameter of  $\sim 70 \mu\text{m}$ , sufficiently large to sample both matrix and exsolved inclusions. Standards used were natural hematite and pure Fe metal. Counting times were 40 s on peak and 20 s on background for oxygen, and 20 s and 10 s for iron, respectively. Line scans were between 1549 and 1920  $\mu\text{m}$  long and the spacing between adjacent spots was 10  $\mu\text{m}$  for Si and Cr, and 60  $\mu\text{m}$  for O. At least two parallel scans were made on each sample in order to check for reproducibility and possible convective mixing. More detailed analytical procedure is given in Section 5.3.2 for Si and Cr and Section 6.3.2 for oxygen.

### *2.2.3 Experimental data fitting*

It is generally assumed in experimental studies of diffusion in crystalline solids and high viscosity liquids that laboratory-induced diffusion profiles form at a single (peak) temperature with negligible diffusion occurring during heating and quenching. In the case of isothermal annealing, retrieved diffusion coefficients from individual experiments can be directly used to determine diffusion parameters according to the Arrhenius relation (Eq. 1.1), which is typically valid for experiments conducted on slow diffusing systems. However, diffusion during heating and quenching is non-negligible in materials with a large diffusion coefficient, such as metallic melts and other low viscosity liquids including highly depolymerized silicate melts (Liebske et al., 2005; Ni et al., 2015), which can lead to significant errors.

Non-isothermal annealing (i.e. when diffusion occurs during heating) can result in an overestimation of the inferred diffusion coefficient if the quenched concentration profile is assumed to have formed solely at the peak annealing temperature,  $T_f$ . The extent of diffusion that occurs during ramp heating increases with temperatures above the melting point ( $T_m$ ) and, as a

consequence, can lead to an overestimation of the Arrhenian temperature dependence term,  $\Delta H$  (Eq. 1.3). The ramped heating rate significantly influences the shape of the concentration profile upon reaching  $T_f$ , especially at  $T \gg T_m$ , as described in greater detail in the Section 5.3.4.

In order to account for non-isothermal diffusion annealing, we developed a numerical model that accounts for diffusion during heating by fitting several concentration profiles obtained at a single pressure simultaneously. Initially, an optimized interface location is obtained for each profile using a least squared fit combined with a finite difference simulation of the profile. In order to numerically refine  $D_o$  and  $\Delta H$ , all profiles obtained at a given pressure were fitted simultaneously using a Crank-Nicolson finite difference approximation. The fitting procedure is discussed in further detail in Sections 5.3.4 and 6.3.3.

## 2.3 Computational methods

### *2.3.1. First-principles molecular dynamic simulations*

First-principles molecular dynamics (FP-MD), based on density functional theory (e.g. Hohenberg and Kohn, 1964; Kohn and Sham, 1965) has emerged in recent decades as a powerful and robust tool for investigating the properties of matter (e.g. Mattsson, 2002; Perdew et al., 2005). FP-MD simulations are particularly useful for studying matter under extreme conditions such as those of Earth's core (e.g. Vočadlo et al., 1997; Alfè et al., 1999; 2002; Pozzo et al., 2012; 2013). However, very few computational studies have been performed at experimentally accessible conditions.

In this study, calculations of energy and forces are based on density functional theory (DFT) with exchange and correlation potentials represented

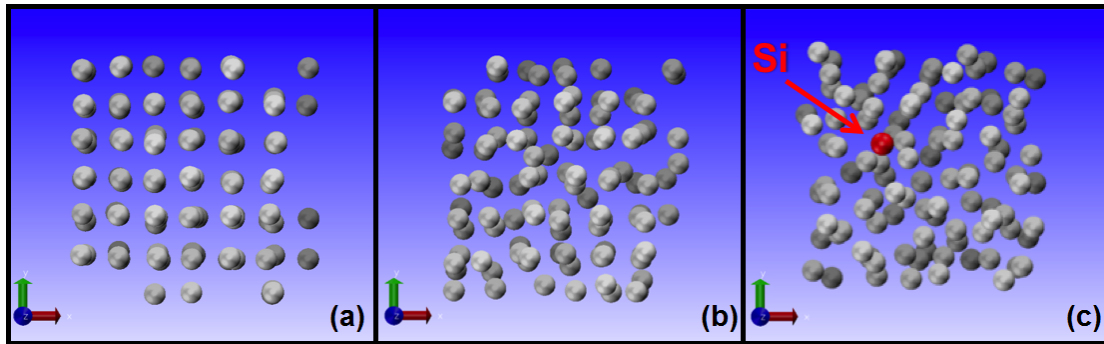


Figure 2.4: Snapshots of a typical simulation cell during the computational set up. Simulations began as (a) a body-centered cubic arrangement of 150 iron (silver) atoms at 1000 K. (b) The simulation cell was overheated to 4000 K to induce melting and then compressed to the desired volume. (c) Fe atoms were substituted for solute species (Si, O, or Cr). In this snapshot, there is only one solute atom (Si, in red) but most production runs included either 6 and 12 solute atoms.

by the generalized gradient approximation (GGA) (Perdew et al., 1996). Valence electron states are expanded into plane waves with a cutoff energy of 550 eV in the projected augmented wave (PAW) method (Kresse and Joubert, 1999). We used PAW atomic files for Si, O, Cr, and Fe with the  $3s^23p^2$ ,  $2s^22p^4$ ,  $4s^13d^5$ , and  $4s^13d^7$  valence electronic configurations, respectively.

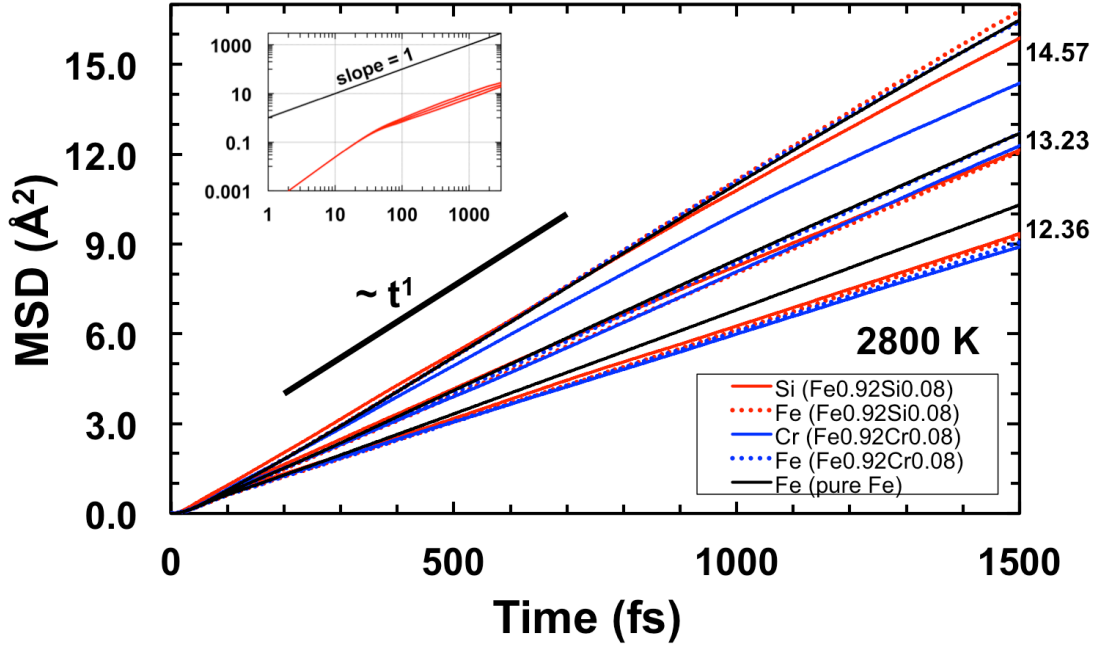
We performed molecular dynamic simulations in the canonical  $N$ - $V$ - $T$  ensemble, in which the number of atoms ( $N$ ) and simulation volume ( $V$ ) are kept fixed, and the temperature ( $T$ ) is controlled by a Nosé–Hoover thermostat (Anderson, 1980). We used the Vienna *ab-initio* simulation package (VASP) (Kresse and Furthmüller, 1996) with a time step of 1 fs. Simulations were run for at least 22 ps, from which we discarded the first 2 ps to allow for equilibration.

In our simulations, Fe supercells of 150 atoms (Figure 2.4a) are overheated to induce melting (Figure 2.4b) and compressed to volumes along several isobars (0 – 330 GPa) using the thermodynamic model of Lu et al. (2005a, 2005b). Densities of the simulations range from 5.421 g cm<sup>-3</sup> to 11.620 g m<sup>-3</sup> for Fe. We then changed the composition in the cell by substituting either 6 or 12 atoms of Fe by either Si O, or Cr, equating to 4 or 8 atomic percent, respectively, keeping the volume of the simulation cell fixed (Figure 2.4c). Simulations for cells containing 6 solute atoms (4 at. %) were run for 29 ps, longer than those for cells with 12 solute atoms in order to obtain good statistics for the evaluation of the fluctuation formula to determine diffusivities (see below). Additionally, the transport coefficient of the solute was found to change only very slightly with concentration by a factor of approximately 0.02 log units per atom percent solute.

In order to calculate diffusion coefficients, the  $P$ - $T$  dependence of the activation terms, and to investigate liquid structural properties, we performed a minimum of 32 simulations of each liquid composition using densities corresponding to six pressures for the liquid Fe equation of state by Lu et al. (2005a, 2005b) (1 bar, 7, 15, 35, 85, 135 GPa) and at least four different temperatures, with 300 K spacing, at each pressure. We also performed eight additional simulations on liquid Fe<sub>0.92</sub>Si<sub>0.08</sub> along two isobars (60, 110 GPa) (see Chapter 5) and 21 additional simulations on liquid Fe<sub>0.96</sub>O<sub>0.04</sub> along three isobars (5, 10, 25 GPa) and one isotherm (5200 K) (see Chapter 7).

### 2.3.2. Calculation of diffusion coefficients

The self-diffusion coefficient for species  $\alpha$ ,  $D_\alpha$ , is computed using atomic trajectories in the simulation cell and the asymptotic slope of the time-



dependent mean-square displacement (MSD) following the Einstein relation (Allen and Tildesley, 1991):

Figure 2.5: Mean square displacement (MSD),  $\langle (\mathbf{r}_i(\mathbf{t} + \mathbf{t}_0) - \mathbf{r}_i(\mathbf{t}_0))^2 \rangle$  according to Eq. 2.5, for Si, Cr, and Fe in different compositions at 2800 K. Simulation volumes are listed on the right-hand side with values of 14.57, 13.23 and 12.36  $\text{\AA}^3 \text{ atom}^{-1}$  corresponding to approximately 1 bar, 7 GPa, and 15 GPa, respectively. Diffusion coefficients are calculated as 1/6 of the slope over the diffusive regime (200 – 700 fs) ( $\sim t^1$ ), shown in log-scale for Si (inset).

$$D_\alpha = \lim_{t \rightarrow \infty} \frac{1}{N_\alpha} \sum_{i=1}^{N_\alpha} \frac{\langle (r_i(t+t_0) - r_i(t_0))^2 \rangle}{6t}, \quad (2.5)$$

where  $N_\alpha$  is the total number of atoms of species  $\alpha$ ,  $r_i(t)$  is the position of the  $i^{\text{th}}$  atom at time  $t$ , and the angular brackets indicate the ensemble average computed over different origin times,  $t_0$ , along the FP-MD trajectories (Figure 2.5). In addition, we combine self-diffusion coefficients calculated using MSD and interatomic spacings measured from partial radial distribution functions

(RDFs) obtained from the same simulations to calculate the viscosity of liquid iron and binary alloy compositions according to the Stokes-Einstein relation (Eq. 2.4). Calculated viscosities are discussed further in Section 5.6.3.

### 2.3.3. Radial pair distribution function

The radial distribution function (RDF) or pair correlation function,  $g(r)$ , in a system of particles (e.g. atoms) is a statistical tool to describe how density varies as a function of radial distance,  $r$ , from a reference particle. The partial RDF,  $g_{ab}(r)$ , is defined such that, when considering an atom of species  $a$ , the probability of finding an atom of species  $b$  in a spherical shell ( $r, r + dr$ ) is  $\rho_b 4\pi r^2 g_{ab}(r) dr$ , where  $\rho_b = X_b/V$  is the number density of species  $b$  with mole fraction  $X_b$ , and  $V$  is the volume per atom. An illustration of this analytical method is shown in Figure 2.6a with a typical RDF shown in Figure 2.6b.

The position of the first maximum in the RDF represents the average radius of the first coordination sphere (Figure 2.6b). This distance therefore corresponds to the average interatomic distance between the species of interest. Similarly, the position of the second and third maxima in the RDF represent the radii of the second and third coordination spheres, respectively. Additionally, the coordination number,  $N_{ab}^c$ , or the average number of nearest neighbors of species  $b$  surrounding an atom of species  $a$  can be obtained from the integration of the first RDF peak, following

$$N_{ab}^c = 4\pi\rho_b \int_0^{r_{ab}^c} r^2 g_{ab}(r) dr \quad , \quad (2.6)$$

where  $r_{ab}^c$  is the position of the minimum after the first peak of  $g_{ab}$  (Figure 2.6b).

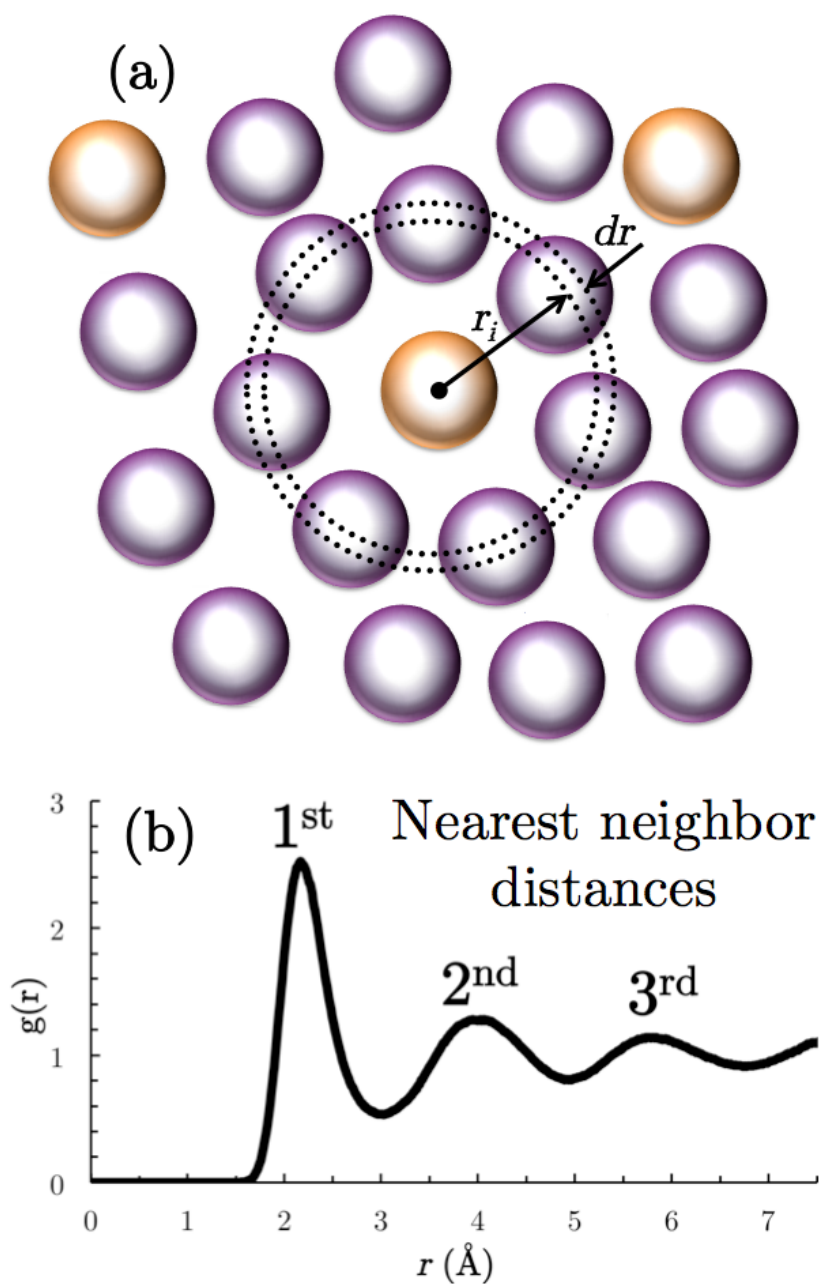


Figure 2.6: (a) The radial distribution function is calculated according to the counting statistics of intercepting an atom of species  $b$  (purple spheres) by a sphere centered around an atom of species  $a$  (gold spheres). (b) Plotting the  $g(r)$  as a function of radial distance ( $r$ ) shows the average distance between coordination spheres, represented by the distance to the each sequential peak. For example, in this simulation of pure iron, the first and second nearest neighbor distances (or radius of the first and second coordination sphere) are approximately 2.1 Å and 4 Å, respectively.

Liquid structural properties can also be obtained experimentally using X-ray diffraction by measuring the structure factor,  $S(Q)$ , which can then be used to calculate the  $g(r)$ . However, such measurements are very challenging to obtain for large wave numbers that correspond to the short-range interaction and for multicomponent liquids at high  $P$ . For multi-component systems, they also require *a priori* assumptions of pair interactions in order to quantify the local coordination environments, which remain poorly constrained.

In this study, we investigated the structural properties of liquid iron and binary iron alloy compositions by analyzing the partial RDFs,  $g_{\text{FeFe}}(r)$ ,  $g_{\text{Fe}\phi}(r)$ , and  $g_{\phi\phi}(r)$ , where  $\phi$  is the alloy species (Si, O, or Cr) from the FP-MD simulations. As a consequence, we were able to obtain information regarding the local packing environments around solute species in liquid iron over a wide  $P$ - $T$  range, as well as gather new insights into a liquid-liquid structural transition that had been previously reported from experiments below 5 GPa (Sanloup et al., 2000; Shibazaki et al., 2015), as described in further detail in Chapter 7.

## 2.4 References

Alfè D., Price G.D. and Gillan M. (1999) Oxygen in the Earth's core: a first-principles study. *Phys. Earth. Planet. Inter.* **110**, 191-210.

Alfè, D., Gillan, M.J. and Price G.D. (2002) Composition and temperature of the Earth's core constrained by combined ab initio calculations and seismic data. *Earth Planet. Sci. Lett.* **195**, 91-98.

Anderson H.C. (1980) Molecular dynamic simulations at constant pressure and/or temperature. *J. of Chem. Phys.* **72**, 2384-2393.

Carslaw H.S. and Jaeger J.C. (1986) *Conduction of Heat in Solids*. 2nd ed. Oxford University Press: New York, pp. 520.

Crank J. (1980) *The Mathematics of Diffusion*. 2nd ed. Oxford University Press: New York, pp. 414.

Darken L.S. (1948) Diffusion, mobility and their interrelation: through free energy in binary metallic systems. *Trans. AIME* **175**, 184.

Dobson, D. P., Brodholt, J.P., Vočadlo, L., and Crichton W.A. (2001) Experimental verification of the Stokes-Einstein relation in liquid Fe-FeS at 5 GPa. *Mol. Phys.* **99**, 773-777.

Hohenberg P. and Kohn W. (1964) Inhomogeneous electron gas. *Phys. Rev.* **136**, B864.

Kohn W. and Sham L.J. (1965) Self-consistent equations including exchange and correlation effects. *Phys. Rev.* **140**, A1133.

Kresse G. and Furthmüller J. (1996) Efficient iterative schemes for *ab initio* total-energy calculations using a plane-wave basis set. *Phys. Rev. B.* **54**, 11169.

Kresse G. and Joubert J. (1999) From ultrasoft pseudopotentials to the projector augmented-wave method. *Phys. Rev. B* **59**, 1758.

Liebske, C., Schmickler, B., Terasaki, H., Poe, B.T., Suzuki, A., Funakoshi, K., Ando, R. and Rubie D.C. (2005) Viscosity of peridotite liquid up to 13 GPa: implications for magma ocean viscosities. *Earth Planet. Sci. Lett.* **240**, 589-604.

Mattsson A.E. (2002) In Pursuit of the “Divine” Functional. *Science.* **298**, 759–760.

Ni H., Hui H., and Steinle-Neumann G. (2015) Transport properties in silicate melts. *Rev. Geophys.* **53**, 715-744.

Perdew J.P., Burke K. and Wang Y. (1996) Generalized gradient approximation for the exchange-correlation hole of a many-electron system. *Phys. Rev. B* **54**, 533-539.

Perdew J.P., Ruzsinszky A., Tao J. Staroverov V.N., Scuseria G. and Csonka

G. (2005) Prescription for the design and selection of density functional approximations: More constraint satisfaction with fewer fits. *J. Chem. Phys.* **123**, 062201.

Pozzo, M., Davies, C., Gubbins, D. and Alfè D. (2013) Transport properties for liquid silicon-oxygen-iron mixtures at Earth's core conditions. *Phys. Rev. B.* **87**, doi: 10.1103/PhysRevB.87.014110.

Pozzo M., Davies C., Gubbin D., and Alfè D. (2012), Thermal and electrical conductivity of iron at Earth's core conditions. *Nature.* **485**, 355–358.

Saxton H.J. and Sherby O.D. (1962) Viscosity and atomic mobility in liquid metals. *Trans Am. Soc. Metals* **55**, 826-843.

Shibazaki Y., Kono Y. and Fei Y. (2015) Microscopic structural change in a liquid Fe-C alloy of  $\sim 5$  GPa. *Geophys. Res. Lett.* **42**. 5236-5242.

Vočadlo L., de Wijs G.A., Kresse G., Gillan M. and Price G.D. (1997) First principles calculations on crystalline and liquid iron at Earth's core conditions. *Faraday Discuss.* **106**, 205-217.

Zwanzig R. (1983) On the relation between self-diffusion and viscosity of liquids. *J. Chem. Phys.* **25**, 317-318.

# Synopsis of Results

In this chapter, I summarize the three primary projects and major findings of my Ph.D. research. A complete description of this work is given in Chapters 5-7. All three projects included the determination of diffusive kinetic properties of one or more solute elements (Si, O, Cr), as well as Fe self-diffusion, in liquid iron using experimental methods, theoretical methods or both. Two of the three projects involved the analysis of structural properties of these elements in liquid iron using theoretical methods. This is the first comprehensive study to jointly use and compare experimental and theoretical results conducted under similar conditions with the aim to better understand the effects of pressure and temperature on diffusion in liquid iron and liquid iron alloys. Additionally, this is the first experimental study to measure chemical diffusion in liquid iron at high pressure.

### 3.1 Mass transport and structural properties of Si and Cr in liquid iron at high pressure

Experiments were performed using a multi-anvil apparatus over the  $P$ - $T$  range of 1-18 GPa and 1873-2428 K. Diffusion couples consisted of pure iron and iron alloy cylinders placed end to end in a vertical orientation. In order to compare experimental data with diffusion rates calculated by FP-MD under laboratory-accessible conditions and to extend our dataset to the Earth's

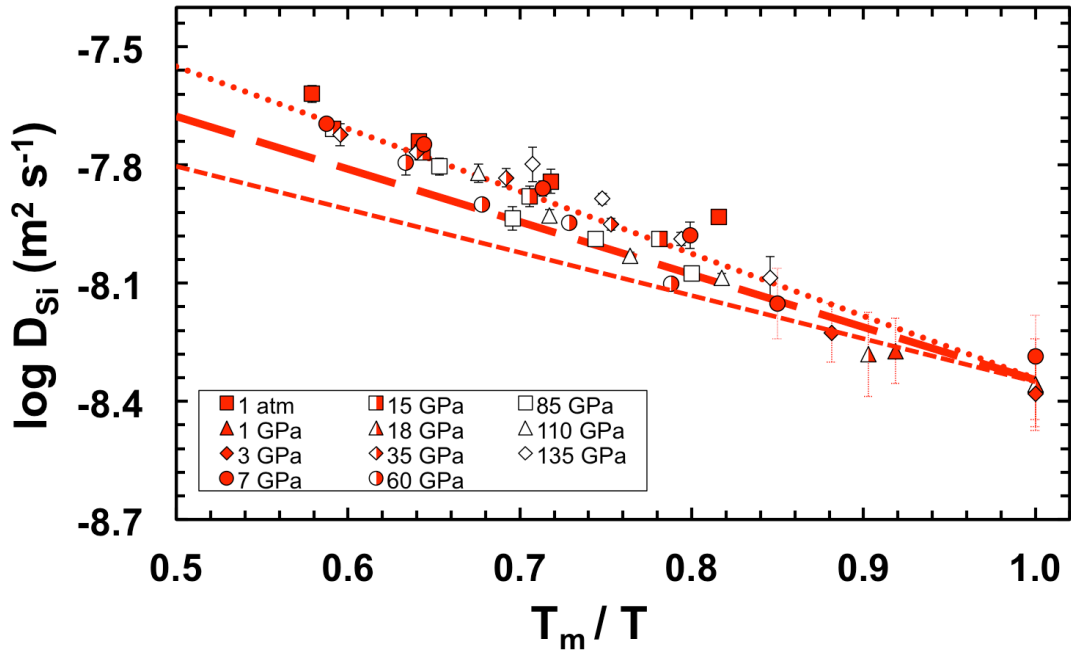


Figure 3.1: Diffusion coefficients of silicon in liquid iron determined from experiments to 18 GPa and calculations to 135 GPa are shown as a function of homologous temperature ( $T_m / T$ ). Linear fits, according to Eq. 1.6, are shown to the experimental data (short-dashed lines) and FP-MD results (dotted lines). Averaged linear fits to both experiments and calculations are shown as long-dashed lines. Cr and Fe diffusion coefficients show a nearly identical behavior, as discussed further in Section 5.6.1.

core-mantle boundary, we have also performed first principles molecular dynamic simulations (FP-MD) and calculated self-diffusion coefficients and activation parameters for Si, Cr, and Fe diffusion in liquid Fe,  $\text{Fe}_{0.92}\text{Si}_{0.08}$  and  $\text{Fe}_{0.92}\text{Cr}_{0.08}$  compositions over the  $P$ - $T$  range of 0 to 135 GPa and 2200-5500 K. Differences between experimental data and computational results are remarkably small ( $< 0.1$  log units).

Over the entire range of pressure and temperatures studied, diffusion coefficients are described well using an exponential function of the homologous temperature relation (Eq. 1.5) for both experimental data and computational

results yielding constant diffusivities along the melting curve from ambient to core pressures (Figure 3.1). Verification of the homologous temperature relation of mass transport in liquid metals, as well as the excellent agreement between experiments and FP-MD simulations, provides a new and simple framework for interpreting and modeling mass transport processes of liquid iron alloys in all planetary bodies, regardless of size. This finding also implies that low pressure experiments can be used with confidence to predict rates of mass transport in the Earth's outer core. Our results are used to evaluate the kinetics of chemical equilibration during core formation and diffusivity contrasts across a solid-liquid metal interface, e.g. inner core boundary. The data can also be reproduced to within an error of  $< 10\%$  using the Arrhenian model (Eq. 1.3) with derivatives of the activation parameters, determined over a very wide range of  $P$ - $T$  conditions.

The activation parameters and self-diffusion coefficients of solute species (Si, Cr) are found to be identical to those of Fe in both alloy and pure iron compositions under the same conditions. Additionally, structural properties analyzed using partial radial distribution functions (RDFs) show the average distance between two Fe atoms,  $\bar{r}_{\text{Fe-Fe}}$ , is identical to that of  $\bar{r}_{\text{Fe-Si}}$  and  $\bar{r}_{\text{Fe-Cr}}$  over the entire  $P$ - $T$  range of study. These findings support the notion that diffusion of Si and Cr (and thus likely other species of similar atomic radii) occurs via direct atomic substitution with Fe. We combine diffusion coefficients with structural properties obtained from partial radial distribution functions of the simulations to estimate a viscosity profile of liquid iron, liquid  $\text{Fe}_{0.92}\text{Si}_{0.08}$  and liquid  $\text{Fe}_{0.92}\text{Cr}_{0.08}$  as a function of density from surface to inner core conditions (Figure 3.2). Our findings show good agreement with the recent computations by Pozzo et al. (2013), which employed the

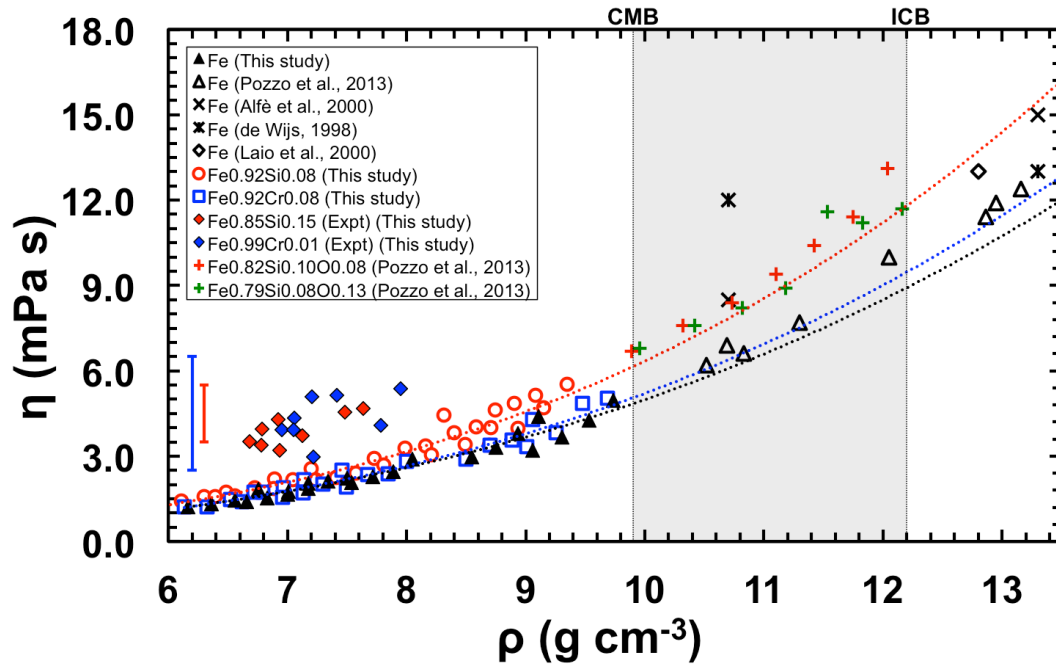


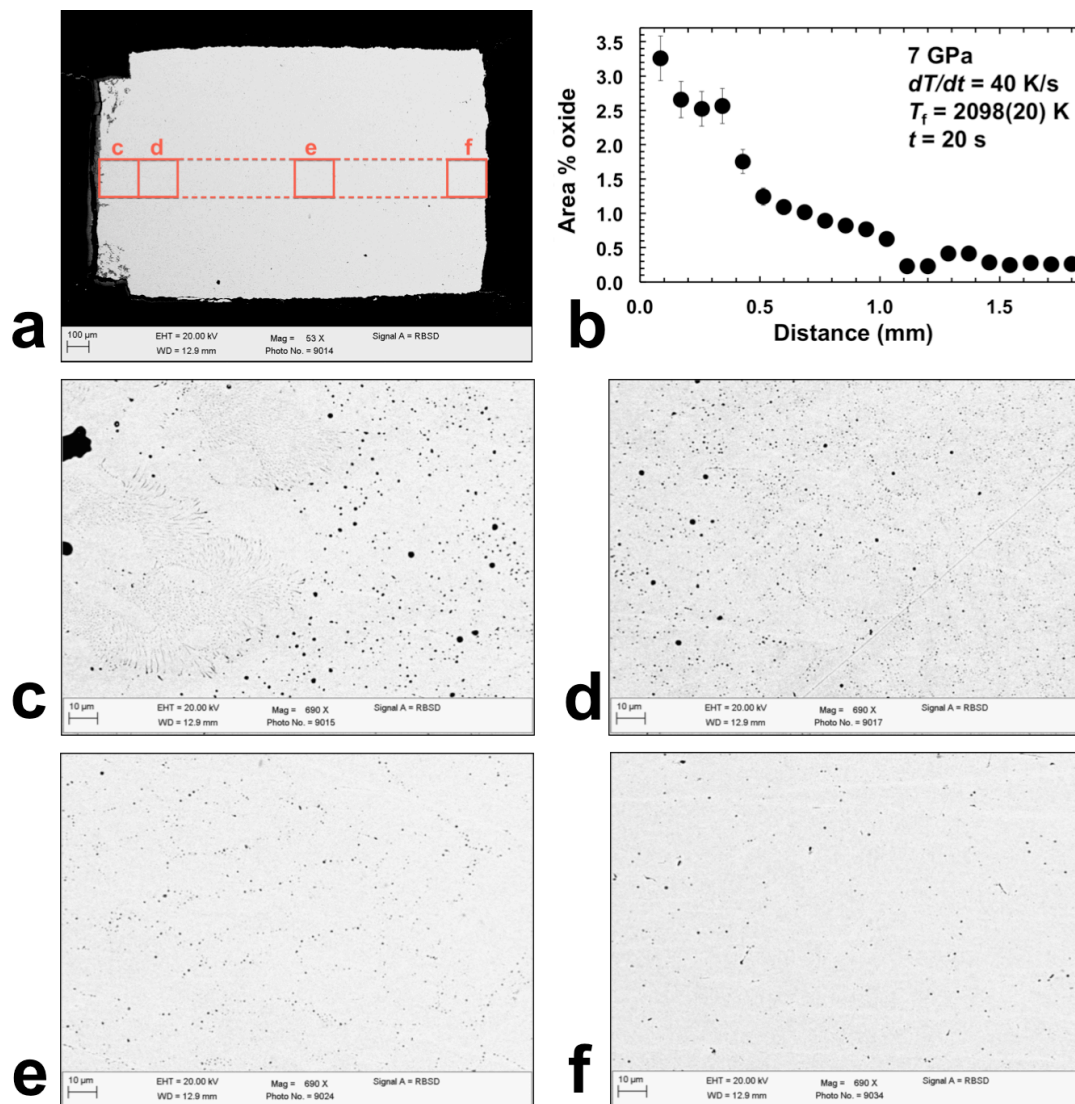
Figure 3.2: Viscosities of liquid iron and its alloys as a function of density. Viscosities were calculated via the Stokes-Einstein relation with self-diffusion coefficients and interatomic spacings obtained from mean-square displacement (MSD) and partial RDFs, respectively. The relationship between density and interatomic spacing was used to estimate viscosities from experimental Si and Cr diffusion data. Standard  $1\sigma$  experimental errors are shown on the left for Si (red) and Cr (blue). Liquid iron viscosities reported in previous studies are shown as open triangles (Pozzo et al., 2013); crosses (Alfè et al., 2000); stars (de Wijs et al., 1998); and open diamonds (Laio et al., 2000). Extrapolation of best-fit curves to viscosities determined in the present study to densities of the Earth's outer core (shaded region) are shown as black, red, and blue dotted lines for liquid Fe,  $Fe_{0.92}Si_{0.08}$  and  $Fe_{0.92}Cr_{0.08}$ , respectively.

computationally more expensive Green-Kubo relation that relates viscosity to the integral of the stress tensor autocorrelation function.

## 3.2 Mass transport properties of oxygen in liquid iron at high pressure

We have measured the diffusivity of oxygen in liquid iron using a multi-anvil apparatus over the  $P$ - $T$  range of 3-18 GPa and 1975-2643 K. Diffusion couples consisted of a pure iron rod and a sintered  $\text{Fe}_{0.85}\text{O}_{0.15}$  disk placed end-to-end in a vertical orientation. Quenched samples consisted of an iron-rich matrix that contains small oxygen-rich spheroids that formed by exsolution during quench (Figure 3.3). EPMA spot analyses were acquired along the full length of the diffusion couple along a line perpendicular to the diffusion interface with an effective beam diameter of  $\sim 70$   $\mu\text{m}$ , sufficiently large to sample both the matrix and exsolved inclusions. Additionally, the solubility of oxygen in liquid iron has been shown to increase with  $T$  at fixed  $P$ . We therefore use quenched concentration profiles in order to estimate the total dissolved oxygen and to assign an appropriate “initial concentration” for each individual experiment, as described further in Section 6.3.3.

Pressure is found to have a negligible effect on oxygen diffusion coefficient in liquid iron between 3 and 18 GPa. The activation volume is very small ( $\Delta V = 0.1 \pm 0.1$   $\text{cm}^3$   $\text{mol}^{-1}$ ), which, despite the large uncertainty, is in qualitative agreement with values reported from FP-MD simulations of liquid  $\text{Fe}_{0.9}\text{O}_{0.1}$  at 100-350 GPa ( $\Delta V = 0.25 \pm 0.11$   $\text{cm}^3$   $\text{mol}^{-1}$ ; Ichikawa and Tsuchiya, 2015). Extrapolation of the oxygen diffusion coefficient to  $P$ - $T$  conditions of the Earth’s core using activation parameters obtained from the Arrhenian fits are 0.3 to 0.4 log units faster than those reported from computations (Alfè et al., 1999; Pozzo et al., 2013; Ichikawa and Tsuchiya, 2015). Considering the very wide extrapolation range in  $P$  and the different methodologies employed in the two approaches, the agreement between



experiments and calculations is very good and suggests that any pressure effect that may develop between 18 and 100 GPa cannot be significant.

We use oxygen diffusion parameters obtained in this study to constrain the maximum size of descending liquid metal droplets in a magma ocean that is required for chemical equilibrium to be achieved (Figure 3.4). Oxygen diffusion in liquid iron is sufficiently rapid such that chemical equilibration in small liquid droplets ( $r \sim 1$  mm) would require less than 1 min even at very low magma ocean temperatures ( $\sim 2500$  K), but larger droplets ( $r \gtrsim 20$  cm)

*Figure 3.3 (opposite page): Backscattered electron (BSE) images and analysis of a quenched sample from a diffusion experiment annealed at 7 GPa and 2098(20) K for 20 seconds. (a) 115  $\mu\text{m}$  x 170  $\mu\text{m}$  BSE images were collected every 60 microns along a traverse perpendicular to the diffusion couple interface. In this run, the initial  $\text{Fe}_{0.85}\text{O}_{0.15}$  disk (on the left) has a slightly smaller radius than the pure iron cylinder due to shrinkage during preparatory sintering. BSE images were converted to a binary raster and analyzed using the ImageJ software (<http://imagej.nih.gov/ij/>). The area percentage of dark material, consisting of exsolved oxide, in each image along the transect is shown in panel (b). (c) Exsolution textures change from feathery features or dendrites surrounding oblong grains in the vicinity of the  $\text{Fe}_{0.85}\text{O}_{0.15}$  to bimodally-sized spheroids away from the diffusion interface. (d) The concentration of large ( $\sim 1 \mu\text{m}$ ) exsolution spheroids decreases from left to right and submicron spheroids dominate on the right. (e) Exsolution spheroids are visible along grain boundaries with a marked decrease in concentration compared with previous panels. The proportion of matrix metal becomes increasingly dominant from left to right in panels (e) and (f).*

would remain in chemical disequilibrium upon sinking to primordial CMB depths (Figure 3.4). Our results indicate that if the composition of Earth's core is representative of equilibrium chemical exchange with a silicate magma ocean, then it could only have been accomplished by large-scale break-up of impactor cores to liquid metal droplet sizes significantly smaller than a few tens of centimeters.

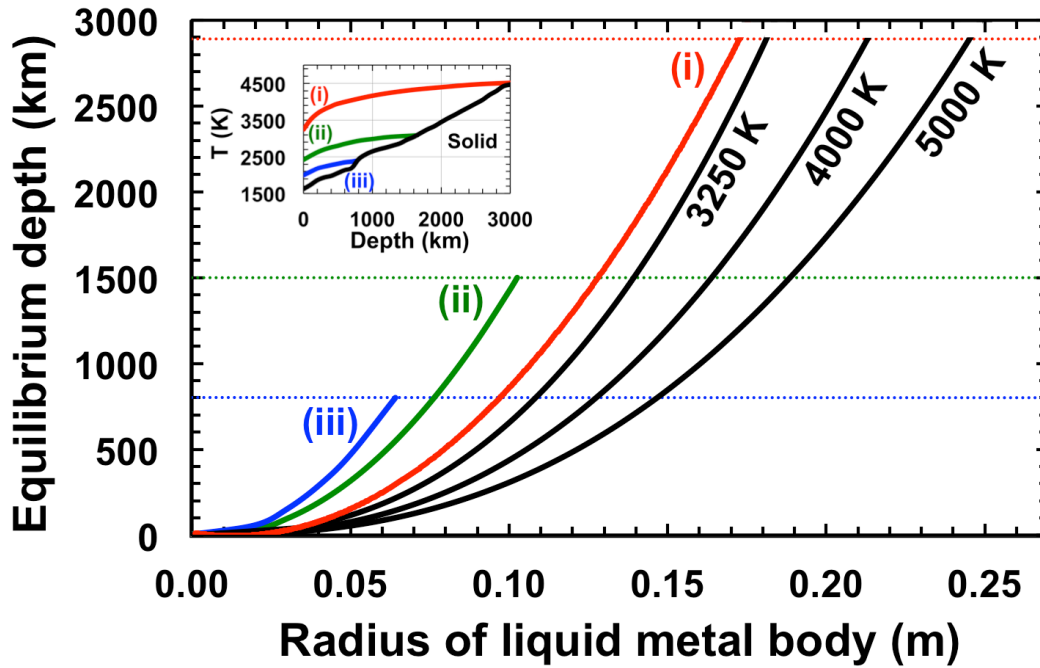


Figure 3.4: Equilibrium depths as a function of liquid metal droplet radius along isentropes (inset; Miller et al., 1991) for a magma ocean of (i) 2891 km, (ii) 1500 km, and (iii) 800 km depth. Primordial CMB depths are shown as horizontal lines of the corresponding color. Also shown are equilibrium depths for droplets along fixed isotherms (black curves). The maximum droplet radius for chemical equilibrium of oxygen between liquid metal and liquid silicate in a deep magma ocean is therefore constrained to a few tens of centimeters.

### 3.3 Mass transport and structural properties of liquid $\text{Fe}_{0.96}\text{O}_{0.04}$ at high pressure

We have investigated the structural and transport properties of liquid  $\text{Fe}_{0.96}\text{O}_{0.04}$  using first principles molecular dynamics (FP-MD) in order to better understand the effects of  $P$  and  $T$  on the mechanics of light element incorporation in liquid iron. Simulations were performed over a wide density range, corresponding to pressures of 0 to 330 GPa and temperatures between

2200-5500 K in order to bridge the gap between low pressure experiments (Section 3.2 and Chapter 6) and high pressure calculations (Ichikawa and Tsuchiya, 2015).

Our results indicate a change in the dominant compression mechanism operating in liquid  $\text{Fe}_{0.96}\text{O}_{0.04}$  at approximately  $8 \text{ g cm}^{-3}$ , corresponding to a low-pressure structural change from body centered cubic (bcc)-like to a combination of bcc-like + face centered cubic (fcc)-like, in agreement with previous experimental studies of liquid Fe (Sanloup et al., 2000) and liquid Fe-3.5 wt.% C (Shibazaki et al., 2015). The pressure-induced structural transition and associated transport anomaly provides a reasonable explanation for the previously reported change from a negative to a positive pressure dependence of oxygen solubility in liquid iron over this density range (Asahara et al., 2007; Ozawa et al., 2008; Frost et al., 2010).

For densities  $\lesssim 8 \text{ g cm}^{-3}$ , compression is accommodated by a closer packing of both oxygen and iron with coordination numbers increasing from  $\sim 3$  to  $\sim 6$  and  $\sim 10$  to  $\sim 13$ , respectively (Figure 3.5c). Over this density range, the average distance between iron and neighboring iron atoms ( $\bar{r}_{\text{Fe-O}}$ ) increases with density to a maximum (Figure 3.5b), while the average distance between neighboring iron atoms ( $\bar{r}_{\text{Fe-Fe}}$ ) remains essentially constant (Figure 3.5a). Additionally, the oxygen self-diffusion coefficient ( $D_{\text{O}}$ ) shows a negligible pressure dependence for densities  $\lesssim 8 \text{ g cm}^{-3}$ , in agreement with experiments up to 18 GPa (Section 3.2, Chapter 6). Our results are consistent with previous studies that attribute anomalous pressure-dependencies in the viscosity of liquids (Kono et al., 2013; Brazhkin et al., 2009; 2010) to pressure-induced coordination changes.

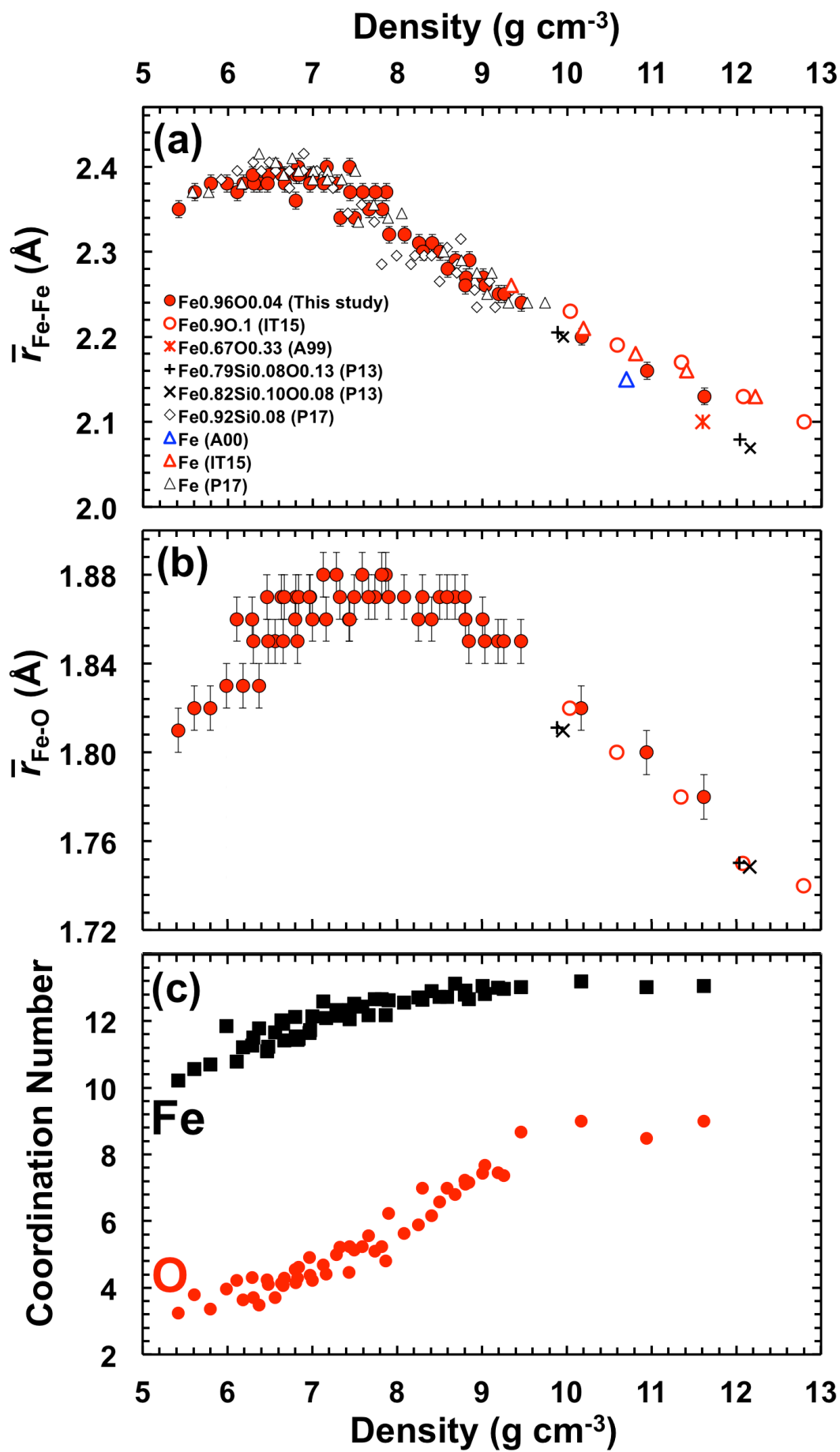


Figure 3.5 (opposite page): Computed structural properties of liquid  $\text{Fe}_{0.96}\text{O}_{0.04}$ . (a) Average interatomic distances between neighboring Fe atoms (filled squares) alongside those previously reported for liquid  $\text{Fe}_{0.9}\text{O}_{0.1}$  (IT15, Ichikawa and Tsuchiya, 2015), liquid  $\text{Fe}_{0.67}\text{O}_{0.33}$  (A99, Alfè et al., 1999),  $\text{Fe}_{0.82}\text{Si}_{0.10}\text{O}_{0.08}$  and  $\text{Fe}_{0.79}\text{Si}_{0.08}\text{O}_{0.13}$  liquids (P13, Pozzo et al., 2013), pure liquid Fe (A00, Alfè et al., 2000; IT15; P17, this study, Chapter 5) and liquid  $\text{Fe}_{0.92}\text{Si}_{0.08}$  (P17) as a function of density. Error bars represent  $\pm 1\sigma$  of the peak position. All liquid compositions show only small variations in the Fe-Fe distance of  $\sim 2.38 \text{ \AA}$  between  $\sim 5.5 \text{ g cm}^{-3}$  and  $\sim 7.6 \text{ g cm}^{-3}$ . Above  $\sim 7.6 \text{ g cm}^{-3}$ , the Fe-Fe distance for all compositions decreases monotonically to  $2.13 \text{ \AA}$  at  $11.62 \text{ g cm}^{-3}$ . (b) Average interatomic distance between Fe and O atoms in liquid  $\text{Fe}_{0.96}\text{O}_{0.04}$  shows an increase with density from  $\sim 1.81 \text{ \AA}$  at  $5.4 \text{ g cm}^{-3}$  to a maximum of  $\sim 1.88 \text{ \AA}$  at  $\sim 8 \text{ g cm}^{-3}$ . Above  $\sim 8 \text{ g cm}^{-3}$ , Fe-O distances decrease monotonically to  $\sim 1.78 \text{ \AA}$  at  $11.62 \text{ g cm}^{-3}$ . Fe-O distances reported for liquid  $\text{Fe}_{0.9}\text{O}_{0.1}$  (IT15) show that this trend continues to at least  $12.8 \text{ g cm}^{-3}$ . (c) Average coordination number of Fe and O in the  $\text{Fe}_{0.96}\text{O}_{0.04}$  simulation cells following Eq. (2.6). Oxygen coordination increases from  $\sim 3.3$  at  $5.4 \text{ g cm}^{-3}$  to  $\sim 8.7$  at  $\sim 9.5 \text{ g cm}^{-3}$ . Above  $\sim 9.5 \text{ g cm}^{-3}$ , the coordination of oxygen remains constant in a range of  $\sim 8.5$  to  $\sim 9$ . Iron coordination increases from  $\sim 10.2$  at  $5.4 \text{ g cm}^{-3}$  to  $\sim 12.6$  at  $\sim 8 \text{ g cm}^{-3}$  and remains approximately constant with increasing density.

For density  $\gtrsim 8 \text{ g cm}^{-3}$ , interatomic distances and diffusion coefficients for both species decrease monotonically although – interestingly – differences between  $D_{\text{Fe}}$  and  $D_{\text{O}}$  increase with density, while  $\bar{r}_{\text{FeFe}}$  and  $\bar{r}_{\text{FeO}}$  become more similar (Figure 3.6). The average iron coordination remains constant at  $\sim 13$ , characteristic of a close-packed liquid, while oxygen coordination increases to approximately 8.5 at  $\sim 10 \text{ g cm}^{-3}$  and remains essentially constant with further compression to  $11.6 \text{ g cm}^{-3}$ . The average oxygen coordination of approximately 8-9 at outer core densities (Figure 3.5c) implies local bcc packing around oxygen, which distorts the bulk close-packing of iron atoms.

These findings support previous suggestions (e.g. Alfè et al., 1999) that oxygen should partition strongly into the liquid upon core crystallization due to its small size relative to iron, while silicon and sulfur, with atomic radii similar to that of iron, should have liquid-solid partition coefficients close to unity.

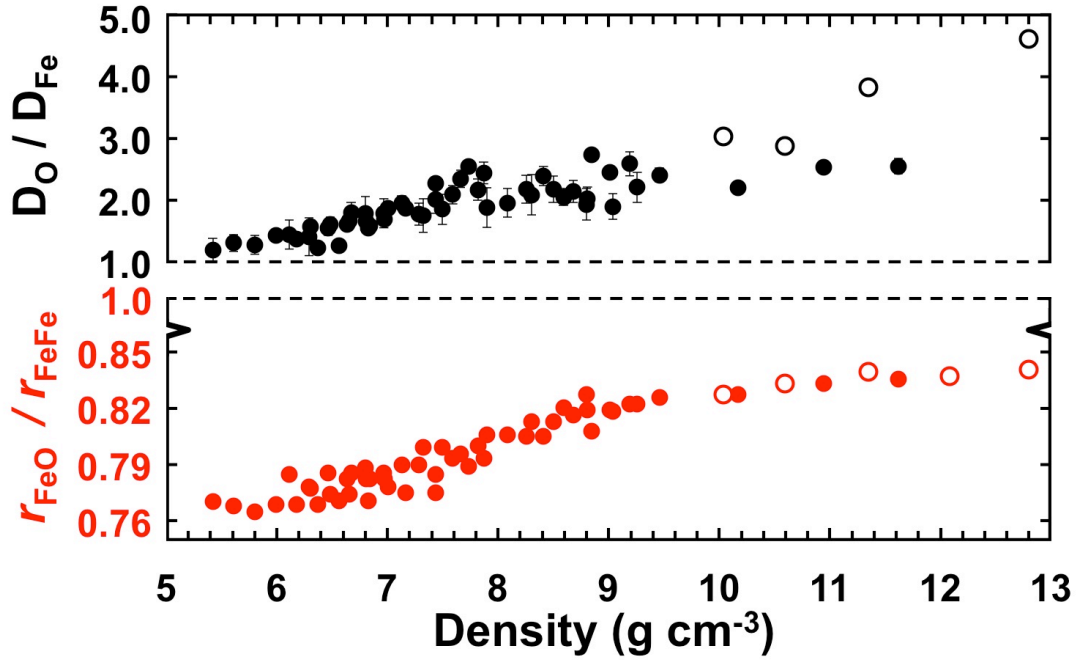


Figure 3.6: Mass transport (black) and nearest neighbor distance (red) ratios of oxygen and iron in liquid  $Fe_{0.96}O_{0.04}$  as a function of density. Vertical error bars represent  $\pm 1\sigma$ . Open symbols are for liquid  $Fe_{0.9}O_{0.1}$  simulations reported by Ichikawa and Tsuchiya (2015). With increasing density, the difference between  $D_O$  and  $D_{Fe}$  increases while average Fe-O and Fe-Fe distances become more similar, although they remain significantly different.

### 3.4 References

Alfè D., Price G.D. and Gillan M. (1999) Oxygen in the Earth's core: a first-principles study. *Phys. Earth. Planet. Inter.* **110**, 191-210.

Alfè, D., Kresse, G. and Gillan M.J. (2000) Structure and dynamics of liquid iron under Earth's core conditions. *Phys. Rev. B* **61**, 132-142.

Allègre C.J., Poirier J.P., Humler E. and Hofmann A.W. (1995) The chemical composition of the Earth, *Earth Planet. Sci. Lett.*, **134**, 515–526.

Asahara Y., Frost D.J. and Rubie D.C. (2007) Partitioning of FeO between magnesiowüstite and liquid iron at high pressures and temperatures: Implications for the compositions of the Earth's outer core. *Earth Planet. Sci. Lett.* **257**, 435-559.

Brazhkin V.V., Kanzaki M., Funakoshi K. and Katayama Y. (2009) Viscosity behavior spanning four orders of magnitude in As-S melts under high pressure. *Phys. Rev. Lett.* **102**, 115901.

Brazhkin V.V., Farnan I., Funakoshi K., Kanzaki M., Katayama Y., Lyapin A.G. and Saitoh H. (2010) Structural transformation and anomalous viscosity in the B<sub>2</sub>O<sub>3</sub> melt under high pressure. *Phys. Rev. Lett.* **105**, 115701.

de Wijs, G.A., Kresse, G., Vočadlo, L., Dobson, D., Alfè, D., Gillan, M.J. and Price G.D. (1998) The viscosity of liquid iron at the physical conditions of the Earth's core. *Lett. Nature* **392**, 805-807.

Frost D.J., Asahara Y., Rubie D.C., Miyajima N., Dubrovinsky L.S., Holzapfel C., Ohtani E., Miyahara M. and Sakai T. (2010) Partitioning of oxygen between the Earth's mantle and core. *J. Geophys. Res.* **115**, B02202. doi:10.1029/2009JB006302.

Ichikawa, H. and Tsuchiya T. (2015) Atomic transport property of Fe-O liquid alloys in the Earth's outer core P,T condition. *Phys. Earth Planet. Int.* **247**, 27-35.

Kono Y., Kenney-Benson C., Park C., Shen G., and Wang Y. (2013) Anomaly in the viscosity of liquid KCl at high pressures. *Phys. Rev. B* **87**, 024302.

Laio A., Bernard S., Chiarotti G. L., Scandolo S. and Tosatti E. (2000)

Physics of iron at Earth's core conditions, *Science* **287**, 1027 – 1030.

Ozawa H., Hirose K., Mitome M., Bando Y., Sata N. and Ohishi Y. (2008) Chemical equilibrium between ferropericlase and molten iron to 134 GPa and implications for iron content at the bottom of the mantle. *Geophys. Res. Lett.* **35**, L05308, doi:10.1029/2007GL032648.

Poirier J.P. (1988) Transport properties of liquid metals and viscosity of the Earth's core. *Geophys. J.* **92**, 99-105.

Pozzo, M., Davies, C., Gubbins, D. and Alfè D. (2013) Transport properties for liquid silicon-oxygen-iron mixtures at Earth's core conditions. *Phys. Rev. B.* **87**, DOI: 10.1103/PhysRevB.87.014110.

Sanloup C., Guyot F., Gillet P., Fiquet G., Hemley R.J., Mezouar M. and Martinez I. (2000) Structural changes in liquid Fe at high pressures and temperatures from synchrotron X-ray diffraction. *Europhys. Lett.* **52**, 151-157.

Shibazaki Y., Kono Y. and Fei Y. (2015) Microscopic structural change in a liquid Fe-C alloy of  $\sim 5$  GPa. *Geophys. Res. Lett.* **42**. 5236-5242.

### Individual contributions to publications

The current publication statuses of each manuscript (Chapters 5-7) included in this dissertation are summarized below, in addition to an estimate of my individual contribution to the total work performed on a variety of tasks.

#### 1. High $P$ - $T$ experiments and first principles calculations of the diffusion of Si and Cr in liquid iron (Chapter 5)

Author list: Posner E.S., Rubie D.C., Frost D.J., Vlček V. and  
Steinle-Neumann G.

Publication status: Accepted in *Geochimica et Cosmochimica Acta*

- Project idea: 50%
- Experiments: 100%
- Experimental design: 50%
- Experimental analysis: 100%
- Development of numerical model: 20%
- Use of numerical model: 100%
- FP-MD calculations: 100%
- Software development: 0%
- Calculation of diffusion coefficients: 100%
- Measurement of structural properties: 100%
- Idea development for discussion section: 80%
- Writing manuscript: 95%

## 2. Experimental determination of oxygen diffusion in liquid iron at high pressure (Chapter 6)

Author list: Posner E.S., Rubie D.C., Frost D.J., and Steinle-Neumann G.

Publication status: Accepted in *Earth and Planetary Science Letters*

- Project idea: 50%
- Experiments: 100%
- Experimental design: 50%
- Experimental analysis: 100%
- Development of numerical model: 20%
- Development of data fitting scheme: 75%
- Use of numerical model: 100%
- Idea development for discussion section: 80%
- Writing manuscript: 95%

## 3. Structural changes and anomalous self-diffusion of oxygen in liquid iron at high pressure (Chapter 7)

Author list: Posner E.S., Steinle-Neumann G., Vlček V. and Rubie D.C.

Publication status: Accepted in *Geophysical Research Letters*

- Project idea: 100%
- FP-MD calculations: 100%
- Calculation of diffusion coefficients: 100%
- Measurement of structural properties: 100%
- Idea development for discussion section: 90%
- Writing manuscript: 95%

# High $P$ - $T$ experiments and first principles calculations of the diffusion of Si and Cr in liquid iron

ESTHER S. POSNER<sup>1</sup>, DAVID C. RUBIE<sup>1</sup>, DANIEL J. FROST<sup>1</sup>, VOJTĚCH VLČEK<sup>1,2,3</sup>, GERD STEINLE-NEUMANN<sup>1</sup>

Accepted for publication in *Geochimica et Cosmochimica Acta*

## 5.1 Abstract

Chemical diffusion rates of Si and Cr in liquid iron have been measured over the  $P$ - $T$  range of 1–18 GPa and 1873–2428 K. The experiments were performed using a multi-anvil apparatus with diffusion couples comprised of pure iron and iron alloy placed end to end in a vertical orientation. In order to extend our dataset to the Earth’s core-mantle boundary and to compare experimental data with theoretical diffusion rates calculated under laboratory-accessible conditions, we have also performed first principles molecular dynamic simulations (FP-MD) and calculated self-diffusion coefficients and activation parameters for Si, Cr, and Fe diffusion in liquid Fe, Fe<sub>0.92</sub>Si<sub>0.08</sub> and Fe<sub>0.92</sub>Cr<sub>0.08</sub> compositions over the  $P$ - $T$  range of 1 bar to 135 GPa and 2200-

---

<sup>1</sup> Bayerisches Geoinstitut, Universität Bayreuth, 95440 Bayreuth, Germany

<sup>2</sup> Fritz Haber Center for Molecular Dynamics, Institute of Chemistry, The Hebrew University of Jerusalem, Jerusalem 91904, Israel

<sup>3</sup> now at: Department of Chemistry and Biochemistry, University of California, Los Angeles, CA 90095, USA

5500 K. Over the entire range of pressures and temperatures studied using both methods, diffusion coefficients are described well using an exponential function of the homologous temperature relation,  $D = D_h \exp(-gT_h)$ , where  $T_h = T_m/T$ ,  $T_m$  is the melting temperature at the pressure of interest and  $g$  and  $D_h$  are constants. Our findings indicate constant diffusivities of approximately  $4 \times 10^{-9} \text{ m}^2 \text{ s}^{-1}$  for Si and Cr and  $5 \times 10^{-9} \text{ m}^2 \text{ s}^{-1}$  for Fe along the melting curve from ambient to core pressures in all liquid compositions studied, with an increase of  $\sim 0.8$  log units at  $T = 2T_m$ . Differences between experimental data and computational results are less than 0.1 log units. Structural properties of liquid iron alloys analyzed using partial radial distribution functions (RDFs) show the average distance between two Fe atoms,  $r_{\text{Fe-Fe}}$ , is identical to that of  $r_{\text{Fe-Si}}$  and  $r_{\text{Fe-Cr}}$  over the entire  $P$ - $T$  range of study, which supports that the diffusion of Si and Cr (and thus likely other species of similar atomic radii) occurs via direct substitution with Fe. Diffusion coefficients and interatomic distances used to calculate liquid viscosities via the Stokes-Einstein relation yield constant viscosity along the melting curve of  $\sim 6 \text{ mPa s}$  for liquid Fe,  $\sim 7 \text{ mPa s}$  for liquid  $\text{Fe}_{0.92}\text{Cr}_{0.08}$ , and  $\sim 8 \text{ mPa s}$  for liquid  $\text{Fe}_{0.92}\text{Si}_{0.08}$ , with a decrease of  $\sim 0.8$  log units at  $T = 2T_m$ . The data can also be reproduced within  $< 10\%$  using the Arrhenian model with derivatives of the activation parameters determined over a very wide range of  $P$ - $T$  conditions. Verification of a homologous temperature dependence of diffusion in liquid metals, as well as the excellent agreement between experimental results and FP-MD simulations, provides a new and simple framework for interpreting and modeling mass transport processes of liquid iron alloys in all planetary bodies regardless of size. Our results are used to evaluate the kinetics of metal-silicate chemical equilibration during core formation and diffusivity contrasts across a solid-liquid metal interface, i.e. at the inner core boundary.

## 5.2 Introduction

Mass transport properties, such as diffusivity and viscosity, of molten iron and its alloys at high pressures and temperatures are important for understanding large-scale planetary processes including the physical and chemical differentiation of early-formed terrestrial bodies into a dense metallic core and an outer silicate mantle (e.g. Ringwood, 1959; Stevenson, 1990; Rubie et al., 2003) and the length and time scale of chemical equilibration during core formation. Chemical diffusion data is also required for understanding the origin and evolution of geomagnetism that is generally considered to result from thermochemical convection in the liquid outer core (Braginsky, 1963; Gubbins et al., 2003; 2004).

Nevertheless, the effects of pressure ( $P$ ) and temperature ( $T$ ) on mass transport in liquid iron and its alloys remain poorly understood. Previous experimental studies of self-diffusion in liquid iron (Dobson, 2002), liquid  $\text{Fe}_3\text{C}$  (Dobson and Wiedenbeck, 2002) and liquid  $\text{FeS}$  (Dobson, 2000; Dobson et al., 2001) report a mixture of either very large or very small  $P$ - $T$  dependencies (i.e. activation parameters). First principles molecular dynamic (FP-MD) calculations (de Wijs et al., 1998; Alfè et al., 2000; Laio et al., 2000; Pozzo et al., 2013; Ichikawa and Tsuchiya, 2015; Umemoto and Hirose, 2015) have been conducted mostly under extreme  $P$ - $T$  conditions of the Earth's core ( $\sim 135$ – $330$  GPa), far removed from those currently accessible in laboratory experiments ( $\leq 25$  GPa). Disagreement between the extrapolated experimental data and high  $P$ - $T$  computational results yield large uncertainties in the diffusivity and viscosity of the outer core with values ranging over ten orders of magnitude (e.g. Poirier, 1988; Secco, 1995; Dobson, 2002). Additionally, high-pressure experimental data for chemical diffusion in liquid iron alloys,

which are required for understanding length- and timescales of chemical equilibration of light (Si, O, S, C, H, He, etc.) and siderophile (Cr, V, Mn, W, etc.) elements during core formation and compositional convection processes in the Earth's outer core, have not been reported in the literature.

Self-diffusion coefficients ( $D$ ) in simple dissociated liquids, such as metallic melts, have been shown to be related to viscosity,  $\eta$ , via the Stokes-Einstein relation,

$$D\eta = \frac{k_B T}{2\pi a} \quad , \quad (5.1)$$

where  $a$  is an atomic diameter and  $k_B$  is the Boltzmann constant. The Stokes-Einstein relation has been verified experimentally for liquid metals (e.g. Saxton and Sherby, 1962; Dobson et al., 2001), and can be justified theoretically (e.g. Zwanzig, 1983). However, laboratory measurements of self-diffusion and viscosity in liquids can be challenging: the former requires secondary ionization mass spectroscopic (SIMS) analyses of isotopic diffusion profiles, and the latter is limited to pressures below  $\sim 13$  GPa due to geometric limitations of *in-situ* falling sphere X-ray imaging using synchrotron radiation (e.g. Liebske et al., 2005). Additional challenges responsible for the scarcity of experimental data for high-pressure diffusion in liquid metals include (1) low liquid viscosities ( $\gtrsim 0.02$  Pa s) which means fast diffusion rates and thus very short timescales for preserving diffusion profiles within small ( $\sim 1$ - $2$  mm) samples, (2) possible gravity-driven flow or convection, (3) reaction with capsule material, and/or (4) non-isothermal annealing (i.e. the occurrence of substantial diffusion during heating and/or quenching) (Dobson, 2002). In the case of liquid alloys, quenched chemical concentration profiles, on the other hand, can be analyzed routinely by electron microprobe.

A numerical evaluation of concentration profiles that accounts for diffusion that occurs during heating, prior to reaching the maximum temperature, was first proposed by Dobson et al. (2001) to simultaneously solve the time-integrated diffusion equation for a set of experiments conducted at different  $P$ - $T$ - $t$  conditions. In a subsequent experimental study on Fe self-diffusion in liquid iron, Dobson (2002) compared various diffusion models: the free volume model (Cohen and Turnbull, 1959), fluctuation model (Swalin, 1959) and the vibrational model (Nachtrieb, 1967) with the traditional Arrhenius model:

$$D(P, T) = D_0 \exp\left(-\frac{Q}{RT}\right) \quad (5.2)$$

where  $D_0$  is the pre-exponential diffusion coefficient,  $R$  is the universal gas constant, and  $Q$  is the activation energy:

$$Q = \Delta H(P) + P\Delta V(T) . \quad (5.3)$$

Here  $\Delta H$  and  $\Delta V$  are the activation enthalpy and activation volume, respectively. Dobson (2002) fitted the Arrhenius terms  $D_0$ ,  $\Delta H$  and  $\Delta V$  to eleven diffusion profiles produced at 2–20 GPa and 1883–2393 K. Although the activation volumes obtained led to unreasonably low diffusivities when extrapolated to conditions of the Earth's outer core ( $10^{-20}$ – $10^{-30}$  m<sup>2</sup> s<sup>-1</sup>), Dobson (2002) was able to extrapolate diffusion coefficients to values more consistent with the simulations (Alfè et al., 2000) by using a free volume model (see Cohen and Turnbull, 1959). The free volume model, however, requires accurate thermodynamic parameters for the liquid metals, which remain poorly constrained to date.

In order to make a realistic comparison of diffusion coefficients and Arrhenius activation parameters obtained from both experimental and theoretical methods and to check the validity of extrapolated diffusion data to

*P-T* conditions of the Earth’s outer core, we have performed (1) high-pressure diffusion-couple experiments to investigate Si and Cr chemical diffusion in liquid iron using a multi-anvil press up to 18 GPa, and (2) FP-MD calculations for metallic liquid compositions of Fe, Fe<sub>0.92</sub>Si<sub>0.08</sub> and Fe<sub>0.92</sub>Cr<sub>0.08</sub> over a very wide pressure range (1 bar to 135 GPa) that overlaps with *P-T* conditions of our experimental study. This is the first comprehensive study to jointly use and compare experimental and theoretical results conducted under similar conditions with the goal of better understanding the effect of pressure on diffusion in liquid iron and iron alloys. We use our diffusion data to calculate length- and timescales of chemical equilibration during core formation, to estimate the viscosity profile of the Earth’s outer core, and to discuss how transport and structural properties of light elements in liquid iron may provide insights into liquid-solid partitioning at the inner core boundary (ICB) and, as a consequence, the systematics of compositional convection.

## 5.3 Experimental procedure and analysis

### *5.3.1 Multi-anvil sample assembly and procedure*

Chemical diffusion experiments were carried out in 1200 and 5000 tonne multi-anvil presses at the Bayerisches Geoinstitut employing Cr<sub>2</sub>O<sub>3</sub>-doped MgO octahedra with 18 mm edge lengths as the pressure medium and tungsten carbide cubes with 11 mm corner truncations (18/11 configuration). The experimental conditions are listed in Table 5.1. Stepped LaCrO<sub>3</sub> heaters were used to minimize the temperature gradient across the sample (Rubie, 1999). All diffusion couples were contained vertically within an MgO capsule (Figure 5.1) with the lighter alloy on top to maintain gravitational stability, as described in the Supplemental Material (SM). A W<sub>97</sub>Re<sub>3</sub>—W<sub>75</sub>Re<sub>25</sub>

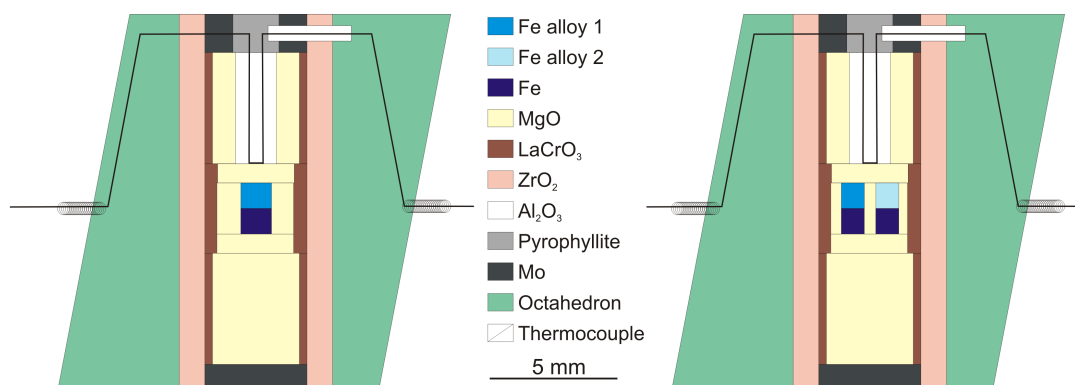


*Figure 5.1: Schematic representation of 18/11 multi-anvil assembly with single chamber (left) and double chamber (right) capsule, showing the Fe-Fe alloy diffusion couple at the center of the assembly.*

thermocouple was used with the junction positioned at the top of the MgO capsule, 0.75 mm from the top of the metallic diffusion couple. No correction for the effect of pressure on thermocouple emf was applied.

Diffusion couples consisted of 0.9 or 1.2 mm diameter cylinders of iron and iron alloy of compositions listed in Table SM5.1. Iron cylinders of 99.98% purity were machined and one end was polished to a 0.25- $\mu\text{m}$  finish. Alloys of the desired composition were prepared from a mixture of fine-grained (10–40  $\mu\text{m}$ ) metallic powders of 99.9% pure Fe, 99.9% pure Si, Fe<sub>0.91</sub>Si<sub>0.09</sub> and/or 99.2% pure Cr powders. Powders were sintered into solid rods in a piston-cylinder apparatus at 15 kbar and 1473 K for 5 hours using a talc-pyrex pressure assembly and graphite furnace. Sintered rods were carefully removed, cut, doubly polished to a 0.25- $\mu\text{m}$  finish and checked for chemical homogeneity by electron microprobe. Chemical and textural analyses of representative alloys from each mixture are given in the Supplemental Material (Table SM5.1).

Experiments were performed at 1, 3, 7, and 18 GPa by compressing slowly to the desired press load and then heated to high temperature using a proportional-integral-derivative (PID) controller with output values (e.g. thermocouple temperature, power) recorded every 100 ms (Figure SM5.3). In order to avoid temperature overshoot and to minimize diffusion prior to reaching the peak anneal temperature ( $T_f$ ), all experiments were heated from room temperature to 1273 K in 600 s, maintained at this temperature for 180 s, rapidly heated at a constant ramp rate ( $dT/dt$ ) of 20–50 K s<sup>-1</sup> to the desired peak temperature ( $T_f$ ), maintained at  $T_f$  for the desired time, and then quenched by shutting off the electrical power. Initial quench rates were in excess of 500 K s<sup>-1</sup>. Diffusion annealing of experiments above 3 GPa also included a second heating step, with  $T$  being held at 1473 K for 24 s, which substantially improved the stability of the furnace during rapid ramp heating. Zero-time experiments with peak annealing durations of 0 s were performed by quenching immediately upon reaching the desired  $T_f$ . Quoted temperatures and associated errors are the average and standard deviations, respectively, of the measured values during the post-ramping stage, as determined from the  $T$ - $t$  log.

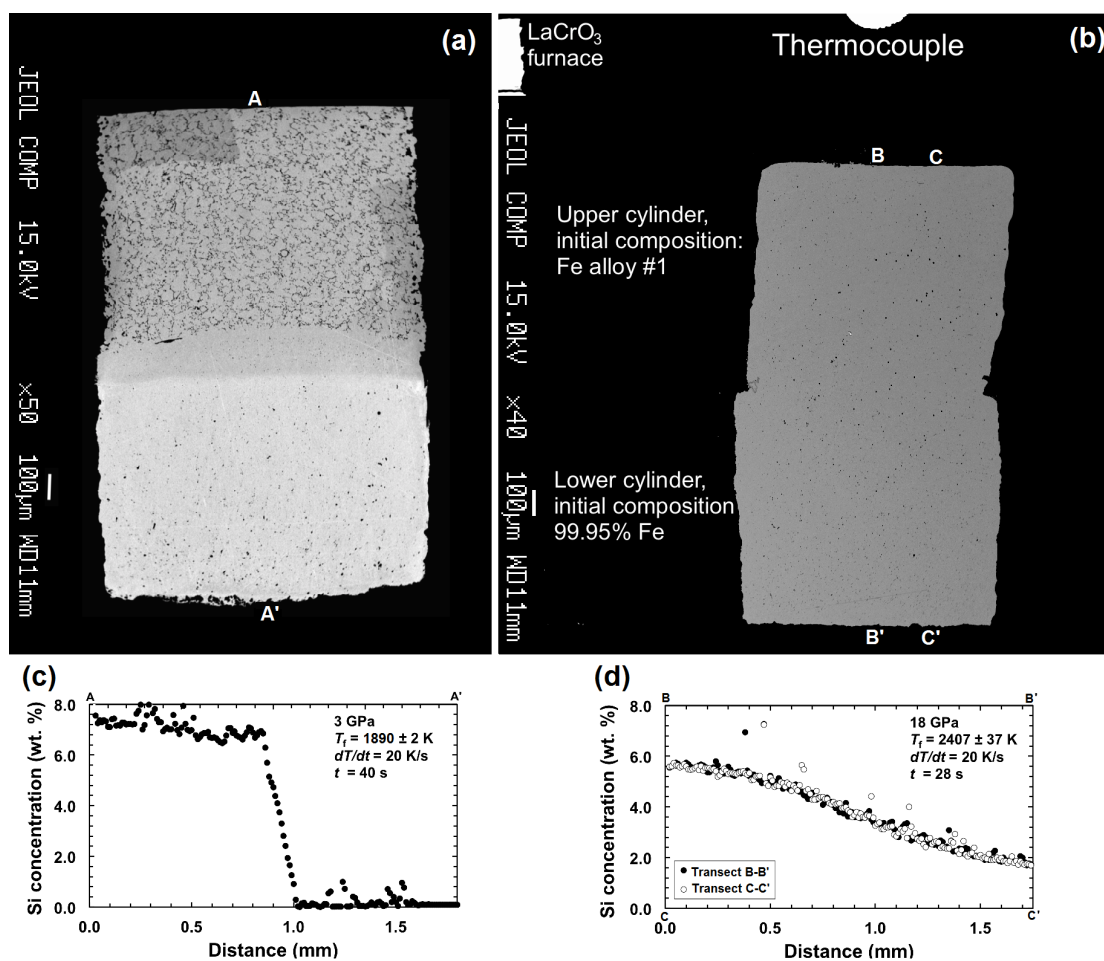
A number of experiments were conducted at 3 and 7 GPa to measure the compositional effect of diffusion. In these runs, two diffusion couples were loaded into a double chamber capsule (Figure 5.1) and annealed simultaneously. In order to check for thermal variability across the capsule, we performed a dummy experiment using two identical diffusion couple chemistries in each chamber. Analyses of the quenched samples show identical diffusion profiles in both chambers. Subsequent experiments included diffusion couples of differing alloy composition (i.e. Fe-8wt % Si compared to Fe-4wt % Si) where both alloys were coupled to pure iron in their respective chamber.

### 5.3.2 Analytical procedure

Recovered capsules (Figure 5.2) were cut and polished parallel to the axis of the cylindrical sample. Spot analyses were acquired along the full length of the diffusion couple on a line perpendicular to the diffusion interface using a JEOL-JXA-8200 electron probe micro-analyzer at the Bayerisches Geoinstitut. The probe current and accelerating voltage were 15 nA and 15 kV, respectively, with a beam diameter of 20  $\mu\text{m}$ . Standards used were Fe metal, Cr metal and natural andradite. Counting times were 20 s on peak and 10 s on background. The standard error ranges between 5% and 10% except at very low concentrations (below  $\sim 0.1$  wt% Si and  $\sim 0.2$  wt% Cr) where the error increases to  $> 20\%$ . Line scans were between 1730 and 1878  $\mu\text{m}$  long and the spacing between adjacent spots was 10  $\mu\text{m}$ . At least two parallel scans were made on each sample in order to check for reproducibility and possible convective mixing. Some quenched samples contained small regions of non-metallic oxide phases (mostly silica and/or magnesiowüstite) typically in the alloy half of the diffusion couple, due to reaction with the capsule. In such samples, line scans were chosen that avoided these small regions. Samples with pervasive regions ( $> 25\%$ ) of non-metallic phases were excluded from the analysis.

### 5.3.3 Melting criteria for diffusion modeling

Subsolidus inter-diffusion rates in iron alloys do not exceed  $\sim 10^{-12} \text{ m}^2 \text{ s}^{-1}$  at temperatures close to the melting point (Goldstein et al., 1965; Yunker and Van Orman, 2007; Reaman et al., 2012). The length scale of solid-state diffusion that occurs during the rapid heating sequence prior to melting is therefore exceedingly small compared to the quenched liquid diffusion length



( $\sim 10^{-3}$  m) and is not considered in the modeling. In order to estimate the melting temperature ( $T_m$ ) and its associated error at each pressure, we conducted experiments of non-zero peak anneal duration ( $\sim 30$  s) at incrementally lower peak temperatures at each pressure. The lowest temperature at which chemical diffusion occurred across the molten diffusion couple interface was constrained by textural and chemical analysis of both the alloy and pure iron after decompression. Back-scattered electron (BSE) imaging of unmelted alloys preserved visible grain boundaries (dark) that had formed during sintering preparation (Figure 5.2a), while alloys quenched from a liquid displayed uniform (bright) texture with no signs of grain boundaries

*Figure 5.2 (opposite page): Backscattered electron (BSE) images and analyses of quenched unmelted (left) and melted (right) samples from the diffusion experiments. EPMA analyses were collected every 10  $\mu\text{m}$  along a traverse perpendicular to the diffusion couple interface, indicated by A-A' in panel (a) and B-B' and C-C' in panel (b). Due to the nature of the experiments, it was not possible to quench a molten sample prior to diffusion occurring within the liquid. Unmelted samples were identified by the preservation of visible grain boundaries within the alloy cylinder that had formed during sintering preparation (a) and the steep concentration gradient that did not flatten significantly with increased run time (c). Alloys quenched from a liquid displayed uniform (bright) texture (b) and smooth concentration profiles that flattened with increased run time (d, Figure 5.4). Both transects in panel (d) are virtually indistinguishable verifying the absence of convective mixing as isopleths are parallel to the top and bottom of the capsule. Small exsolution features are mostly silica or Mg-Fe silicate. Silicon content is typically higher in these regions as shown in the concentration profiles obtained along transects B-B' and C-C'.*

(Figure 5.2b). Low temperature runs that exceeded the alloy liquidus only produced a diffusion profile if the pure iron cylinder also melted. If not, a sharp drop in alloy contents was measured across the interface that did not change significantly with longer annealing durations at the same temperature. The melting temperature  $T_m$  was therefore bracketed by these low temperature test runs at each pressure. The error is approximated as half of the difference between the lowest melting  $T$  and highest unmelted  $T$  runs (Table 5.1).

#### 5.3.4 Experimental data fitting and calculation of diffusion parameters

In experimental studies of diffusion in crystalline solids and high viscosity liquids it is generally assumed that laboratory-induced diffusion

profiles form at a single (peak) temperature with negligible diffusion occurring during heating and quenching. In the case of isothermal annealing and a semi-infinite reservoir, diffusion coefficients retrieved from individual experiments by fitting an equation based on the error function can be used directly to determine diffusion parameters according to the Arrhenius relation (Eq. 5.2). However, diffusion during heating and quenching is non-negligible in materials with a large diffusion coefficient, such as metallic melts and other low viscosity liquids such as depolymerized silicate melts (Reid et al., 2001; Liebske et al., 2005; Ni et al., 2015). In such cases, ignoring diffusion that occurs during heating and quenching may lead to significant errors. Here we ignore diffusion that occurs during quenching because of the high rate of the quench in multi-anvil experiments (initially  $>500 \text{ K s}^{-1}$ ).

Non-isothermal annealing (i.e. when diffusion occurs during heating) can result in an overestimation of the derived diffusion coefficient if the quenched concentration profile is assumed to have formed solely at the peak annealing temperature,  $T_f$ . The extent of diffusion that occurs during ramp heating increases with temperatures above  $T_m$  and, as a consequence, can lead to an overestimation of the Arrhenian temperature dependence term,  $\Delta H$ , given as

$$\frac{\partial \ln D}{\partial (1/T)} = -\frac{\Delta H(P)}{R} \quad . \quad (5.4)$$

The ramped heating rate significantly influences the shape of the concentration profile upon reaching  $T_f$ , especially at  $T \gg T_m$ , as described in greater detail in the Supplemental Material (Figure SM5.4).

In order to correct for non-isothermal diffusion annealing, we conducted a series of experiments at each pressure using variable controlled heating rates ( $dT/dt$ ), final quench temperatures  $T_f$  and durations ( $t$ ) at  $T_f$ . The motivation

for using a range of  $dT/dt$  values is the improved accuracy of  $\Delta H$  values retrieved from the simultaneous fit of several profiles obtained at the same pressure.

In all experiments, the concentrations at both ends of the sample changed because of diffusion, which means that the samples cannot be considered as semi-infinite reservoirs. In order to treat the samples as finite reservoirs, the fitting of concentration profiles has been performed using a Crank-Nicolson finite difference approach with concentration gradients at the ends of the sample set to zero as boundary conditions. Least squares regressions were performed using the “amoeba” algorithm (Press et al., 2002), which performs multidimensional minimization using the downhill simplex method (Nelder and Mead, 1965). The procedure requires that we make  $n + 1$  initial guesses of  $n$  fit parameters.

The first step involved determining the original interface location for each concentration profile by refining this parameter together with an effective diffusion coefficient (that was subsequently discarded). The second step consisted of refining  $D_0$  and  $\Delta H$  for all profiles obtained at a given pressure simultaneously using the initial interface locations as determined in the first step. Each simulation starts at the melting temperature with the heating rate, peak temperature and time at  $T_f$  specified as measured experimentally for each profile. We used a time step of 0.1 s but reducing this to 0.01 s has no effect on the results. We minimize the squared sum of the weighted residuals,

$$\chi^2 = \sum_{i=1}^n ((C_C^i - C_M^i) / \sigma_M^i)^2 \quad , \quad (5.5)$$

where  $C_C^i$  is the calculated wt. % concentration of element  $i$ ,  $C_M^i$  is the measured wt. % concentration and  $\sigma_M^i$  is the uncertainty on  $C_M^i$  estimated

from the reproducibility of EPMA analyses to be 0.1 %. This is a conservative estimate based on the dependence of the standard error on the absolute concentration, described in Section 5.3.2. We report reduced  $\chi^2$  values,

$$\chi_{\text{red}}^2 = \frac{\chi^2}{u} \quad , \quad (5.6)$$

where  $u$  is the number of degrees of freedom determined from  $u = N - n - 1$ , with  $N$  being the number of observations and  $n$  the number of fit parameters. In the present study,  $n = 2$  ( $D_0$  and  $\Delta H$ ). We also tested for compositional effects on diffusion, however, incorporating a compositional dependence did not improve the quality of fit to the data nor did it change the value of retrieved diffusion coefficients (see SM).

Once  $D_0$  and  $\Delta H$  are refined from a set of experiments at constant pressure, the pressure dependence or activation volume,  $\Delta V$ , of diffusion can be determined at constant temperature, according to

$$\frac{\partial \ln D}{\partial P} = - \frac{\Delta V(T)}{RT} \quad . \quad (5.7)$$

Most experimental studies report  $\Delta V$  as a single value, as opposed to a function of temperature, due to a limited range of temperatures accessible at each experimental pressure interval. For example, for pure iron,  $T_m$  at 1 GPa is ~300 K lower than  $T_m$  at 18 GPa (Komabayashi, 2014), such that annealing low pressure experiments at the high temperatures required for high pressure melting often results in complete equilibration of the low  $P$  / high  $T$  sample. However, extrapolation of the diffusion coefficient to conditions far beyond those currently accessible in laboratory experiments requires an understanding of the  $P$  and  $T$  derivatives of  $\Delta H$  and  $\Delta V$ , respectively, which are readily accessible by computational methods.

## 5.4 Computational methods

### 5.4.1 FP-MD

Calculations of energy and forces presented in this work are based on density functional theory (DFT) with exchange and correlation potentials represented by the generalized gradient approximation (GGA) (Perdew et al., 1996). Valence electron states are expanded into plane waves with a cutoff energy of 550 eV in the projected augmented wave (PAW) method (Kresse and Joubert, 1999). The PAW potential for Si, Cr, and Fe have the  $3s^23p^2$ ,  $4s^13d^5$ , and  $4s^13d^5$  valence electronic configurations, respectively. Additional runs were performed with  $3p^6$  electrons included in the valence configuration for both Fe and Cr, as well for Fe in the  $\text{Fe}_{0.92}\text{Si}_{0.08}$  simulations, but self-diffusion coefficients using either electronic configuration were found to be identical within error of the calculations.

Molecular dynamics simulations have been performed in the canonical ( $N$ - $V$ - $T$ ) ensemble using the Vienna *ab-initio* simulation package (VASP) (Kresse and Furthmüller, 1996), with the temperature controlled by a Nosé–Hoover thermostat (Anderson, 1980) and a time step of 1 fs. Simulations were run for at least 22 ps, from which we discarded the first 2 ps to allow for equilibration. In our simulations, Fe supercells of 150 atoms are overheated to induce melting and compressed to volumes along several isobars (0 – 135 GPa) using the thermodynamic model of Lu et al. (2005a, 2005b). Densities of the simulations range from  $6.166 \text{ g cm}^{-3}$  to  $9.738 \text{ g m}^{-3}$  for Fe and are listed—along with the corresponding pressure, temperature and cell volumes—in Table 5.2. A comparison of cell volumes used here with the thermodynamic model of Komabayashi (2014) shows better than 10% agreement for all conditions examined.

We changed the composition in the cell by substituting either 3, 6, or 12 atoms of Fe by either Si or Cr, equating to 2, 4, or 8 atomic percent, respectively, keeping the volume of the simulation cell fixed. Simulations for cells containing 3 solute atoms (2 at. %) were run for 29 ps, longer than those for cells with 6 or 12 solute atoms in order to obtain good statistics for the evaluation of the fluctuation formula to determine diffusivities (see below). Additionally, the transport coefficient of the solute was found to change only very slightly with concentration by a factor of approximately 0.02 log units per atom percent solute. Most production runs were therefore performed using 12 solute atoms to achieve the best statistics, i.e.  $\text{Fe}_{138}\text{Si}_{12}$  and  $\text{Fe}_{138}\text{Cr}_{12}$ .

In order to calculate diffusion coefficients and the  $P$ - $T$  dependence of the activation terms, we performed 32 simulations on  $\text{Fe}_{0.92}\text{Si}_{0.08}$  using densities corresponding to eight pressures for the liquid Fe equation of state by Lu et al. (2005a, 2005b) (1 bar, 7, 15, 35, 60, 85, 110, 135 GPa) and four different temperatures, with 300 K spacing, at each pressure (Table 5.2). Results on a subset of  $P$ - $T$  conditions demonstrate that Si self-diffusion rates are nearly identical to those of Fe and Cr (Table 5.2). We therefore conducted fewer simulations for Fe and  $\text{Fe}_{0.92}\text{Cr}_{0.08}$  liquid compositions (i.e. 60 and 110 GPa isobars were excluded) in order to compare the transport properties of Fe and Cr to that of the better-explored Si self-diffusion.

#### 5.4.2 Calculation of self-diffusion coefficients and viscosities

The self-diffusion coefficient for species  $\alpha$ ,  $D_{\alpha}$ , is computed using atomic trajectories in the simulation cell and the asymptotic slope of the time-dependent mean-square displacement (MSD) following the Einstein relation (Allen and Tildesley, 1991):

$$D_{\alpha} = \lim_{t \rightarrow \infty} \frac{1}{N_{\alpha}} \sum_{i=1}^{N_{\alpha}} \frac{\langle (r_i(t+t_0) - r_i(t_0))^2 \rangle}{6t}, \quad (5.8)$$

where  $N_{\alpha}$  is the total number of atoms of species  $\alpha$ ,  $r_i(t)$  is the position of the  $i^{\text{th}}$  atom at time  $t$ , and the angular brackets indicate the ensemble average computed over different origin times,  $t_0$ , along the FP-MD trajectories. In addition, we combine self-diffusion coefficients calculated using MSD and interatomic spacings measured from partial radial distribution functions (RDFs) obtained from the same simulations to calculate the viscosity of liquid iron,  $\text{Fe}_{0.92}\text{Si}_{0.08}$ , and  $\text{Fe}_{0.92}\text{Cr}_{0.08}$  compositions according to the Stokes-Einstein relation (Eq. 5.1).

As in most traditional diffusion studies, we calculate  $\Delta H$  from the results obtained at each isobar according to Eq. 5.4. In a similar fashion,  $\Delta V$  was obtained at eight different fixed isotherms between 2800–4900 K with 300 K spacing. For each  $\Delta V$ , at least three different pressures were considered (Eq. 5.7).

## 5.5 Results

### 5.5.1 Experimental results of Si and Cr chemical diffusion

Diffusion profiles from experiments conducted at 1 and 18 GPa are shown in Figures 5.3 and 5.4. All Si and Cr diffusion profiles are symmetric relative to the interface location, regardless of pressure, temperature or time, indicating diffusion rates similar to that of Fe. The length of the diffusion profiles increases with temperature at constant pressure and run duration (Figure 5.4) as expected for the thermally activated diffusion process. Rapid equilibration of small (mm size) high-pressure samples limited the temperature range of study to 200-400 K above the liquidus with typical anneal durations at  $T_f$  between 10 and 180 s.

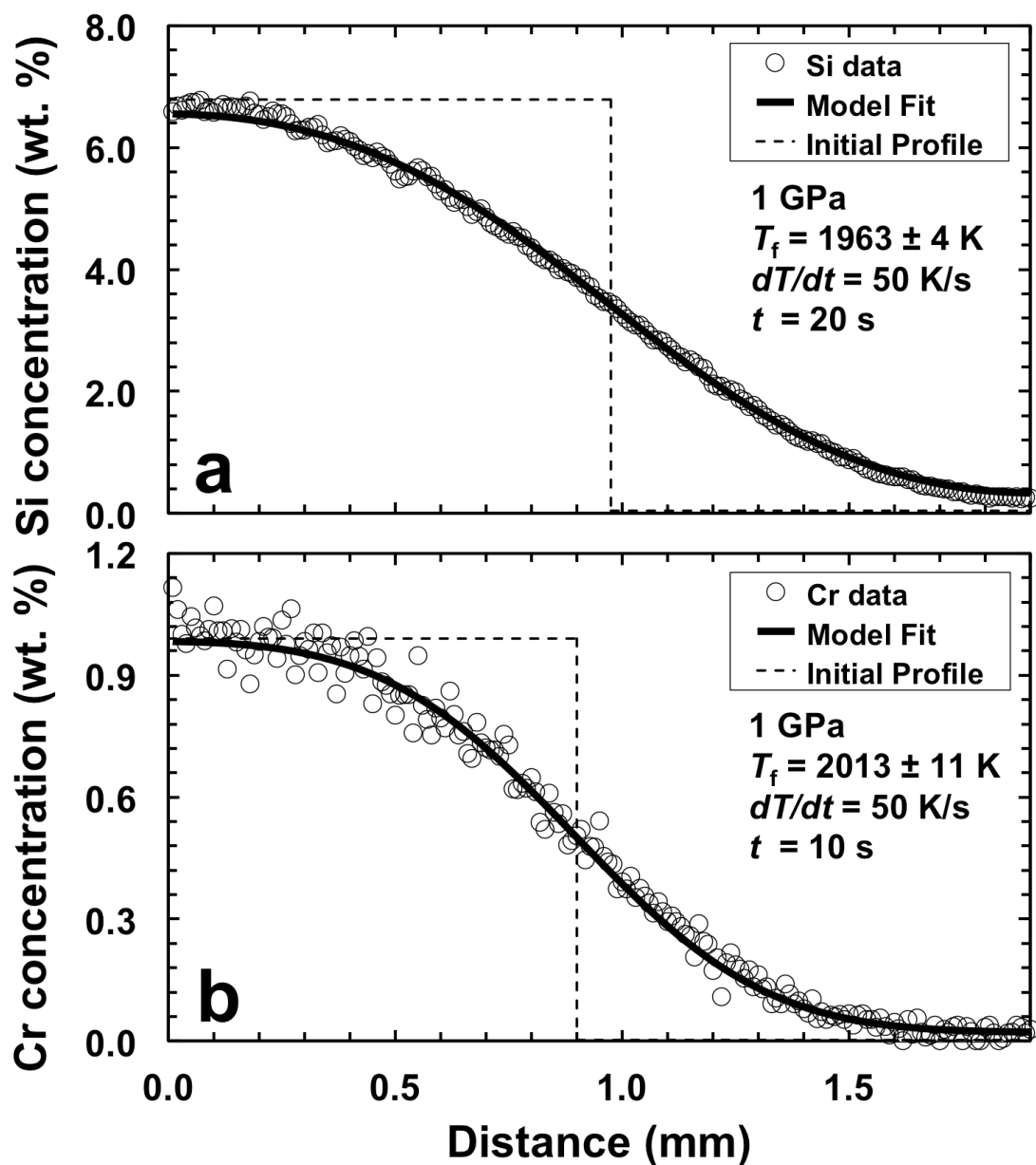


Figure 5.3: Typical diffusion profiles showing (a) Si concentration and (b) Cr concentration versus distance. The model fit to the data represents a global solution to all experiments conducted at 1 GPa ( $n = 6$ ). Dashed lines show the optimized interface locations and model initial profiles.

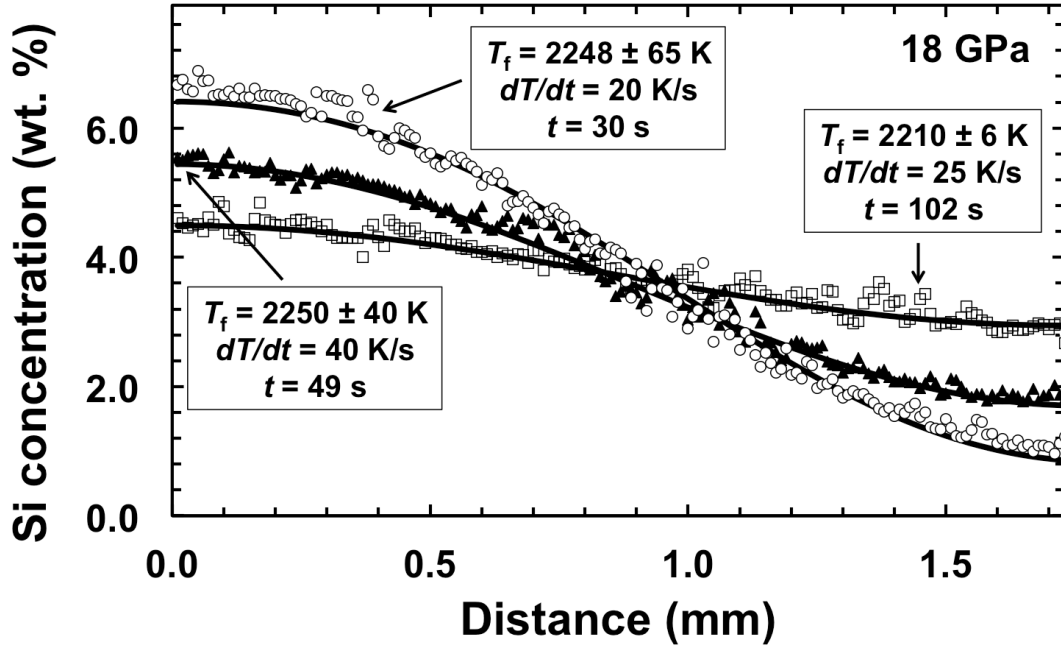
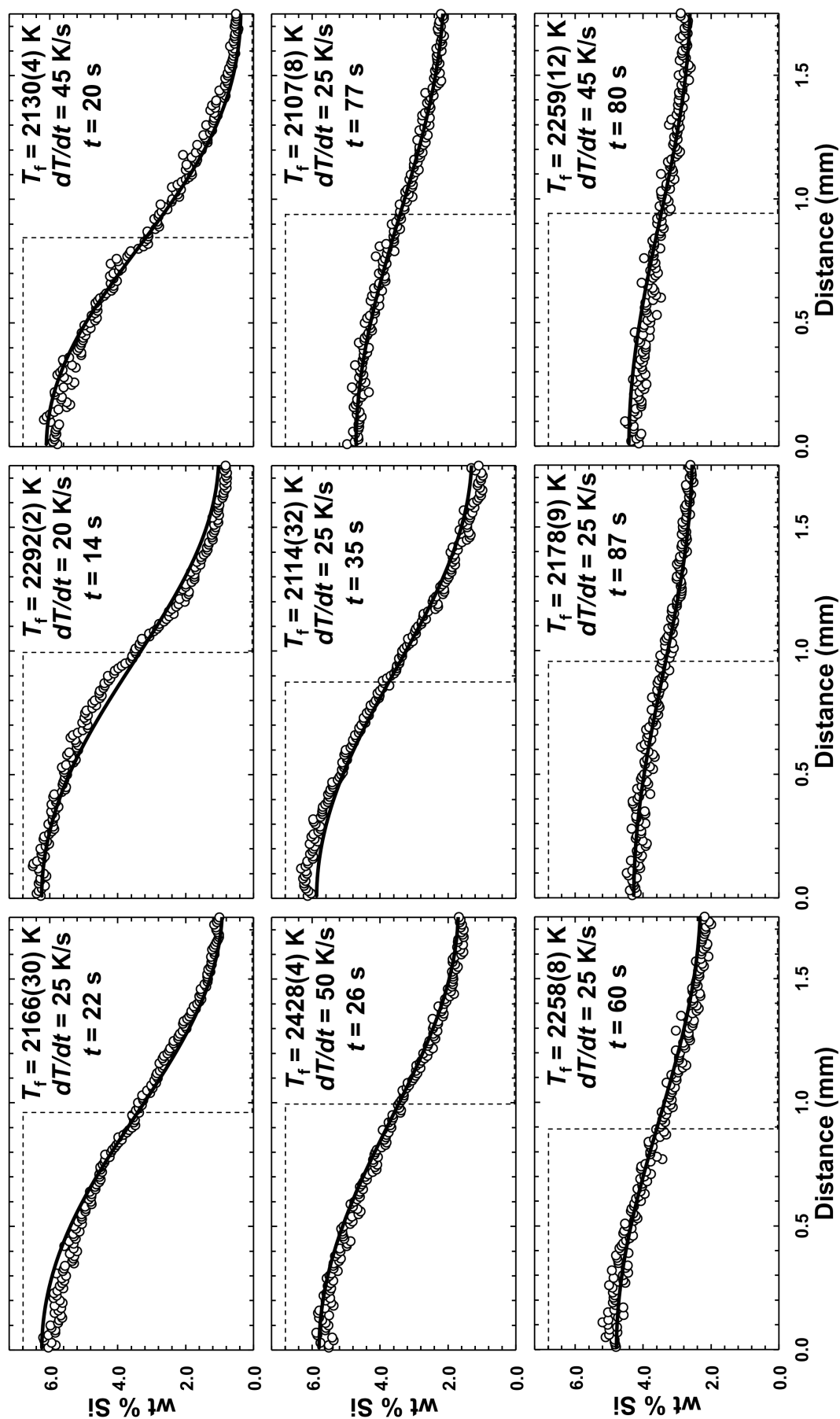


Figure 5.4: Si concentration profiles for three experiments at 18 GPa (Table 5.1). The model fit to the data represents a global solution to all experiments conducted at 18 GPa ( $n = 6$ ). Diffusion profiles flatten with increasing time and temperature.

The global least-squares best fit to all diffusion profiles at 7 GPa ( $n = 9$ ) is shown in Figure 5.5. Refined diffusion parameters,  $D_0$  and  $\Delta H$ , determined at each pressure are listed in Table 5.1. Arrhenius plots for each element from the global fits are shown in Figure 5.6. Diffusion coefficients for Si and Cr in liquid iron are identical within error and change by less than a factor of five over the entire  $P$ - $T$  range of study ( $3 \times 10^{-9} \text{ m}^2 \text{ s}^{-1}$  to  $9 \times 10^{-9} \text{ m}^2 \text{ s}^{-1}$  and from  $2 \times 10^{-9} \text{ m}^2 \text{ s}^{-1}$  to  $1 \times 10^{-8} \text{ m}^2 \text{ s}^{-1}$  for  $D_{\text{Fe-Si}}$  and  $D_{\text{Fe-Cr}}$ , respectively). Our results are in good agreement with ambient pressure data for Si chemical diffusion (Calderon et al., 1971) and Cr (Kubíček, 1975), shown as dashed lines in Figure 5.6.



*Figure 5.5 (opposite page): Si diffusion profiles for all experiments conducted at 7 GPa (Table 5.1). The model fit to the data represents a global solution to all experiments at this pressure ( $n = 9$ ), simultaneously yielding  $D_o = 4.1 \times 10^8 \text{ m}^2 \text{ s}^{-1}$  and  $\Delta H = 35 \pm 5 \text{ kJ mol}^{-1}$ , respectively. Dashed lines show the optimized interface locations and model initial profiles.*

The temperature dependence of Si and Cr diffusion in liquid iron up to 18 GPa is small ( $\Delta H \sim 20\text{--}70 \text{ kJ mol}^{-1}$ ) and changes only slightly with increasing pressure, as discussed below. Errors in  $\Delta H$  obtained from experiments are estimated using a simultaneous least-squares best fit to all data obtained at a given pressure and range from approximately 7% to 17% for  $\Delta H_{\text{Fe-Si}}$  to slightly larger (15% to 50%) for  $\Delta H_{\text{Fe-Cr}}$ , most likely due to the lower concentration of Cr. However, even large errors (e.g.  $\Delta H \pm 0.5(\Delta H)$ ) bracketing low magnitude  $\Delta H$  values (e.g.  $\lesssim 50 \text{ kJ mol}^{-1}$ ) have a minor effect on diffusion coefficients calculated from Eq. 5.2. The ambient pressure  $\Delta H$  of Cr diffusion reported by Kubíček (1975) is considerably larger ( $\Delta H = 93 \pm 7 \text{ kJ mol}^{-1}$ ) than those refined in our study. A possible explanation for this difference is a more simple treatment of non-isothermal diffusion annealing employed by Kubíček (1975), involving the assignment of an average annealing temperature, as opposed to the numerical treatment employed here.

Activation enthalpies determined in this study are consistent with previously reported high pressure experimental values for self-diffusion of Fe in liquid  $\text{Fe}_3\text{C}$  ( $52 \pm 3 \text{ kJ mol}^{-1}$ ; Dobson and Wiedenbeck, 2002), computational results in liquid Fe-FeO ( $55\text{--}83 \text{ kJ mol}^{-1}$ ; Ichikawa and Tsuchiya, 2015) and liquid Fe- $\text{Fe}_{76}\text{H}_{52}$  ( $48\text{--}77 \text{ kJ mol}^{-1}$ ; Umemoto and Hirose, 2015), as well as theoretical estimates ( $\sim 48 \text{ kJ mol}^{-1}$ ; Poirier, 1988). Other experimental studies reported larger  $\Delta H$  for Fe self-diffusion in liquid iron

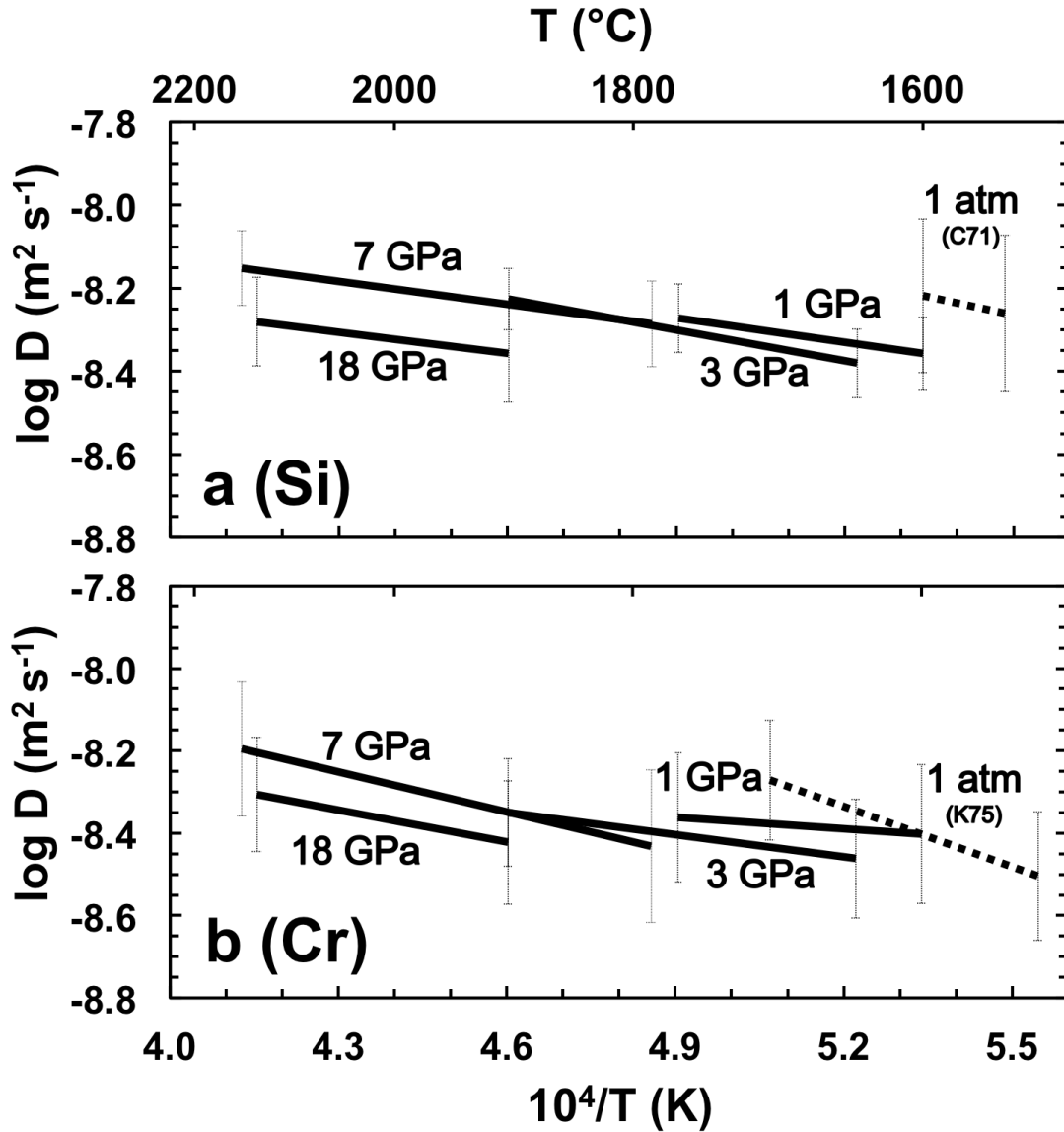


Figure 5.6: Arrhenius plots for Si and Cr chemical diffusion in liquid iron at 1, 3, 7 and 18 GPa as determined by the simultaneous least-squares fit to all diffusion profiles conducted at each respective pressure. Error bars represent  $1\sigma$ . Ambient pressure chemical diffusion data for Si (Calderon et al., 1971) and Cr (Kubíček, 1975) are shown as dashed lines. Activation enthalpies for Si diffusion remain mostly constant ( $\sim 40 \text{ kJ mol}^{-1}$ ) over the pressure and temperature range of study, while activation enthalpies for Cr diffusion determined in our study increase slightly with increasing pressure (Table 5.1). The effect of pressure on  $\Delta H$  is shown in Figure 5.9.

Table 5.1: Experimental conditions and Arrhenius parameters,  $D_0$  and  $\Delta H$ , refined from the least-squares best-fit to all concentration profiles measured at each pressure. Due to coupling of the fitted  $D_0$  and  $\Delta H$  values, all errors are assigned to  $\Delta H$  (see Supplemental Material).

$P$ GPa	$T_m$ K ( $1\sigma$ )	$T_f$ K ( $1\sigma$ )	Heating rate (K s $^{-1}$ )	Time @ $T_f$ (s)	$D_{0,Fe-Si}$ $10^{-8} \text{ m}^2 \text{ s}^{-1}$ ( $1\sigma$ )	$\Delta H_{Fe-Si}$ kJ mol $^{-1}$ ( $1\sigma$ )	$\chi^2_{red}$	$D_{0,Fe-Cr}$ $10^{-8} \text{ m}^2 \text{ s}^{-1}$ ( $1\sigma$ )	$\Delta H_{Fe-Cr}$ kJ mol $^{-1}$ ( $1\sigma$ )	$\chi^2_{red}$
1	1873(25)	1873(4)	25	30	4.9	38(3)	1.823	1.3	18(8)	0.1443
		1953(5)	50	10						
		1963(4)	50	20						
		1973(6)	50	40						
		2013(11)	50	10						
2063(10)	50	15								
3	1915(25)	1916(13)	20	175	8.4	48(3)	2.409	3.0	34(6)	0.1737
		1928(25)	20	124						
		1978(3)	25	63						
		1995(12)	25	70						
		2020(28)	40	40						
		2021(17)	20	59						
		2091(19)	20	42						
2153(6)	25	27								
7	2059(25)	2107(8)	25	77	4.1	35(5)	3.173	14	62(9)	0.2884
		2114(32)	25	35						
		2130(4)	45	20						
		2166(30)	25	22						
		2178(9)	25	87						
		2258(8)	25	60						
		2259(12)	45	80						
		2292(2)	20	14						
		2428(4)	50	26						
18	2173(25)	2210(6)	25	102	2.7	33(6)	5.448	6.0	50(8)	0.1942
		2248(65)	20	30						
		2250(40)	40	49						
		2317(41)	25	50						
		2361(56)	25	33						
		2407(37)	20	28						

( $100 \pm 40 \text{ kJ mol}^{-1}$ ; Dobson, 2002) and liquid eutectic FeS ( $213 \pm 34 \text{ kJ mol}^{-1}$  at 2.2 GPa and  $252 \pm 23 \text{ kJ mol}^{-1}$  at 5 GPa; Dobson et al., 2000). However, the high magnitude of the  $\Delta H$  of diffusion in the S-bearing liquids was later refuted in a theoretical study (Vočadlo et al., 2000), as well as experimentally (Dobson et al., 2001).

In order to ensure that diffusion parameters obtained from the numerical model fit to  $n$  profiles are unaffected by potential outlier data, we

also model  $n-1$  and  $n-2$  profiles (i.e. excluding 1 or 2 profiles) at each pressure interval. The resulting family of  $\log D_0$  and  $\Delta H$  paired solutions form a linear trend (Figure SM5.5). Although this finding verifies a robust and reproducible calculation of  $D$  using the model-derived range of  $(D_0, \Delta H)$  pairs at a particular pressure (Figure SM5.5, inset), it also reveals limitations in the precision of the model to define unique values of  $D_0$  and  $\Delta H$  because these parameters are strongly correlated. Errors reported on our diffusion parameters are therefore large despite a rather good fit to several diffusion profiles simultaneously (Figure 5.5).

### 5.5.2 Computational results of Si, Cr, and Fe self-diffusion

The analysis of atomic trajectories for Si, Cr and Fe from the FP-MD simulations shows a linear trend of the mean square displacement  $\left\langle \left( r_i(t+t_0) - r_i(t_0) \right)^2 \right\rangle$  at  $t > 0.2$  ps, which confirms that the system is indeed liquid (Figure SM5.6). Following Eq. 5.8, we have computed self-diffusion coefficients for each species in every simulation, and the activation terms are fitted according to Eqs. 5.4 and 5.7. Self-diffusion coefficients and calculated activation terms for each species are listed in Table 5.2. We show Arrhenius diagrams for each species in the three compositions alongside diffusion data determined from experiments in Figure 5.7. Calculated self-diffusion coefficients in all three systems (Fe,  $\text{Fe}_{0.92}\text{Si}_{0.08}$ ,  $\text{Fe}_{0.92}\text{Cr}_{0.08}$ ) are identical within error for Si and Cr (in agreement with our experimental results), and Fe. We find a small effect of pressure and temperature on Si, Cr, and Fe mobility with self-diffusion coefficients changing by less than a factor of five over the full  $P$ - $T$  range of study, that is, 1 bar/2200 K to 135 GPa/5500 K. At low

Table 5.2: Self-diffusion coefficients,  $D_i$ , and bulk viscosities,  $\eta$ , computed from FP-MD simulations according to Eqs. 8 and 1, respectively. The equation of state for Fe to determine the simulation  $V$  is taken from Lu et al. (2005a, 2005b).

$P$ GPa	$T$ K	$V$ $\text{\AA}^3$ atom $^{-1}$	Fe		$\text{Fe}_{0.92}\text{Si}_{0.08}$			$\text{Fe}_{0.92}\text{Cr}_{0.08}$		
			$D_{\text{Fe}}$ $10^{-8} \text{ m}^2$ $\text{s}^{-1}$	$\eta$ mPa s	$D_{\text{Fe}}$ $10^{-8} \text{ m}^2$ $\text{s}^{-1}$	$D_{\text{Si}}$ $10^{-8} \text{ m}^2$ $\text{s}^{-1}$	$\eta$ mPa s	$D_{\text{Fe}}$ $10^{-8} \text{ m}^2$ $\text{s}^{-1}$	$D_{\text{Cr}}$ $10^{-8} \text{ m}^2$ $\text{s}^{-1}$	$\eta$ mPa s
0.0001	2200	13.73	1.09(1)	1.8(2)	1.11(1)	1.17(1)	1.7(2)	1.15(1)	1.15(2)	1.7(3)
0.0001	2500	14.14	1.58(1)	1.4(1)	1.47(1)	1.44(5)	1.6(6)	1.50(1)	1.56(2)	1.5(2)
0.0001	2800	14.57	1.92(1)	1.3(1)	1.95(1)	1.82(2)	1.4(2)	1.93(1)	2.12(5)	1.2(3)
0.0001	3100	15.04	2.35(1)	1.2(1)	2.31(2)	2.40(6)	1.2(3)	2.41(2)	2.27(9)	1.2(5)
7	2500	12.92	1.12(1)	2.0(2)	1.05(1)	1.05(4)	2.2(9)	1.09(1)	1.04(1)	2.2(3)
7	2800	13.23	1.46(1)	1.8(1)	1.37(1)	1.38(3)	1.9(4)	1.44(1)	1.33(2)	1.9(3)
7	3100	13.57	1.87(1)	1.5(1)	1.81(1)	1.79(1)	1.6(1)	1.75(1)	1.61(4)	1.7(4)
7	3400	13.93	2.25(1)	1.4(1)	2.02(1)	2.02(2)	1.6(2)	2.19(2)	2.26(7)	1.4(5)
15	2800	12.36	1.15(1)	2.2(2)	1.02(1)	1.03(2)	2.6(6)	1.01(1)	1.02(4)	2.5(10)
15	3100	12.63	1.34(1)	2.1(2)	1.38(1)	1.32(4)	2.2(7)	1.35(2)	1.41(4)	2.0(6)
15	3400	12.93	1.68(1)	1.9(1)	1.66(1)	1.71(2)	1.9(2)	1.71(1)	1.82(3)	1.7(3)
15	3700	13.25	2.06(1)	1.7(1)	2.02(1)	1.96(1)	1.8(1)	2.04(1)	2.19(3)	1.6(2)
35	3400	11.52	1.10(1)	2.9(3)	1.07(1)	1.12(2)	2.9(6)	1.13(1)	1.10(3)	2.8(8)
35	3700	11.76	1.42(1)	2.4(2)	1.27(1)	1.47(4)	2.4(7)	1.40(1)	1.45(2)	2.4(4)
35	4000	12.01	1.64(1)	2.3(1)	1.64(1)	1.71(2)	2.3(3)	1.67(1)	1.60(5)	2.3(7)
35	4300	12.30	1.95(1)	2.1(1)	1.90(2)	1.89(6)	2.2(7)	1.96(1)	2.12(3)	1.9(3)
60	3700	10.71	-	-	0.87(1)	0.79(1)	4.5(6)	-	-	-
60	4000	10.91	-	-	1.11(1)	1.13(2)	3.4(7)	-	-	-
60	4300	11.14	-	-	1.38(1)	1.26(2)	3.3(6)	-	-	-
60	4600	11.40	-	-	1.66(2)	1.61(6)	2.7(11)	-	-	-
85	4000	10.18	0.88(1)	4.4(1)	0.86(1)	0.84(1)	4.6(1)	0.90(1)	0.90(1)	4.3(1)
85	4300	10.38	1.09 (1)	3.8(3)	1.05(1)	1.03(1)	4.0(5)	1.03(1)	1.13(2)	3.6(7)
85	4600	10.60	1.33(1)	3.3(2)	1.29(2)	1.16(4)	3.8(14)	1.41(1)	1.27(1)	3.4(4)
85	4900	10.85	1.57(1)	3.0(2)	1.56(2)	1.57(4)	3.0(9)	1.61(1)	1.62(1)	2.9(3)
110	4300	9.80	-	-	0.84(1)	0.82(1)	5.2(6)	-	-	-
110	4600	10.00	-	-	0.98(1)	0.93(1)	4.9(1)	-	-	-
110	4900	10.23	-	-	1.29(2)	1.18(2)	4.0(9)	-	-	-
110	5200	10.48	-	-	1.52(1)	1.51(4)	3.4(9)	-	-	-
135	4600	9.52	0.91(1)	5.0(1)	0.83(1)	0.82(5)	5.6(3)	0.88(1)	0.90(3)	5.0(2)
135	4900	9.73	1.13(1)	4.3(4)	1.02(1)	1.03(2)	4.7(10)	1.07(1)	0.98(3)	4.9(5)
135	5200	9.97	1.39(1)	3.7(3)	1.30(2)	1.30(2)	4.0(9)	1.31(1)	1.32(1)	3.8(4)
135	5500	10.24	1.68(1)	3.2(2)	1.66(1)	1.59(8)	3.4(9)	1.53(1)	1.59(5)	3.3(11)

pressures ( $\leq \sim 15$  GPa), theoretically determined diffusion coefficients are  $\sim 0.1$  log units faster than those determined experimentally (Figure 5.7). Activation enthalpies over this pressure interval derived from FP-MD are in good agreement with the experimental values ( $\sim 40$ – $60$  kJ mol $^{-1}$ ), but smaller than those reported from Fe self-diffusion experiments ( $100 \pm 40$  kJ mol $^{-1}$ ; Dobson, 2002). The effects of pressure and temperature on the activation terms are described below.

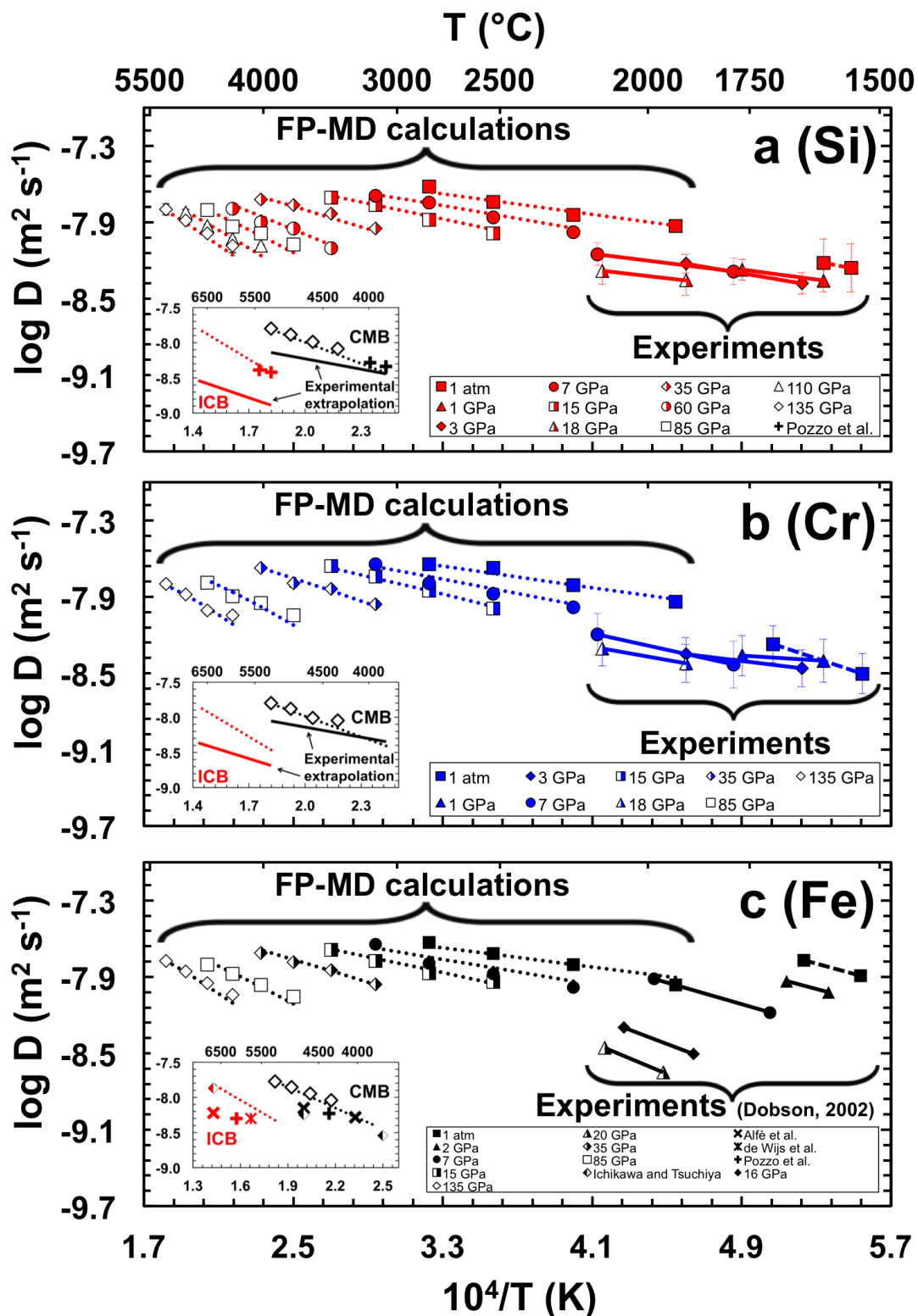


*Figure 5.7 (opposite page): Arrhenius diagrams of (a) Si, (b) Cr, and (c) Fe chemical and self-diffusion in liquid iron. Dotted lines represent the global Arrhenius model (Eq. 2) fit to FP-MD results and extrapolation to ICB pressures (inset). Solid curves for Si and Cr experimental data are the simultaneous least-squares fits to all diffusion profiles conducted at each respective pressure. Extrapolation of the experimental data to CMB and ICB pressures are shown in insets. Previously reported experimental diffusion data measured at 1 bar are shown as thick dashed lines for Si (Calderon et al., 1971), Cr (Kubíček, 1975) and Fe (Yang et al., 1956). High pressure experimental Fe self-diffusion data (Dobson, 2002) are shown as solid curves in panel (c). Previously reported FP-MD diffusion results are shown as plus signs for Si self-diffusion in liquid  $Fe_{0.82}Si_{0.10}O_{0.08}$  and liquid  $Fe_{0.79}Si_{0.08}O_{0.13}$  (Pozzo et al., 2013), and as crosses (Alfè et al., 2000), stars (de Wijs et al., 1998), and half-filled diamonds (Ichikawa and Tsuchiya, 2015) for self-diffusion in pure liquid Fe. Black and red colored symbols correspond to simulations conducted at CMB and ICB pressures, respectively (insets).*

### 5.5.3 Structural properties

The structural properties of liquid iron alloy compositions were investigated by analyzing the partial RDFs,  $g_{FeFe}(r)$ ,  $g_{Fe\phi}(r)$ , and  $g_{\phi\phi}(r)$ , where  $\phi$  is the alloy species (Si or Cr). The partial RDF,  $g_{ab}(r)$ , is defined such that, when considering an atom of species  $a$ , the probability of finding an atom of species  $b$  in a spherical shell  $(r, r + dr)$  is  $\rho_b 4\pi r^2 g_{ab}(r) dr$ , where  $\rho_b = X_b/V$  is the number density of species  $b$  with mole fraction  $X_b$ , and  $V$  is the volume per atom. In Figure 5.8, we show the partial RDFs for all species in liquid  $Fe_{0.92}Si_{0.08}$  and liquid  $Fe_{0.92}Cr_{0.08}$  at the largest ( $15.04 \text{ \AA}^3/\text{atom}$ ) and smallest ( $9.53 \text{ \AA}^3/\text{atom}$ ) volume simulations, corresponding to approximate  $P$ - $T$  conditions of 1 bar and 3100 K, and 135 GPa and 4600 K, respectively.

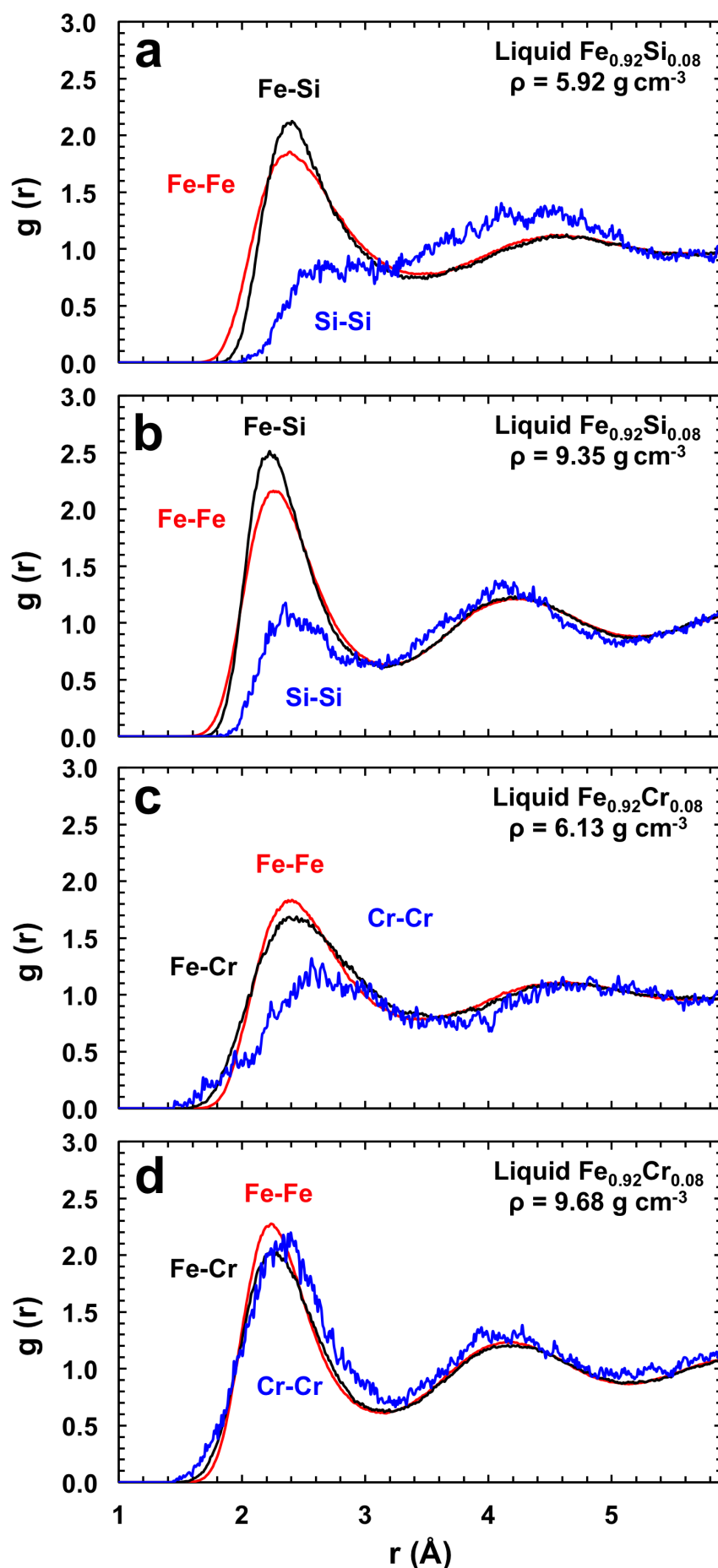


*Figure 5.8 (opposite page): Partial radial distribution functions for liquid  $Fe_{0.92}Si_{0.08}$  at densities corresponding to approximately (a) 1 bar and 3100 K and (b) 135 GPa and 4600 K. Partial RDFs of liquid  $Fe_{0.92}Cr_{0.08}$  for the same volumes are shown in panels (c) and (d), respectively. Over the entire pressure and temperature range of study, the distance between two Fe atoms is similar to that between one Fe atom and one alloy species (Si or Cr). Distances between two alloy atoms (Si-Si or Cr-Cr) decreases with increasing density (see Supplemental Material, Figure SM5.8).*

In all simulations, the average distance ( $\bar{r}$ ) between neighboring iron and alloy atoms, as obtained from the position of the first peak of  $g_{Fe\phi}(r)$ , is roughly the same as  $g_{FeFe}(r)$ , as reported in previous studies (Pozzo et al., 2013; Morard et al., 2014; Alfè et al., 2002). This suggests that there is one single effective radius when the two species interact with each other or with themselves and that Si and Cr should be incorporated into liquid iron by atomic substitution. The only effects of moving from ambient to CMB conditions is a gradual decrease in the average Fe-Fe and Fe- $\phi$  distances from  $\bar{r} \sim 2.4$  Å at  $6.166 \text{ g cm}^{-3}$  to  $\bar{r} \sim 2.2$  Å at  $9.738 \text{ g cm}^{-3}$  and a sharpening of peaks (Figures 5.8, SM5.8). Species with dissimilar  $\bar{r}$  with neighboring Fe atoms, on the other hand, such as those reported for oxygen ( $\sim 1.7$  Å; Pozzo et al., 2013; Morard et al., 2014) and S ( $\sim 2.0$  Å; Vočadlo et al., 2000; Morard et al., 2014), are substantially smaller than Fe-Fe  $\bar{r}$  and can, therefore, also be incorporated interstitially.

#### 5.5.4 Effect of pressure on activation enthalpy

The effect of pressure on experimentally and computationally determined activation enthalpies,  $\Delta H$ , is shown and compared to previous studies in Figure 5.9. Activation enthalpies determined from the two methods

in the present study are in good agreement at low pressure conditions where they overlap ( $\leq 18$  GPa), with average  $\Delta H$  values of  $38 \pm 8$  kJ mol<sup>-1</sup> (experiments) and  $53 \pm 8$  kJ mol<sup>-1</sup> (calculations) for Si, and  $41 \pm 20$  kJ mol<sup>-1</sup> and  $59 \pm 15$  kJ mol<sup>-1</sup> for Cr, respectively. Activation enthalpies computed from FP-MD simulations increase monotonically with pressure (Figure 5.9). Pressure derivatives are approximately 0.8 kJ mol<sup>-1</sup> GPa<sup>-1</sup> for Si diffusion in liquid Fe<sub>0.92</sub>Si<sub>0.08</sub>,  $\sim 0.7$  kJ mol<sup>-1</sup> GPa<sup>-1</sup> for Fe self-diffusion in liquid iron, and  $\sim 0.6$  kJ mol<sup>-1</sup> GPa<sup>-1</sup> for Cr diffusion in liquid Fe<sub>0.92</sub>Cr<sub>0.08</sub> to 135 GPa, yielding approximately a three-fold increase in  $\Delta H$  from ambient to CMB pressures. The high  $\Delta H$  here is broadly consistent with that for Fe self-diffusion in liquid iron determined at 130 GPa with  $\Delta H > 100$  kJ mol<sup>-1</sup> (Ichikawa and Tsuchiya, 2015). The combined effect of both  $P$  and  $T$  on the activation energy,  $Q$ , is discussed below.

A positive pressure derivative of  $\Delta H$  is consistent with previous findings of subsolidus interdiffusion in metals, although the magnitude of  $\Delta H/\Delta P$  in liquid iron alloys found in the present study is appreciably smaller than those reported for solids ( $\Delta H/\Delta P \sim 7$  kJ mol<sup>-1</sup> GPa<sup>-1</sup> for both Ag diffusion in Pb to 5 GPa; Weyland et al., 1971, and Au diffusion in Pb to 4 GPa; Curtin et al., 1965). The pressure derivative of  $\Delta H$  for liquid metals, however, is poorly understood compared with that for solids, with previously reported  $\Delta H/\Delta P$  values ranging from zero for Fe and C self-diffusion in liquid Fe<sub>3</sub>C (Dobson and Wiedenbeck, 2002) to as large as  $\sim 14$  kJ mol<sup>-1</sup> GPa<sup>-1</sup> for Fe and Co self-diffusion in liquid FeS of eutectic composition (Dobson, 2000), although the derived value of  $\Delta H$  in the FeS system was later reported to be significantly smaller (Dobson et al., 2001).

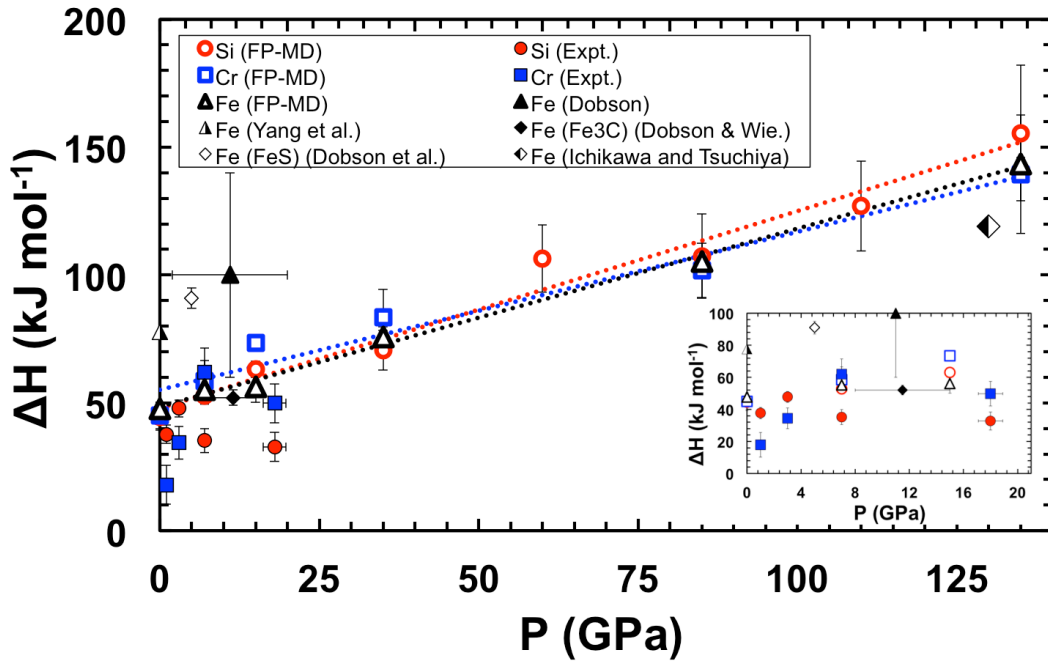


Figure 5.9: Activation enthalpy,  $\Delta H$ , of diffusion in liquid iron and its alloys as a function of pressure to 135 GPa. Activation enthalpies of Si and Cr chemical diffusion (from experiments in this study) are shown as filled red circles and filled blue squares, respectively. Activation enthalpies of Si self-diffusion in  $Fe_{0.92}Si_{0.08}$ , Cr self-diffusion in  $Fe_{0.92}Cr_{0.08}$ , and Fe self-diffusion in liquid iron (from FP-MD simulations in this study) are represented as unfilled red circles, unfilled blue squares, and unfilled triangles, respectively. FP-MD results for Fe self-diffusion at 130 GPa by Ichikawa and Tsuchiya (2015) are represented by a half-filled diamond. Also shown are  $\Delta H$  values previously reported from experiments of Fe self-diffusion in liquid iron by Dobson (2002) (filled triangles) and Yang et al., (1956) (striped triangles), liquid  $Fe_3C$  (Dobson and Wiedenbeck, 2002) (filled diamonds), and liquid FeS (Dobson et al., 2001) (unfilled diamonds). Horizontal error bars represent  $\pm 1\sigma$  uncertainty in pressure, except in the case of data from Dobson (2002) and Dobson et al. (2001), where horizontal error bars represent the pressure range over which  $\Delta H$  is reported. Vertical error bars represent  $\pm 1\sigma$  uncertainty in  $\Delta H$ . At pressures below 20 GPa (inset),  $\Delta H$  values determined from experiments and calculations are in good agreement and range between approximately 20-80  $\text{kJ mol}^{-1}$  for all represented species. Above 20 GPa, calculated  $\Delta H$  values increase monotonically, with pressure derivatives of  $\sim 0.8 \text{ kJ mol}^{-1} \text{ GPa}^{-1}$  for Si,  $\sim 0.7 \text{ kJ mol}^{-1} \text{ GPa}^{-1}$  for Fe and  $\sim 0.5 \text{ kJ mol}^{-1} \text{ GPa}^{-1}$  for Cr.

### 5.5.5 Pressure dependence at constant temperature

The effects of pressure on the Si, Cr, and Fe diffusion coefficients calculated from FP-MD simulations are shown in Figure 5.10 along several isotherms from 2800 K to 4300 K. Experimental Si and Cr diffusion coefficients are shown as a function of pressure at 2200 K and 2400 K in the respective inset (Figure 5.10). We show the effects of the temperature dependence of the activation volume,  $\Delta V$ , in Figure 5.10d, calculated from FP-MD simulations, as the change in diffusivity at fixed temperature and 3 or 4 different pressures. The activation volumes of Si, Cr, and Fe self-diffusion gradually decrease with increasing temperature from  $\sim 0.9 \text{ cm}^3 \text{ mol}^{-1}$  at 2800 K to  $\sim 0.4 \text{ cm}^3 \text{ mol}^{-1}$  at 4900 K. Activation volumes are consistent with the results of Ichikawa and Tsuchiya (2015) at temperatures higher than those considered here, and appear to converge to  $\sim 0.4 \text{ cm}^3 \text{ mol}^{-1}$ . Experimentally determined activation volumes of  $\Delta V_{\text{Si}} \sim 0.4 \text{ cm}^3 \text{ mol}^{-1}$  and  $\Delta V_{\text{Cr}} \sim 0.2 \text{ cm}^3 \text{ mol}^{-1}$  at 2200 K are more consistent with high temperature MD results. This might be attributed to a pressure effect on the thermocouple emf although such an effect, if any, remains unknown.

The small activation volumes ( $< 1 \text{ cm}^3 \text{ mol}^{-1}$ ) determined in the present study are in excellent agreement with theoretical results of O self-diffusion in liquid Fe-FeO ( $\Delta V \sim 0.3 \text{ cm}^3 \text{ mol}^{-1}$ , Ichikawa and Tsuchiya, 2015) and H self-diffusion in liquid Fe-Fe<sub>76</sub>H<sub>52</sub> ( $\Delta V \sim 0.2 \text{ cm}^3 \text{ mol}^{-1}$ , Umemoto and Hirose, 2015) at outer core conditions, empirical estimates ( $\Delta V \sim 0.6 \text{ cm}^3 \text{ mol}^{-1}$ , Poirier, 1988), and experimental results of Fe and C self-diffusion in liquid Fe<sub>3</sub>C ( $\Delta V_{\text{Fe}} = 1.1 \pm 0.1 \text{ cm}^3 \text{ mol}^{-1}$  and  $\Delta V_{\text{C}} = 1.1 \pm 0.1 \text{ cm}^3 \text{ mol}^{-1}$ , Dobson and Wiedenbeck, 2002). Other experimental studies have reported much a larger pressure effect on diffusion ( $\Delta V \sim 9 \text{ cm}^3 \text{ mol}^{-1}$  for Fe and Co self-diffusion in

liquid Fe-FeS of eutectic composition between 2.2 and 5 GPa, Dobson, 2002;  $\Delta V = 2.8 \pm 0.6 \text{ cm}^3 \text{ mol}^{-1}$  for Fe self-diffusion in liquid Fe, Dobson, 2002).

### 5.5.6 Arrhenius model

Pressure and temperature derivatives of Arrhenian activation terms determined in this study can be described empirically by:

$$Q(P, T) = (aT^2 + bT + c)P + d \quad (5.9)$$

where  $a$ ,  $b$ ,  $c$ , and  $d$  are constants determined from a least-squares fit to the data (Table 5.3). Self-diffusion coefficients computed from the simulations (Eq. 5.8) are reproduced using the Arrhenian model within  $< 10\%$ . Model curves are shown at each computational pressure in Figure 5.7. Equation 5.9 is also fit to experimental datasets for Si and Cr chemical diffusion; however, the parameters  $a$  and  $b$  are then fixed to zero due to the smaller  $P$ - $T$  range investigated (i.e. a weaker constraint on  $P$ - $T$  derivatives of  $Q$ ). In this case,  $c$  and  $d$  represent the activation volume and enthalpy, respectively (Table 5.3).

Arrhenian extrapolations of Si and Cr experimental diffusion coefficients to 135 GPa are shown as solid black curves in the insets of Figures 5.7a-c. Diffusivities are in very good agreement with computational results yielding  $\sim 4 \times 10^{-9} \text{ m}^2 \text{ s}^{-1}$  at 4200 K for both species and both methods, as well as with previously reported  $D_{\text{Si}}$  values (Pozzo et al., 2013) from simulations of liquid Fe-Si-O alloys ( $4.6(2) \times 10^{-9} \text{ m}^2 \text{ s}^{-1}$  at 4112 K and  $5.2(2) \times 10^{-9} \text{ m}^2 \text{ s}^{-1}$  at 4260 K). Differences in the diffusion coefficients calculated using experimental and computational methods increase at higher CMB temperatures because model  $\Delta H$ s derived from simulations ( $\sim 200 \text{ kJ mol}^{-1}$ ) are considerably larger than those from experiments ( $\sim 100 \text{ kJ mol}^{-1}$ ), although the mismatch remains small ( $\sim 0.2 \text{ log units}$  at 5000 K).

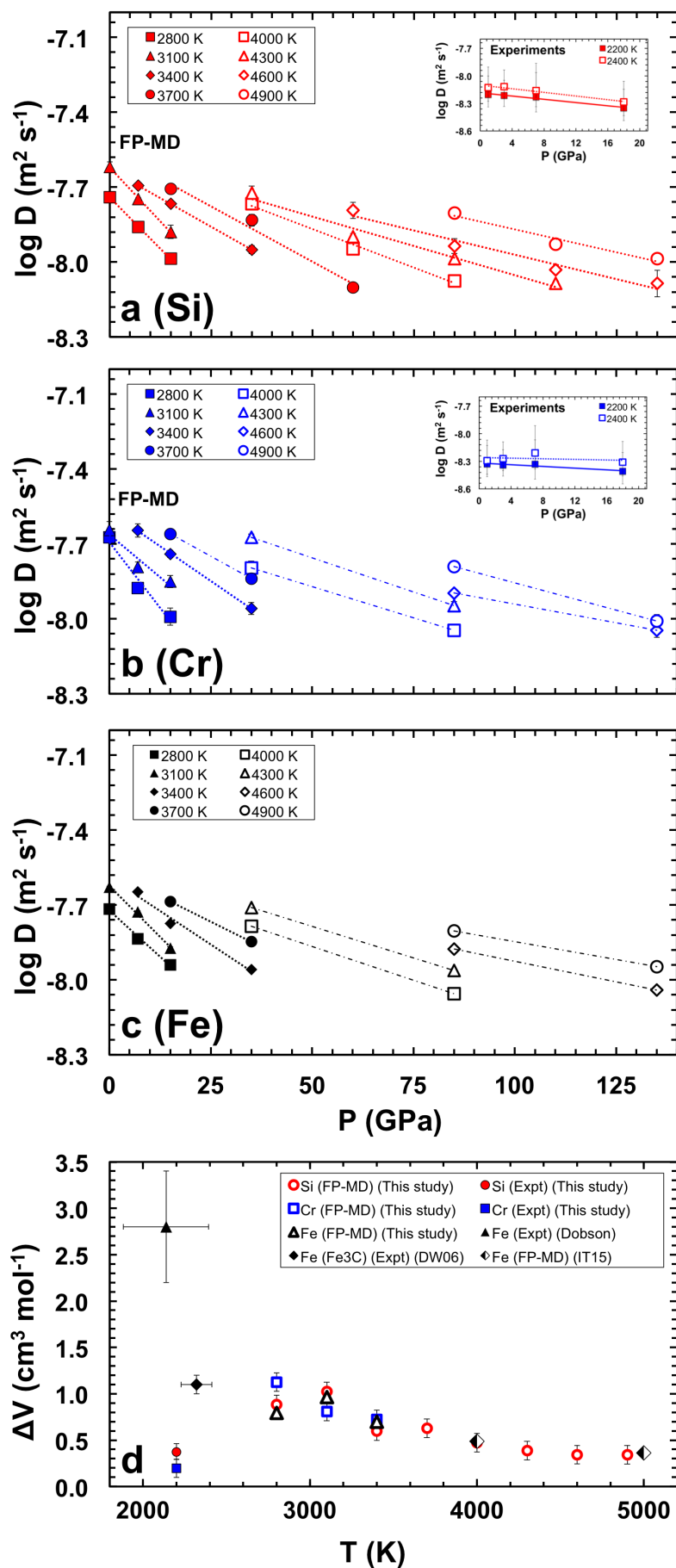


Figure 5.10 (opposite page): Effect of pressure on (a) Si, (b) Cr, and (c) Fe self-diffusion coefficients in liquid iron along several isotherms between 2800 and 4900 K. Linear fits are shown as dotted lines for isotherms containing at least three  $P$  points and dash-dot lines for fits to only two  $P$  points. Insets show (a) Si and (b) Cr chemical diffusion data from experiments as a function of pressure at 2200 and 2400 K. Calculated activation volumes,  $\Delta V$ , are shown for each species as a function of temperature in (d) together with previously reported experimental values for Fe self-diffusion in liquid Fe (Dobson, 2002) and Fe self-diffusion in liquid  $\text{Fe}_3\text{C}$  (Dobson and Wiedenbeck, 2002). Horizontal error bars represent the temperature range over which  $\Delta V$  is reported. Vertical error bars represent  $\pm 2\sigma$  in  $\Delta V$ . Activation volumes calculated from FP-MD simulations show a gradual decrease with increasing temperature from  $\sim 1 \text{ cm}^3 \text{ mol}^{-1}$  at 2800 K to  $\sim 0.3 \text{ cm}^3 \text{ mol}^{-1}$  at 4900 K. Activation volumes are consistent with FP-MD results for Fe self-diffusion (IT15) (Ichikawa and Tsuchiya, 2015), represented by half-filled diamonds, at  $T$  higher than ones considered here, and appear to converge to  $\sim 0.4 \text{ cm}^3 \text{ mol}^{-1}$ . Activation volumes determined experimentally at lower temperatures are more consistent with high temperature calculations. With the exception of the large value reported by Dobson (2002) ( $2.8 \pm 0.6 \text{ cm}^3 \text{ mol}^{-1}$ ), all other  $\Delta V$  values are  $\ll 1.5 \text{ cm}^3 \text{ mol}^{-1}$ .

Table 5.3: Arrhenius model parameters from FP-MD simulations and experiments. Also listed are constants,  $A$  and  $B$ , to the viscosity-density relation,  $\eta(\rho) = A\rho^B$ .

	FP-MD			Experiments	
	Fe	$\text{Fe}_{0.92}\text{Si}_{0.08}$	$\text{Fe}_{0.92}\text{Cr}_{0.08}$	Fe-Si	Fe-Cr
$D_0$ ( $10^{-8} \text{ m}^2 \text{ s}^{-1}$ )	9.0(10)	9.5(11)	10.6(14)	5.7(13)	6.6(27)
$a$ ( $10^{-14} \text{ m}^3 \text{ mol}^{-1} \text{ T}^2$ )	3.1(19)	2.1(20)	5.9(24)	-	-
$b$ ( $10^{-10} \text{ m}^3 \text{ mol}^{-1} \text{ T}^1$ )	-4.5(18)	-3.5(19)	-7.0(23)	-	-
$c$ ( $10^{-6} \text{ m}^3 \text{ mol}^{-1}$ )	1.8(4)	1.6(4)	2.4(5)	0.41(6)	0.34(11)
$d$ ( $10^4 \text{ J mol}^{-1}$ )	3.633(264)	3.807(286)	3.985(327)	3.95(39)	4.57(71)
$R^2$	0.954	0.946	0.942	0.934	0.839
$A$ ( $10^{-15} \text{ m}^3 \text{ Pa s kg}^{-1}$ )	10.1(4)	2.0(5)	4.7(5)	-	-
$B$	2.92(12)	3.12(12)	3.01(13)	-	-

Extrapolations to the Earth’s ICB pressure (330 GPa) are shown as red curves in the insets of Figures 5.7a-c with diffusivities ranging from  $\sim 4 \times 10^{-9} \text{ m}^2 \text{ s}^{-1}$  to  $\sim 2 \times 10^{-8} \text{ m}^2 \text{ s}^{-1}$  at 5500 K and 7000 K, respectively. Values extrapolated from the simulation datasets are in good agreement with previously reported FP-MD diffusion coefficients of  $D_{\text{Si}}$  and  $D_{\text{Fe}}$  in liquid Fe-Si-O alloys reported by Pozzo et al. (2013), as well as for  $D_{\text{Fe}}$  in pure liquid iron (de Wijs et al., 1998; Alfè et al., 2000; Pozzo et al., 2013; Ichikawa and Tsuchiya, 2015). Model extrapolations of the experimental data to 330 GPa are  $\sim 0.4$  log units slower ( $\sim 1\text{-}2 \times 10^{-9} \text{ m}^2 \text{ s}^{-1}$ ) at 5500 K than those obtained from computations ( $\sim 4 \times 10^{-9} \text{ m}^2 \text{ s}^{-1}$ ).

The similarity of Fe, Si and Cr transport properties obtained from FP-MD simulations in the present study (e.g. self-diffusivities, activation parameters and interatomic distances) strongly supports the notion that Si and Cr are incorporated in liquid Fe by atomic substitution (e.g. Figure 5.8 and Alfè et al., 2002). Excellent agreement between experimental and theoretical results for diffusion at low pressures, as well as Arrhenian model extrapolations, implies that Fe self-diffusion rates should be similar to those of Si and Cr. Additionally, we have accounted for the effect of pressure on the activation enthalpy by refining  $\Delta H$  at four different pressures, as compared to a simultaneous fit to data from 2 to 20 GPa employed by Dobson (2002). We therefore suggest that high pressure Fe self-diffusion experiments should be revisited and anticipate similar diffusivities and activation parameters to those obtained in Si and Cr diffusion experiments.

## 5.6 Discussion

### *5.6.1 Diffusion at homologous temperature*

Several experimental studies reporting diffusion rates in solid metals at high pressure suggest transport coefficients can be scaled to melting temperature, i.e. be a function of homologous temperature  $T_h = T_m/T$ . In this case, the Arrhenius equation for diffusion (Eq. 5.2) can be simplified to:

$$D = D_h \exp(-gT_h) \quad (5.10)$$

where  $g$  and  $D_h$  are empirical constants. A homologous temperature relation has been reported by two experimental studies of solid Fe-Ni interdiffusion: Yunker and Van Orman (2007) used a multi-anvil apparatus to 23 GPa and Reaman et al. (2012) used a diamond-anvil cell to 65 GPa, to obtain solid iron diffusion rates of approximately  $4 \times 10^{-13} \text{ m}^2 \text{ s}^{-1}$  near the liquidus ( $T_h = 1.05$ ). A homologous temperature relation was proposed by Poirier (1988) for diffusion in liquid metals based on experiments on liquid Hg over a very small pressure range (1 to ~11 bar; Bridgman, 1958), but this relation has not been verified by experiments at higher pressures.

We show Si, Cr, and Fe diffusion coefficients as a function of homologous temperature in Figure 5.11, using the melting curve of Komabayashi (2014). Experimental results are well described by Eq. 5.10 yielding constant diffusivities along the melting curve of  $\sim 4 \times 10^{-9} \text{ m}^2 \text{ s}^{-1}$  for both Si and Cr. These values are in good agreement with previous theoretical studies that report nearly constant and identical Si and Fe self-diffusivities of  $\sim 5 \times 10^{-9} \text{ m}^2 \text{ s}^{-1}$  along the outer core adiabat (Pozzo et al., 2013), as well as empirical predictions over the same  $P$ - $T$  region of  $\sim 10^{-8} \text{ m}^2 \text{ s}^{-1}$  (Poirier, 1988). The activation constant,  $g$ , derived from experiments is  $\sim 2.5$  for Si and  $\sim 2.9$  for Cr, which is consistent with theoretical studies that report  $g \sim 3$  (Saxton and Sherby, 1962) and  $g \sim 3.6$  (Poirier, 1988) for self-diffusion in liquid metals. Our MD results of self-diffusion yield  $D(T_m) \sim 5 \times 10^{-9} \text{ m}^2 \text{ s}^{-1}$  for Fe, Si and Cr, with  $g \sim 3.6$  for Si and Cr and  $\sim 3.3$  for Fe. Constants fitted to

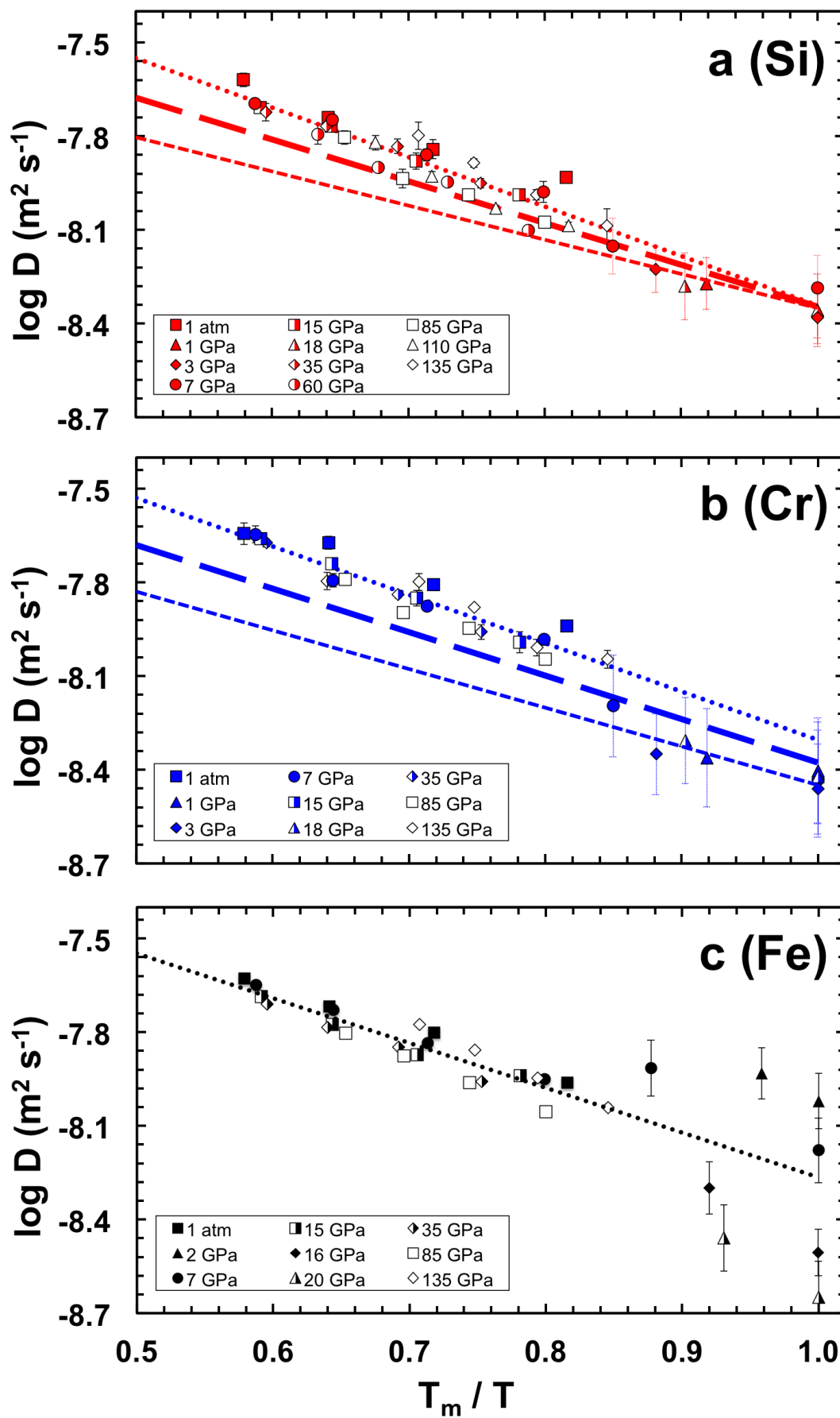


*Figure 5.11 (opposite page): Diffusion coefficients determined from experiments to 18 GPa and calculations to 135 GPa are shown as a function of homologous temperature ( $T_m/T$ ) for (a) Si, (b) Cr, and (c) Fe. Experimental Fe self-diffusion data are from (Dobson, 2002). Linear fits, according to Eq. 10, are shown to the experimental data (short-dashed lines) and FP-MD results (dotted lines). Averaged linear fits to both experiments and calculations are shown as long-dashed lines for Si and Cr.*

experimental and FP-MD results according to Eq. 5.10 are listed in Table 5.4. A two-fold increase of the temperature above  $T_m$  ( $T_h = 0.5$ ) results in an increase of Si and Cr diffusion rates by  $\sim 0.8$  log units.

We chose the melting curve assessed in the thermodynamic model of Komabayashi (2014) as it is based on low pressure data – where the diffusion experiments were performed – and extrapolates well to pressures of the core. By contrast, many experimental melting curves are based on a restricted pressure range (e.g. Murphy et al., 2011; Jackson et al., 2013). Scaling with the melting curve of Anzellini et al. (2013) gives a slightly better fit to the FP-MD results, but this melting curve is unconstrained below 50 GPa. Using a melting curve with a shallower slope (e.g. Boehler et al., 1993; Laio et al., 2000) results in a slightly worse fit of the homologous relation to the diffusivities at lower temperatures, the range mostly covered by the experiments.

Using the homologous temperature relation fitted to the FP-MD results, we obtain diffusivity values of  $\sim 5 \times 10^{-9} \text{ m}^2 \text{ s}^{-1}$  for Fe and  $\sim 4 \times 10^{-9} \text{ m}^2 \text{ s}^{-1}$  for Si and Cr at the ICB ( $T_h = 1$ ). These values are very close to  $D$  values at 5600 K value for the Arrhenian model fit ( $D_{\text{Fe}} \sim 5 \times 10^{-9} \text{ m}^2 \text{ s}^{-1}$ ,  $D_{\text{Si}} \sim D_{\text{Cr}} \sim 4 \times 10^{-9} \text{ m}^2 \text{ s}^{-1}$ ) which—if both model predictions are accurate—constrain the

temperature at the ICB approximately to this value. This finding is in excellent agreement with the ICB temperature predicted by a combination of computing the melting curve of Fe and the melting point depression due to the presence of light elements (Alfè et al., 2002), in addition to  $T_h$  values used in geodynamic and thermal evolution studies (Labrosse, 2003; Nimmo, 2015). For  $T_h = 0.9$  at the CMB (Nimmo, 2015) diffusivities computed by the homologous temperature model at 135 GPa ( $D_{\text{Fe}} \sim D_{\text{Si}} \sim 7 \times 10^{-9} \text{ m}^2 \text{ s}^{-1}$  and  $D_{\text{Cr}} \sim 6 \times 10^{-9} \text{ m}^2 \text{ s}^{-1}$ ) are consistent with the values of the Arrhenian model at 4500 K. The temperature decrease across the liquid outer core, as estimated using the  $P$ - $T$  overlap of both Arrhenian and  $T_h$  models, is consistent with those following an adiabat through the core with a temperature drop of  $\sim 1200$  K from ICB to CMB (Labrosse, 2003; Nimmo, 2015).

### 5.6.2 Mass transport contrast and element partitioning across ICB

A homologous temperature relation for diffusion in liquid iron (this study) and solid iron (Yunker and Van Orman, 2007; Reaman et al., 2012) helps to constrain relative mass transport rates at temperatures that range across the melting point at all pressures or planetary depths, where  $T_m/T = 1$ . Diffusion rates in liquid iron increase by approximately four orders of magnitude upon complete melting from the solid (Figure SM5.7). Although the presence of a mushy zone of partial melt is predicted to exist at Earth's ICB (see Loper and Roberts, 1981; Fearn et al., 1981; Deguen et al., 2007) the diffusion rates within this region are constrained to lie between  $\sim 5 \times 10^{-9}$  (this study) and  $\sim 5 \times 10^{-13} \text{ m}^2 \text{ s}^{-1}$  (Yunker and Van Orman, 2007; Reaman et al., 2012) (the liquidus and solidus diffusion rates, respectively).

Alfè et al. (2002) calculated the chemical potentials in liquid and crystalline iron alloys at conditions of the ICB and estimated that solid-liquid

fractionation of elements with similar atomic radius to that of Fe, such as silicon, should be near unity. Elements with dissimilar radii to that of Fe, such as oxygen and to a lesser extent sulfur, should partition more strongly into the liquid. An additional proxy for estimating solid alloy-liquid alloy partition coefficients may be the relative transport properties and average interatomic distances between Fe and candidate light elements within the liquid. For example, Pozzo et al. (2013) reported that Fe and Si have nearly identical self-diffusion coefficients and average interatomic distances under conditions of the Earth's outer core, while oxygen atoms are ~20% smaller and diffused 2-3 times faster. These findings, in addition to those in the present study, suggest that elements that behave Fe-like in the liquid may crystallize more congruently than non-Fe-like species such as small atoms (e.g. O, C, H, He) that most likely also can diffuse interstitially. In such a scenario, Si cannot contribute to chemical buoyancy in the outer core because there is no mechanism to preferentially enrich Si in the liquid upon inner core crystallization. Such postulations, however, require considerable further study into the structures of liquid and crystalline phases, as well as accurate iron alloy phase diagrams at high  $P$ - $T$ , which are active areas of current research (see Fischer, 2016; Campbell, 2016).

### 5.6.3 Viscosity profile of the outer core

Liquid viscosities are calculated via the Stokes-Einstein relation (Eq. 5.1) using the aggregate diffusivity of all atoms in the cell and the average species diameter from the sum over the individual radial distribution functions (Figure 5.8). This approach is equivalent to defining the interdiffusion coefficient according to the Darken rule  $D_{\text{Fe-}\phi} = X_{\text{Fe}}D_{\phi} + X_{\phi}D_{\text{Fe}}$  where  $X_i$  is the mol fraction of species  $i$  (Darken, 1948). Results are shown in Figure 5.12, in

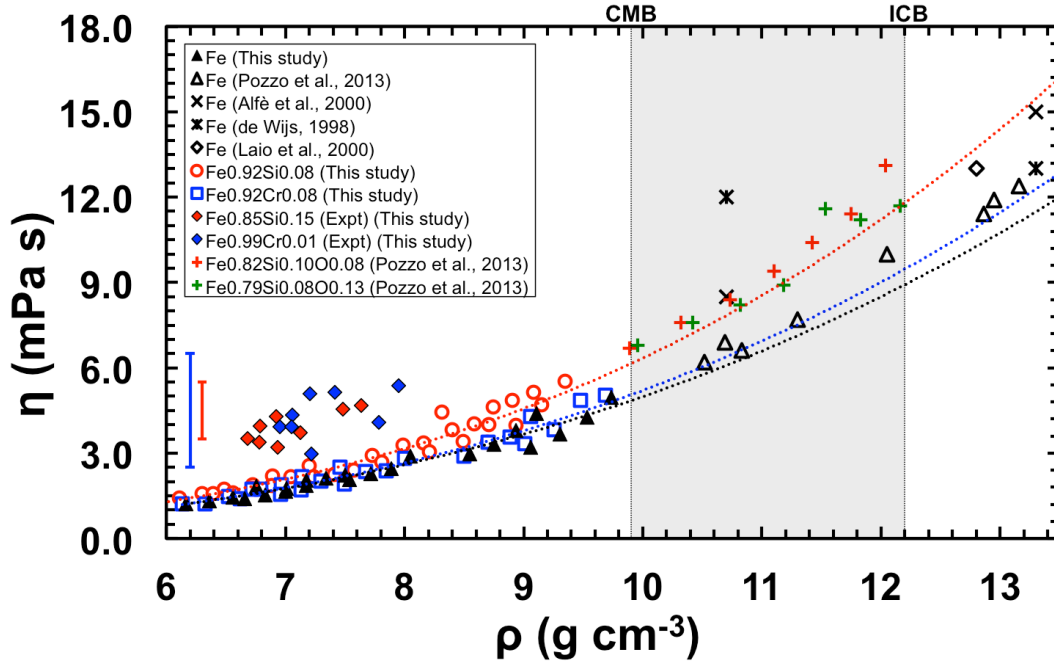


Figure 5.12: Viscosities of liquid iron and its alloys as a function of density. Viscosities were calculated via the Stokes-Einstein relation (Eq. 1) with self-diffusion coefficients and interatomic spacings obtained from MSD and partial RDFs, respectively. The relationship between density and interatomic spacing was used to estimate viscosities from experimental Si and Cr diffusion data. Standard  $1\sigma$  experimental errors are shown on left for Si (red) and Cr (blue). Liquid iron viscosities reported in previous studies are shown as open triangles (Pozzo et al., 2013); crosses (Alfè et al., 2000); stars (de Wijs et al., 1998); and open diamonds (Laio et al., 2000). Extrapolation of best-fit curves to viscosities determined in the present study to densities of the Earth's outer core (shaded region) are shown as black, red, and blue dotted lines for liquid Fe,  $Fe_{0.92}Si_{0.08}$  and  $Fe_{0.92}Cr_{0.08}$ , respectively.

comparison to previously reported viscosities, as a function of density. All three compositions are well described by a power-law relationship in the form  $\eta(\rho) = A\rho^B$  where  $A$  and  $B$  are constants that are listed in Table 5.3. Extrapolations of our data to higher liquid densities are in good agreement

with previous theoretical studies (de Wijs et al., 1998; Alfè et al., 2000) and show particularly good agreement with the recent computations by Pozzo et al. (2013), which employed the computationally more expensive Green-Kubo relation that relates  $\eta$  to the integral of the stress tensor autocorrelation function.

Viscosities based on experimental diffusion data are estimated via Eq. 5.1 using the  $r_{\text{Fe-}\phi}(\rho)$  relation from the MD results (Figure SM5.8) and are shown in Figure 5.12 for the highest and lowest temperatures achieved at each experimental pressure. Viscosities calculated from experiments are larger by a factor of  $\sim 2$  compared to viscosities estimated from the computations for the same composition. This is due to differences in diffusion coefficients measured using the two methods (i.e. experimental  $D$ 's are  $\sim 0.1$  log units slower than computed  $D$ 's). A linear extrapolation of the experimental results to higher  $\rho$  is in agreement with viscosities reported by Pozzo et al. (2013) for Fe-Si-O compositions that are significantly richer in light elements. In both studies, the viscosities of liquid iron alloys are higher than those of pure liquid iron at the same density (Figure 5.12).

Similar to the homologous temperature scaling of diffusivity, we can take into account the effect of pressure on viscosity by

$$\eta = \eta_o \exp(g_v T_h) \quad , \quad (5.11)$$

where  $g_v$  and  $\eta_o$  are empirical constants listed in Table 5.4. Viscosities along the melting curve are approximately 6 mPa s for liquid Fe,  $\sim 7$  mPa s for liquid  $\text{Fe}_{0.92}\text{Cr}_{0.08}$  and  $\sim 8$  mPa s for liquid  $\text{Fe}_{0.92}\text{Si}_{0.08}$  with a decrease of  $\sim 0.8$  log units at  $2T_m$  (Figure 5.13). For  $T_h = 0.9$  at the CMB (Nimmo, 2015), viscosities computed by Eq. 5.11 yield  $\sim 4$  mPa s for liquid Fe,  $\sim 5$  mPa s for liquid  $\text{Fe}_{0.92}\text{Cr}_{0.08}$  and  $\sim 6$  mPa s for liquid  $\text{Fe}_{0.92}\text{Si}_{0.08}$ . Our results are in good agreement with previous theoretical studies of liquid iron viscosities conducted

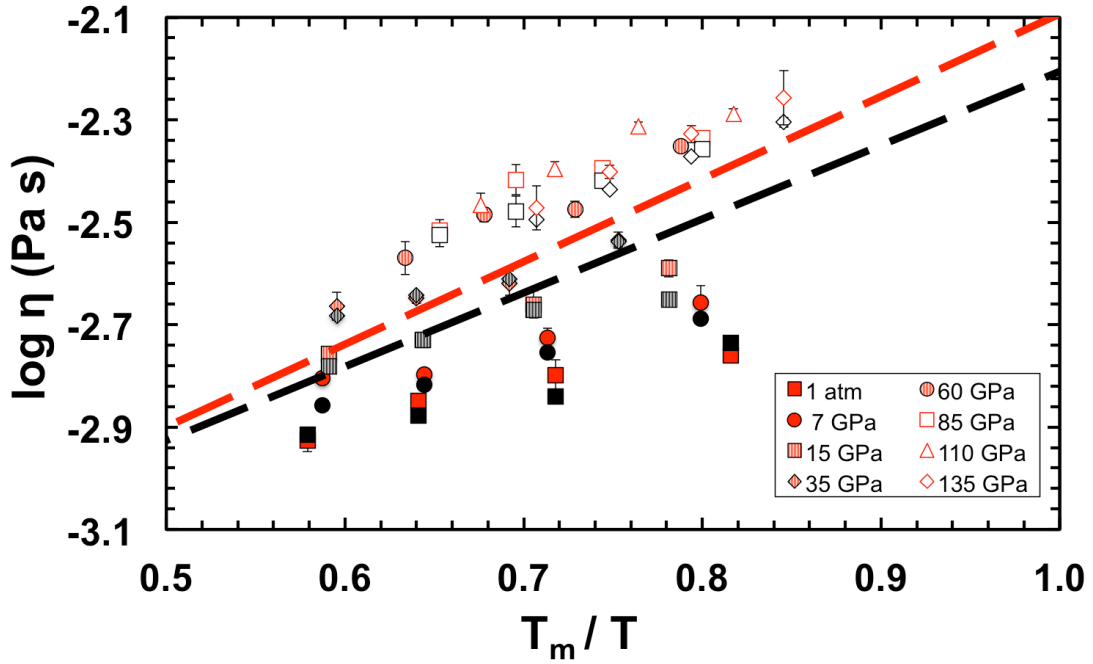


Figure 5.13: Calculated viscosities based on diffusion coefficients in liquid  $Fe_{0.92}Si_{0.08}$  (red symbols) and Fe in liquid iron (black symbols of same representation as listed in legend) as a function of  $T_m / T$ . Dashed lines show best fit to the data from all pressure intervals, yielding approximately 6 mPa s at  $T_m$  for Fe, ~8 mPa s for  $Fe_{0.92}Si_{0.08}$  and ~7 mPa s for  $Fe_{0.92}Cr_{0.08}$  (not shown), with a decrease by ~0.8 log units at  $2T_m$ .

over a higher range of  $P$ - $T$  conditions along the outer core adiabat (6–12 mPa s, Pozzo et al., 2013; 12 - 15 mPa s, de Wijs et al., 1998; 2 – 15 mPa s, Alfè et al., 2000). As with calculated diffusion rates as a function of homologous temperature, however, viscosity predictions according to Eq. 5.11 are sensitive to the melting curve, which remains debated in the literature (e.g. Boehler et al., 1993; Laio et al., 2000; Murphy et al., 2011; Jackson et al., 2013; Anzellini et al., 2013; Komabayashi, 2014).

Table 5.4: Homologous temperature model parameters according to Eqs. 5.10 and 5.11 for diffusion and viscosity, respectively.

	<i>FP-MD</i>			<i>Experiments</i>	
	Fe	Fe <sub>0.92</sub> Si <sub>0.08</sub>	Fe <sub>0.92</sub> Cr <sub>0.08</sub>	Fe-Si	Fe-Cr
$D_h$ ( $10^{-7}$ m <sup>2</sup> s <sup>-1</sup> )	1.5(3)	1.8(3)	1.8(3)	0.54(36)	0.62(94)
$g$	3.3(3)	3.7(3)	3.6(3)	2.5(5)	2.9(5)
$\eta_h$ ( $10^{-4}$ Pa s)	2.3(13)	2.0(11)	1.9(11)	-	-
$g_v$	3.3(9)	3.7(8)	3.3(9)	-	-

#### 5.6.4 Chemical equilibration during core formation

The concentration of Si in the Earth’s core remains controversial due mostly to experimental and analytical difficulties in measuring elemental solubility in liquid iron at extreme  $P$ - $T$  conditions, complex compositional effects on metal-silicate partitioning, as well as large uncertainties in the  $P$ - $T$ - $X$ - $f_{O_2}$  path of the terrestrial planets during accretion and core formation. Depending on the assumptions and the model, Si-contents as high as 10 wt. % (Fischer et al., 2015) or as low as 1 wt. % (Siebert et al., 2013) have been predicted for the core.

Calculation of chemical equilibration timescales,  $t_{eq}$ , of liquid metal droplets sinking in a magma ocean during accretion is largely controlled by the droplet size (i.e. diffusion distance). A metallic core from an impacting body may remain largely intact, partially or completely emulsify, depending on its initial size and viscosity contrast with the surrounding silicate mantle (Rubie et al., 2003; Samuel, 2012). In order to estimate maximum timescales for chemical equilibration within sinking metallic bodies, we use a simple model for diffusion in a sphere of radius  $a$  based on chemical potential alone. Using diffusion coefficients calculated for a range of  $T_h$  values, we can evaluate the diffusion equation in spherical geometry,

$$\frac{\partial C^i}{\partial t} = D \left( \frac{\partial^2 C^i}{\partial r^2} + \frac{2}{r} \frac{\partial C^i}{\partial r} \right) \quad , \quad (5.12)$$

where  $C^i$  is the concentration of species  $i$ . If one substitutes  $u = C^i r$ , then the above equation becomes

$$\frac{\partial u}{\partial t} = D \frac{\partial^2 u}{\partial r^2} \quad , \quad (5.13)$$

which is the one-dimensional equation. Initially ( $t = 0$ ),  $C^i = C_{\text{eq}}^i$  at  $r = a$  (the radius of the sphere) and  $C^i = 0$  for  $r < a$ ; at times smaller than the equilibration time ( $t_{\text{eq}} > t > 0$ ),  $\frac{\partial C^i}{\partial t} = 0$  at  $r = a$  and  $\frac{\partial C^i}{\partial t} > 0$  for  $r < a$ . Here  $C_{\text{eq}}^i$  is the concentration of  $i$  in the metal determined by the metal-silicate exchange coefficient. Surrounding silicate liquid ( $r > a$ ) is assumed to behave as an infinite reservoir, such that the concentration of  $i$  at the metal-silicate interface is constant as the metal sinks through the magma ocean. For simplicity, we ignore the time-dependent coefficients of expansion and compression in the metal and silicate liquids and assume that the volume of the descending metallic liquid remains fixed ( $dV/dt = 0$ ).

In order to calculate length and timescales of Si equilibration within a liquid iron droplet explicitly, we assign the initial  $C^{\text{Si}}$  of the sphere interior ( $r < a$ ) to zero, which is consistent with the observation of highly Si-depleted iron meteorites as representatives of planetesimal cores (Pack et al., 2011). Our results are shown in Figure 5.14 alongside solid-state equilibration timescales calculated from diffusion data reported by Yunker and Van Orman (2007) and Reaman et al. (2012). Chemical equilibration in highly-emulsified metal-silicate mixtures ( $r \ll 1$  cm) is nearly instantaneous ( $t_{\text{eq}} \ll 1$  min), while metallic droplets of  $r \sim 0.5$  cm – which is the estimated stable droplet size (Rubie et al., 2003; Terasaki et al., 2012) – would require several tens of

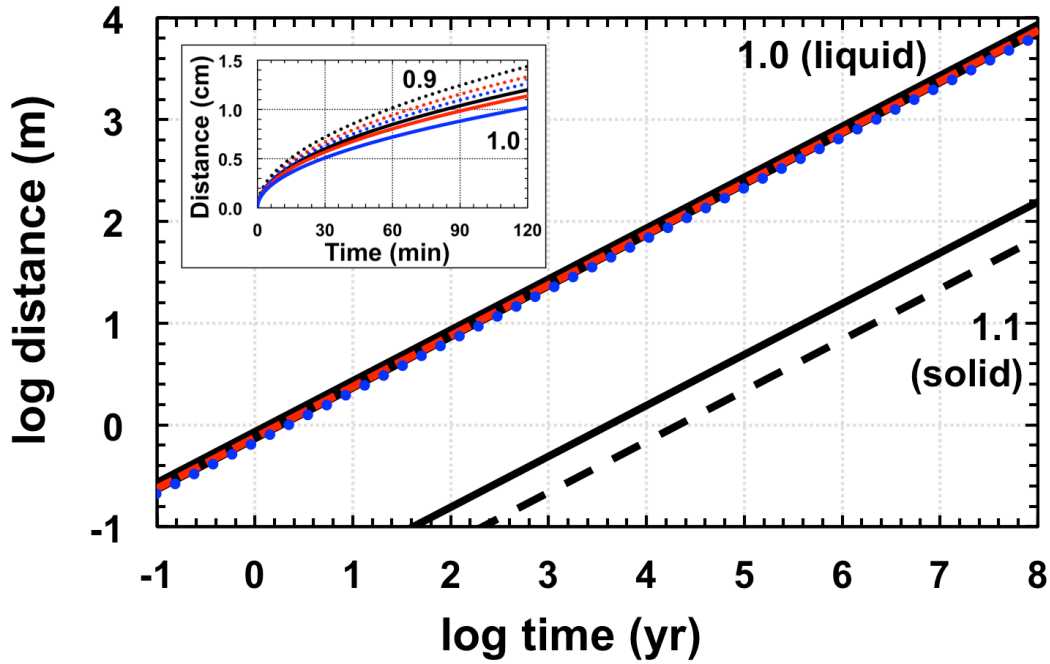


Figure 5.14: Characteristic diffusion distances are shown as a function of time for Fe (black curves), Si (red curves), and Cr (blue curves) at liquidus temperatures. For comparison, Fe-Ni interdiffusion in solid iron ( $T_h = 1.1$ ) is shown following Reaman *et al.* (2012) (black curve) and Yunker and Van Orman (2007) (dashed curve). The inset shows diffusion times at significantly shorter length scales in liquid iron and its alloys for  $T_h = 1$  and  $T_h = 0.9$  (dotted curves).

minutes (Figure 5.14 inset). Impactor cores of 500 m radius, on the other hand, even if completely molten during descent, would not equilibrate on realistic timescales of metal segregation and core formation, requiring  $10^4 - 10^5$  years for diffusive equilibration. This finding implies that large impactor cores fail to equilibrate with the surrounding silicate liquid during rapid gravitational descent through a magma ocean. Solid-state diffusion timescales near  $T_m$  are four to five orders of magnitude longer than those in the liquid

state. The effects of turbulent mixing and/or non-zero initial solute concentration in the liquid sphere interior that could significantly reduce the equilibration timescale should be investigated in future studies to yield timescales that incorporate additional mixing processes.

## 5.7 Conclusions

We have conducted the first experimental study of chemical diffusion (Si and Cr) in liquid iron at high pressure. Experimental data are in excellent agreement with diffusive transport properties that we have calculated using FP-MD simulations at comparable conditions. The FP-MD simulations can thus be used with greater confidence over a wide  $P$ - $T$  range.

Interatomic spacings, determined by partial RDFs of the liquid simulations, show that Fe-Fe distances are similar to Fe-Si and Fe-Cr distances which implies that there is one single effective radius when the two species interact with each other or with themselves. This observation and the similarity of Si, Cr, and Fe diffusion transport properties indicates that Si and Cr exchange with Fe via direct substitution, which also plays an important role in the systematics of element partitioning between solid and liquid metal at the ICB.

The experimental diffusion data are well described by a homologous temperature relation (Eq. 5.10) yielding constant Si and Cr diffusivities at  $T_m$  of approximately  $4 \times 10^{-9} \text{ m}^2 \text{ s}^{-1}$ . Fitting the homologous temperature relation to computational results over a much larger pressure range, however, is very sensitive to the Clapeyron slope of the Fe melting curve. Shallow melting curves (e.g. Boehler et al., 1993) produce model  $D(T_m)$  values that decrease by approximately 0.005 log units per GPa, while steep melting curves (e.g.

Komabayashi 2014; Anzellini et al., 2013) yield constant  $D(T_m)$  of  $\sim 5 \times 10^{-9} \text{ m}^2 \text{ s}^{-1}$  for Fe and  $\sim 4 \times 10^{-9} \text{ m}^2 \text{ s}^{-1}$  for Si and Cr. Diffusivities within the mushy layer of the ICB are therefore constrained to lie between  $\sim 5 \times 10^{-9} \text{ m}^2 \text{ s}^{-1}$  and  $\sim 5 \times 10^{-13} \text{ m}^2 \text{ s}^{-1}$  (Yunker and Van Orman, 2007; Reaman et al., 2012), the liquidus and solidus diffusion rates, respectively. We further use the homologous temperature relation of diffusion to estimate maximum timescales of chemical equilibration within liquid metal droplets and report that km-sized impactor cores will fail to equilibrate while sinking through a magma ocean. We have also fitted the Arrhenian model to our data with pressure and temperature derivatives on the activation parameters determined over a very wide range of conditions. Both models provide a temperature estimate of  $\sim 5600 \text{ K}$  at the ICB and  $\sim 4500 \text{ K}$  at the CMB, although additional studies on the phase relations and equations of state of relevant liquid alloys are required for greater certainty. The verification of the homologous temperature relation of mass transport in liquid metals, as well as the excellent agreement between experiments and FP-MD simulations, implies that low pressure experiments can be used with greater confidence of mass transport in the Earth's outer core.

## 5.8 Acknowledgements

We would like to thank James Van Orman and two anonymous reviewers for their helpful and constructive comments. E.S.P. would like to thank Hongzhan Fei and Vera Laurenz for laboratory assistance and helpful discussions on diffusion, as well as Razvan Caracas, Alexandra Seclaman and Fabian Wagle for their assistance with computations and computational theory. We are grateful to Hubert Schulze, Heinz Fischer, Rafael Njul and

Stefan Übelhack for assistance with experimental sample and assembly preparation. D.C.R. and E.S.P. were supported by the European Research Council (ERC) Advanced Grant “ACCRETE” (Contract No. 290568) and by the German Research Foundation (DFG) Priority Programme SPP1385 "The First 10 Million Years of the Solar System - a planetary materials approach" (Ru1323/2). G.S.N. and V.V. were supported by DFG grant STE1102/10 in the Priority Programme SPP1488 “Planetary Magnetism”. V.V. was also supported by the Minerva Foundation of the Max Planck Society for his work at The Hebrew University of Jerusalem.

## 5.9 References

- Alfè D., Kresse G. and Gillan M.J. (2000) Structure and dynamics of liquid iron under Earth’s core conditions. *Phys. Rev. B* **61**, 132-142.
- Alfè D., Gillan M.J. and Price G.D. (2002) Composition and temperature of the Earth’s core constrained by combined ab initio calculations and seismic data. *Earth Planet. Sci. Lett.* **195**, 91-98.
- Allen M.P. and Tildesley D.J. (1991) *Computer Simulation of Liquids*. Clarendon Press, Oxford.
- Anderson H.C. (1980) Molecular dynamic simulations at constant pressure and/or temperature. *J. of Chem. Phys.* **72**, 2384-2393.
- Anzellini S., Dewaele A., Mezouar M., Loubeyre P. and Morard G. (2013) Melting of iron at Earth’s inner core boundary based on fast X-ray diffraction. *Science*. **340**, 464-466.
- Boehler R. (1993) Temperatures in the Earth’s core from melting-point measurements of iron at high static pressures. *Nature* **363**, 534–536.
- Braginsky S. (1963) Structure of the F layer and reasons for convection in the Earth’s core. *Dokl. Akad. Nauk. SSR Engl. Trans.* **149**, 1311-1314.

Bridgman P.W. (1958) *The Physics of High-Pressure*, G. Bell & Sons Ltd, London.

Calderon F.P., Sano N. and Matsushita Y. (1971) Diffusion of manganese and silicon in liquid iron over the whole range of composition. *Metal. Trans.* **2**, 3325-3332.

Campbell A.J. (2016) Phase diagrams and thermodynamics of core materials. In *Deep Earth: Physics and Chemistry of the Lower Mantle and Core* (eds. H. Terasaki and R.A. Fischer), American Geophysical Union, Washington D.C., DOI: 10.1002/9781118992487.

Cohen M.H. and Turnbull D. (1959) Molecular transport in liquids and glasses. *J. Chem. Phys.* **31**, 1164-1169

Curtin H.R., Decker D.L. and Vanfleet H.B. (1965) Effect of pressure on the intermetallic diffusion of silver in lead. *Phys. Rev.* **139**, 1552-1557.

Darken L.S. (1948) Diffusion, mobility and their interrelation: through free energy in binary metallic systems. *Trans. AIME* **175**, 184.

Deguen R., Alboussière T. and Brito D. (2007) On the existence and structure of a mush at the inner core boundary of the Earth. *Phys. Earth Planet. Int.* **164**, 36-49.

de Wijs G.A., Kresse G., Vočadlo L., Dobson D., Alfè D., Gillan M.J. and Price G.D. (1998) The viscosity of liquid iron at the physical conditions of the Earth's core. *Lett. Nature* **392**, 805-807.

Dobson D.P. (2000) <sup>57</sup>Fe and Co tracer diffusion in liquid Fe-FeS at 2 and 5 GPa. *Phys. Earth. Planet. Int.* **120**, 137-144.

Dobson D.P. (2002) Self-diffusion in liquid Fe at high pressure. *Phys. Earth Planet. Int.* **130**, 271-284.

Dobson D. P., Brodholt J.P., Vočadlo L., and Crichton W.A. (2001) Experimental verification of the Stokes-Einstein relation in liquid Fe-FeS at 5 GPa. *Mol. Phys.* **99**, 773-777.

Dobson D.P. and Wiedenbeck M. (2002) Fe- and C-self-diffusion in liquid Fe<sub>3</sub>C to 15 GPa. *Geophys. Res. Lett.* **29**, doi:10.1029/2002GL015536.

Fearn D.R., Loper D.E. and Roberts P.H. (1981) Structure of the Earth's inner core. *Nature* **292**, 232-233.

Fischer R.A., Nakajima Y., Campbell A.J., Frost D.J., Harries D., Langenhorst F., Miyajima N., Pollok K. and Rubie D.C. (2015) High pressure metal-silicate partitioning of Ni, Co, V, Cr, Si and O. *Geochim. Cosmochim. Acta* **167**, 177-194.

Fischer R.A. (2016) Melting of Fe alloys and the thermal structure of the core. In *Deep Earth: Physics and Chemistry of the Lower Mantle and Core* (eds. H. Terasaki and R.A. Fischer), American Geophysical Union, Washington D.C., DOI: 10.1002/9781118992487.

Goldstein J.I., Hanneman R.E. and Ogilvie R.E. (1965) Diffusion in the Fe-Ni system at 1 atm and 40 kbar pressure. *Trans. Metal. Soc. AIME.* **233**, 812-820.

Gubbins D., Alfè D., Masters T.G., Price D. and Gillan M.J. (2003) Can the Earth's dynamo run on heat alone? *Geophys. J. Int.*, **155**, 609-622.

Gubbins D., Alfè D., Masters G., Price G.D. and Gillan M. (2004.) Gross thermodynamics of two-component core convection. *Geophys. J. Int.* **157**, 1407-1414.

Ichikawa H. and Tsuchiya T. (2015) Atomic transport property of Fe-O liquid alloys in the Earth's outer core  $P,T$  condition. *Phys. Earth Planet. Int.* **247**, 27-35.

Jackson J.M., Sturhahn W., Lerche M., Zhao J., Toellner T.S., Ercan Alp E., Sinogeikin S.V., Bass J.D., Murphy C.A. and Wicks J.K. (2013) Melting of compressed iron by monitoring atomic dynamics. *Earth Planet. Sci. Lett.* **362**, 143-150.

Komabayashi T. (2014) Thermodynamics of melting relations in the system Fe-FeO at high pressure: implications for oxygen in the Earth's core. *J. Geophys. Res. Solid Earth* **119**, 4164-4177.

Kresse G. and Furthmüller J. (1996) Efficient iterative schemes for *ab initio* total-energy calculations using a plane-wave basis set. *Phys. Rev. B* **54**, 11169.

Kresse G. and Joubert J. (1999) From ultrasoft pseudopotentials to the projector augmented-wave method. *Phys. Rev. B* **59**, 1758.

Kubiček P. (1975) Heterodiffusion of Cr in molten Fe in the temperature range of 1800 to 1970 K. *Czech J. Phys. B* **28**, 300-305.

Labrosse S. (2003) Thermal and magnetic evolution of the Earth's core. *Phys. Earth Planet. Int.* **140**, 127-143.

Laio A., Bernard S., Chiarotti G. L., Scandolo S. and Tosatti E. (2000) Physics of iron at Earth's core conditions, *Science* **287**, 1027 – 1030.

Liebske C., Schmickler B., Terasaki H., Poe B.T., Suzuki A., Funakoshi K., Ando R. and Rubie D.C. (2005) Viscosity of peridotite liquid up to 13 GPa: implications for magma ocean viscosities. *Earth Planet. Sci. Lett.* **240**, 589-604.

Loper D.E. and Roberts P.H. (1981) A study of conditions at the inner core boundary of the Earth. *Phys. Earth Planet. Int.* **24**, 302-307.

Lu X.-G., Selleby M. and Sundman B. (2005a) Implementation of a new model for pressure dependence of condensed phases in Thermo-Calc. *Comp. Coupl. Phase Diag. Thermochem.* **29**, 49-55.

Lu X.-G., Selleby M. and Sundman B. (2005b) Assessments of molar volume and thermal expansion for selected bcc, fcc and hcp metallic elements. *Comp. Coupl. Phase Diag. Thermochem.* **29**, 68-89.

Morard G., Andraut D., Antonangeli D. and Bouchet J. (2014) Properties of iron alloys under the Earth's core conditions. *Comptes Rendus Geosci.* **346**, 130-139.

Murphy C. A., Jackson J.M., Sturhahn W. and Chen B. (2011) Melting and thermal pressure of hcp-Fe from the phonon density of states. *Physics Earth Planet. Int.* **188**, 114-120.

- Nachtrieb N. (1967) Self diffusion in liquid metals. *Adv. Phys.* **16**, 309-323.
- Nelder J.A. and Mead R. (1965) A simplex method for function minimization. *Computer J.* **7**, 308-313.
- Ni H., Hui H., and Steinle-Neumann G. (2015) Transport properties in silicate melts. *Rev. Geophys.* **53**, 715-744.
- Nimmo F. (2015) Thermal and Compositional Evolution of the Core. In *Evolution of the Earth* (eds. P. Olson, and G. Schubert), 2<sup>nd</sup> Edn. Vol. 9., Elsevier B.V., Amsterdam, p. 201-219.
- Pack A., Vogel I., Rollion-Bard C., Luias B. and Palme H. (2011) Silicon in iron meteorite metal. *Meteor. Planet. Sci.* **46**, 1470-1483.
- Perdew J.P., Burke K. and Wang Y. (1996) Generalized gradient approximation for the exchange-correlation hole of a many-electron system. *Phys. Rev. B* **54**, 533-539.
- Poirier J.P. (1988) Transport properties of liquid metals and viscosity of the Earth's core. *Geophys. J.* **92**, 99-105.
- Pozzo M., Davies C., Gubbins D. and Alfè D. (2013) Transport properties for liquid silicon-oxygen-iron mixtures at Earth's core conditions. *Phys. Rev. B.* **87**, DOI: 10.1103/PhysRevB.87.014110.
- Press W.H., Teulolsky S.A., Vetterling W.T. and Flannery B.P. (2002) *Numerical Recipes in C++*, 2nd edition. Cambridge Univ. Press, Cambridge, pp. 413-417.
- Reaman D.M., Colijn H.O., Yang F., Hauser A.J., and Panero W.R. (2012) Interdiffusion of Earth's core materials to 65 GPa and 2200 K. *Earth Planet. Sci. Lett.* **349-350**, 8-14.
- Reid J.E., Poe B.T., Rubie D.C., Zotov N. and Wiedenbeck M. (2001) The self-diffusion of silicon and oxygen in diopside (CaMgSi<sub>2</sub>O<sub>6</sub>) liquid up to 15 GPa. *Chem. Geol.* **174**, 77-86.
- Ringwood A.E. (1959) On the chemical evolution and densities of the planets. *Geochim. Cosmochim. Acta.* **15**, 257-283.

Rubie D.C. (1999) Characterising the sample environment in multianvil high-pressure experiments. *Phase Trans.* **68**, 431-451.

Rubie D.C., Melosh H.J., Reid J.E., Liebske C. and Righter K. (2003) Mechanisms of metal-silicate equilibration in the terrestrial magma ocean. *Earth Planet. Sci. Lett.* **205**, 239-255.

Samuel H. (2012) A re-evaluation of metal diapir breakup and equilibration in terrestrial magma oceans. *Earth Planet. Sci. Lett.* **313-314**, 105-114.

Saxton H.J. and Sherby O.D. (1962) Viscosity and atomic mobility in liquid metals. *Trans Am. Soc. Metals* **55**, 826-843.

Secco R.A. (1995) Viscosity of the outer core. In *Handbook of physical constants* (ed. T.J. Ahrens), American Geophysical Union reference shelf 2, Washington, D.C., p. 218-227.

Siebert J., Badro J., Antonangeli D. and Ryerson F.J. (2013) Terrestrial accretion under oxidizing conditions. *Science*. DOI: 10.1126/science.1227923

Stevenson D.J. (1990) Fluid dynamics of core formation, In *The Origin of the Earth* (eds. H. Newsom and J.H. Jones), Oxford Press, London, 1990, pp. 231-249.

Swalin R.A. (1959) On the theory of self diffusion in liquid metals. *Acta Metall.* **7**, 736-740.

Terasaki H., Urakawa S., Rubie D.C., Funakoshi K., Sakamaki T., Shibasaki Y., Ozawa S. and Ohtani E. (2012) Interfacial tension of Fe-Si liquid at high pressure: Implication for liquid Fe-alloy droplet size in magma oceans. *Phys. Earth Planet. Int.* **202-203**:1-6.

Umemoto K. and Hirose K. (2015) Liquid iron-hydrogen alloys at outer core conditions by first-principles calculations. *Geophys. Res. Lett.* **42**, 7513-7520.

Vočadlo L., Alfè D., Price G.D. and Gillan M.J. (2000) First principles calculations on the diffusivity and viscosity of liquid Fe-S at experimentally accessible conditions. *Phys. Earth Planet. Int.* **120**, 145-152.

Weyland J.A., Decker D.L. and Vanfleet H.B. (1971) Effect of pressure on the diffusion of gold in lead to 50 kbar. *Phys. Rev. B* **4**, 4225-4234.

Yang L., Simnad M.T. and Derge G. (1956) Self diffusion in molten Fe-C alloys. *J. Met. Soc. Am.* **206**, 1577-1580.

Yunker M.L. and Van Orman J.A. (2007) Interdiffusion of solid iron and nickel at high pressure. *Earth Planet. Sci. Lett.* **254**, 203-213.

Zwanzig R. (1983) On the relation between self-diffusion and viscosity of liquids. *J. Chem. Phys.* **25**, 317-318.

## 5.10 Supplemental Material

The Supplemental Material contains the following information:

- Table SM5.1 showing the starting composition of the experiments.
- An extended discussion of gravitational stability in diffusion experiments (associated with Figure SM5.1)
- An extended discussion on the concentration dependence of diffusion (associated with Figure SM5.2).
- Eight figures (SM5.1 – SM5.8)

### 5.10.1 Introduction

Table SM5.1 lists starting compositions of iron and iron alloys used in the diffusion experiments. The data represent the mean of 25 spot analyses on each sample;  $\sigma$  stands for standard deviation from the mean. Sintered alloys were comprised of mostly sub-spherical grains with an average diameter of  $\sim 20 \mu\text{m}$ .

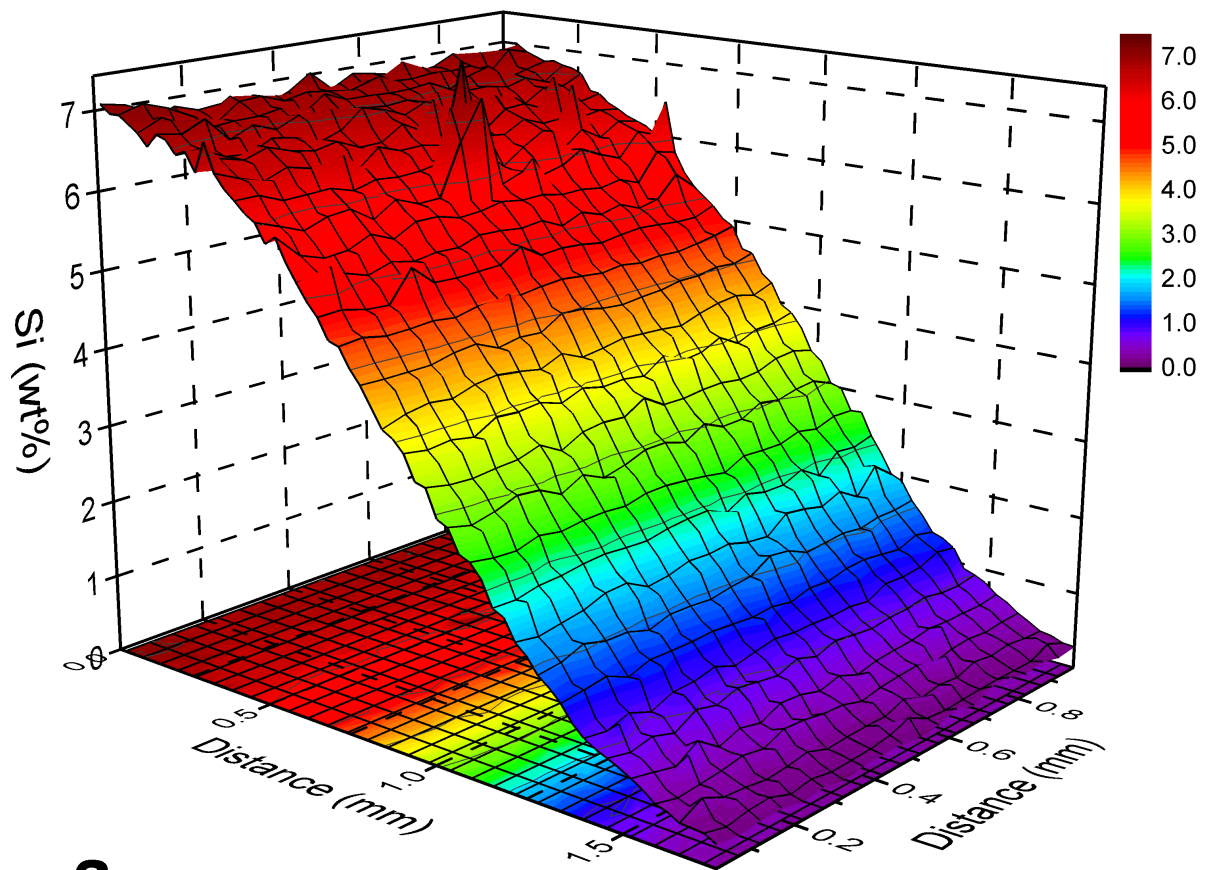
Table SM5.1: Starting composition of iron and iron alloys used in the diffusion experiments.

Metals	Iron		Alloy #1		Alloy #2		Alloy #3		Alloy #4	
	wt%	1 $\sigma$	wt%	1 $\sigma$	wt%	1 $\sigma$	wt%	1 $\sigma$	wt%	1 $\sigma$
Fe	99.97	0.47	91.22	0.40	91.13	0.42	98.69	0.51	95.39	0.49
Si	0.006	0.005	7.86	0.21	8.03	0.31	0.04	0.03	3.89	0.12
Cr	-	-	1.01	0.05	-	-	0.99	0.04	-	-
Mg	-	-	0.01	0.01	0.02	0.02	0.04	0.04	0.01	0.01
Total	99.98	0.47	100.1	0.31	99.18	0.34	99.76	0.40	99.29	0.45

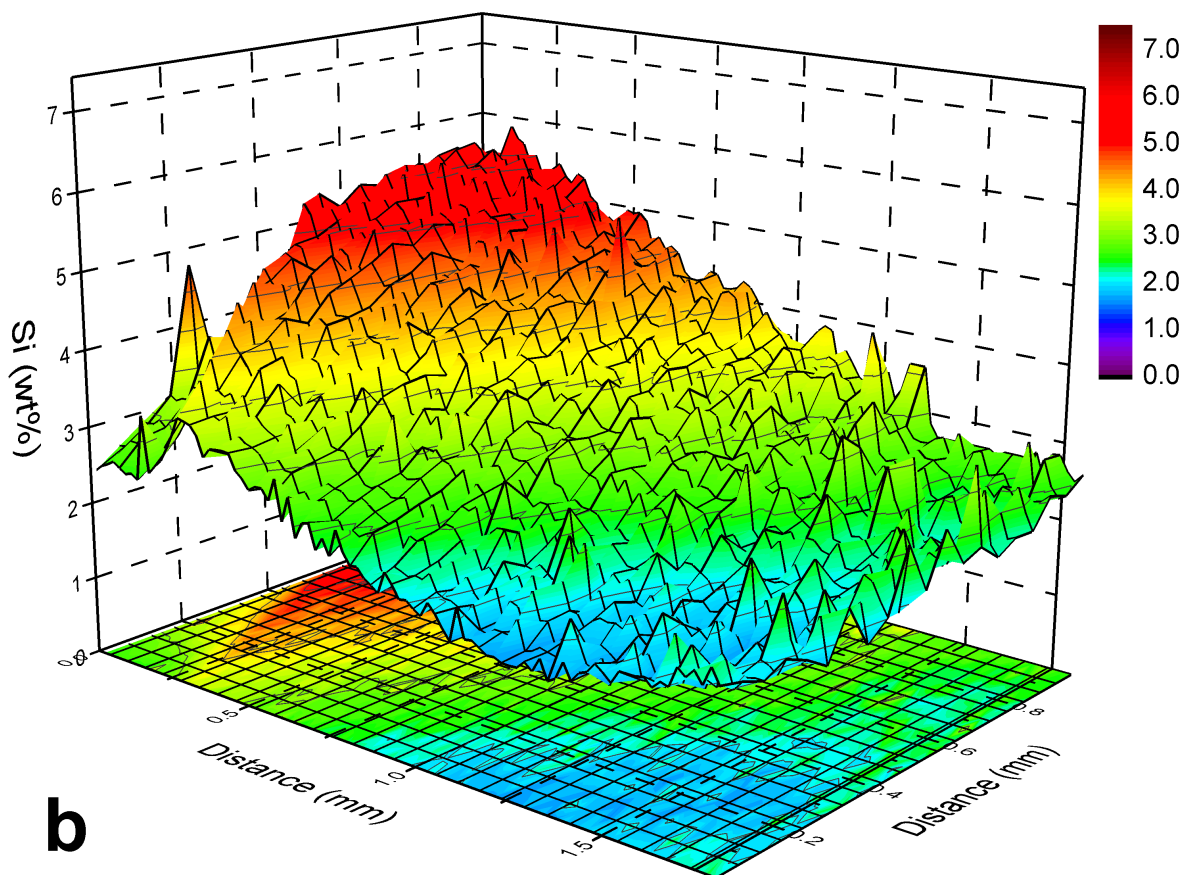
### 5.10.2 Gravitational stability in diffusion experiments

In order to ensure gravitational stability and eliminate the possibility of convective mixing of the molten sample, the cylindrical axis of the diffusion couple was oriented vertically with less-dense alloy on top. A limited number of experiments were conducted to test the effect of sample orientation by orienting the cylindrical axis horizontally. In order to compare the spatial distribution of the alloying element, we measured a  $900\ \mu\text{m} \times 1760\ \mu\text{m}$  grid (1780 individual points) across the polished surface of two quenched zero-time experiments annealed under different loading orientations (vertical vs. horizontal) and identical  $P$ - $T$  conditions (Figure SM5.1). The orientation of measured isopleths (lines of equal composition) in the vertically-annealed charge are parallel to the top and bottom of the capsule (Figure SM5.1a), whereas isopleths in the horizontally-annealed charge (Figure SM5.1b) are dipping approximately  $45^\circ$  between the planes of the capsule top and bottom, indicating a combination of diffusive and non-diffusive mixing. The preservation of multiple identical diffusion profiles perpendicular to the diffusion interface was therefore used as an indicator that convective mixing was negligible in diffusion experiments loaded in vertical orientation.

*Figure SM5.1 (next page): 3-dimensional representations of mapped cross-sections across two zero-time sample capsules run at 7 GPa and a peak temperature  $T_f = 2123\ \text{K}$ . The diffusion couple in sample (a) was annealed in a vertical orientation with the iron alloy cylinder directly above the pure iron cylinder, while sample (b) was annealed in a horizontal orientation so that the diffusion couple interface was vertical. Both samples were quenched immediately upon reaching  $T_f$ . In sample (a), isopleths are parallel with the top and bottom of the capsule illustrating that no observable convection took place. Isopleths in sample (b) are dipping approximately  $45^\circ$  between the planes of the capsule top and bottom, indicating a combination of diffusive and non-diffusive mixing due to gravitational instability.*



**a**



**b**

### 5.10.3 Concentration dependence of diffusion

At low concentrations ( $< 8$  wt. %) of alloying Si, the Fe-Si diffusion coefficient was found to remain constant within error of the experimental model fit at both 3 and 7 GPa. Two quenched diffusion profiles (one using a Fe-4 wt. % Si alloy, one using a Fe-8 wt. % Si alloy) were measured from experiments at 7 GPa in a double chamber capsule (Figure 5.1) at a heating rate of  $25 \text{ K s}^{-1}$  to 2173 K with a duration of 35 s at this peak temperature (Figure SM5.3). In order to compare diffusion coefficients at a single (peak) temperature, we fix  $\Delta H$  to the value obtained from the much larger dataset at 7 GPa ( $n = 9$ ) and refine the pre-exponential term independently. Retrieved diffusion coefficients for the experimental run shown in Figure SM5.3 are  $(8.4 \pm 1.3) \times 10^{-9} \text{ m}^2 \text{ s}^{-1}$  and  $(7.7 \pm 1.1) \times 10^{-9} \text{ m}^2 \text{ s}^{-1}$  for initial alloy composition of 4 wt. % Si and 8 wt. % Si, respectively.

In a previous experimental study of Si diffusion in liquid iron at ambient  $P$ , Calderon et al. (1971) explored a much larger compositional range (up to 40 wt. % Si) and reported a concentration effect on the diffusion coefficient, increasing by a factor of approximately 0.04 log units per weight percent Si with a maximum at approximately 20 wt. %. The fact that we do not observe a concentration effect above the level of uncertainty is likely explained by the much smaller range of alloy concentrations studied here. Nevertheless, as most estimates of Si concentrations in the Earth's core do not exceed 10 wt. % (e.g. Rubie et al., 2015; Siebert et al., 2013), any effect of solute concentration on diffusion can therefore be neglected.

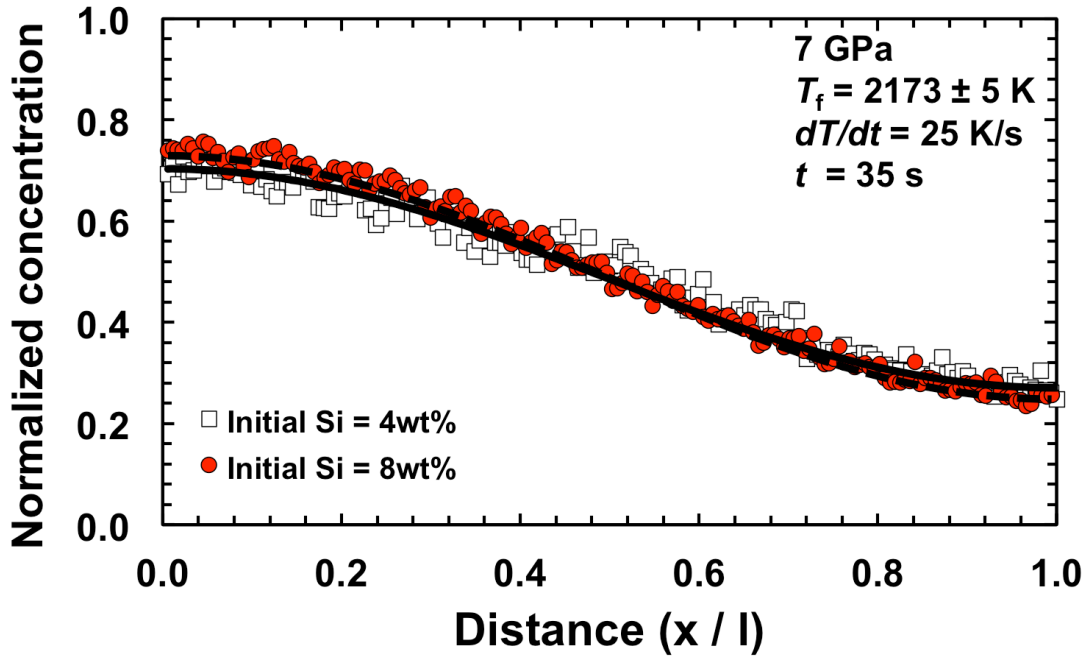


Figure SM5.2: Two diffusion profiles obtained simultaneously in separate parallel chambers of a double-chamber capsule (Figure 5.1) at 7 GPa using a heating rate of  $25 \text{ K s}^{-1}$  to peak temperature  $T_f = 2173 \pm 5 \text{ K}$ , maintained at  $T_f$  for 35 s and quenched by shutting off the electrical power. Si data are normalized to the initial alloy concentration, shown as red circles (8 wt. %) and unfilled squares (4 wt. %). To account for diffusion during heating, model curves show the least-squares best fit to the data using fixed  $\Delta H$  of  $35 \text{ kJ mol}^{-1}$ , as refined from the larger 7 GPa data set ( $n = 9$ ). Model diffusion coefficients are identical within error for the two starting compositions with  $D(T_f) = (7.7 \pm 1.1) \times 10^{-9} \text{ m}^2 \text{ s}^{-1}$  for Fe-8 wt.% Si (dashed line), and  $D(T_f) = (8.4 \pm 1.3) \times 10^{-9} \text{ m}^2 \text{ s}^{-1}$  for Fe-4 wt. % Si (solid line).

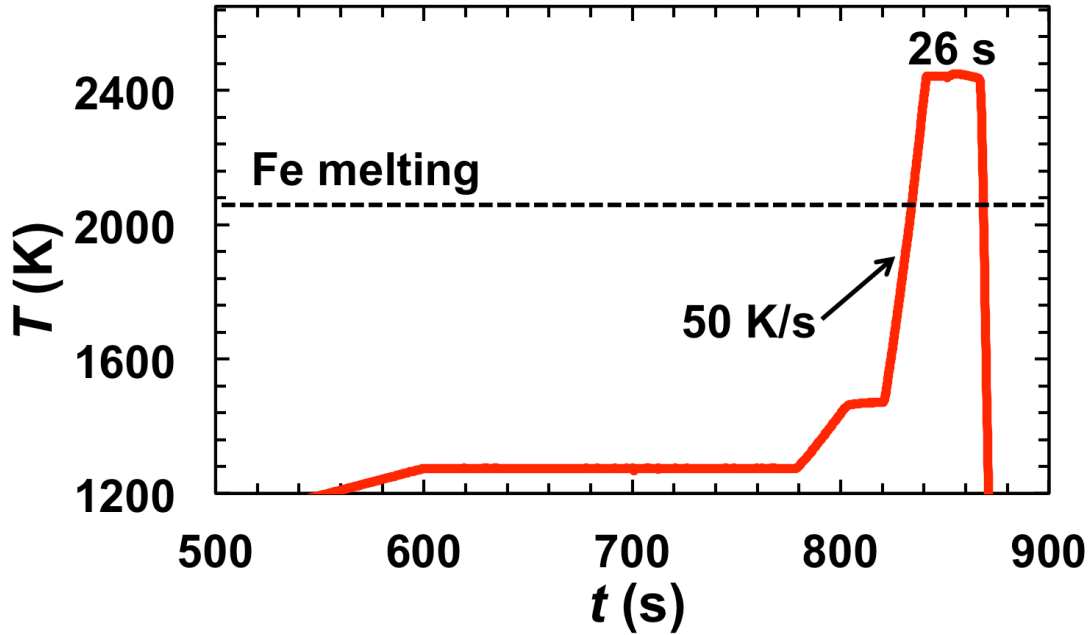


Figure SM5.3: Thermocouple signal during a diffusion experiment as recorded by the  $T$ - $t$  logger at intervals of 100 ms. The sample was compressed to 7 GPa at room temperature, heated to 1273 K over 10 minutes and then allowed to stay at 1273 K for 180 s and 1473 K for 18 s. Solid-state diffusion during these periods at low  $T$  ( $\ll T_m$ ) was negligible. The sample was then heated at a rate of  $50 \text{ K s}^{-1}$  to above the melting temperature  $T_m$  of pure iron ( $2059 \pm 25 \text{ K}$ ; shown as a dashed line) to a peak temperature of  $T_f = 2428 \pm 4 \text{ K}$  and maintained at  $T_f$  for 26 seconds. In this run, a combination of automatic and manual heating was used to minimize a decrease in heating rate upon approaching  $T_f$ . A fictive target temperature was set using a PID controller several hundred degrees above  $T_f$  and then switched to manual control about 50 K below the true target temperature. The upper and lower power limits were then fixed to a very small interval ( $\sim 0.1 \text{ W}$ ) so that the temperature would not fluctuate and the temperature profile would flatten very quickly to  $T_f$ . The sample was quenched by shutting off the electrical power at an initial rate in excess of  $\sim 500 \text{ K s}^{-1}$ . We also used a fully automated heating protocol in some experiments but due to the gradual decrease of the heating rate as  $T_f$  was approached, errors associated with  $T_f$  were then slightly larger.

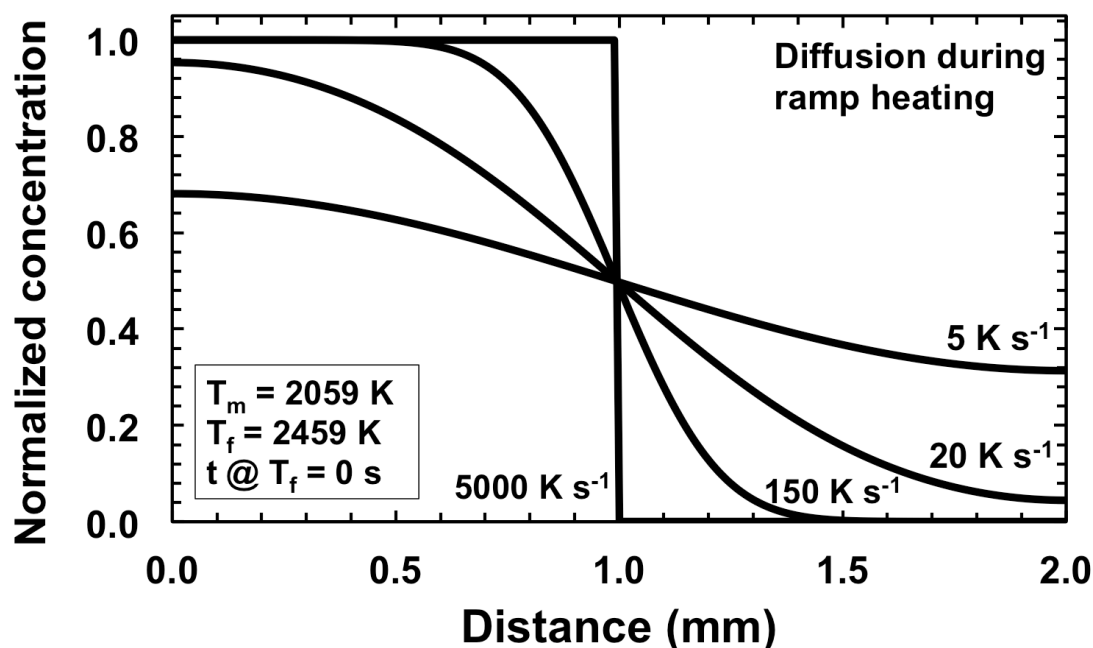


Figure SM5.4: Model simulations of non-isothermal diffusion in liquid iron using variable rates of ramp heating ( $dT/dt$ ). Diffusion parameters are estimated from theory (Poirier, 1988) with  $D_o = 9 \times 10^8 \text{ m}^2 \text{ s}^{-1}$  and  $\Delta H = 48 \text{ kJ mol}^{-1}$ . For experiments with target temperatures substantially above the melting temperature ( $T_f > T_m$ ), the extent of diffusion upon reaching  $T_f$  is strongly dependent on  $dT/dt$ . Under these conditions,  $dT/dt$  of several thousand  $\text{K s}^{-1}$  would be required for the concentration profile to appear as a step-function upon reaching  $T_f$ . The consequence of assuming isothermal annealing for diffusion experiments involving low viscosity liquids is an increasing overestimation of derived diffusion coefficients with increasing temperatures above  $T_m$ , which will also result in an overestimation of the activation enthalpy.

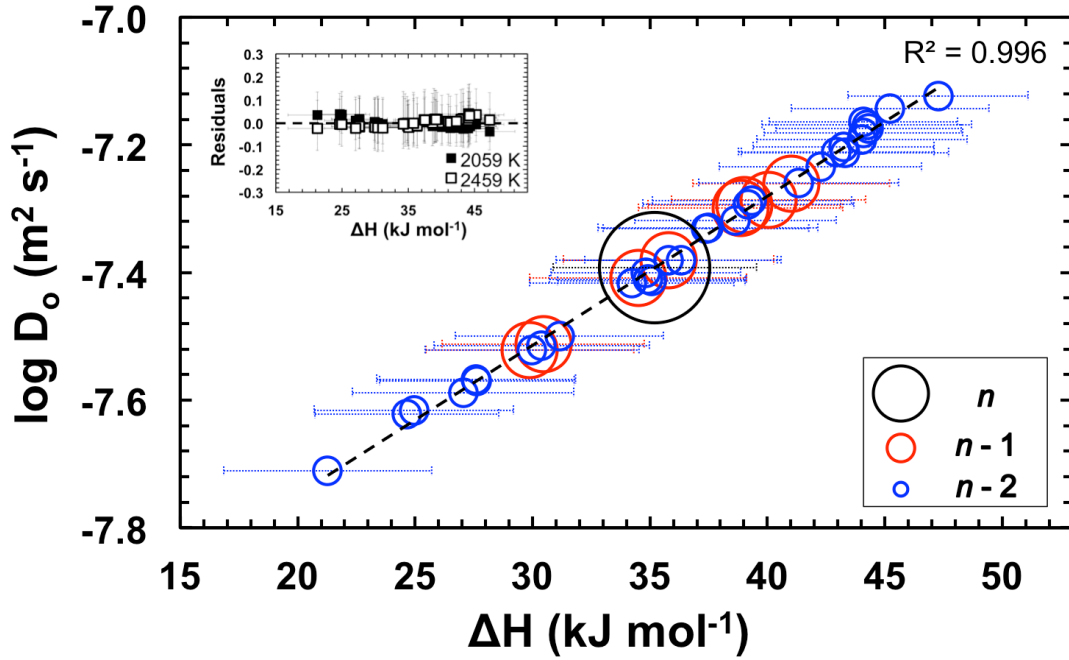


Figure SM5.5: Diffusion parameters,  $D_0$  and  $\Delta H$ , evaluated numerically for Si data at 7 GPa using  $n$ ,  $n-1$  and  $n-2$  diffusion profiles, where  $n = 9$  (Table 5.1, Figure 5.5), form a strongly linear relationship. The average error of the  $\Delta H$  is  $\pm 4 \text{ kJ mol}^{-1}$ . Residuals of diffusion coefficients at 2059 K and 2459 K calculated from parameters according to Eq. (5.2) using  $n-1$  and  $n-2$  profiles and those using  $n$  profiles do not exceed  $\sim 0.1$  (inset). The reduced chi squared ( $\chi_{\text{red}}^2$ ) to the full data set ( $n = 9$ ) is 3.17. For  $n-1$  and  $n-2$  profiles,  $\chi_{\text{red}}^2$  values range from 2.44 to 3.79.

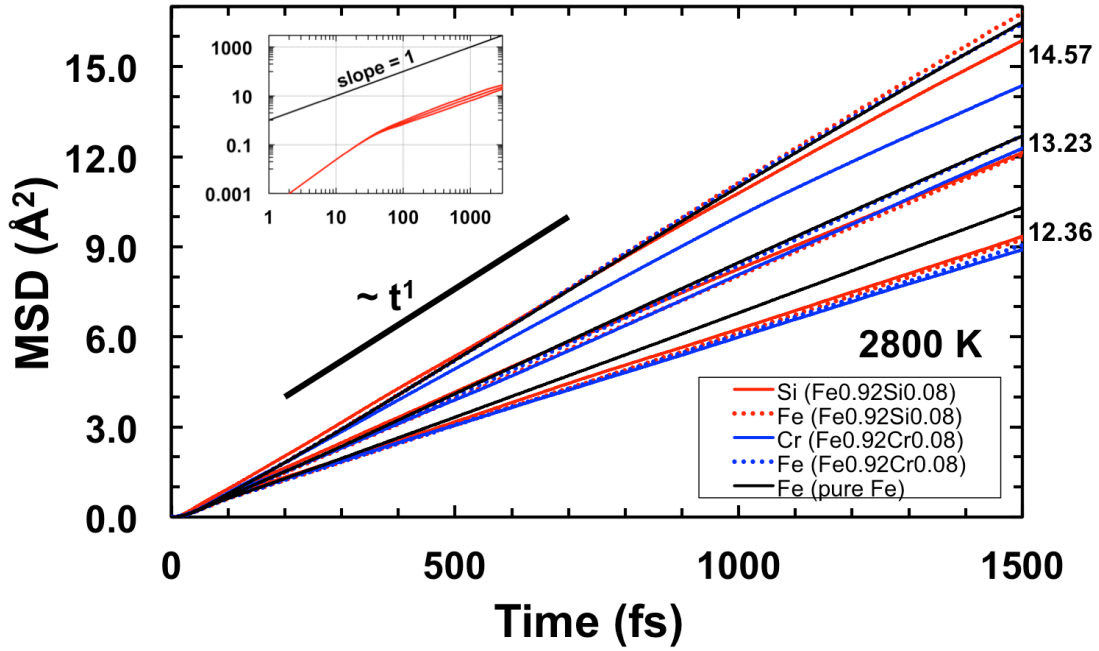


Figure SM5.6: Mean square displacement (MSD),  $\langle (\mathbf{r}_i(t+t_0) - \mathbf{r}_i(t_0))^2 \rangle$  from Eq. 8, for Si, Cr, and Fe in different compositions at 2800 K. Simulation volumes are listed on the right-hand side with values of 14.57, 13.23 and 12.36  $\text{\AA}^3 \text{atom}^{-1}$  corresponding to approximately 1 bar, 7 GPa, and 15 GPa, respectively. Diffusion coefficients are calculated as 1/6 of the slope over the diffusive regime (200 – 700 fs) ( $\sim t^1$ ), shown in log-scale for Si (inset).

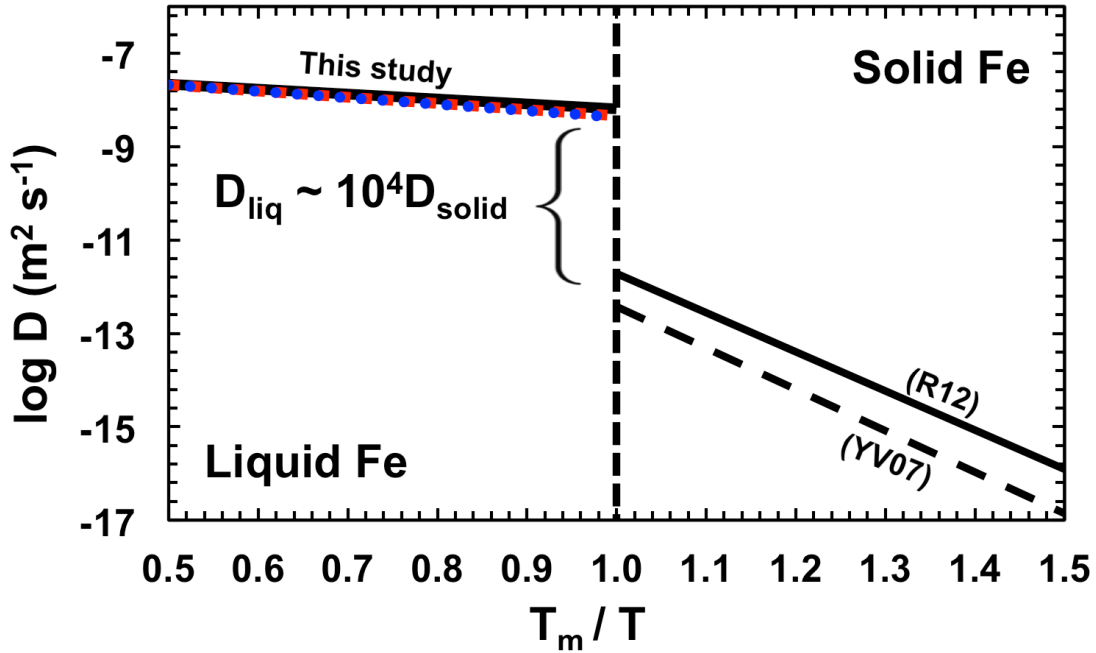


Figure SM5.7: Diffusivity in liquid iron and its alloys as a function of  $T_m / T$  across the melting temperature (dashed vertical line). Liquid ( $T_h < 1$ ) diffusion data, as determined from FP-MD simulations in the current study, are represented by a solid black curve for Fe self-diffusion, red dashed curve for Si self-diffusion in liquid  $Fe_{0.92}Si_{0.08}$ , and blue dotted curve for Cr self-diffusion in liquid  $Fe_{0.92}Cr_{0.08}$ . The subsolidus ( $T_h > 1$ ) homologous temperature relation for Fe-Ni interdiffusion data is reported by Reaman et al. (2012) (solid line) and Yunker and VanOrman (2007) (dashed curve). Diffusion rates increase by a factor of  $\sim 10^4$  between liquidus and solidus temperatures, a range that likely represents the mass transport contrast across the inner-core boundary or liquid metal-solid metal interface of a planetary core.

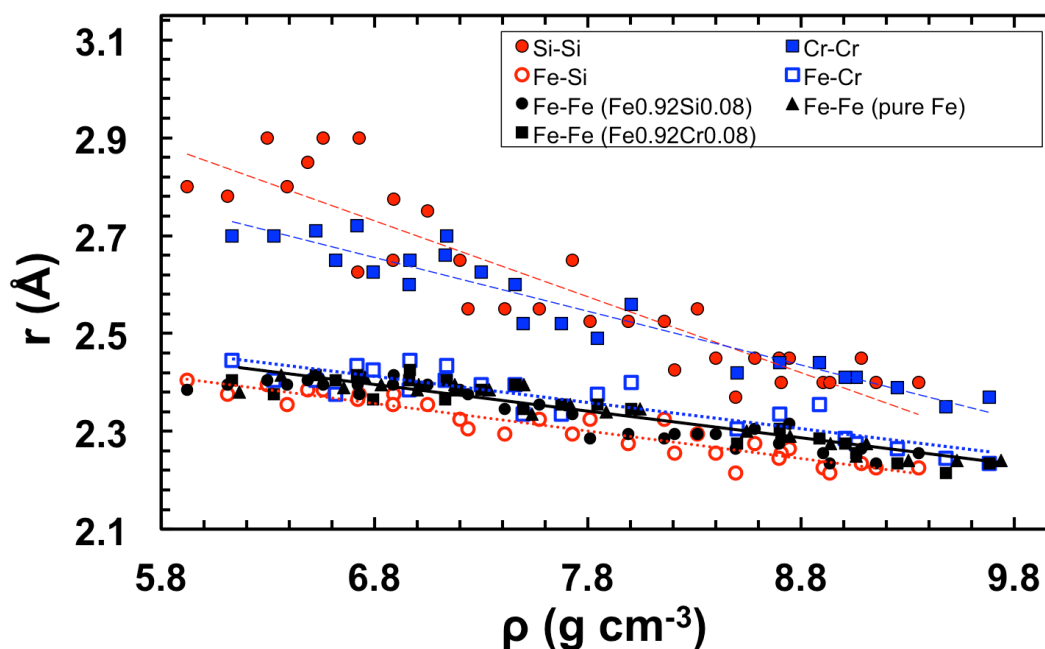


Figure SM5.8: Interatomic distances between species in all liquid compositions are shown as function of density. Fe-Fe and Fe-alloy distances in all compositions decrease at a rate of  $\sim 0.05 \text{ \AA} (\text{g cm}^{-3})^{-1}$  from approximately  $2.4 \text{ \AA}$  at the largest cell volume ( $15.04 \text{ \AA/atom}$ ) to  $2.2 \text{ \AA}$  at the smallest cell volume ( $9.53 \text{ \AA/atom}$ ). The average interatomic distance between two alloy species, which at low concentration are more indicative of chemical ordering within the liquid, decreases more rapidly with density than Fe-Fe and Fe-alloy distances by a factor of three for Si-Si distances and two for Cr-Cr distances.



# Experimental determination of oxygen diffusion at high pressure

ESTHER S. POSNER<sup>1</sup>, DAVID C. RUBIE<sup>1</sup>, DANIEL J. FROST<sup>1</sup>, GERD STEINLE-NEUMANN<sup>1</sup>

Submitted to *Earth and Planetary Science Letters*

## 6.1 Abstract

Oxygen diffusion experiments in liquid iron have been performed at 3-18 GPa and 1975-2643 K using a multi-anvil apparatus. Diffusion couples consisted of a pure iron rod and a sintered disk of  $\text{Fe}_{0.85}\text{O}_{0.15}$  placed end-to-end in a vertical orientation. Image and chemical spot analyses were acquired along the full length of the quenched sample on lines perpendicular to the diffusion interface. Exsolution features that formed during quenching consist mostly of spherical oxide blobs of at least two size populations, as well as feathery dendritic textures in more oxygen-rich regions near the top of the samples. Diffusion during heating (i.e. prior to reaching the peak annealing temperature,  $T_f$ ) is treated numerically to refine Arrhenian parameters from simultaneous least-squares fits to several concentration profiles obtained from experiments at constant pressure and variable  $T_f$ . Diffusion coefficients range from  $\sim 6 \times 10^{-9}$  to  $\sim 2 \times 10^{-8}$   $\text{m}^2 \text{s}^{-1}$  over the  $P$ - $T$  range of the study, with activation enthalpies of less than 100  $\text{kJ mol}^{-1}$ . We find a very weak effect of

---

<sup>1</sup> Bayerisches Geoinstitut, Universität Bayreuth, 95440 Bayreuth, Germany

pressure on oxygen diffusion with an activation volume of  $0.1 \pm 0.1 \text{ cm}^3 \text{ mol}^{-1}$ , in agreement with computational studies performed above 100 GPa. Arrhenian extrapolation of diffusion coefficients for oxygen to  $P$ - $T$  conditions of the Earth's outer core yields faster average diffusion rates ( $\sim 3 \times 10^{-8} \text{ m}^2 \text{ s}^{-1}$ ) than for Si or Fe in silicon-rich liquid iron alloys or pure liquid iron ( $\sim 5 \times 10^{-9} \text{ m}^2 \text{ s}^{-1}$ ) reported previously. Oxygen diffusion data are used to constrain the maximum size of descending liquid metal droplets in a magma ocean that is required for chemical equilibration to be achieved. Our results indicate that if the Earth's core composition is representative of equilibrium chemical exchange with a silicate magma ocean, then it could only have been accomplished by large-scale break-up of impactor cores to liquid iron droplet sizes no larger than a few tens of centimeters.

## 6.2 Introduction

Oxygen is the Earth's most abundant element, constituting nearly half of our planet's atoms and is potentially an important alloying element in the Earth's iron-rich core (e.g. Ringwood, 1977; Alfè et al., 1999). The presence of elements with low atomic mass, such as O, Si, S, C, H, relative to iron has been used to explain the  $\sim 10\%$  density deficit of the Earth's core compared to pure iron-nickel alloy (e.g. Birch, 1952; Allègre et al., 1995; McDonough, 2003; Poirier, 1994). The solubility of oxygen in liquid iron has been shown to increase at the extreme pressure ( $P$ ) and temperature ( $T$ ) conditions associated with the early accretion and metal-silicate differentiation of the terrestrial planets (Frost et al. 2010; Ozawa et al. 2008; Asahara et al. 2007; Rubie et al. 2004). Additionally, compositional convection in the liquid outer core likely occurs due to the partitioning of light incompatible elements at the Earth's inner core boundary (ICB) during crystallization (e.g. Gubbins, 1977;

Loper and Roberts, 1978; Deguen, 2012) and/or redox reactions between silicates and oxides at the core-mantle boundary (CMB) (e.g. Knittle and Jeanloz, 1991; Frost et al., 2010). The solubility of oxygen in liquid iron at core conditions as well as its low atomic mass makes it a prominent candidate for the light element in the core. Nevertheless, mass transport properties, such as diffusion and viscosity, of oxygen-bearing liquid iron alloys at extreme  $P$ - $T$  conditions remain poorly constrained.

The traditional Arrhenian model describes diffusion in liquid iron (Dobson, 2002) and liquid iron alloys (Dobson, 2002; Dobson and Wiedenbeck, 2002; Posner et al., 2017) well, and is given as:

$$D(P,T)=D_0\exp\left(-\frac{\Delta H+P\Delta V}{RT}\right), \quad (6.1)$$

where  $D_0$  is the pre-exponential diffusion coefficient,  $R$  is the universal gas constant, and  $\Delta H$  and  $\Delta V$  are the activation enthalpy and activation volume, respectively. Extrapolation of diffusion coefficients measured from laboratory experiments to extreme  $P$ - $T$  conditions of the Earth's core requires an accurate determination of the activation parameters in Eq. 1, which can be determined from the  $T$  and  $P$  dependences, respectively.

While early experimental data on Fe self-diffusion over the  $P$  range 2-20 GPa suggested a large dependence of  $D$  on  $P$  (Dobson, 2002), later studies on liquid iron alloys constrained the activation volume ( $\Delta V$ ) to be less than  $1.1 \text{ cm}^3 \text{ mol}^{-1}$  (Dobson and Wiedenbeck, 2002; Posner et al., 2017). Posner et al. (2017) also measured Fe self-diffusion coefficients with first principles molecular dynamic (FP-MD) simulations using Fe,  $\text{Fe}_{0.92}\text{Si}_{0.08}$ , and  $\text{Fe}_{0.92}\text{Cr}_{0.08}$  liquid compositions between 1 bar and 135 GPa and report even smaller values for  $\Delta V$  that converge to  $\sim 0.4 \text{ cm}^3 \text{ mol}^{-1}$  at high  $T$ . This small value is in agreement with results on Fe diffusivity from simulations of liquid Fe-FeO at similar conditions (Ichikawa and Tsuchiya, 2015). The small  $P$ - $T$

dependencies determined in most recent experimental and theoretical studies suggest that rates of solute diffusion in liquid iron change very little (i.e. less than an order of magnitude) along the entire geotherm of the Earth's core (Pozzo et al., 2013; Posner et al., 2017).

Oxygen diffusion in liquid iron alloys has been studied using FP-MD between  $\sim 100$  and  $\sim 350$  GPa (Alfè et al. 1999, 2002; Pozzo et al. 2013; Ichikawa and Tsuchiya, 2015), while experimental oxygen diffusion data are limited to ambient pressure (Shurygin and Kryuk, 1963; Suzuki and Mori, 1971). The simulations at high  $P$ - $T$  suggest that oxygen atoms diffuse 2-3 times faster than Fe and Si under conditions of the Earth's core. However, more work is needed to test if these findings can be reproduced experimentally. In this study, we use the experimental approach of Posner et al. (2017) to investigate the effects of  $P$  and  $T$  on oxygen diffusion in liquid iron. We use our diffusion data to (i) estimate length and timescales of metal-silicate chemical equilibration in a magma ocean scenario and (ii) constrain a maximum liquid metal droplet size that is required to achieve chemical equilibrium prior to reaching a primordial CMB.

## 6.3 Experimental procedure and analysis

### *6.3.1 Multi-anvil sample assembly and procedure*

Oxygen diffusion experiments were performed in 1200 and 5000 tonne multi-anvil presses employing  $\text{Cr}_2\text{O}_3$ -doped MgO octahedra with 18 mm edge lengths as the pressure medium and cubic tungsten carbide anvils with 11 mm truncations. The experimental conditions are listed in Table 6.1. Stepped  $\text{LaCrO}_3$  heaters were used to minimize the temperature gradient across the sample (Rubie, 1999). All diffusion couples were contained vertically within an MgO capsule with the alloy on top to maintain gravitational stability, as

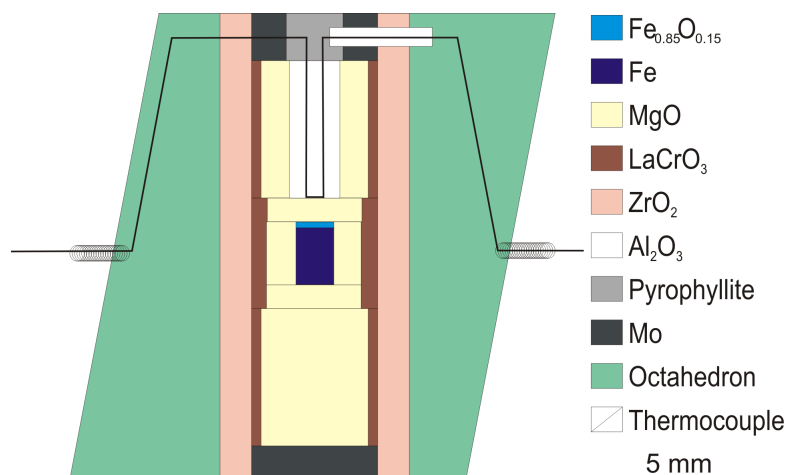


Figure 6.1: Schematic representation of 18/11 multi-anvil assembly used in the diffusion experiments. Diffusion couples were contained vertically within an MgO capsule with the alloy (light blue) on top of the pure iron (dark blue) to maintain gravitational stability. All experiments were performed by slowly compressing to the desired peak pressure at room temperature, heated to 1273 K in 600 s, maintained at this temperature for 180 s, heated rapidly at a constant ramp rate of 25-125 K s<sup>-1</sup> to the peak target temperature ( $T_f$ ), maintained at  $T_f$  for the desired time, and then quenched rapidly by shutting off the electrical power. Ambient pressure oxygen diffusion data in magnetite (Sharp, 1991; Crouch and Robertson, 1990; Gilletti and Hess, 1988) are  $\sim 10^6$  times slower than oxygen diffusion rates reported for liquid iron (Shurygin and Kryuk, 1963; Suzuki and Mori, 1971), such that any contribution to the final diffusion profile that developed below liquidus temperatures must be negligible.

shown in Figure 6.1 and described in more detail in Posner et al. (2017). A  $W_{97}Re_3$ — $W_{75}Re_{25}$  thermocouple was used with the junction positioned at the top of the MgO capsule, initially 0.8 mm from the top of the metallic sample.

Diffusion couples consisted of 1.2 mm diameter rods of iron and  $Fe_{0.85}O_{0.15}$ . Iron cylinders of 99.98% purity were machined to a length of 1.8 mm and one end was polished to a 0.25-micron finish. The alloy starting

Table 6.1: Experimental conditions and Arrhenius parameters,  $D_o$  and  $\Delta H$ , refined from the least-squares best-fit to all concentration profiles measured at each pressure. The melting temperature and peak annealing temperature and at each pressure are given as  $T_m$  and  $T_f$ , respectively. Also listed are the initial enriched concentrations ( $C_U$ ) fitted to the data according to Eq. 3, and the refined initial depleted concentrations ( $C_L$ ). Due to coupling of the fitted  $D_o$  and  $\Delta H$  values, all errors are assigned to  $\Delta H$ .

$P$ GPa	$T_m$ K (1 $\sigma$ )	$T_f$ K (1 $\sigma$ )	Heating rate (K s $^{-1}$ )	Time @ $T_f$ (s)	$C_U$ (1 $\sigma$ )	$C_L$ (1 $\sigma$ )	$D_o$ 10 $^{-7}$ m $^2$ s $^{-1}$	$\Delta H$ kJ mol $^{-1}$ (1 $\sigma$ )	$\chi_{red}^2$
3	1915(25)	1975 $\pm$ 17	50	30	2.7 $\pm$ 0.3	0.15 $\pm$ 0.02	1.2	50 $\pm$ 17	0.2405
		1978 $\pm$ 3	25	65	2.6 $\pm$ 0.3	0.17 $\pm$ 0.03			
		1988 $\pm$ 10	25	55	2.5 $\pm$ 0.3	0.12 $\pm$ 0.02			
		2028 $\pm$ 8	50	40	2.8 $\pm$ 0.3	0.18 $\pm$ 0.02			
		2060 $\pm$ 19	25	30	2.7 $\pm$ 0.3	0.14 $\pm$ 0.02			
7	2059(25)	2073 $\pm$ 13	25	60	2.4 $\pm$ 0.3	0.14 $\pm$ 0.02	8.1	84 $\pm$ 16	0.2408
		2098 $\pm$ 20	40	20	2.2 $\pm$ 0.3	0.10 $\pm$ 0.02			
		2157 $\pm$ 19	25	60	3.6 $\pm$ 0.4	0.21 $\pm$ 0.02			
		2166 $\pm$ 44	25	40	3.2 $\pm$ 0.3	0.21 $\pm$ 0.02			
		2399 $\pm$ 34	50	25	4.1 $\pm$ 0.4	0.21 $\pm$ 0.02			
18	2273(50)	2299 $\pm$ 38	125	50	1.7 $\pm$ 0.7	0.15 $\pm$ 0.02	1.8	55 $\pm$ 17	0.1472
		2531 $\pm$ 14	90	25	1.8 $\pm$ 0.3	0.11 $\pm$ 0.02			
		2532 $\pm$ 80	40	10	3.3 $\pm$ 0.3	0.17 $\pm$ 0.03			
		2630 $\pm$ 17	40	25	4.9 $\pm$ 0.1	0.20 $\pm$ 0.04			
		2643 $\pm$ 19	120	10	4.7 $\pm$ 0.3	0.25 $\pm$ 0.05			
Global Fit									
	$D_o$ (10 $^{-7}$ m $^2$ s $^{-1}$ )	2.7 $\pm$ 1.0							
	$\Delta H$ (kJ mol $^{-1}$ )	62 $\pm$ 6							
	$\Delta V$ (10 $^{-7}$ m $^3$ mol $^{-1}$ )	1.1 $\pm$ 1.1							
	$R^2$	0.972							

material for the Fe $_{0.85}$ O $_{0.15}$  disks consisted of a mixture of fine-grained (<10  $\mu$ m) high-purity metallic iron and ferric oxide powders previously dried in air at 1273 K to remove excess moisture. Powders were sintered into a solid rod in a piston-cylinder apparatus at 15 kbar and 1473 K for 5 hours. Sintered rods were carefully removed, cut into 0.2 mm thick discs and doubly polished to a 0.25-micron finish.

Experiments were performed at 3, 7, and 18 GPa by compressing slowly to the desired press load. All experiments were heated from room temperature to 1273 K in 600 s, maintained at this temperature for 180 s, and were then heated rapidly at a fixed ramp rate ( $dT/dt$ ) of 25–125 K s $^{-1}$  to the

target peak temperature ( $T_f$ ). The temperature  $T_f$  was maintained for the desired time (several tens of seconds, Table 6.1), and the sample was then quenched by shutting off the electrical power, which resulted in initial quench rates in excess of  $500 \text{ K s}^{-1}$ . The thermocouple temperature was recorded every 100 ms. No correction for the effect of pressure on thermocouple emf was applied. Quoted temperatures (1975-2643 K) and associated errors (Table 6.1) are the averages and standard deviations, respectively, of the measured values during the post-ramping stage.

### *6.3.2 Analytical procedure*

Oxygen dissolved in liquid iron is well known to exsolve to form an oxide phase upon quenching (Kato and Ringwood, 1989; Ringwood and Hibberson, 1990; O'Neill et al., 1998; Gessmann and Rubie, 1998; Kawazoe and Ohtani, 2006; Asahara et al., 2007). In the present study, quench products of low oxygen content metal typically consist of small (radius,  $r \leq \sim 1 \mu\text{m}$ ) spherical to semi-spherical oxide blobs, while quench products of higher oxygen content metal consist of a finely spaced dendritic exsolution texture, as discussed by Kawazoe and Ohtani (2006).

Recovered samples were cut and polished parallel to the cylindrical axis. Spot analyses were acquired along the full length of the diffusion couple on a line perpendicular to the diffusion interface using a JEOL-JXA-8200 electron probe micro-analyzer. The probe current and accelerating voltage were 15 kV and 50 nA, respectively, with an effective beam diameter of  $\sim 70 \mu\text{m}$ , sufficiently large to sample both matrix and exsolved inclusions. Standards used were natural hematite and pure Fe metal. Counting times were 40 s on peak and 20 s on background for oxygen, and 20 s and 10 s for iron, respectively. The standard error ranges between 5% and 15% except at

very oxygen concentrations (below  $\sim 0.15$  wt. %) where the error increases to 20-30%. Line scans were between 1549 and 1920  $\mu\text{m}$  long across the total length of the quenched sample. Due to the large beam diameter and spacing between spot analyses, it was not possible to measure the oxygen concentration at the absolute bottom of the capsule of every experiment. Analyses that overlapped with the capsule wall were excluded. At least two parallel scans were made on each sample in order to check for reproducibility and possible mechanical mixing.

### 6.3.3 Experimental data fitting and calculation of diffusion parameters

Laboratory experiments involving materials with a large diffusion coefficient, such as liquid metals, require very rapid heating rates above the melting temperature ( $T_m$ ) to minimize diffusion prior to reaching the target temperature (Dobson, 2002; Posner et al., 2017). However, such rapid heating rates in a large volume press typically result in significant overshoot of the target temperature and thermal instability. Non-isothermal annealing (i.e. when diffusion occurs during heating) can result in an overestimation of the derived diffusion coefficient if the quenched concentration profile is assumed to have formed solely at the peak temperature,  $T_f$ . Additionally, the extent of diffusion that occurs during heating increases with temperatures above  $T_m$  and, as a consequence, can also lead to an overestimation of the Arrhenian temperature dependence term,  $\Delta H$ , given as

$$\frac{\partial \ln D}{\partial (1/T)} = -\frac{\Delta H}{R} \quad (6.2)$$

The heating rate can therefore significantly influence the shape of the concentration profile upon reaching  $T_f$ , especially for temperatures significantly higher than  $T_m$ , as discussed by Posner et al. (2017). In order to correct for non-isothermal annealing, we have conducted a series of diffusion

couple experiments at each pressure using variable heating rates (25-125 K s<sup>-1</sup>), final quench temperatures and durations ( $t$ ) at  $T_f$ . Our previous study (Posner et al., 2017) showed that using a range of  $dT/dt$  values improved the accuracy of retrieved  $\Delta H$  values from the simultaneous fitting of several profiles obtained at the same pressure, as described below.

An additional challenge in modeling the  $P$ - $T$  dependence of oxygen diffusion is the fact that the solubility of oxygen in liquid iron has been shown to increase with  $T$  at fixed  $P$  (e.g. Distin et al. 1971; Asahara et al. 2007). As a consequence, the total oxygen available for transport across the diffusion couple interface changes with the peak annealing temperature. The first step of the fitting procedure involved determining the original interface location,  $x_i$ , for each concentration profile by refining this parameter together with an “effective diffusion coefficient” (that was subsequently discarded). Prior to compression, the initial thickness of the oxygen source layer was 0.2 mm, i.e., 10% of the total diffusion couple length (Figure 6.1). All retrieved values of  $x_i$  were between 0.12 and 0.16 mm, which is consistent with ~20% compressive shortening of the sample length during compression.

In the next step, quenched concentration profiles were used to estimate the total dissolved oxygen and assign an appropriate “initial enriched concentration” ( $C_U$ ) value for each individual experiment within the fitting procedure. We normalize the integral of each concentration profile to the optimized thickness of the enriched part of the diffusion couple according to:

$$C_U = \frac{1}{x_i} \int_{x_0}^{x_f} dC dx \quad , \quad (6.3)$$

where  $x_0$  and  $x_f$  are the locations of the first and last analysis points, respectively. In most experiments, the model  $C_U$  determined from Eq. 6.3 is less than the bulk FeO content of the starting material, which therefore indicates FeO saturation. Results on the total dissolved O in the experiments

are discussed in the online Supplemental Material and are included in Table 6.1. The “initial depleted concentration” ( $C_L$ ) was varied between 0.0 and 0.5 wt. % in order to minimize the root-squared error. All  $C_L$  values determined from the fit were between 0.10 – 0.25 wt. % (Table 6.1).  $C_U$  and  $C_L$  values and errors in Table 6.1 represent the average and standard deviation derived from two or three concentration curves collected across each quenched sample perpendicular to the diffusion couple interface. In all experiments, the initial concentrations at both ends of the sample changed because of diffusion, which means that the samples cannot be considered as semi-infinite reservoirs. In order to treat the samples as finite reservoirs, concentration gradients at the ends of the sample were set to zero as boundary conditions.

The final step of the fitting procedure consisted of refining  $D_o$  and  $\Delta H$  for all profiles at a given pressure simultaneously using a Crank-Nicolson finite difference approximation. Each simulation starts at  $T_m$  with  $dT/dt$ ,  $T_f$  and  $t$  at  $T_f$  specified as measured experimentally for each profile. We used a time step of 0.1 s but reducing this to 0.01 s did not affect the results. The reduced squared sum of the weighted residuals was minimized according to

$$\chi_{\text{red}}^2 = \frac{1}{u} \sum_{i=1}^n ((C_C - C_M) / \sigma_M)^2 \quad , \quad (6.4)$$

where  $u$  is the number of degrees of freedom ( $u = N - n - 1$ ), with  $N$  being the number of observations (i.e. number of data points at a given pressure),  $n$  the number of fit parameters,  $C_C$  and  $C_M$  are the wt. % concentrations of oxygen from the fit and those measured, respectively. Uncertainty on  $C_M$  ( $\sigma_M$ ) estimated from reproducibility of EPMA analyses is 0.1 wt. %. This is a conservative estimate based on the dependence of the standard error on the absolute concentration, described in Section 2.2. We use the “amoeba” algorithm (Press et al. 2002) to perform least squares regressions and

multidimensional minimization of the Arrhenius equation (Eq. 1) at constant  $P$  using the downhill simplex method (Nelder and Mead, 1965). For the fit parameters, we make  $n + 1$  initial guesses that allows for a rapid and efficient exploration of a broad parameter space. In an earlier diffusion study we found a correlation between the fits to  $D_0$  and  $\Delta H$  values (Posner et al., 2017). All errors are therefore assigned to  $\Delta H$ .

Once diffusion parameters are refined from a set of experiments at constant pressure, the pressure dependence or activation volume,  $\Delta V$ , of diffusion can be determined at constant temperature according to:

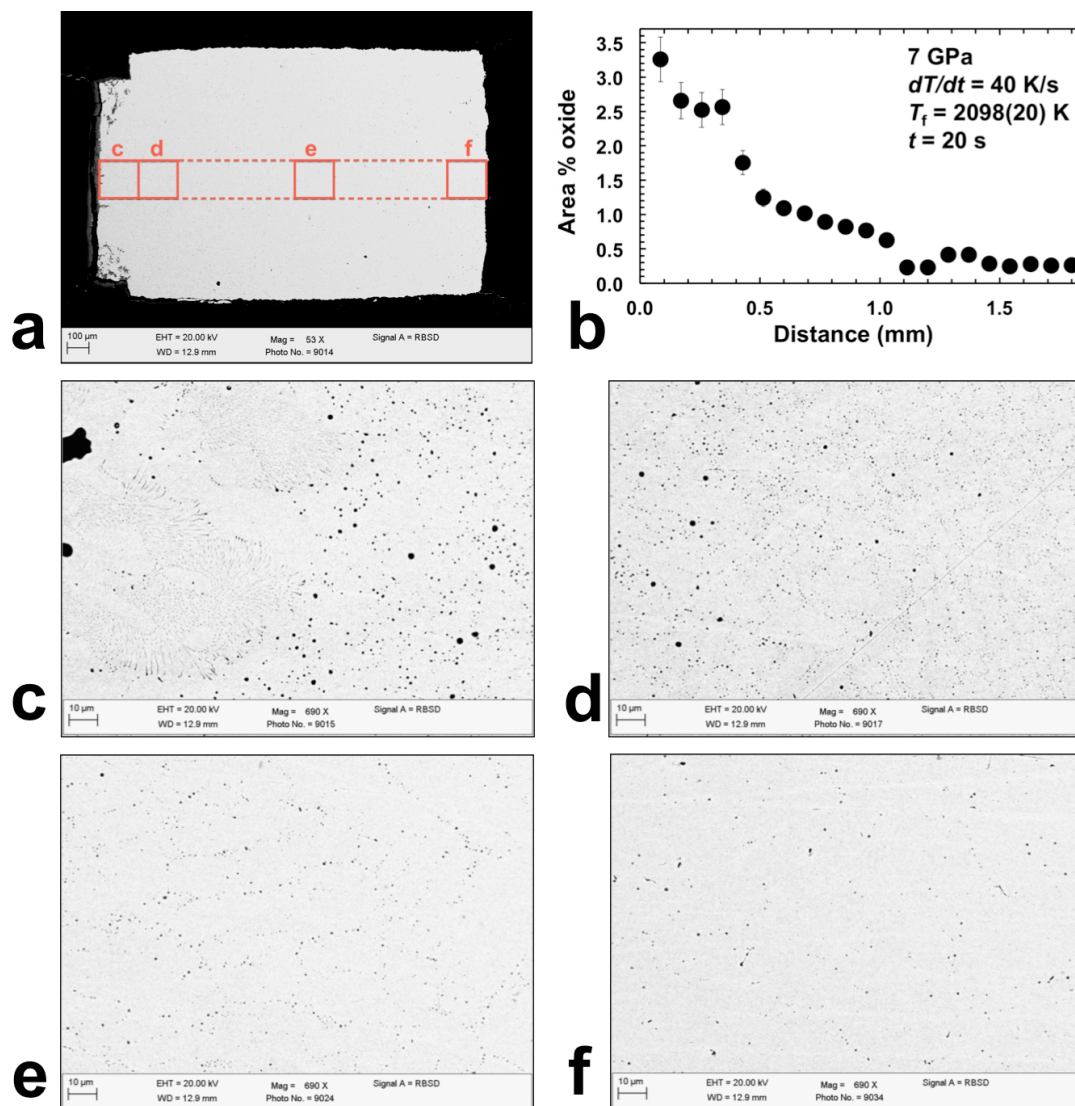
$$\frac{\partial \ln D}{\partial P} = -\frac{\Delta V}{RT} \quad . \quad (6.5)$$

The range of  $T_f$  values that is accessible in experiments between 3 and 18 GPa is limited due to a relatively steep melting curve ( $\sim 30$  K/GPa) and rapid equilibration of samples at low  $P$  and high  $T$  due to fast diffusion. The uncertainty of the temperature derivative of  $\Delta V$  determined from experiments is therefore considerably larger than values obtained from computational methods (i.e. FP-MD) in which a much wider temperature range can be explored.

## 6.4 Results

### 6.4.1 Quench products and image analysis

Quenched samples consisted mostly of an iron-rich matrix that contains small ( $\leq 1 \mu\text{m}$  diameter) oxygen-rich spheroids that form by exsolution during quench, as described in detail previously (e.g. O'Neill et al., 1998; Gessman and Rubie, 1998; Kawazoe and Ohtani, 2006). Feathery dendritic exsolution textures were also observed in some highly enriched regions (i.e. near the



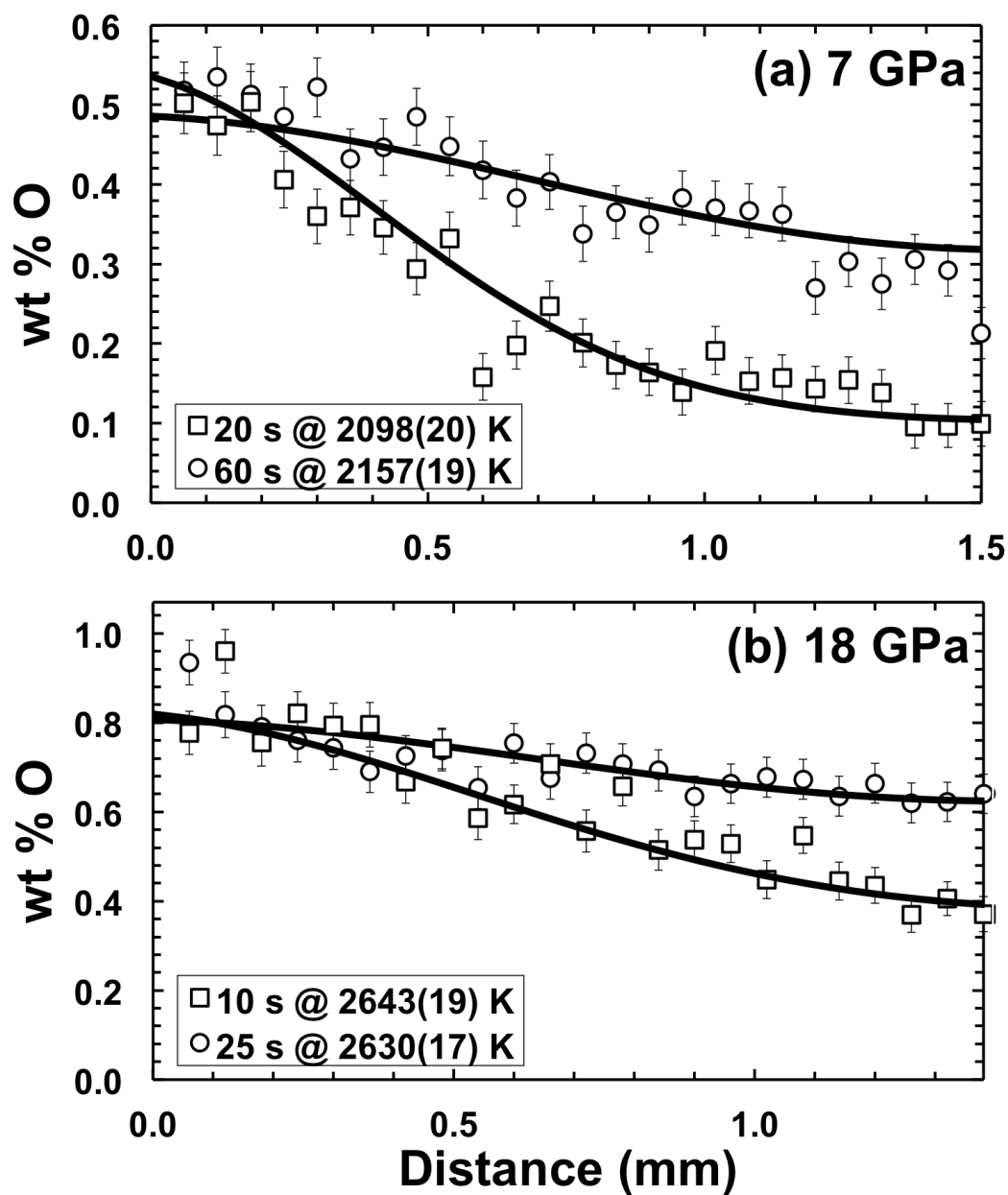
diffusion couple interface). In Figure 6.2, we show a series of back-scattered electron (BSE) images collected along a transect of quenched sample #079. This sample was annealed at 7 GPa using a heating rate ( $dT/dt$ ) of  $40 \text{ K s}^{-1}$  to  $T_f = 2098(20) \text{ K}$  and kept at  $T_f$  for 20 s. As shown in Figures 6.2c-f, the concentration of oxygen-rich spheroids visibly decreases with distance beyond the initial diffusion couple interface (left side in Figure 6.2a), verifying the preservation of an oxygen diffusion profile along the sample length during quenching. Area proportions of oxide inclusions of this sample were estimated

Figure 6.2 (opposite page): Backscattered electron (BSE) images and analysis of a quenched sample from a diffusion experiment annealed at 7 GPa and 2098(20) K for 20 seconds (#079). (a) 115  $\mu\text{m}$  x 170  $\mu\text{m}$  BSE images were collected every 60 microns along a traverse perpendicular to the diffusion couple interface. In this run, the initial  $\text{Fe}_{0.85}\text{O}_{0.15}$  disk (on the left) has a slightly smaller radius than the pure iron cylinder due to shrinkage during preparatory sintering. BSE images were converted to a binary raster and analyzed using the ImageJ software. The area percentage of dark material, consisting of exsolved oxide, in each image along the transect is shown in panel (b). (c) Exsolution textures change from feathery features or dendrites surrounding oblong grains in the vicinity of the  $\text{Fe}_{0.85}\text{O}_{0.15}$  to bimodally-sized spheroids away from the diffusion interface. (d) The concentration of large ( $\sim 1 \mu\text{m}$ ) exsolution spheroids decreases from left to right and submicron spheroids dominate on the right. (e) Exsolution spheroids are visible along grain boundaries with a marked decrease in concentration compared with previous panels. The proportion of matrix metal becomes increasingly dominant from left to right in panels (e) and (f).

using the public domain software, ImageJ (<http://imagej.nih.gov/ij/>), as shown in Figure 6.2b.

#### 6.4.2 Oxygen diffusion at high $P$ - $T$

Oxygen concentration profiles from experiments conducted at 7 and 18 GPa are shown in Figure 6.3. Concentration-distance curves show the expected time-dependent flattening of the oxygen profile for runs annealed 2-3 times longer at similar  $T_r$ . (Figure 6.3). The global least-squares best fit to five diffusion profiles at 7 GPa is shown in Figure 6.4. Refined diffusion parameters,  $D_0$  and  $\Delta H$ , determined from simultaneous fits at each pressure are listed in Table 6.1.



An Arrhenius diagram summarizing the results at each pressure is shown in Figure 6.5. Ambient pressure diffusion coefficients reported by Shurygin and Kryuk (1963) who used the rotating disc method are slightly higher than our high  $P$  dataset, while diffusivity data by Suzuki and Mori

*Figure 6.3 (opposite page): Typical diffusion profiles for two different annealing times at similar  $T_f$  showing oxygen concentration versus distance at (a) 7 GPa and (b) 18 GPa. The model fit to the data represents a solution to all experiments conducted at the respective pressure ( $n = 5$ ). Rapid chemical equilibration in the small liquid samples limited annealing times to  $\sim 90$  s for  $T_f$  when close to  $T_m$ , and  $\sim 40$  s for  $T_f + 400$  K.*

(1971) who used the capillary method, plot slightly lower. When diffusion parameters obtained from the global fit of Eq. 1 to our data are used to extrapolate to ambient conditions, they are in better agreement with the larger diffusion coefficients reported by Shurygin and Kryuk (1963); agreement with Suzuki and Mori (1971) would imply a negative activation volume. We discuss the effect of pressure in greater detail below.

#### *6.4.3 Temperature dependence of oxygen diffusion at constant pressure*

The temperature dependence of oxygen diffusion in liquid iron is small, with a best-fit value over the entire  $P$  range of  $\Delta H = 62 \pm 6$  kJ mol<sup>-1</sup> (Eq. 1). Activation enthalpies refined at each pressure do not reveal a clear trend within the range of the experiments (Table 6.1), and values overlap within error. Ambient pressure experimental  $\Delta H$  values ( $105 \pm 3$  kJ mol<sup>-1</sup>, Shurigin and Kryuk, 1963;  $81 \pm 3$  kJ mol<sup>-1</sup>, Suzuki and Mori, 1971) are most consistent with the largest  $\Delta H$  determined in the present study (at 7 GPa).

Small activation enthalpies ( $< 100$  kJ mol<sup>-1</sup>) are also consistent with previously reported high-pressure experimental values for chemical diffusion of Si and Cr in liquid iron up to 18 GPa (20-70 kJ mol<sup>-1</sup>; Posner et al., 2017), self-diffusion of Fe in liquid Fe up to 20 GPa ( $100 \pm 40$  kJ mol<sup>-1</sup>; Dobson, 2002) and liquid Fe<sub>3</sub>C up to 15 GPa ( $52 \pm 3$  kJ mol<sup>-1</sup>; Dobson and

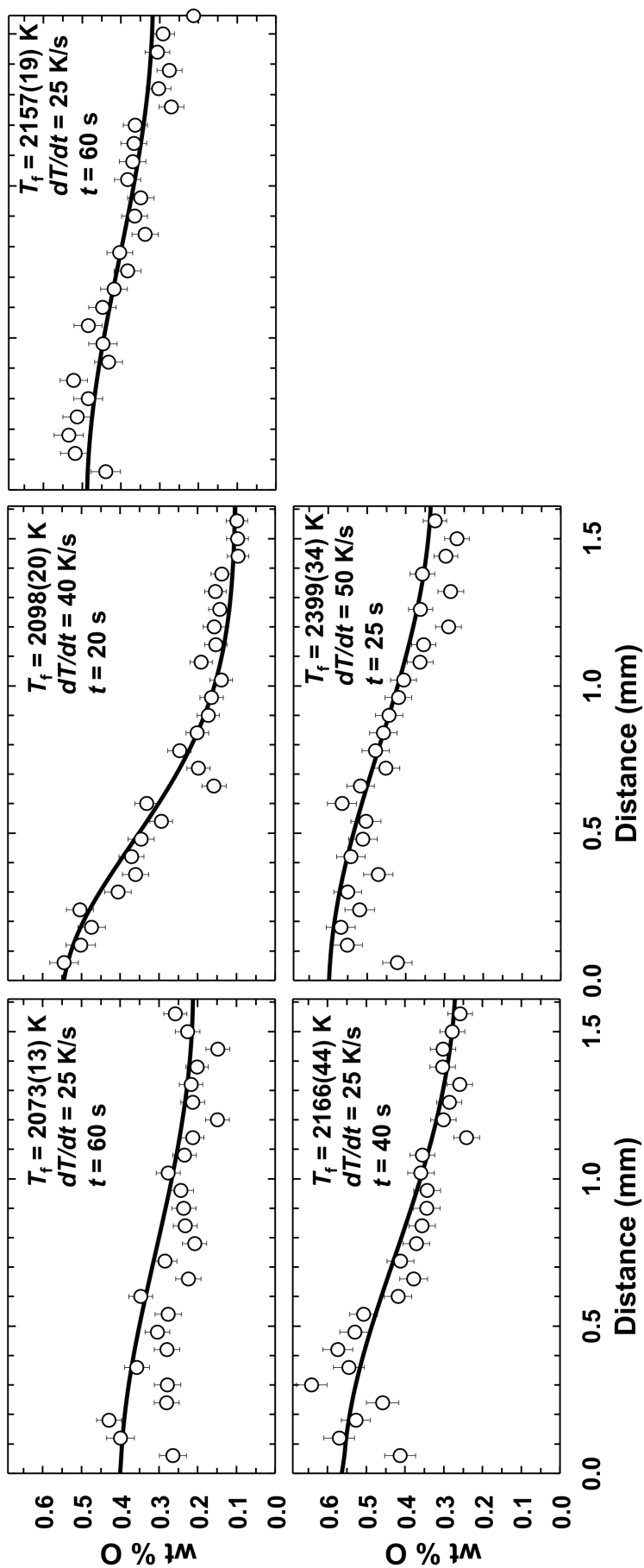


Figure 6.4 (opposite page): Oxygen diffusion profiles for all experiments conducted at 7 GPa (Table 6.1). The model fit to the data represents a global solution to five experiments at this pressure simultaneously, yielding  $D_0 = 8.1 \times 10^7 \text{ m}^2 \text{ s}^{-1}$  and  $\Delta H = 84 \pm 16 \text{ kJ mol}^{-1}$ , respectively.

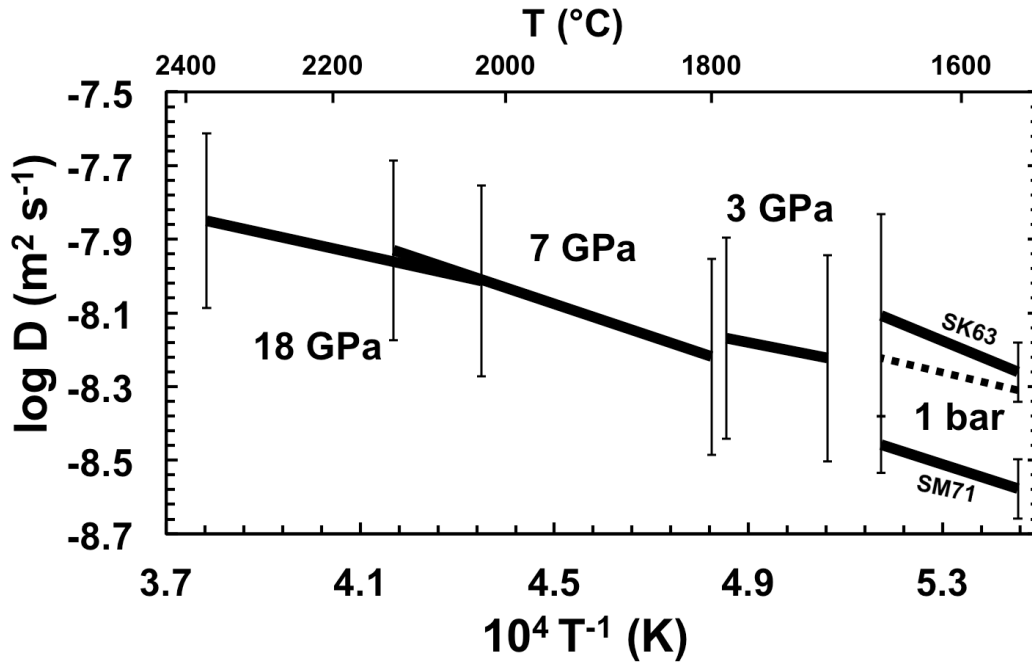


Figure 6.5 (above): Arrhenius curves of oxygen diffusion in liquid iron measured at 3, 7, and 18 GPa. Ambient pressure data by Shurygin and Kryuk (1963) and Suzuki and Mori (1971) are included. The dotted line shows the extrapolation of the 3 GPa data to 1 bar using the Arrhenius constants determined in the present study.

Wiedenbeck, 2002). Previous computational studies report a similar range of  $\Delta H$  at  $P$ - $T$  conditions of the Earth's outer core in liquid Fe-FeO (55-83 kJ mol<sup>-1</sup>; Ichikawa and Tsuchiya, 2015) and liquid Fe-Fe<sub>76</sub>H<sub>52</sub> (48-77 kJ mol<sup>-1</sup>; Umemoto and Hirose, 2015).

#### 6.4.4 Effect of pressure

Pressure has a negligible effect on the oxygen diffusion coefficient between 3 and 18 GPa. Arrhenian curves at 3, 7, and 18 GPa, determined independently from 5 experiments at each pressure, lay practically on top of one another and diffusion coefficients change by less than 0.4 log units over the full  $P$ - $T$  range of the study (Figure 6.5). The scatter of the experimental data, however, and large error bars refined from the fit procedure limits the precision of the determined activation volume. The activation volume is very small ( $\Delta V = 0.1 \pm 0.1 \text{ cm}^3 \text{ mol}^{-1}$ ). Despite the large uncertainty, this is in qualitative agreement with values reported from simulations of liquid  $\text{Fe}_{0.9}\text{O}_{0.1}$  at 100-350 GPa ( $\Delta V = 0.25 \pm 0.11 \text{ cm}^3 \text{ mol}^{-1}$ ; Ichikawa and Tsuchiya, 2015).

## 6.5 Discussion

### 6.5.1 Extrapolation to Earth's outer core

Extrapolation to  $P$ - $T$  conditions of the Earth's outer core using diffusion parameters obtained from the Arrhenian fits yield slightly faster diffusion coefficients ( $\sim 0.3$  to  $\sim 0.4$  log units) than those reported from theory (Alfè et al., 1999; Pozzo et al. 2013; Ichikawa and Tsuchiya, 2015). Considering the very wide pressure range of the extrapolation, however, and the different methodologies employed in the two separate approaches, the agreement between experiments and calculations is extremely good. The agreement also suggests that any pressure effect that may develop between 18 and 100 GPa cannot be significant. Experiments at higher pressures and/or liquid simulations at lower pressures are required to cross-check results obtained from the two methods over mutually accessible conditions.

The weak  $P$ - $T$  dependence found in this study implies that oxygen diffusion rates are nearly constant in the liquid Fe portions of any

differentiated planetary body. In the Earth's outer core we can therefore expect that  $D$  ranges between  $\sim 2 \times 10^{-8} \text{ m}^2 \text{ s}^{-1}$  and  $\sim 6 \times 10^{-8} \text{ m}^2 \text{ s}^{-1}$  for temperatures in the range 4250–6000 K. These values are nearly an order of magnitude faster than Fe self-diffusion rates in pure liquid iron (e.g. Alfè et al. 1999; Pozzo et al., 2013), Si-bearing and Cr-bearing liquid iron alloys (Posner et al., 2017), as well as Fe-Si-O liquid alloys (Pozzo et al. 2013).

Faster solute diffusivities can lower liquid viscosities ( $\eta$ ) by a factor depending on its interatomic distance,  $a$ , and concentration according to the Eyring relation:

$$\eta = \frac{k_B T}{Da} \quad (6.6)$$

where  $k_B$  is the Boltzmann constant. Average Fe-O interatomic distances reported from computations are  $\sim 20\%$  shorter than those between two Fe atoms (Pozzo et al., 2013; Ichikawa and Tsuchiya, 2015), which suggests that even very high oxygen contents ( $\sim 10 \text{ wt. } \%$ ) will have little effect on the bulk viscosity of the core because faster oxygen diffusion coefficients are balanced by smaller  $a$  (Pozzo et al. 2013; Ichikawa and Tsuchiya, 2015).

### 6.5.2 Length and timescales of chemical equilibration

The effects of  $P$  and  $T$  on the metal-silicate partition coefficient of oxygen ( $K_D^O$ ) was parameterized by Fischer et al. (2015) using experimental data obtained up to 100 GPa and 5700 K. Estimates of  $\log K_D^O$  range from approximately -1.5 at 1 bar and 1815 K to  $\sim 0.4$  at 135 GPa and 4250 K. Assuming equilibrium partitioning between liquid metal and liquid silicate, the authors conclude that the Earth's core should contain  $1.6 \pm 0.3 \text{ wt. } \%$  O and  $8.5 \pm 1.4 \text{ wt. } \%$  Si to match the density profile of the Earth's core. However, an often-overlooked factor affecting partitioning, in general, is the requirement that atoms must first diffuse to and away from the metal-silicate

interface. In a magma ocean scenario, the minimum diffusion distance required for metal-silicate equilibrium is the radius,  $r$ , of a descending body of liquid metal (i.e. droplet, diapir, or planetesimal core) (e.g. Rubie et al., 2003; Samuel, 2012).

In order to estimate maximum diffusion timescales for chemical equilibration within purely metallic bodies, we use a simple model for diffusion based on chemical potential differences alone. For simplification, gravitational forces (i.e. barodiffusion; Gubbins and Davies, 2013) and turbulent mixing within low viscosity liquid metals (Deguen et al., 2011) are presently ignored, which would decrease timescale estimates for equilibration. As such, chemical diffusion provides a “maximum equilibration timescale.”

The effect of pressure on oxygen diffusion is found to be negligible due to the very small magnitude of  $\Delta V$  established in this study and in a computational study above 100 GPa (Ichikawa and Tsuchiya, 2015). Using diffusion coefficients calculated over a range of temperatures, we can evaluate the diffusion equation in spherical geometry,

$$\frac{\partial C}{\partial t} = D \left( \frac{\partial^2 C}{\partial r^2} + \frac{2}{r} \frac{\partial C}{\partial r} \right) \quad (6.7)$$

where  $C$  is the oxygen concentration in the metal and  $r$  is the radius of the sphere. Initially ( $t = 0$ ) at  $r = a$  (the radius of the metallic sphere in contact with silicate),  $C$  is determined by the metal-silicate partition coefficient, and at  $r < a$ ,  $C = 0$ . At times smaller than or equal to the equilibration time ( $0 < t \leq t_{\text{eq}}$ ),  $\frac{\partial C}{\partial t} = 0$  at  $r = a$  and  $\frac{\partial C}{\partial t} > 0$  for  $r < a$ . Droplets are continually in contact with unequilibrated silicate liquid during descent in a magma ocean which makes diffusion in the liquid metal rate-limiting. The surrounding silicate liquid ( $r > a$ ) is therefore assumed to act as an infinite reservoir such that  $C$  at the metal-silicate interface is constant.

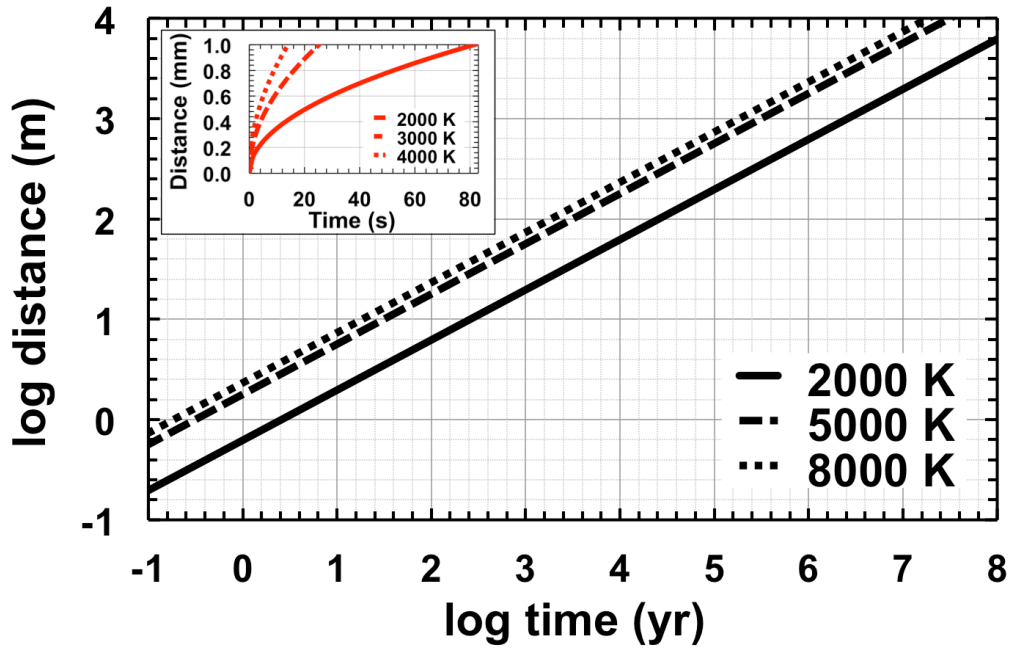


Figure 6.6: Length and timescales of chemical equilibration in a liquid metal body of radius  $r$  at constant temperature. The effect of pressure on oxygen diffusion rates is negligible due to the very small magnitude of  $\Delta V$  established in this study and in a computational study performed above 100 GPa (Ichikawa and Tsuchiya, 2015). Equilibration times for small metal droplets ( $r \leq 1$  mm), such as those in multi-anvil and diamond anvil cell experiments, are shown in the inset.

In order to calculate length and timescales of oxygen equilibration within a liquid iron droplet, we assign the initial oxygen concentration of the sphere interior ( $r < a$ ) to zero. Our results are shown in Figure 6.6 for temperatures in the range of 2000-8000 K. In the case of small liquid metal droplets ( $r < 1$  mm), such as samples in multi-anvil experiments, the chemical equilibration time is on the order of a few seconds (Figure 6.6, inset). For example, full chemical equilibration across the diffusion couple interface ( $\sim 1.8$  mm) in the present study was achieved in less than  $\sim 90$  s at near-liquidus

annealing temperatures (Figure 6.3a,b). However, in the case of much larger diffusion distances, such as in impactor cores or across boundary layers between core and mantle, the timescales are considerably longer. In our simple model, oxygen will require fractions of a year to a few years to diffuse a distance of 1 m (Figure 6.6).

### 6.5.3 Metal-silicate equilibration of oxygen in a magma ocean

The extent of chemical equilibration between descending liquid metal bodies and surrounding silicate magma during core formation is limited by the settling time ( $t_{\text{set}}$ ) of the former to reach the primordial CMB. Previous studies on the mechanisms of metal-silicate equilibration (Rubie et al., 2003; Samuel, 2012) showed that the terminal settling velocity ( $v_s$ ) of a liquid metallic body in a completely molten silicate mantle can be calculated according to

$$v_s = \sqrt{\frac{8(\rho_m - \rho_s)gr_o}{3\rho_s C_D}} \quad , \quad (6.8)$$

where  $\rho_m$  (7800 kg m<sup>-3</sup>) and  $\rho_s$  (3750 kg m<sup>-3</sup>) are the liquid metal and silicate melt densities, respectively,  $g$  is the acceleration due to gravity ( $g_{\text{Earth}} \approx 10$  m s<sup>-2</sup>;  $g_{\text{planetesimal}} \approx 0.1$  m s<sup>-2</sup>),  $r_o$  is the droplet radius, and  $C_D$  is the drag coefficient.  $C_D$  has been shown to stay fixed at  $\sim 0.3$  within the Newtonian regime of low viscosity liquids with Reynold's numbers greater than  $\sim 10^3$  (e.g. Samuel, 2012; Crowe et al., 1997). The fraction of oxygen equilibration ( $\tau$ ) within a descending metal droplet can therefore be calculated as

$$\tau^2 = \frac{1}{I_o^2} \int_{t_o}^t D(t) dt \quad . \quad (6.9)$$

For the purpose of this simple model, we assume that metal-silicate chemical exchange terminates once the droplet has reached the bottom of the magma

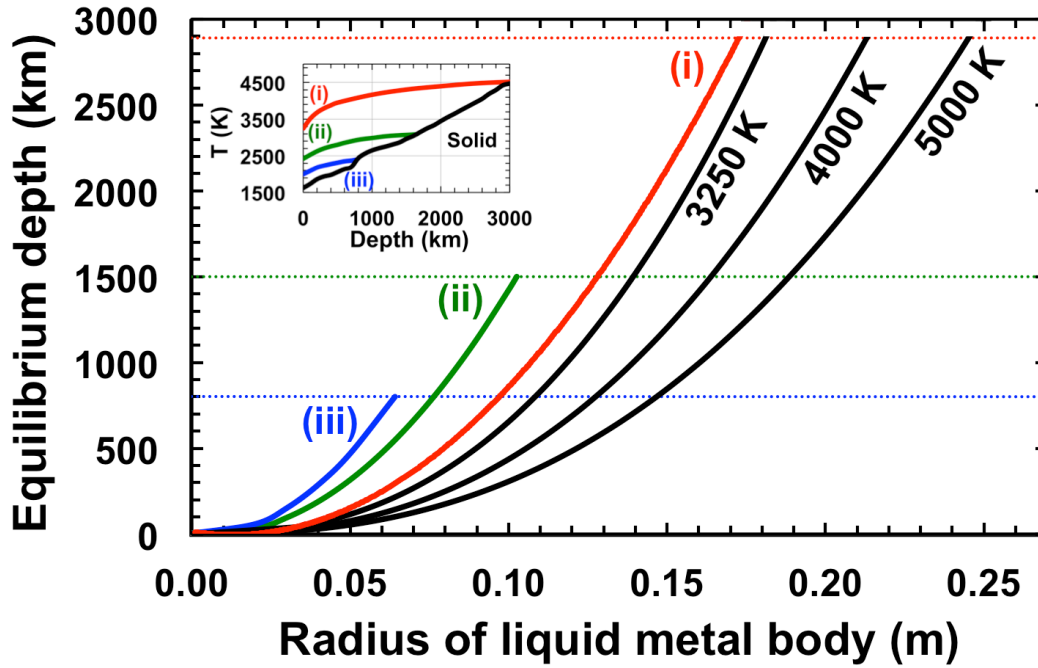


Figure 6.7: Equilibrium depths as a function of liquid metal droplet radius along isentropes (inset; Miller et al., 1991) for a magma ocean of (i) 2891 km, (ii) 1500 km, and (iii) 800 km depth. Primordial CMB depths are shown as horizontal lines of the corresponding color. Also shown are equilibrium depths for droplets along fixed isotherms (black curves). The maximum droplet radius for chemical equilibrium of oxygen between liquid metal and liquid silicate in a deep magma ocean is therefore constrained to a few tens of centimeters.

ocean, such that disequilibrium between metal and silicate is preserved if  $\tau < 1$ , (i.e.,  $t_{\text{set}} < t_{\text{eq}}$ ) and  $\tau = 1$  only when  $t_{\text{set}} \geq t_{\text{eq}}$ .

In order to evaluate  $\tau$  as a function of  $r_o$ , we use (a) magma ocean isentropes taken from shock-wave data on molten komatiite (Miller et al., 1991) to model magma ocean solidus depths of (i) 2891 km, (ii) 1500 km, and (iii) 800 km, respectively (Figure 6.7, inset), as well as (b) isotherms in the range 3250 – 5000 K. We show in Figure 6.7 that a fully equilibrated droplet

( $\tau = 1$ ) is limited to a maximum  $r_o$  of  $\sim 17$  cm in a completely molten mantle (isentropes i), while the maximum droplet radius for metal-silicate equilibration in a magma ocean of 800 km depth (isentropes iii) is even smaller ( $r_o \sim 6$  cm). Small accretionary bodies with much smaller values of  $g$  yield similar results ( $r_o < 10$  cm) owing to shallower CMB depths. Following a high temperature isotherm (i.e. 5000 K) or increasing the diffusion coefficient by an order of magnitude, due to gravitational instability and/or turbulent mixing, increases the maximum equilibrium radius by approximately a factor of 1.5 and 3.5, respectively, which is not substantial in relation to planetesimal core dimensions (several kilometers). Our finding is consistent with previous numerical models (Rubie et al., 2003; Samuel, 2012) and implies that impactor cores must have either entirely emulsified or broken up into smaller bodies of no larger than  $r \sim 0.2$  m in order to achieve chemical equilibrium with the mantle. Following fluid dynamical constraints, Rubie et al. (2003) proposed that larger droplets would break up during descent in a magma ocean. However, if large metallic bodies remained intact upon impact, then it is not kinetically feasible to achieve chemical equilibrium during core formation.

The assumption of a quasi-infinite reservoir of oxygen in the silicate surrounding a sinking metallic body and its availability as a “diffusion couple” may not be applicable to oxygen isotopic equilibration between metal and silicate. Similarly, trace element (i.e. Hf, W) equilibration timescales would be also controlled by their diffusivities in liquid silicate. Neither of these have been explored but may offer interesting perspectives on geochronometry and the terrestrial oxygen isotope composition relative to chondrites if oxygen was indeed sequestered to the early Earth’s core.

## 6.6 Conclusions

Oxygen diffusion in liquid iron has been measured experimentally at 3, 7 and 18 GPa and 1975-2643 K. The effects of pressure and temperature on the diffusion coefficient are weak with activation parameters of  $\Delta H = 62 \pm 6$  kJ mol<sup>-1</sup> and  $\Delta V = 0.1 \pm 0.1$  cm<sup>3</sup> mol<sup>-1</sup>. Extrapolation from a global fit to high pressures of the Earth's outer core yields diffusivities approximately 2 to 4 times faster than those reported from FP-MD simulations (Ichikawa and Tsuchiya, 2015; Pozzo et al. 2013). Oxygen diffusion in liquid iron is sufficiently rapid such that chemical equilibration in small liquid droplets ( $r \sim 1$  mm) would require less than 1 min even at very low magma ocean temperatures ( $\sim 2500$  K), but larger droplets ( $r > \sim 20$  cm) would remain in chemical disequilibrium upon sinking to primordial CMB depths. Slower diffusion coefficients, such as that reported for silicon (Pozzo et al., 2013; Posner et al., 2017) and likely other large siderophile elements (i.e. tungsten), further decrease the maximum droplet radius permitted for metal-silicate chemical equilibration. Additional experiments at higher pressures and/or FP-MD simulations at lower pressures are required in order to better constrain the  $P$ - $T$  derivatives of the activation parameters.

## 6.7 Acknowledgements

We would like to thank two anonymous reviewers for their helpful and constructive comments and John Brodholt for handling the manuscript. E.S.P. and D.C.R. were supported by the European Research Council (ERC) Advanced Grant "ACCRETE" (Contract No. 290568). Support was also provided by the German Science Foundation (DFG) Priority Programmes SPP1385 "The First 10 Million Years of the Solar System - a planetary materials approach" (RU1323/9-1) and SPP1488 "Planetary Magnetism"

(STE1105/10-1). We are grateful to Stefan Überhack, Heinz Fischer, Hubert Schulke and Raphael Njul for their support with sample and experimental materials preparations and Detlef Krauß for assistance with EPMA analyses. E.S.P. would like to thank Hongzhan Fei for laboratory assistance and helpful discussions on diffusion and Dmitry Druzhbin for acquiring and translating Russian references.

## 6.8 References

Alfè D., Price G.D. and Gillan M. (1999) Oxygen in the Earth's core: a first-principles study. *Phys. Earth. Planet. Inter.* **110**, 191-210.

Alfè D., Gillan M.J. and Price G.D. (2002) Composition and temperature of the Earth's core constrained by combined ab initio calculations and seismic data. *Earth Planet. Sci. Lett.* **195**, 91-98.

Allègre C.J., Poirier J.P., Humler E. and Hofmann A.W. (1995) The chemical composition of the Earth, *Earth Planet. Sci. Lett.*, **134**, 515–526.

Asahara Y., Frost D.J. and Rubie D.C. (2007) Partitioning of FeO between magnesiowüstite and liquid iron at high pressures and temperatures: Implications for the compositions of the Earth's outer core. *Earth Planet. Sci. Lett.* **257**, 435-559.

Birch F. (1952) Elasticity and constitution of the Earth's interior. *J. Geophys. Res.* **57**, 227-286.

Crouch A.G. and Robertson J. (1990) Creep and oxygen diffusion in magnetite. *Acta Metall. Mater.* **38**, 2567-2572.

Crowe C., Sommerfeld M. and Tsuji Y. (1997) Multiphase flow with droplet and particles. CRC Press, Boca Raton.

Deguen R., Olson P. and Cardin P. (2011) Experiments on turbulent metal-silicate mixing in a magma ocean. *Earth Planet. Sci. Lett.* **310**, 303-313.

Deguen R. (2012) Structure and dynamics of Earth's inner core. *Earth Planet. Sci. Lett.* **333-334**, 211-225.

Distin P.A., Whiteway S.G. and Masson C.R. (1971) Solubility of oxygen in liquid iron from 1785° to 1960°C. A new technique for the study of slag-metal equilibria. *Canadian J. of Metal. And Mat. Sci.* **10**, 13-18.

Dobson D.P. (2002) Self-diffusion in liquid Fe at high pressure. *Phys. Earth Planet. Int.* **130**, 271-284.

Dobson D.P. and Wiedenbeck M. (2002) Fe- and C-self-diffusion in liquid Fe<sub>3</sub>C to 15 GPa. *Geophys. Res. Lett.* **29**, doi:10.1029/2002GL015536.

Fischer R.A., Nakajima Y., Campbell A.J., Frost D.J., Harries D., Langenhorst F., Miyajima N., Pollok K. and Rubie D.C. (2015) High pressure metal-silicate partitioning of Ni, Co, V, Cr, Si, and O. *Geochem. Cosmochim. Acta.* **167**, 177-194.

Frost D.J., Asahara Y., Rubie D.C., Miyajima N., Dubrovinsky L.S., Holzappel C., Ohtani E., Miyahara M. and Sakai T. (2010) Partitioning of oxygen between the Earth's mantle and core. *J. Geophys. Res.* **115**, B02202. doi:10.1029/2009JB006302.

Gessman C.K. and Rubie D.C. (1998) The effect of temperature on the partitioning of nickel, cobalt, manganese, chromium, and vanadium at 9 GPa and constraints on formation of the Earth's core. *Geochim. Cosmochim. Acta* **62**, 867-882.

Giletti B.J. and Hess K.C. (1988) Oxygen diffusion in magnetite. *Earth Planet. Sci. Lett.* **89**, 115-122.

Gubbins D.J. (1977) Energetics of the Earth's core. *J. Geophysics.* **43**, 453-464.

Gubbins D. and Davies C.J. (2013) The stratified layer at the core-mantle boundary caused by barodiffusion of oxygen, sulphur and silicon. *Phys. Earth Planet. Int.* **215**, 21-28.

Ichikawa H. and Tsuchiya T. (2015) Atomic transport property of Fe-O liquid alloys in the Earth's outer core *P,T* condition. *Phys. Earth Planet. Int.* **247**, 27-35.

Kato T. and Ringwood A.E. (1989) Melting relationships in the system Fe-FeO at high pressures: implications for the composition and formation of the Earth's core. *Phys. Chem. Min.* **16**, 524-538.

Kawazoe T. and Ohtani E. (2006) Reaction between liquid iron and (Mg,Fe)SiO<sub>3</sub>-perovskite and solubilities of Si and O in molten iron at 27 GPa. *Phys. Chem. Min.* **33**, 227-234.

Knittle E. and Jeanloz R. (1991) Earth's core-mantle boundary: results from experiments at high pressures and high temperatures. *Science*. **51**, 1438-1443.

Loper D.E. and Roberts P.H. (1978) On the motion of an iron-alloy core containing a slurry. I. General theory. *Geophys. Astrophys. Fluid. Dyn.* **9**, 289-321.

McDonough W.F. (2003) Compositional model for the Earth's core. In: Carlson, R.W. (Ed.), *Treatise on Geochemistry, Vol. 2: The Mantle and Core*, ed. RW Carlson, pp. 547-68. Oxford: Elsevier-Pergamon.

Miller G.H., Stolper E.M. and Ahrens T.J. (1991) The equation of state of a molten komatiite 2. Application to komatiite petrogenesis and the Hadean Matte. *J. Geophys. Res.* **96**, 849-864.

Nelder J.A. and Mead R. (1965) A simplex method for function minimization. *Computer J.* **7**, 308-313.

O'Neill H. S. C., Canil D. and Rubie D.C. (1998) Oxide-metal equilibria to 2500°C and 25 GPa: Implications for core formation and the light component in the Earth's core, *J. Geophys. Res.*, **103**, 239-260.

Ozawa H., Hirose K., Mitome M., Bando Y., Sata N. and Ohishi Y. (2008) Chemical equilibrium between ferropericlase and molten iron to 134 GPa and implications for iron content at the bottom of the mantle. *Geophys. Res. Lett.* **35**, L05308, doi:10.1029/2007GL032648.

Poirier J.P. (1994) Light elements in the Earth's outer core: a critical review. *Phys. Earth. Planet. Inter.* **85**, 319-337.

Posner E.S., Rubie D.C., Frost D.J., Vlček V. and Steinle-Neumann G. (submitted) High P-T experiments and first principles calculations of the diffusion of Si and Cr in liquid iron. *Geochim. Cosmochim. Acta*.

Pozzo M., Davies C., Gubbins D. and Alfè D. (2013) Transport properties for liquid silicon-oxygen-iron mixtures at Earth's core conditions. *Phys. Rev. B.* **87**, DOI: 10.1103/PhysRevB.87.014110.

Press W.H., Teulolsky S.A., Vetterling W.T. and Flannery B.P. (2002) *Numerical Recipes in C++*, 2nd edition. Cambridge Univ. Press, Cambridge, pp. 413-417.

Ringwood A. E. (1977) On the composition of the core and implications for the origin of the Earth. *Geochim. Cosmochim. Acta* **11**, 111-135.

Ringwood A.E. Hibberson W. (1990) The system Fe-FeO revisited. *Phys. Chem. Minerals*, **17**, 313-319.

Rubie D.C. (1999) Characterising the sample environment in multianvil high-pressure experiments. *Phase Trans.* **68**, 431-451.

Rubie D.C., Melosh H.J., Reid J.E., Liebske C. and Righter K. (2003) Mechanisms of metal-silicate equilibration in the terrestrial magma ocean. *Earth Planet. Sci. Lett.* **205**, 239-255.

Rubie D.C., Gessman C.K. and Frost D.J. (2004) Partitioning of oxygen during core formation on the Earth and Mars. *Nature* **429**, 58-61.

Samuel H. (2012) A re-evaluation of metal diapir breakup and equilibration in terrestrial magma oceans. *Earth Planet. Sci. Lett.* **313-314**, 105-114.

Sharp Z.D. (1991) Determination of oxygen diffusion rates in magnetite from natural isotopic variations. *Geology* **19**, 653-656.

Shurygin P.M. and Kryuk V.I. (1963) Oxygen diffusion in iron and copper melts. *Izv. Akad. Nauk SSSR, Metall. Gorn. Delo.* **3**, 94.

Suzuki K. and Mori K. (1971) Diffusion of oxygen in molten iron. *J. Iron Steel Inst. Jpn.* **57**, 2219-2229.

Umemoto K. and Hirose K. (2015) Liquid iron-hydrogen alloys at outer core conditions by first-principles calculations. *Geophys. Res. Lett.* **42**, 7513-7520.

## 6.9 Supplemental Material

The Supplemental Material contains the following information:

- An extended discussion of initial enriched oxygen concentrations in diffusion experiments (associated with Figure SM6.1)
- One figure (SM6.1)

### *6.9.1 Introduction*

Initial enriched oxygen concentrations ( $C_U$ ) determined from Eq. 4 are shown in Figure SM6.1 at 3, 7, and 18 GPa as a function of peak annealing temperature ( $T_f$ ). Data points represent the average and standard deviation of two or three integrated concentration curves collected across each quenched sample perpendicular to the diffusion couple interface. Asahara et al. (2007) report a change in the sign of the pressure derivative of the equilibrium coefficient (from negative to positive) at  $\sim 10$  GPa while Ozawa et al. (2008) report the discontinuity to occur at higher  $P$  ( $\sim 38$  GPa). In our experiments, a clear pressure anomaly in oxygen solubility is not observed below 18 GPa. The possibility of such a discontinuity cannot be ruled out, however, due to the substantial scatter of our high  $P$  data. For example, two separate experiments conducted at 18 GPa and similar  $T_f$  ( $\sim 2530$  K) yield differences in dissolved oxygen contents by nearly a factor of two ( $\sim 1.8$  wt. % vs.  $\sim 3.3$  wt. %), while the 3 and 7 GPa  $C_U$  estimates are more self-consistent within the subset of data at those pressure intervals.

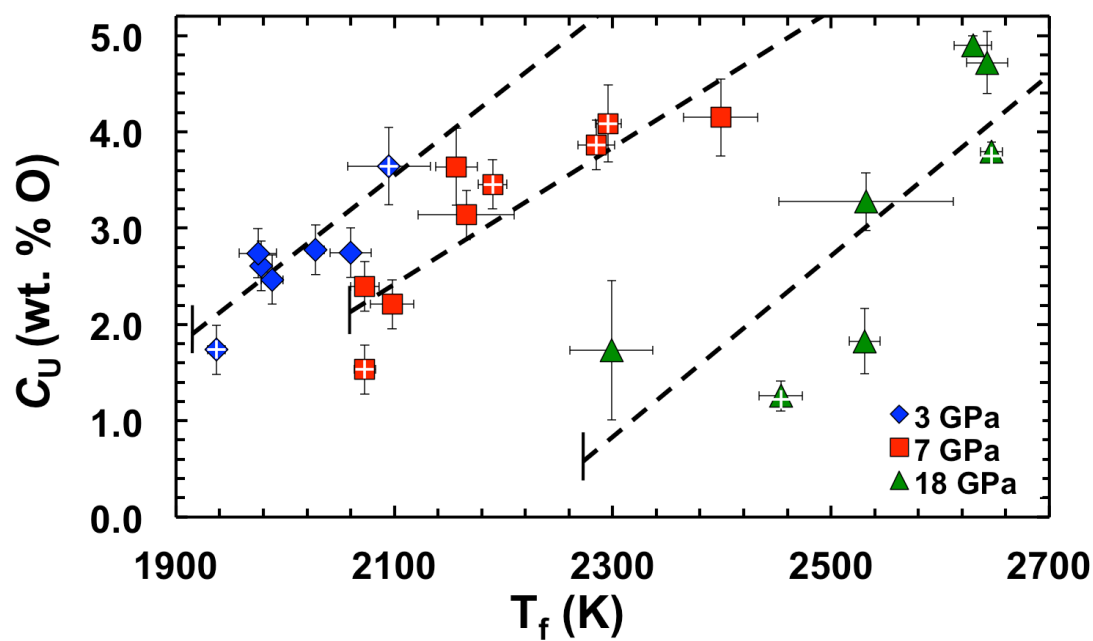


Figure SM6.1: Initial enriched oxygen contents (wt. %), estimated using Eq. 4, is shown for all experiments at 3, 7 and 18 GPa. We also show data points from equilibrated samples (white crosses inside respective labels) that were not included in the diffusion modeling. Melting temperature estimates are shown by the short vertical lines. Error bars represent  $\pm 1\sigma$ .



# Structural changes and anomalous self-diffusion of oxygen in liquid iron at high pressure

ESTHER S. POSNER<sup>1</sup>, GERD STEINLE-NEUMANN<sup>1</sup>, VOJTĚCH VLČEK<sup>1,2,3</sup>, DAVID C. RUBIE<sup>1</sup>

Accepted for publication in *Geophysical Research Letters*

## 7.1 Abstract

We report structural properties and diffusivity of liquid  $\text{Fe}_{0.96}\text{O}_{0.04}$  over a density range of 5.421-11.620  $\text{g}\cdot\text{cm}^{-3}$ , corresponding to a pressure range of 0-330 GPa, and 2200-5500 K, using first-principles molecular dynamics. We predict a change in compression mechanism near 8  $\text{g}\cdot\text{cm}^{-3}$ . At lower density, Fe and O coordinations increase from  $\sim 10$  to  $\sim 13$  and  $\sim 3$  to  $\sim 6$ , respectively, the average Fe-O distance increases from  $\sim 1.81$  Å to  $\sim 1.88$  Å, and the Fe-Fe distance remains essentially constant. Calculated oxygen diffusivities,  $D_{\text{O}}$ , remain constant over the corresponding pressure range, consistent with experiments. For larger densities, interatomic distances and diffusion rates for both species decrease monotonically. Oxygen coordination reaches a maximum

---

<sup>1</sup> Bayerisches Geoinstitut, Universität Bayreuth, 95440 Bayreuth, Germany

<sup>2</sup> Fritz Haber Center for Molecular Dynamics, Institute of Chemistry, The Hebrew University of Jerusalem, Jerusalem 91904, Israel

<sup>3</sup> now at: Department of Chemistry and Biochemistry, University of California, Los Angeles, CA 90095, USA

of  $\sim 8.5$  at  $\sim 9.4 \text{ g}\cdot\text{cm}^{-3}$ , indicating a local B2 packing for Fe around O under conditions of the Earth's core. The pressure-induced structural change provides an explanation for a previously reported change in pressure dependence of oxygen solubility in liquid iron.

## 7.2 Introduction

The Earth's outer core is a liquid iron-rich alloy containing some nickel and several weight percent of elements lighter than iron (Birch, 1952). The light element component is likely a combination of silicon, oxygen, carbon, sulfur, nitrogen, and/or hydrogen (e.g. Poirier, 1994; Allègre et al., 1995; McDonough, 2003), although there is extensive disagreement about species proportions and properties (e.g. Siebert et al., 2013; Fischer et al., 2015; Rubie et al., 2015). The nature and behavior of relevant light element species in liquid iron at high pressures ( $P$ ) and temperatures ( $T$ ) therefore have important implications for the transport properties and buoyancy of core liquids, as well as the composition of the solid inner core, fractional crystallization and associated compositional convection processes that drive the geodynamo. However, the effects of  $P$  and  $T$  on the nature/mechanism of light element incorporation in liquid iron, which is required for modeling the formation and thus the composition of the core, remain poorly understood.

Metallurgical studies reveal that liquid metals generally possess a short-range order reminiscent of the structure of the solid state coexisting with the liquid (e.g. Campbell, 2008). Liquid iron has been shown to be close-packed (cp) between 27-58 GPa in experiments (Shen et al, 2004) and between 135-330 GPa in computations (Vočadlo et al., 1997). Shen et al. (2004) argued against a possible structural change below 27 GPa based on the similarity of

their high pressure data with the ambient pressure structure factor (Waseda and Suzuki, 1970; Waseda and Ohtani, 1974), although the latter studies report a much lower coordination number (9.0 – 10.8) than expected for a cp liquid ( $\geq 12$ ). In contrast to Shen et al. (2004), Sanloup et al. (2000) and Shibazaki et al. (2015) report a structural change in liquid Fe and liquid Fe-3.5 wt. % C, respectively, from a body centered cubic (bcc) to a combination of bcc and face-centered cubic (fcc), near the bcc-fcc-liquid triple point.

It is well known that mass transport properties, such as diffusivity and viscosity, are sensitive to structural properties of liquids and can therefore be used as ‘tracers’ for the liquid structure. For example, recent first-principles molecular dynamic (FP-MD) simulations at high  $P$ - $T$  reveal that the diffusion properties of silicon and the iron-silicon partial radial distribution function (RDF) in liquid iron are similar to those of iron itself (Pozzo et al., 2013; Posner et al., 2017a), while oxygen diffuses several times faster and its atomic diameter is predicted to be smaller by 1/5 (Alfè et al., 1999; Pozzo et al., 2013; Ichikawa and Tsuchiya, 2015). Additionally, experiments and computations on the diffusivities of Si and Fe show the expected behavior of a reasonably strong pressure dependence, as expressed through their activation volumes, ( $\Delta V \sim 0.4 \text{ cm}^3 \text{ mol}^{-1}$ ; Posner et al., 2017a), defined as

$$\frac{\partial \ln D}{\partial P} = -\frac{\Delta V}{RT} \quad , \quad (7.1)$$

where  $D$  is the diffusion coefficient and  $R$  is the universal gas constant. By contrast, oxygen diffusion experiments up to 18 GPa show a negligible pressure effect ( $\Delta V = 0.1 \pm 0.1 \text{ cm}^3 \text{ mol}^{-1}$ ; Posner et al., 2017b) and a computational study on the transport and structural properties of Fe-FeO liquids report only a slightly larger pressure effect ( $\Delta V \sim 0.3 \text{ cm}^3 \text{ mol}^{-1}$ ; Ichikawa and Tsuchiya, 2015). However, the simulations were conducted at

pressures above 100 GPa only, which is far beyond the pressure range accessible in the experiments and therefore provide little basis for a reasonable comparison.

Incorporation of an alloying atom in solid metal is ‘stable’ if its radius is (i) similar to that of the framework atom (i.e. iron) and it can therefore be directly substituted or (ii) similar to or smaller than that of a framework void and can therefore be incorporated interstitially. Two different interstitial void polyhedra exist within bcc and cp systems (tetrahedral and octahedral) although their relative sizes differ. A cp structure contains small tetrahedral voids and larger octahedral voids while the opposite is true for bcc-structural voids, where both of these are strongly distorted. Alloy incorporation in either packing arrangement is ‘unstable’ if local stresses caused by size mismatch significantly disrupt the local structure. If strain exceeds a certain value, the solution becomes unstable and transforms into different structures upon quenching (e.g. O’Neill et al., 1998). For liquids with related structures, one can expect similar mechanisms to operate. Ozawa et al. (2011) observed a B1 to B2 phase transition in crystalline FeO above 235 GPa and 3840 K and predicted a similar change to occur in the liquid at comparable or slightly lower pressures. Unfortunately, structure factors obtained using *in-situ* X-ray diffraction are very challenging to obtain for large wave numbers that correspond to the short-range interaction and for multicomponent liquids at high  $P$ . For multi-component systems, they require *a priori* assumptions of pair interactions in order to quantify the local coordination environments, which remain poorly constrained.

Experimental studies have reported a change from a negative to a positive pressure dependence of the equilibrium partitioning of FeO between liquid iron and ferropericlase (Asahara et al., 2007; Ozawa et al., 2008; Frost

et al., 2010), although the exact conditions of the discontinuity remain uncertain, ranging between  $\sim 10$  GPa (Asahara et al., 2007) and  $\sim 38$  GPa (Ozawa et al., 2008). In these studies, the solubility of oxygen in liquid iron was found to decrease to a minimum and then increase (Asahara et al., 2007; Frost et al., 2010) or show a discontinuous  $P$ -effect (Ozawa et al. 2008). Such anomalies have been attributed to changes in excess free energy or liquid structure properties, both of which are challenging to determine precisely from experiments at high pressure. However, pressure-induced coordination changes of small (i.e. non-framework) atoms have been used to explain anomalous pressure-dependencies of the viscosity of liquids of ionic and covalent bonding types such as KCl (Kono et al., 2013), As-S (Brazhkin et al., 2009),  $B_2O_3$  (Brazhkin et al., 2010) and a wide range of silicate melt compositions (e.g. Angel et al., 1982; Liebske et al., 2005; Wang et al., 2014; Ni et al., 2015). Analogously, changes in the incorporation mechanism or coordination of oxygen in liquid iron under compression could explain its anomalous solubility and partitioning behavior. In order to bridge the gap between low pressure experiments and high pressure calculations and to better understand the behavior of oxygen in core-forming liquids, we have determined structural and mass transport properties of liquid  $Fe_{0.96}O_{0.04}$  using FP-MD over a wide density range corresponding to pressures from 0 to 330 GPa and temperatures from 2200 to 5500 K.

### 7.3 Computational methods

Molecular dynamics simulations have been performed in the canonical ( $N$ - $V$ - $T$ ) ensemble using the Vienna *ab-initio* simulation package (VASP) (Kresse and Furthmüller, 1996), with the temperature controlled by a Nosé–

Hoover thermostat (Anderson, 1980) and a time step of 1 fs. Calculations of energy and forces are based on density functional theory (DFT) with exchange and correlation potentials represented by the generalized gradient approximation (GGA) (Perdew et al., 1996). Valence electron states are expanded into plane waves with a cutoff energy of 550 eV in the projected augmented wave (PAW) method (Kresse and Joubert, 1999). The PAW atomic files for Fe and O have the  $4s^13d^7$  and  $2s^22p^4$  valence electronic configurations, respectively. Additional runs were performed with a  $3p^64s^13d^7$  valence configuration for Fe: self-diffusion coefficients and structural properties using either electronic configuration were found to be identical within error of the calculation.

In our simulations, Fe supercells of 150 atoms are overheated to induce melting and compressed to volumes along several isobars (1 bar – 330 GPa) using the thermodynamic model of Lu et al. (2005a, 2005b). We changed the composition in the cell by substituting 6 atoms of Fe by O, equating to 4 atomic percent (1.2 wt. %), keeping the volume of the simulation cell fixed. Densities of the simulations are listed along with the corresponding pressure (for pure Fe) and temperature in Table 7.1. Computations were performed for at least four different temperatures, with 300 K spacings, at each pressure (Table 7.1). Three additional simulations at 5200 K were conducted at densities corresponding to pressures of approximately 210, 270 and 330 GPa in order to compare our results with previously reported FP-MD simulations under conditions of the Earth’s core (Pozzo et al., 2013; Ichikawa and Tsuchiya, 2015). As in previous computational studies on liquid iron alloys (e.g. deKoker et al., 2012; Pozzo et al., 2013), the Brillouin-zone integration was performed using the  $\Gamma$ -point only. Simulations were run for at least 29 ps in order to obtain good statistics for the evaluation of the fluctuation formula

to determine diffusivities (see below) and RDF. The first 2 ps were discarded to allow for equilibration.

## 7.4 Results and discussion

### 7.4.1 Structural properties

Structural properties were investigated by analyzing the partial radial distribution functions (RDF),  $g_{\text{FeFe}}(r)$ ,  $g_{\text{FeO}}(r)$ , and  $g_{\text{OO}}(r)$ . The partial RDF,  $g_{ab}(r)$ , is defined such that, when considering an atom of species  $a$ , the probability of finding an atom of species  $b$  in a spherical shell  $(r, r + dr)$  is  $4\pi r^2 \rho_b g_{ab}(r) dr$ , where  $\rho_b = X_b/V$  is the number density of species  $b$  with mole fraction  $X_b$ , and  $V$  is the volume per atom. The coordination number,  $N_{ab}^c$ , or the average number of nearest neighbors of species  $b$  surrounding an atom of species  $a$  from the integration of the first RDF peak, was calculated following

$$N_{ab}^c = 4\pi \rho_b \int_0^{r_{ab}^c} r^2 g_{ab}(r) dr \quad , \quad (7.2)$$

where  $r_{ab}^c$  is the position of the minimum after the first peak of  $g_{ab}$  (Figure 7.1). The very low oxygen contents in our study (i.e. 6 oxygen atoms out of 150 total atoms) result in very small contributions of oxygen to the total coordination of either species, where  $[N_{aO}^c / (N_{aO}^c + N_{aFe}^c)] < 0.03$ . Additionally, average O-O distances at low densities are significantly larger than the packing environment defined by nearest iron neighbors (i.e.  $r_{OO}^c \gg r_{FeFe}^c$ ) and as a consequence, the calculation of  $N_{OO}^c$  under these conditions does not yield meaningful results. As the contribution of  $N_{aO}^c$  is practically negligible, its exclusion does not affect the overall result.

Table 7.1: Simulation conditions for the MD computations (temperature,  $T$ , and density,  $\rho$ ) as obtained from a  $P$ - $T$ - $\rho$  equation of state by Lu et al. (2005a, 2005b). Self-diffusion coefficients computed for iron ( $D_{\text{Fe}}$ ) and oxygen ( $D_{\text{O}}$ ) and average iron-iron ( $\bar{r}_{\text{FeFe}}$ ) and iron-oxygen ( $\bar{r}_{\text{FeO}}$ ) distances computed from FP-MD simulations according to Eq. 7.2 and the distance to the first peak of the radial pair distribution function, respectively.

$P$ GPa	$T$ K	$\rho$ g cm <sup>-3</sup>	$D_{\text{Fe}}$ 10 <sup>-8</sup> m <sup>2</sup> s <sup>-1</sup>	$D_{\text{O}}$ 10 <sup>-8</sup> m <sup>2</sup> s <sup>-1</sup>	$\bar{r}_{\text{FeFe}}$ 10 <sup>-10</sup> m	$\bar{r}_{\text{FeO}}$ 10 <sup>-10</sup> m
0.0001	2200	6.563	1.02(1)	1.3(1)	2.40(1)	1.85(1)
0.0001	2500	6.372	1.29(1)	1.6(1)	2.38(1)	1.83(1)
0.0001	2800	6.181	1.70(2)	2.3(1)	2.38(1)	1.83(1)
0.0001	3100	5.990	2.09(1)	3.0(2)	2.38(1)	1.83(1)
0.0001	3400	5.800	2.58(2)	3.3(4)	2.38(1)	1.82(1)
0.0001	3700	5.610	2.97(5)	3.9(3)	2.37(1)	1.82(1)
0.0001	4000	5.421	3.35(11)	4.0(5)	2.35(1)	1.81(1)
5	2500	6.828	1.29(1)	2.0(1)	2.40(1)	1.85(1)
5	2800	6.657	1.69(2)	2.8(1)	2.39(1)	1.85(1)
5	3100	6.483	2.05(2)	3.3(1)	2.39(1)	1.85(1)
5	3400	6.307	2.46(2)	3.9(2)	2.38(1)	1.85(1)
7	2500	6.972	1.21(1)	2.1(1)	2.39(1)	1.87(1)
7	2800	6.806	1.55(1)	2.6(1)	2.39(1)	1.87(1)
7	3100	6.637	1.92(1)	3.1(2)	2.39(1)	1.87(1)
7	3400	6.465	2.37(3)	3.7(2)	2.38(1)	1.87(1)
7	3700	6.290	2.69(3)	3.8(8)	2.39(1)	1.86(1)
7	4000	6.113	3.09(6)	4.5(6)	2.37(1)	1.86(1)
10	2500	7.164	1.08(1)	2.0(1)	2.40(1)	1.86(1)
10	2800	7.005	1.40(1)	2.6(1)	2.39(1)	1.86(1)
10	3100	6.841	1.76(1)	2.8(1)	2.39(1)	1.87(1)
10	3400	6.673	2.14(1)	3.8(3)	2.38(1)	1.87(1)
15	2500	7.435	0.92(1)	2.1(1)	2.40(1)	1.86(1)
15	2800	7.286	1.42(3)	2.5(2)	2.38(1)	1.88(1)
15	3100	7.130	1.47(1)	2.9(2)	2.38(1)	1.88(1)
15	3400	6.968	1.82(1)	3.3(4)	2.38(1)	1.87(1)
15	3700	6.801	2.18(3)	3.9(5)	2.36(1)	1.86(1)
25	2500	7.870	0.68(1)	1.7(1)	2.37(1)	1.88(1)
25	2800	7.735	0.92(1)	2.3(1)	2.37(1)	1.87(1)
25	3100	7.591	1.20(1)	2.5(2)	2.37(1)	1.88(1)
25	3400	7.439	1.51(1)	3.0(3)	2.37(1)	1.86(1)
35	3400	7.817	1.29(2)	2.8(2)	2.35(1)	1.88(1)
35	3700	7.662	1.51(1)	3.6(2)	2.35(1)	1.87(1)
35	4000	7.497	1.85(1)	3.4(4)	2.34(1)	1.87(1)
35	4300	7.324	2.15(3)	3.8(5)	2.34(1)	1.87(1)
60	3700	8.411	1.07(1)	2.6(1)	2.31(1)	1.86(1)
60	4000	8.254	1.35(1)	2.9(3)	2.31(1)	1.86(1)
60	4300	8.084	1.54(2)	3.0(3)	2.32(1)	1.87(1)

Table 7.1 cont'd

60	4600	7.901	1.89(3)	3.6(6)	2.32(1)	1.85(1)
85	4000	8.848	0.97(1)	2.7(1)	2.29(1)	1.87(1)
85	4300	8.682	1.25(1)	2.7(2)	2.29(1)	1.87(1)
85	4600	8.500	1.46(1)	3.2(3)	2.30(1)	1.87(1)
85	4900	8.302	1.78(1)	3.7(6)	2.30(1)	1.87(1)
110	4300	9.190	0.98(1)	2.5(2)	2.25(1)	1.85(1)
110	4600	9.009	1.18(1)	2.9(1)	2.27(1)	1.86(1)
110	4900	8.809	1.47(1)	3.0(2)	2.27(1)	1.86(1)
110	5200	8.592	1.72(1)	3.5(3)	2.28(1)	1.87(1)
135	4600	9.460	1.00(1)	2.4(1)	2.24(1)	1.85(1)
135	4900	9.259	1.24(1)	2.7(2)	2.25(1)	1.85(1)
135	5200	9.038	1.50(1)	2.9(3)	2.26(1)	1.85(1)
135	5500	8.799	1.68(2)	3.3(4)	2.26(1)	1.87(1)
210	5200	10.171	0.99(1)	2.3(1)	2.20(1)	1.82(1)
270	5200	10.943	0.71(1)	1.8(1)	2.16(1)	1.80(1)
330	5200	11.620	0.58(1)	1.5(1)	2.13(1)	1.78(1)

Partial RDFs for all species in liquid  $\text{Fe}_{0.96}\text{O}_{0.04}$  are shown in Figures 7.1a and 7.1b at the smallest ( $5.421 \text{ g cm}^{-3}$ ) and largest ( $11.620 \text{ g cm}^{-3}$ ) density simulations, corresponding to approximate  $P$ - $T$  conditions of 1 bar and 4000 K, and 330 GPa and 5200 K, respectively. In all simulations, the average Fe-O nearest neighbor distance ( $\bar{r}_{\text{FeO}}$ ) as obtained from the principle peak position of  $g_{\text{FeO}}(r)$ , is approximately 17% - 23% smaller than that of  $g_{\text{FeFe}}(r)$ , with the difference decreasing with density. RDFs from simulations for two volumes/densities at 2500 K and 4000 K are shown in Figures 7.1c and 7.1d, respectively, and are discussed in greater detail below.

Average distances between nearest neighboring atoms ( $\bar{r}$ ) are listed in Table 7.1 and shown in Figures 7.2a and 7.2b alongside previously reported interatomic distances for pure liquid iron (Alfè et al, 2000; Ichikawa and Tsuchiya, 2015; Posner et al., 2017a) and liquid iron alloys (Alfè et al., 1999; Pozzo et al., 2013; Ichikawa and Tsuchiya, 2015; Posner et al., 2017a). As can be seen in Figure 7.2a, the molar volume and compressibility of iron is insensitive to solute species (O and/or Si) and concentration ( $0.67 \leq X_{\text{Fe}} \leq 1$ ).

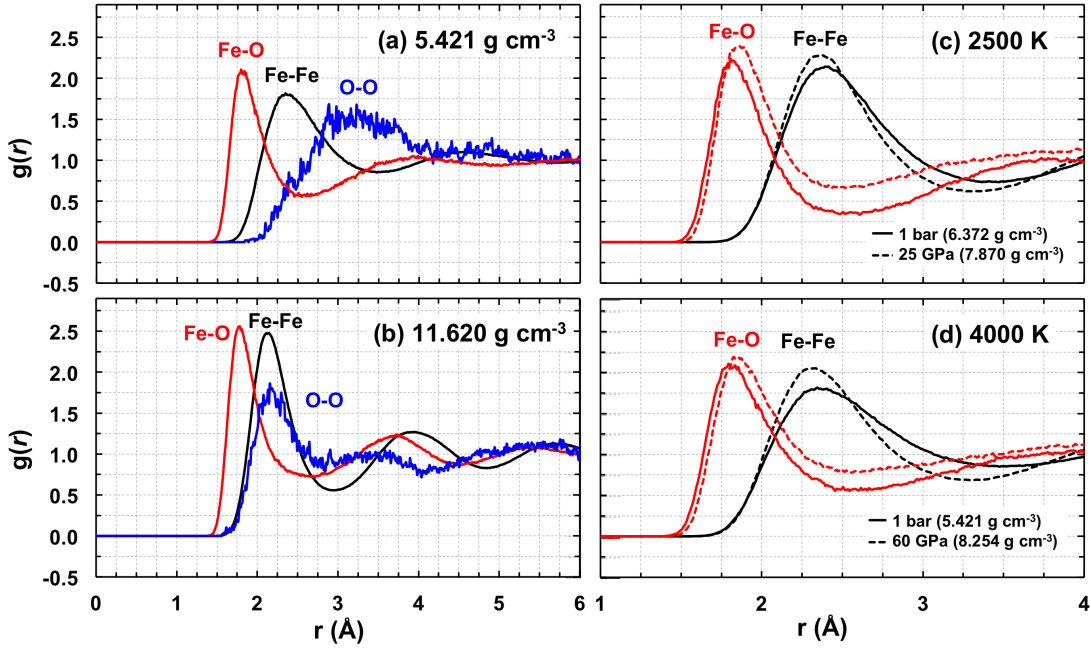


Figure 7.1: Partial radial distribution functions for liquid  $Fe_{0.96}O_{0.04}$  at densities corresponding to approximately (a) 1 bar and 4000 K and (b) 330 GPa and 5200 K. In all simulations, the average Fe-O nearest neighbor distance (red curves), as given by the position of the principle peak, is approximately 17% - 23% smaller than the iron-iron nearest neighbor distance (black curves), with the difference decreasing with density (see also Figure 7.6). Panels (c) and (d) illustrate the anomalous compression behavior at 2500 K and 4000 K, respectively; along both isotherms, the principle peak position of  $g_{FeFe}(r)$  shifts to lower  $r$  with increasing density, while that of  $g_{FeO}(r)$  shifts to larger  $r$ . A comparison of  $g_{FeFe}(r)$  and  $g_{FeO}(r)$  peak positions are shown in Figures 7.2a and 2b as a function of  $\rho$  and their ratios in Figure 7.6. The decrease in  $g_{FeO}(r)$  peak position with increasing density and constant  $T$  is attributed to an increase in the average coordination of oxygen atoms (Figure 7.2c).

Results between  $\sim 5.4 \text{ g cm}^{-3}$  and  $\sim 8 \text{ g cm}^{-3}$  show only small variations in  $\bar{r}_{FeFe}$  ( $\sim 2.38 \text{ \AA}$ ) (Figure 7.2a) while the average coordination number of iron,  $N_{FeFe}^c$ , increases from  $\sim 10.2$  to  $\sim 12.6$  (Figure 7.2c). This implies that liquid compression is dominated by closer packing over this density interval, in

agreement with the low pressure structural change from bcc-like to a combination of bcc-like + fcc-like reported for liquid Fe (Sanloup et al., 2000) and liquid Fe-3.5 wt.% C (Shibazaki et al., 2015).  $N_{\text{FeFe}}^c$  remains approximately constant ( $\sim 13$ ) as a cp liquid above  $\sim 8 \text{ g cm}^{-3}$  and compression is accommodated by a monotonic decrease of  $\bar{r}_{\text{FeFe}}$  to  $\sim 2.1 \text{ \AA}$  at the highest density considered.

Over the same density interval in which Fe approaches close-packing,  $\bar{r}_{\text{FeO}}$  increases from  $\sim 1.81 \text{ \AA}$  to a maximum of  $\sim 1.88 \text{ \AA}$  (Figure 7.2b), accompanied by an increase in oxygen coordination,  $N_{\text{OFe}}^c$ , from  $\sim 3.4$  to  $\sim 6$  (Figure 7.2c). This implies a change in the dominant oxygen incorporation mechanism from tetrahedral voids in the bcc-type liquid to octahedral voids in the cp liquid. Brazhkin et al. (2010) reported a similar observation from high  $P$  experiments on liquid  $\text{B}_2\text{O}_3$ , where an increase in the position of the first RDF peak was found to correspond to an increase in B coordination with pressure. This observation is supported in Figures 1c and 1d with a reduction of  $\bar{r}_{\text{FeFe}}$  with density at fixed  $T$  as expected from the compression of hard spheres, while  $\bar{r}_{\text{FeO}}$  from the same simulations increases.

Above  $\sim 8 \text{ g cm}^{-3}$ ,  $\bar{r}_{\text{FeO}}$  decreases monotonically to  $\sim 1.78 \text{ \AA}$  at  $11.620 \text{ g cm}^{-3}$ . Fe-O distances reported for liquid  $\text{Fe}_{0.9}\text{O}_{0.1}$  (Ichikawa and Tsuchiya, 2015) show that this trend continues to at least  $12.8 \text{ g cm}^{-3}$  (Figure 7.2b). Oxygen coordination increases to  $\sim 9$  at  $\sim 9.5 \text{ g cm}^{-3}$  and remains constant upon further compression, corresponding to mixed substitutional and octahedral interstitial incorporation. Within the cp liquid regime (i.e.,  $\gtrsim 8 \text{ g cm}^{-3}$ ),  $\bar{r}_{\text{FeFe}}$  decreases linearly with density approximately 2.5 times faster than the decrease of  $\bar{r}_{\text{FeO}}$ .

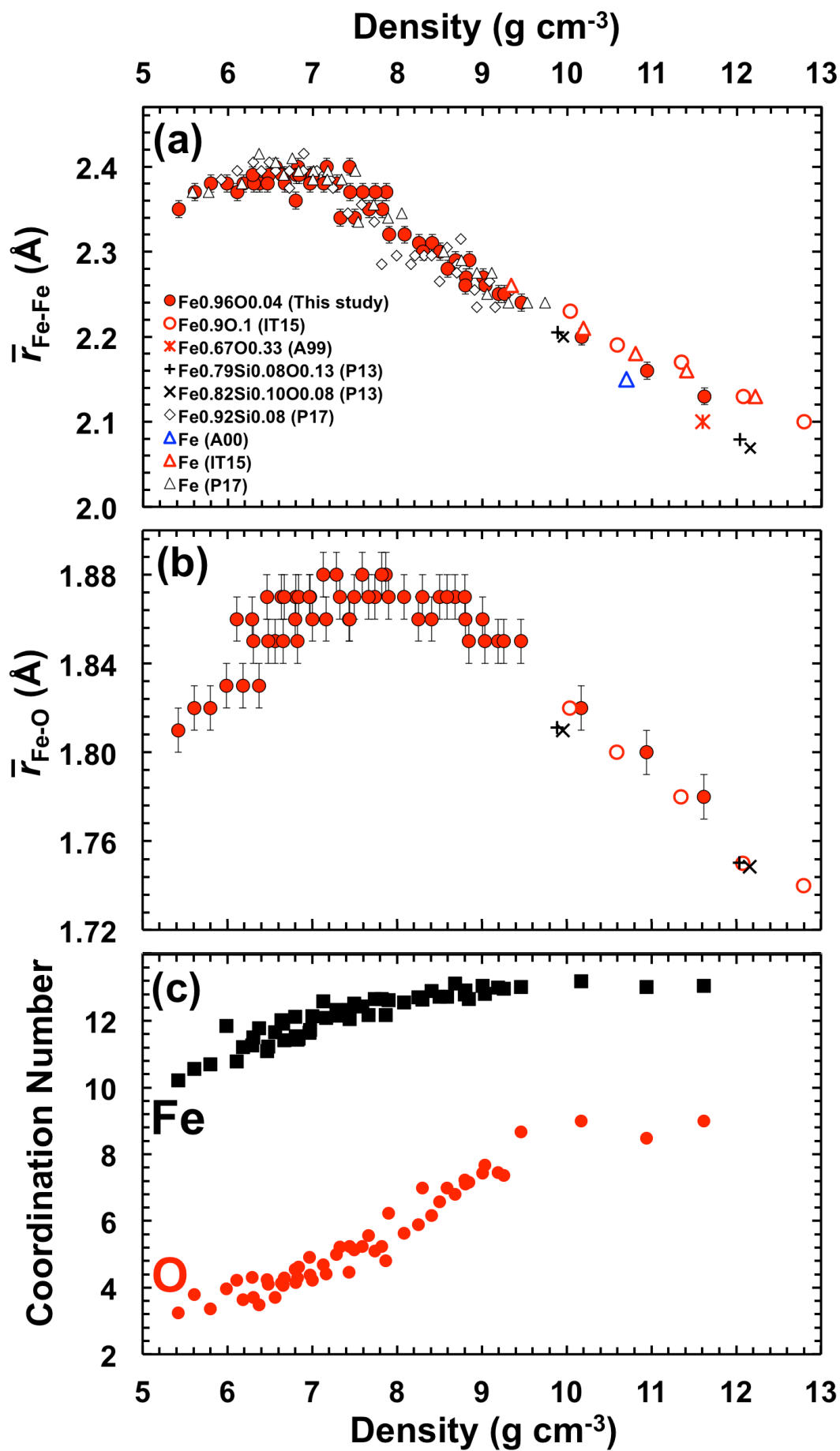


Figure 7.2 (opposite page): Computed structural properties of liquid  $\text{Fe}_{0.96}\text{O}_{0.04}$ . (a) Average interatomic distances between neighboring Fe atoms (filled squares) alongside those previously reported for liquid  $\text{Fe}_{0.9}\text{O}_{0.1}$  (IT15, Ichikawa and Tsuchiya, 2015), liquid  $\text{Fe}_{0.67}\text{O}_{0.33}$  (A99, Alfè et al., 1999),  $\text{Fe}_{0.82}\text{Si}_{0.10}\text{O}_{0.08}$  and  $\text{Fe}_{0.79}\text{Si}_{0.08}\text{O}_{0.13}$  liquids (P13, Pozzo et al., 2013), pure liquid Fe (A00, Alfè et al., 2000; IT15; P17, Posner et al., 2017a) and liquid  $\text{Fe}_{0.92}\text{Si}_{0.08}$  (P17; Posner et al., 2017a) as a function of density. Error bars represent  $\pm 1\sigma$  of the peak position. All liquid compositions show only small variations in the Fe-Fe distance of  $\sim 2.38 \text{ \AA}$  between  $\sim 5.5 \text{ g cm}^{-3}$  and  $\sim 7.6 \text{ g cm}^{-3}$ . Above  $\sim 7.6 \text{ g cm}^{-3}$ , the Fe-Fe distance for all compositions decreases monotonically to  $2.13 \text{ \AA}$  at  $11.620 \text{ g cm}^{-3}$ . (b) Average interatomic distance between Fe and O atoms in liquid  $\text{Fe}_{0.96}\text{O}_{0.04}$  shows an increase with density from  $\sim 1.81 \text{ \AA}$  at  $5.4 \text{ g cm}^{-3}$  to a maximum of  $\sim 1.88 \text{ \AA}$  at  $\sim 8 \text{ g cm}^{-3}$ . Above  $\sim 8 \text{ g cm}^{-3}$ , Fe-O distances decrease monotonically to  $\sim 1.78 \text{ \AA}$  at  $11.620 \text{ g cm}^{-3}$ . Fe-O distances reported for liquid  $\text{Fe}_{0.9}\text{O}_{0.1}$  (IT15) show that this trend continues to at least  $12.8 \text{ g cm}^{-3}$ . (c) Average coordination number of Fe and O in the  $\text{Fe}_{0.96}\text{O}_{0.04}$  simulation cells following Eq. (7.2). Oxygen coordination increases from  $\sim 3.3$  at  $5.4 \text{ g cm}^{-3}$  to  $\sim 8.7$  at  $\sim 9.5 \text{ g cm}^{-3}$ . Above  $\sim 9.5 \text{ g cm}^{-3}$ , the coordination of oxygen remains constant in a range of  $\sim 8.5$  to  $\sim 9$ . Iron coordination increases from  $\sim 10.2$  at  $5.4 \text{ g cm}^{-3}$  to  $\sim 12.6$  at  $\sim 8 \text{ g cm}^{-3}$  and remains approximately constant with increasing density.

#### 7.4.2 Self-diffusion of oxygen and iron

The self-diffusion coefficient for species  $\alpha$ ,  $D_\alpha$ , is calculated from the atomic trajectories in the simulation cell and the asymptotic slope of the time-dependent mean-square displacement (MSD) (Allen and Tildesley, 1991):

$$D_\alpha = \lim_{t \rightarrow \infty} \frac{1}{N_\alpha} \sum_{i=1}^{N_\alpha} \frac{\left\langle \left( r_{i,\alpha}(t+t_0) - r_{i,\alpha}(t_0) \right)^2 \right\rangle}{6t}, \quad (7.2)$$

where  $N_\alpha$  is the total number of atoms of species  $\alpha$ ,  $r_i(t)$  is the position of the

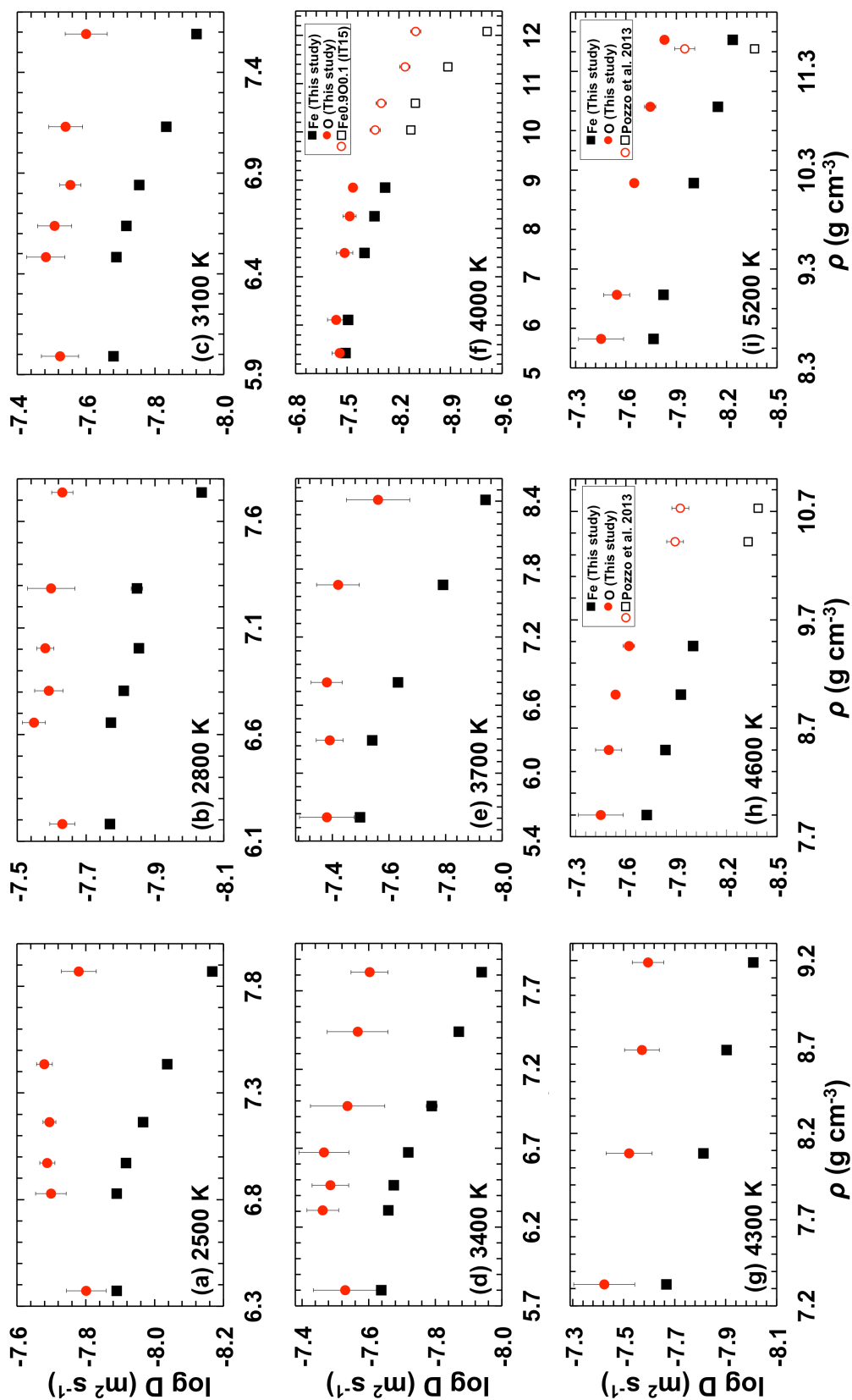


*Figure 7.3 (opposite page): Oxygen (red) and iron (black) self-diffusion coefficients obtained in this study as a function of simulation cell density at different temperatures (Table 7.1). Error bars represent  $\pm 1\sigma$ . Previous computational results for liquid  $Fe_{0.9}O_{0.1}$ , IT15, (Ichikawa and Tsuchiya, 2015) are included in panel f (4000 K) and for liquid  $Fe_{0.82}Si_{0.10}O_{0.08}$  and  $Fe_{0.79}Si_{0.08}O_{0.13}$  compositions (Pozzo et al., 2013) in panels h (4600 K) and i (5200 K). In panels (a) – (f),  $D_{Fe}$  remains approximately constant between the two lowest density points at each  $T$  and then decreases monotonically.  $D_O$  initially increases slightly with density and then remains essentially constant up to  $\sim 8 \text{ g cm}^{-3}$ . Above  $\sim 8 \text{ g cm}^{-3}$ ,  $D_O$  decreases monotonically with density at a rate similar to that of  $D_{Fe}$ .*

$i^{\text{th}}$  atom at time  $t$ , and the angular brackets indicate the ensemble average computed over different origin times,  $t_0$ , along the FP-MD trajectories. Diffusion coefficients calculated using Eq. (7.2) are listed in Table 7.1, together with standard deviations. We show MSD curves and diffusion coefficients of oxygen and iron along a 7 GPa isobar and 5200 K isotherm in Figure SM7.1 in the supplementary material.

Calculated  $D_O$  values change only slightly over the entire  $P$ - $T$  range studied, from  $\sim 1 \times 10^{-8} \text{ m}^2 \text{ s}^{-1}$  to  $\sim 4 \times 10^{-8} \text{ m}^2 \text{ s}^{-1}$ . In general, calculated  $D_{Fe}$  values are 2-4 times slower than  $D_O$ , consistent with previous studies on liquid iron alloys with low oxygen contents ( $X_O \lesssim 0.2$ ) (Pozzo et al. 2013; Ichikawa and Tsuchiya, 2015). Low pressure results are in good agreement with experimental oxygen diffusion data at 7 GPa (Posner et al., 2017b).

The effect of density (i.e. simulation cell volume) on the diffusion coefficient at fixed  $T$  is shown in Figure 7.3. Between the two lowest density points at each  $T$ ,  $D_{Fe}$  remains relatively constant and then decreases monotonically with density. By contrast,  $D_O$  initially increases slightly with

density and then remains essentially constant to  $\sim 8 \text{ g cm}^{-3}$ . Above  $\sim 8 \text{ g cm}^{-3}$ ,  $D_{\text{O}}$  decreases monotonically with density at a rate similar to that of  $D_{\text{Fe}}$  (Figures 7.3g-7.3i). Our results are in good agreement with  $D_{\text{Fe}}$  and  $D_{\text{O}}$  previously reported from simulations of liquids with  $\text{Fe}_{0.9}\text{O}_{0.1}$  (Ichikawa and Tsuchiya, 2015) and liquid  $\text{Fe}_{0.82}\text{Si}_{0.10}\text{O}_{0.08}$  and  $\text{Fe}_{0.79}\text{Si}_{0.08}\text{O}_{0.13}$  compositions (Pozzo et al., 2013) at higher  $P$  and  $T$ , as shown in Figures 7.3f, 7.3h and 7.3i, respectively.

We show the effect of temperature on  $D_{\alpha}$  in Figure 7.4 alongside values previously reported for pure liquid Fe and liquid  $\text{Fe}_{0.92}\text{Si}_{0.08}$  (Posner et al., 2017a). At fixed  $P$ , the Arrhenian activation enthalpy ( $\Delta H_{\alpha}$ ) is defined as

$$\frac{\partial \ln D_{\alpha}}{\partial (1/T)} = -\frac{\Delta H_{\alpha}(P)}{R} \quad (7.3)$$

where  $R$  is the gas constant. At the lowest isobars investigated,  $\Delta H$  values are similar ( $\sim 50 \text{ kJ mol}^{-1}$ ) for all species and compositions. With increasing  $P$ , however,  $\Delta H_{\text{O}}$  remains essentially constant while  $\Delta H_{\text{Fe}}$  increases monotonically by a factor of two at 135 GPa, similar to the behavior of  $\Delta H_{\text{Fe}}$  for pure Fe and  $\Delta H_{\text{Si}}$  for Fe-Si liquid.

For further comparison, we show an Arrhenius diagram alongside experimental oxygen diffusion data between 1 bar and 18 GPa (Posner et al., 2017b; Shurygin and Kryuk, 1963; Suzuki and Mori, 1971) in Figure 7.5. It can be seen that calculated  $D_{\text{O}}$  values increase with pressure between 1 bar and 5 GPa and then decrease slightly. For example,  $D_{\text{O}}$  values at 2800 K are virtually indistinguishable between 1 bar and 25 GPa (Table 7.1). Similarly, low pressure experimental data show a negligible effect of pressure and Posner et al. (2017b) report an activation volume of  $0.1 \pm 0.1 \text{ cm}^3 \text{ mol}^{-1}$ . Beyond the range of the experiments ( $\gtrsim 25 \text{ GPa}$ ), however, calculated  $D_{\text{O}}$  values decrease with  $P$ . Our findings are similar to those reported for several silicate melt

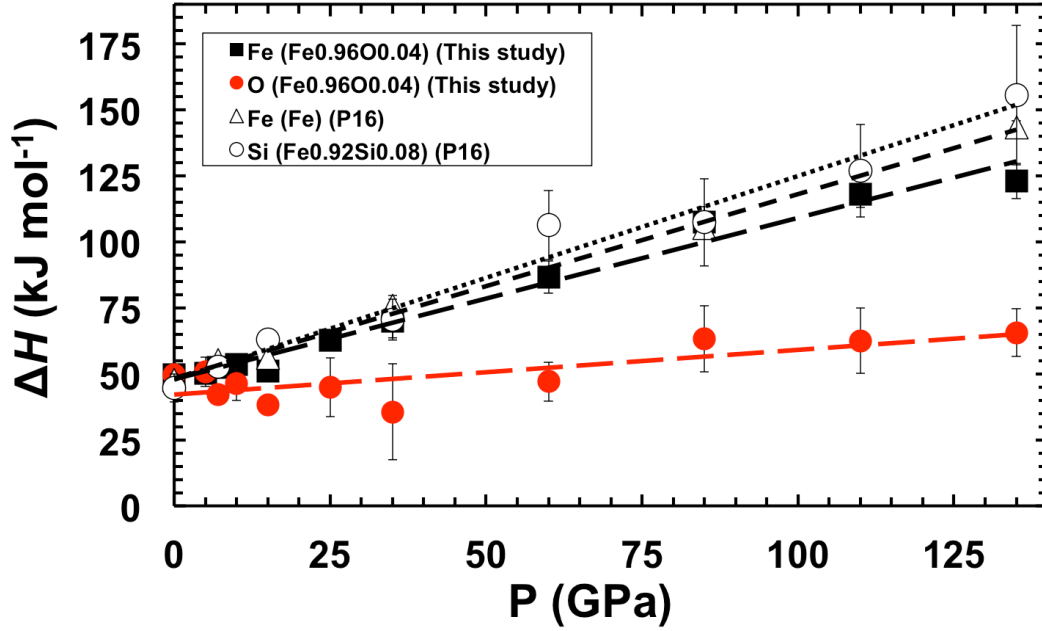


Figure 7.4: Activation enthalpy,  $\Delta H$ , of diffusion in liquid  $Fe_{0.96}O_{0.04}$  (this study), liquid Fe and liquid  $Fe_{0.92}Si_{0.08}$  (Posner et al., 2017a) as a function of pressure to 135 GPa. Vertical error bars represent  $\pm 1\sigma$  uncertainty in  $\Delta H$ . At pressures below  $\sim 10$  GPa,  $\Delta H$  values for all species and compositions are similar ( $\sim 50$  kJ mol $^{-1}$ ). With increasing  $P$ ,  $\Delta H_O$  remains essentially constant within error, while  $\Delta H_{Fe}$ ,  $\Delta H_{Fe,pure}$  and  $\Delta H_{Si}$  increase monotonically at approximately the same rate ( $\sim 0.7$  kJ mol $^{-1}$  GPa $^{-1}$ ). At 135 GPa,  $\Delta H_{Fe}$  is twice as large as  $\Delta H_O$  in liquid  $Fe_{0.96}O_{0.04}$ .

compositions where anomalous maxima in Si and/or O self-diffusivities – or complimentary localized minima in melt viscosity – have been reported to correspond to an increase in Si and/or Al coordination (Reid et al., 2001; 2003; Liebske et al. 2005; Wang et al., 2014; Ni et al., 2015), as described previously.

The difference between  $D_{Fe}$  and  $D_O$ , expressed by a ratio  $D_O/D_{Fe}$ , increases approximately linearly with density from  $\sim 0.1$  to  $\sim 0.4$  log units between  $5.421$  g cm $^{-3}$  and  $11.620$  g cm $^{-3}$  (Figure 7.6), in agreement with results

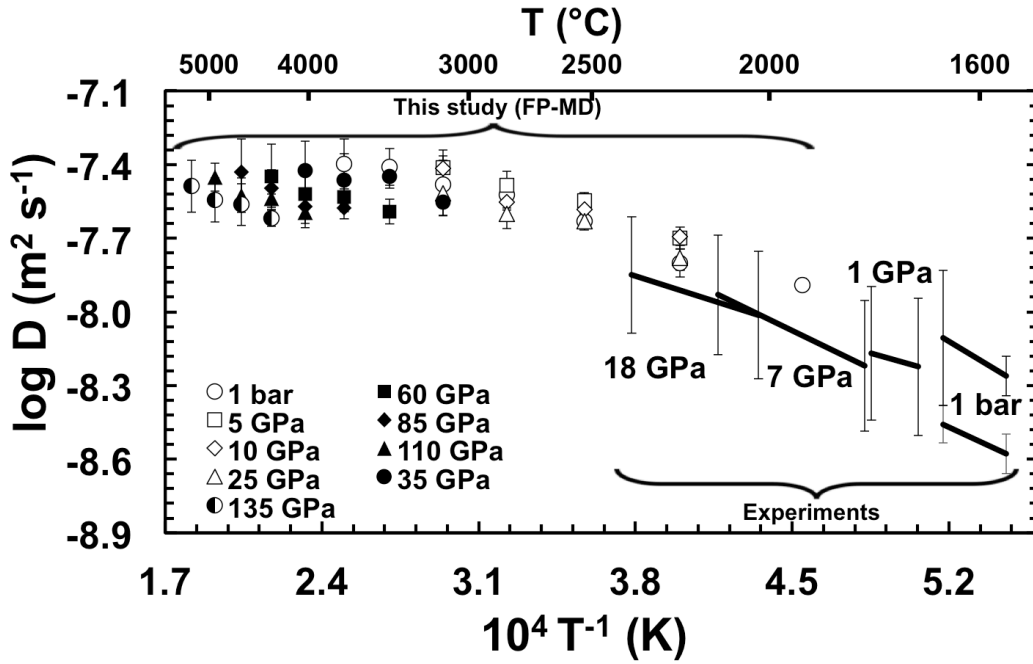


Figure 7.5: Arrhenius diagram of oxygen diffusion obtained in the present study (symbols) and from experimental studies (curves) (Posner et al., 2017b; Shurygin and Kryuk, 1963; Suzuki and Mori, 1971) as a function of inverse temperature, evaluated at constant pressure. Error bars represent  $\pm 1\sigma$ .  $D_O$  increases with pressure between 1 bar (open circles) and 5 GPa (open squares) and then decreases slightly. For example, oxygen diffusion coefficients at  $\sim 2500$  °C are virtually indistinguishable between 1 bar and 25 GPa. Similarly, low pressure experimental data show negligible change in  $D_O$  below  $\sim 18$  GPa. Above  $\sim 25$  GPa (beyond the range of the experiments), there is a discernable effect of  $P$  on diffusivity, with  $D_O$  decreasing with  $P$ .

from simulations conducted at higher densities (Pozzo et al., 2013; Ichikawa and Tsuchiya, 2015), such that  $D_O$  is  $\sim 2.5$  times greater than  $D_{Fe}$  at the density of the inner core boundary. While the atomic size misfit between iron and oxygen is found to decrease with density, their coordinations remain significantly different (Figure 7.2). The increasing difference between  $D_O$  and

$D_{\text{Fe}}$  observed over the same interval negates that oxygen behaves more ‘iron-like’ upon compression.

### 7.4.3 Implications for planetary cores

The nature and concentrations of alloying elements that partitioned into the core largely depend on the conditions of metal-silicate segregation as well as on the effects of  $P$ - $T$ - $X$ - $f_{\text{O}_2}$  on the chemical potentials of light element components in relevant metal and silicate phases. Knowledge of the incorporation mechanism of oxygen and other solutes can, in principle, provide the basis for developing a predictive model for estimating the effect of  $P$  and  $T$  on a solute’s chemical potential in liquid iron.

It is well known from steelmaking that carbon, which has a similar atomic radius to that of oxygen, is nearly two orders of magnitude more soluble in close-packed  $\gamma$ -Fe (austenite) than in bcc-structural  $\alpha$ -Fe (ferrite) owing to differences in strain energy (Goldschmidt, 1967). The increased abundance of close-packed Fe and octahedrally coordinated oxygen in liquid  $\text{Fe}_{0.96}\text{O}_{0.04}$  at  $\sim 8 \text{ g cm}^{-3}$  predicted here (Figure 7.2) therefore provides a reasonable explanation for the previously reported increase in the pressure effect on oxygen solubility from metal-oxide partition experiments (Asahara et al., 2007; Ozawa et al., 2008; Frost et al., 2010), although additional information regarding the relative dissolution energetics associated with different void sizes is required to fully quantify this effect. Increasing oxygen solubility in liquid iron at densities  $\gtrsim 8 \text{ g cm}^{-3}$  will influence the redox potential of other alloying elements, which therefore has important consequences for the composition of the core.

The solute incorporation mechanism operating under  $P$ - $T$  conditions on either side of the inner core-outer core boundary exerts controls on the

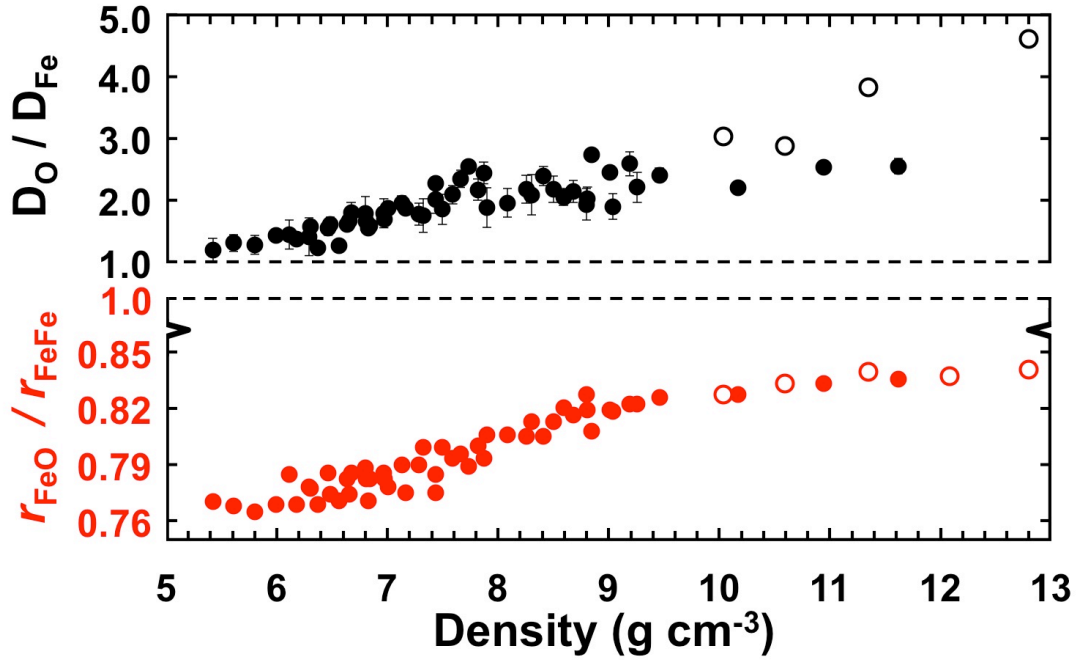


Figure 7.6: Mass transport (black) and nearest neighbor distance (red) ratios of oxygen and iron in liquid  $Fe_{0.96}O_{0.04}$  as a function of density. Vertical error bars represent  $\pm 1\sigma$ . Open symbols are for liquid  $Fe_{0.9}O_{0.1}$  simulations reported by Ichikawa and Tsuchiya (2015). With increasing density, the difference between  $D_O$  and  $D_{Fe}$  increases while average Fe-O and Fe-Fe distances become more similar, although they remain significantly different.

partition coefficient between solid and liquid Fe alloy and thus extent of light element enrichment in the liquid outer core that drives compositional convection. The average oxygen coordination of approximately 8-9 at outer core densities (Figure 7.2) implies local CsCl-type (B2) packing around oxygen, as predicted by Ozawa et al. (2011) which distorts the bulk close-packing of iron atoms. These findings also support previous suggestions by Alfè et al. (1999) that oxygen should partition strongly into the liquid upon core crystallization due to its small size relative to iron, while silicon and

sulfur, with atomic radii similar to that of iron, should have liquid-solid partition coefficients close to unity.

## 7.5 Conclusions

A change in the dominant compression mechanism in liquid  $\text{Fe}_{0.96}\text{O}_{0.04}$  is observed at approximately  $8 \text{ g cm}^{-3}$ . Below this density, compression is accommodated by a closer packing of both iron and oxygen with coordination numbers increasing from  $\sim 10.2$  to  $\sim 12.6$  and  $\sim 3.4$  to  $\sim 6$ , respectively. This structural change coincides with lengthening of average Fe-O distances while average Fe-Fe distances remain constant. Over this density range, the diffusivity of oxygen remains essentially constant along isotherms, in agreement with experimental data up to 18 GPa (Posner et al., 2017b). For densities  $\gtrsim 8 \text{ g cm}^{-3}$ , the liquid is essentially close-packed and compression is accommodated by reduction in the atomic volumes of Fe and O, with the former compressing approximately twice as fast as the latter. There is an increased (i.e. positive) effect of pressure on  $D_{\text{O}}$  above this density.

Our findings are consistent with a previous high pressure experimental study on liquid  $\text{B}_2\text{O}_3$  by Brazhkin et al. (2010) who related an increase in the position of the principle peak in the RDF increase in B coordination to a negative activation volume of viscosity. This structural compression mechanism and its associated anomalous transport phenomena are therefore likely common for liquids with significant size mismatches of solute and solvent atoms. Such structural changes will likely influence (i.e increase) a solute's solubility and its partitioning between coexisting liquid and solid, e.g. at the inner-core boundary. Based on this observation, the structural properties of liquid iron with small alloy species (i.e. H, He, C, N) warrant

further investigation as they may also undergo a sign change in the pressure dependence of their solubility in liquid iron.

## 7.6 Acknowledgements

We would like to thank James Van Orman and an anonymous reviewer for their very helpful and constructive comments. D.C.R. and E.S.P. were supported by the European Research Council (ERC) Advanced Grant “ACCRETE” (Contract No. 290568) and by the German Research Foundation (DFG) Priority Programme SPP1385 "The First 10 Million Years of the Solar System - a planetary materials approach" (Ru1323/2). G.S.N. and V.V. were supported by DFG grant STE1102/10 in the Priority Programme SPP1488 “Planetary Magnetism”. V.V. was also supported by the Minerva Foundation of the Max Planck Society for his work at The Hebrew University of Jerusalem. Computations were performed at the Leibniz Supercomputing Centre of the Bavarian Academy of Sciences and the Humanities.

## 7.7 References

- Alfè D., Price G.D. and Gillan M. (1999) Oxygen in the Earth’s core: a first-principles study. *Phys. Earth. Planet. Inter.* **110**, 191-210.
- Alfè D., Kresse G. and Gillan M.J. (2000) Structure and dynamics of liquid iron under Earth’s core conditions. *Phys. Rev. B* **61**, 132-142.
- Allègre C. J., Poirier J.-P., Humler E. and Hofmann A. W. (1995) The chemical composition of the Earth. *Earth Planet. Sci. Lett.* **134**, 515–526.
- Allen M.P. and Tildesley D.J. (1991) *Computer Simulation of Liquids*, pp. 182–208, Clarendon Press, Oxford.

Anderson H.C. (1980) Molecular dynamic simulations at constant pressure and/or temperature. *J. of Chem. Phys.* **72**, 2384-2393.

Angel C.A., Cheeseman P.A. and Tamaddon S. (1982) Pressure Enhancement of Ion Mobilities in Liquid Silicates from Computer Simulation Studies to 800 Kilobars. *Science* **218**, 885-887.

Asahara Y., Frost D.J. and Rubie D.C. (2007) Partitioning of FeO between magnesiowüstite and liquid iron at high pressures and temperatures: Implications for the compositions of the Earth's outer core. *Earth Planet. Sci. Lett.* **257**, 435-559.

Birch F. (1952) Elasticity and constitution of the Earth's interior. *J. Geophys. Res.* **57**, 227-286.

Brazhkin V.V., Kanzaki M., Funakoshi K. and Katayama Y. (2009) Viscosity behavior spanning four orders of magnitude in As-S melts under high pressure. *Phys. Rev. Lett.* **102**, 115901.

Brazhkin V.V., Farnan I., Funakoshi K., Kanzaki M., Katayama Y., Lyapin A.G. and Saitoh H. (2010) Structural transformation and anomalous viscosity in the B<sub>2</sub>O<sub>3</sub> melt under high pressure. *Phys. Rev. Lett.* **105**, 115701.

Campbell F.C. (2008) Elements of Metallurgy and Engineering Alloys, pp. 95-112, ASM International, Materials Park, Ohio.

de Koker N., Steinle-Neumann G. and Vlček V. (2012) Electrical resistivity and thermal conductivity of liquid Fe alloys at high P and T, and heat flux in Earth's core. *Proc. Nat. Acad. Sci.* **109**, 4070-4073.

Fischer R.A., Nakajima Y., Campbell A.J., Frost D.J., Harries D., Langenhorst F., Miyajima N., Pollok K. and Rubie D.C. (2015) High pressure metal-silicate partitioning of Ni, Co, V, Cr, Si and O. *Geochim. Cosmochim. Acta* **167**, 177-194.

Frost D.J., Asahara Y., Rubie D.C., Miyajima N., Dubrovinsky L.S., Holzapfel C., Ohtani E., Miyahara M. and Sakai T. (2010) Partitioning of oxygen between the Earth's mantle and core. *J. Geophys. Res.* **115**, B02202. doi:10.1029/2009JB006302.

- Goldschmidt H.J. (1967) *Interstitial Alloys*, pp.60–87, Plenum, New York.
- Ichikawa H. and Tsuchiya T. (2015) Atomic transport property of Fe-O liquid alloys in the Earth's outer core  $P,T$  condition. *Phys. Earth Planet. Int.* **247**, 27-35.
- Kono Y., Kenney-Benson C., Park C., Shen G., and Wang Y. (2013) Anomaly in the viscosity of liquid KCl at high pressures. *Phys. Rev. B* **87**, 024302.
- Kresse G. and Furthmüller J. (1996) Efficient iterative schemes for *ab initio* total-energy calculations using a plane-wave basis set. *Phys. Rev. B.* **54**, 11169.
- Kresse G. and Joubert J. (1999) From ultrasoft pseudopotentials to the projector augmented-wave method. *Phys. Rev. B* **59**, 1758.
- Liebske C., Schmickler B., Terasaki H., Poe B.T., Suzuki A., Funakoshi K., Ando R. and Rubie D.C. (2005) Viscosity of peridotite liquid up to 13 GPa: implications for magma ocean viscosities. *Earth Planet. Sci. Lett.* **240**, 589-604.
- Lu X.-G., Selleby M. and Sundman B. (2005a) Implementation of a new model for pressure dependence of condensed phases in Thermo-Calc. *Comp. Coupl. Phase Diag. Thermochem.* **29**, 49-55.
- Lu X.-G., Selleby M. and Sundman B. (2005b) Assessments of molar volume and thermal expansion for selected bcc, fcc and hcp metallic elements. *Comp. Coupl. Phase Diag. Thermochem.* **29**, 68-89.
- McDonough W. F. (2003) Compositional model for the Earth's core. In *Treatise on Geochemistry*, vol. 2 (ed. R. W. Carlson), pp.547–568, Elsevier, Oxford
- Ni H., Hui H., and Steinle-Neumann G. (2015) Transport properties in silicate melts. *Rev. Geophys.* **53**, 715-744.
- O'Neill H. S. C., Canil D. and Rubie D.C. (1998) Oxide-metal equilibria to 2500°C and 25 GPa: Implications for core formation and the light component in the Earth's core, *J. Geophys. Res.*, **103**, 239–260.

Ozawa H., Hirose K., Mitome M., Bando Y., Sata N. and Ohishi Y. (2008) Chemical equilibrium between ferropericlase and molten iron to 134 GPa and implications for iron content at the bottom of the mantle. *Geophys. Res. Lett.* **35**, L05308, doi:10.1029/2007GL032648.

Ozawa H., Takahashi F., Hirose K., Ohishi Y. and Hirao N. (2011) Phase transition of FeO and stratification in Earth's outer core. *Science* **334**, 792-794.

Perdew J.P., Burke K. and Wang Y. (1996) Generalized gradient approximation for the exchange-correlation hole of a many-electron system. *Phys. Rev. B* **54**, 533-539.

Posner E.S., Rubie D.C., Frost D.J., Vlček V. and Steinle-Neumann G. (2017a) High P-T experiments and first principles calculations of the diffusion of Si and Cr in liquid iron. *Geochim. Cosmochim. Acta.* **203**, 323–342.

Posner E.S., Rubie D.C., Frost D.J., and Steinle-Neumann G. (2017b) Experimental determination of oxygen diffusion in liquid iron at high pressure. *Earth Planet. Sci. Lett.* **464**, 116–123.

Poirier J.-P. (1994) Light elements in the Earth's outer core: A critical review. *Phys. Earth Planet. Int.* **85**, 319–337.

Pozzo M., Davies C., Gubbins D. and Alfè D. (2013) Transport properties for liquid silicon-oxygen-iron mixtures at Earth's core conditions. *Phys. Rev. B.* **87**, DOI: 10.1103/PhysRevB.87.014110.

Reid J.E., Poe B.T., Rubie D.C., Zotov N., and Wiedenbeck M. (2001) The self-diffusion of silicon and oxygen in diopside ( $\text{CaMgSi}_2\text{O}_6$ ) liquid up to 15 GPa. *Chem. Geol.* **174**, 77-86.

Reid J.E., Suzuki A., Funakoshi K.-I., Terasaki H., Poe B.T., Rubie D.C., and Ohtani E. (2003) The viscosity of  $\text{CaMgSi}_2\text{O}_6$  liquid at pressures up to 13 GPa. *Phys. Earth Planet. Int.* **139**, 45-54.

Rubie D.C., Jacobson S.A., Morbidelli A., O'Brien D.P., Young E.D., de Vries J., Nimmo F., Palme H. and Frost D.J. (2015) Accretion and differentiation of the terrestrial planets with implications for the compositions of early-formed Solar System bodies and accretion of water. *Icarus* **248**, 89-108.

Sanloup C., Guyot F., Gillet P., Fiquet G., Hemley R.J., Mezouar M. and Martinez I. (2000) Structural changes in liquid Fe at high pressures and temperatures from synchrotron X-ray diffraction. *Europhys. Lett.* **52**, 151-157.

Shen G., Prakapenka V.B., Rivers M.L. and Sutton S.R. (2004) Structure of liquid iron at pressures up to 58 GPa. *Phys. Rev. Lett.* **92**, 185701.

Shibazaki Y., Kono Y. and Fei Y. (2015) Microscopic structural change in a liquid Fe-C alloy of ~5 GPa. *Geophys. Res. Lett.* **42**, 5236-5242.

Shurygin P.M. and Kryuk V.I. (1963) Oxygen diffusion in iron and copper melts. *Izv. Akad. Nauk SSSR, Metall. Gorn. Delo.* **3**, 94.

Siebert J., Badro J., Antonangeli D. and Ryerson F. J. (2013) Terrestrial accretion under oxidizing conditions. *Science* **339**, 1194–1197.

Suzuki K. and Mori K. (1971) Diffusion of oxygen in molten iron. *J. Iron Steel Inst. Jpn.* **57**, 2219-2229.

Vočadlo L., de Wijs G.A., Kresse G., Gillan M., and Price G.D. (1997) First principles calculations on crystalline and liquid iron at Earth's core conditions. *Faraday Discuss.* **106**, 205-217.

Wang Y., Sakamaki T., Skinner L.B., Jing Z., Yu T., Kono Y., Park C., Shen G., Rivers M.L. and Sutton S.R. (2014) Atomistic insight into viscosity and density of silicate melts under pressure. *Nature Comm.* **5**, 3241.

Waseda Y. and Suzuki K. (1970) Atomic distribution and magnetic moment in liquid iron by neutron diffraction. *Phys. Status Solidi.* **39**, 669-678.

Waseda Y. and Ohtani M. (1974) Static structure of liquid noble and transition metals by X-ray diffraction. *Phys. Status Solidi.* **62**, 535-546.

## 7.8 Supplemental Material

The Supplemental Material contains the following information:

- Fig SM7.1 showing the calculated mean squared displacement and diffusion coefficients of oxygen and iron in liquid  $\text{Fe}_{0.96}\text{O}_{0.04}$

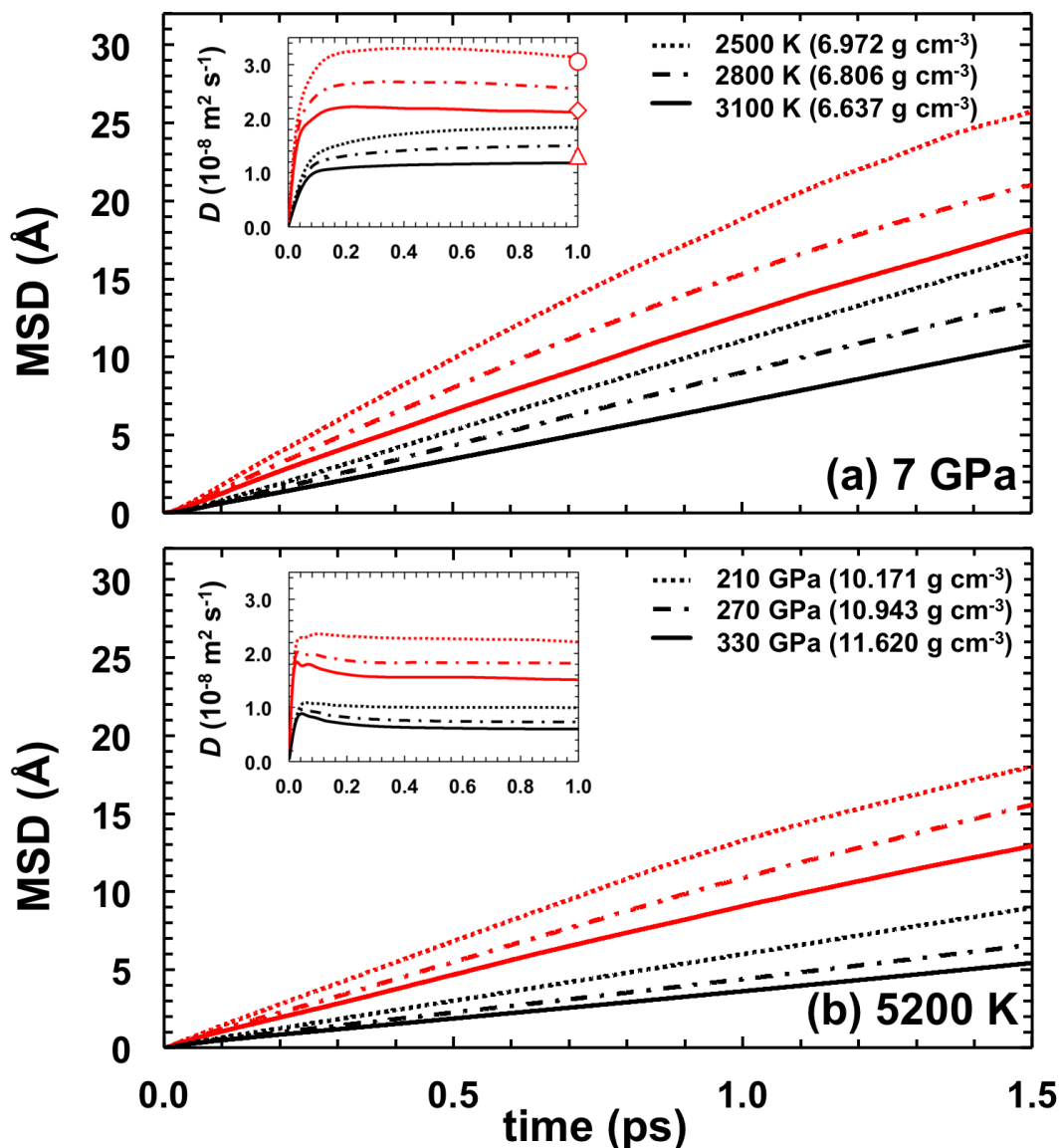


Figure SM7.1: Mean-square displacements of oxygen (red) and iron (black) calculated from the simulation of liquid  $\text{Fe}_{0.96}\text{O}_{0.04}$  along a (a) 7 GPa isobar and at various temperatures and (b) 5200 K isotherm and different densities. Insets show time-dependent diffusion coefficients  $D_x(t)$  for each species computed here.  $D_{\text{O}}$  is 2-4 times faster than  $D_{\text{Fe}}$  over the full  $P$ - $T$  range of study. Extrapolations of experimental data (Posner et al., 2017b) are represented as triangles, diamonds and circles at  $T$  of 2500 K, 2800 K, 3100 K at 7 GPa, respectively (panel a).



## Conclusions and Outlook

The experimental and computational results of mass transport and structural properties of liquid iron alloys obtained in this study provide new insights into the structure and processes of the Earth's core and formation. Most notably, the verification of the homologous temperature relation for diffusive transport (Chapter 5), kinetic constraint on the maximum size of descending liquid metal droplets to achieve chemical equilibration in a magma ocean (Chapter 6), and verification of a structural transition in liquid  $\text{Fe}_{0.96}\text{O}_{0.04}$  around  $8 \text{ g cm}^{-3}$  (Chapter 7) unveil a breadth of new understanding regarding the behavior of liquid iron alloys and their role in Earth history.

The relationship between liquid structure (i.e. local-packing environment, incorporation mechanism, etc.) and the solubility of a solute species is particularly interesting for broad picture questions regarding the effects of pressure and temperature on the equilibrium composition of core-forming liquids, as well as to estimate the solid-liquid partition coefficient of relevant light elements at inner-core boundary conditions. We are therefore continuing the approach outlined in Chapter 7 to investigate the transport and structural properties of different iron alloy compositions to include other important light elements (carbon, sulfur, nitrogen, hydrogen, and helium), as well as magnesium, xenon, and nickel, over a wide range of  $P$ - $T$  conditions (0 – 330 GPa, 2500 – 4500 K).

Preliminary results show that the compression trends and average coordination numbers of carbon and nitrogen are similar to those reported for oxygen (Chapter 7). Hydrogen is significantly smaller with a maximum coordination number of approximately six at inner-core boundary densities. At low  $P$ , magnesium is larger and more compressible than iron, such that the two species are approximately the same size at inner-core boundary pressures. Nickel and silicon behave very similarly to iron. Interestingly, helium and xenon atoms in the simulations are found to rapidly cluster (exsolve) from iron at low pressures. Finally, sulfur shows a wide range of incorporation mechanisms with coordination numbers from  $\sim 4$  to  $\sim 12$  from surface to core pressures. The results from this fourth project will be submitted for publication.

Additional experimental studies of solute diffusion in liquid iron should be performed to test the validity of the homologous temperature relation for additional compositions, as well as to test if the  $P$  dependence of oxygen diffusion in liquid iron does, in fact, increase at  $P$  higher than those explored here (Chapter 6), as predicted from the computations (Chapter 7). Use of the double chamber capsule design (Figure 2.2) will quicken the experimental data collection process. The numerical code used to model diffusion profiles that formed during non-isothermal annealing (Section 5.3.4) may be made available as open domain software in the future to help other researchers accurately model diffusion in low viscosity liquids. In the meantime, we are using this approach to model quenched self-diffusion (isotopic) profiles of Si, O, Mg, and Ca – as well as Ni and Co tracer concentration profiles – in peridotite melt from diffusion experiments performed between 4-24 GPa in a multi-anvil apparatus. Preliminary results show localized minima and maxima in the diffusion coefficient of all species as a function of  $P$ , which can be explained by structural changes within the liquid similar to those identified in Chapter 7.

## (Eidesstattliche) Versicherungen und Erklärungen

(§ 8 S. 2 Nr. 6 PromO)

*Hiermit erkläre ich mich damit einverstanden, dass die elektronische Fassung meiner Dissertation unter Wahrung meiner Urheberrechte und des Datenschutzes einer gesonderten Überprüfung hinsichtlich der eigenständigen Anfertigung der Dissertation unterzogen werden kann.*

(§ 8 S. 2 Nr. 8 PromO)

*Hiermit erkläre ich eidesstattlich, dass ich die Dissertation selbständig verfasst und keine anderen als die von mir angegebenen Quellen und Hilfsmittel benutzt habe.*

(§ 8 S. 2 Nr. 9 PromO)

*Ich habe die Dissertation nicht bereits zur Erlangung eines akademischen Grades anderweitig eingereicht und habe auch nicht bereits diese oder eine gleichartige Doktorprüfung endgültig nicht bestanden.*

(§ 8 S. 2 Nr. 10 PromO)

*Hiermit erkläre ich, dass ich keine Hilfe von gewerblichen Promotionsberatern bzw. -vermittlern in Anspruch genommen habe und auch künftig nicht nehmen werde.*

Bayreuth, 02.02.2017

---

Ort, Datum, Unterschrift